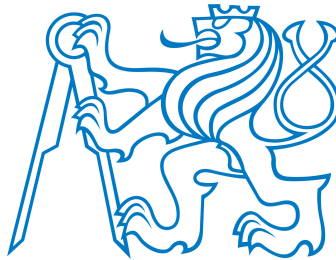


**Czech Technical University in Prague**

Faculty of Electrical Engineering

Department of Physics



**Electrical Properties of Doped Diamond in High  
Electric Field**

Doctoral Thesis

**Ing. Nicolas Lambert, M.Sc.**

In Prague, 2022

Ph.D. Study Programme: P0533D110030 "Applied Physics"

Supervisor: Dr. Vincent Mortet, Ph.D.

Supervisor Specialist: Prof. RNDr. Bohuslav Rezek, Ph.D.

---

## Abstract

In this thesis, the growth of boron-doped and phosphorus-doped diamond layers was studied. A novel technique involving intermittent gas flows was developed to increase the incorporation of phosphorus atoms in diamond during the growth. Using this method, polycrystalline phosphorus-doped diamond layers were grown on (100) oriented Si substrates with a  $sp^3/sp^2$  carbon ratio over 75% and a phosphorus concentration up to  $7.1 \times 10^{20} \text{ cm}^{-3}$  were grown. Epitaxial boron-doped diamond layers with a boron concentration up to  $6.3 \times 10^{19} \text{ cm}^{-3}$  were also grown on (100) oriented diamond substrates. The crystalline quality of the layers was assessed using Raman spectroscopy, and their dopant concentration was determined by glow discharge optical emission spectroscopy and secondary ion mass spectroscopy. The current multiplication and negative differential resistance observed at high electric field in the boron-doped diamond layers were specifically studied. Quasi-static current-voltage characteristics were measured using a transmission-line pulse setup with 100 ns pulse duration. Experimental results were correlated with simulation by finite element method considering self-heating effect and impurity impact ionization. The key results of the thesis are: (i) the successful simulation of current multiplication and negative differential resistance observed at high electric field in boron-doped diamond layers, and (ii) the production of high quality polycrystalline phosphorus-doped diamond layers with record high phosphorus content using pulsed gas growth method.

**Keywords:** boron-doped diamond; phosphorus-doped diamond; plasma enhanced chemical vapor deposition; pulsed gas flow; transmission line pulse generator; impurity impact ionization; self-heating effect; finite element method.

---

## Abstrakt

V této práci byl studován růst diamantových vrstev dopovaných borem a fosforem. Byla vyvinuta nová metoda zahrnující pulzní proudění plynu pro zvýšení inkorporace atomů fosforu do diamantu během procesu růstu. Pomocí této metody byly vypěstovány fosforem dopované polykrystalické diamantové vrstvy na (100) orientovaných Si substrátech s poměrem  $sp^3/sp^2$  uhlíku nad 75% a s koncentrací fosforu až  $7.1 \times 10^{20} \text{ cm}^{-3}$ . Epitaxní diamantové vrstvy dopované bórem s koncentrací bóru až  $6.3 \times 10^{19} \text{ cm}^{-3}$  byly rovněž vypěstovány na (100) orientovaných diamantových substrátech. Krystalická kvalita vrstev byla posouzena pomocí Ramanovy spektroskopie a jejich koncentrace dopantu byla stanovena optickou emisní spektroskopií a hmotnostní spektroskopií sekundárních iontů. Bylo studováno násobení proudu a záporný diferenciální odpor pozorovaný při vysokém elektrickém poli v borem dopovaných diamantových vrstvách. Kvazistatické proudově-napěťové charakteristiky byly měřeny pomocí nastavení impulsů na přenosové lince s dobou trvání impulsu 100 ns. Experimentální výsledky byly korelovány se simulací metodou konečných prvků, která zohledňuje efekt samoohřevu a nárazovou ionizaci nečistot. Klíčovými výsledky práce jsou: (i) úspěšná simulace násobení proudu a záporného diferenciálního odporu pozorovaného při vysokém elektrickém poli v borem dopovaných diamantových vrstvách, a (ii) výroba vysoce kvalitních polykrystalických fosforem dopovaných diamantových vrstev s rekordně vysokým obsahem fosforu metodou pulzního růstu v plynu.

**Klíčová slova:** diamant dopovaný borem; diamant dopovaný fosforem; plazmové nanášanie rozkladem pár; pulzní průtok plynu; pulsní generátor přenosové linky; ionizace nárazem nečistot; samozahřívací efekt; metoda konečných prvků.

---

## Acknowledgments

I would like to first thank my supervisor Dr. Vincent Mortet for his continuous support and guidance during my PhD research. He was always there to answer my questions about my scientific activities or writing.

I would like to thank Prof. Bohuslav Rezek for his scientific advice and his help with the administrative tasks at the University.

I would like to thank Assoc. Prof. Dionyz Pogany for letting me work in his laboratory in the Vienna University of Technology in the framework of the AKTION scholarship program.

I would like to gratefully acknowledge the financial support provided by the GACR projects 20-11140S "Essential Elements of Diamond Power Electronics" and 21-03538S "New Perspectives in Microwave Plasma Synthesis of Doped Diamond", and the student project SGS21/057/OHK3/1T/13 "Phosphorous n-type doped diamond growth using pulsed gas in chemical vapour deposition".

I would like to thank Dr. Karel Řezáč for accepting me as a member of his project SGS22/161/OHK3/3T/13 "Electric Discharges III: experimental research, modeling and applications". It provided me precious additional support for my PhD study.

My sincere thanks also go my colleagues of the Department Functional Materials for making my work at the Institute of Physics a memorable and delightful experience.

Finally, I must express my very profound gratitude to my parents, my family, and my girlfriend for the unfailing support and continuous encouragement they provided during my doctoral studies.

---

## **Declaration**

Hereby I declare, that this thesis entitled “Electrical Properties of Doped Diamond in High Electric Field” has been written by me in its entirety as the result of my own original research. I have acknowledged all the sources of information which have been used in the Thesis in compliance with the Methodological Instruction No. 1/2009 - On maintaining ethical principles when working on a university final project.

Ing. Nicolas Lambert, M.Sc.

A handwritten signature in black ink, appearing to be 'N. Lambert', written in a cursive style.

# Contents

<b>Aims of the Thesis</b>	<b>21</b>
<b>Introduction</b>	<b>22</b>
<b>I STATE OF THE ART</b>	<b>25</b>
<b>1 Diamond Material</b>	<b>26</b>
1.1 Diamond Structure . . . . .	26
1.2 Classification of Diamond . . . . .	27
1.3 Properties . . . . .	29
1.4 Diamond Devices . . . . .	33
1.5 Conclusion . . . . .	36
<b>2 Diamond Growth</b>	<b>37</b>
2.1 Carbon Pressure-Temperature Diagram . . . . .	37
2.2 Chemical Vapor Deposition (CVD) . . . . .	39
2.2.1 Microwave Plasma Enhanced Chemical Vapor Deposition (MWPECVD) . . . . .	41
2.2.2 Role of the Different Precursor Gases . . . . .	49

2.2.3	Influence of the Growth Parameters . . . . .	55
2.3	Diamond Doping . . . . .	59
2.3.1	Diamond P-Type Doping . . . . .	59
2.3.2	Diamond N-Type Doping . . . . .	62
2.3.3	Surface Conductivity . . . . .	66
2.4	Conclusion . . . . .	67
<b>II</b>	<b>EXPERIMENTAL</b>	<b>69</b>
<b>3</b>	<b>MWPECVD Reactors</b>	<b>70</b>
3.1	Reactor Types . . . . .	70
3.1.1	Bell Jar (ASTeX-Type) Reactor . . . . .	70
3.1.2	Tubular (NIRIM-Type) Reactor . . . . .	71
3.2	MWPECVD Reactor Time Response Measurement Setup . . . . .	72
<b>4</b>	<b>Characterization Techniques</b>	<b>75</b>
4.1	Atomic Force Microscopy (AFM) . . . . .	76
4.1.1	AFM Theory . . . . .	76
4.1.2	AFM Setup . . . . .	77
4.2	Scanning Electron Microscopy (SEM) . . . . .	78
4.2.1	SEM Theory . . . . .	78
4.2.2	SEM Setup . . . . .	80
4.3	Secondary Ion-Mass Spectroscopy (SIMS) . . . . .	81
4.3.1	SIMS Theory . . . . .	81
4.3.2	SIMS Setup . . . . .	83
4.4	Glow Discharge Optical Emission Spectroscopy (GDOES) . . . . .	83

4.4.1	GDOES Theory . . . . .	83
4.4.2	GDOES Setup . . . . .	85
4.5	Hall Effect Measurement Method . . . . .	86
4.5.1	Hall Effect Measurement Theory . . . . .	86
4.5.2	Hall Effect Measurement Setup . . . . .	91
4.6	Transmission Line Pulse (TLP) Current-Voltage Measurement . . .	92
4.6.1	TLP Current-Voltage Measurement Theory . . . . .	92
4.6.2	TLP Current-Voltage Measurement Setup . . . . .	99
4.7	Transient Interferometric Mapping (TIM) . . . . .	103
4.7.1	TIM Theory . . . . .	103
4.7.2	TIM Setup . . . . .	106
4.8	Raman Spectroscopy . . . . .	107
4.8.1	Raman Spectroscopy Theory . . . . .	107
4.8.2	Raman Spectroscopy Setup . . . . .	111
<b>III RESULTS</b>		<b>113</b>
<b>5</b>	<b>Boron-Doped Diamond Layers</b>	<b>114</b>
5.1	Boron-Doped Diamond Layer Growth . . . . .	114
5.1.1	Growth Conditions . . . . .	114
5.1.2	Electrical Contacts Microfabrication . . . . .	116
5.2	Boron-Doped Diamond Layers Characterization . . . . .	119
5.2.1	Secondary Ion-Mass Spectroscopy Measurement . . . . .	119
5.2.2	Hall Effect Measurement . . . . .	119
5.3	Conclusion . . . . .	121

<b>6</b>	<b>Electronic Transport under High Electric Fields</b>	<b>123</b>
6.1	Transmission Line Pulse (TLP) Measurements <i>(Results presented in [206])</i> . . . . .	124
6.2	Transient Interferometric Mapping (TIM) Measurements <i>(Results presented in [206])</i> . . . . .	128
6.3	Modeling of Boron-Doped Diamond under High Electric Fields <i>(Results presented in [206])</i> . . . . .	131
6.3.1	Presentation . . . . .	131
6.3.2	Mobility Modeling . . . . .	132
6.3.3	Activation Energy Modeling . . . . .	134
6.3.4	Super-linear Behavior Discussion . . . . .	135
6.4	Conclusion . . . . .	148
<b>7</b>	<b>Phosphorus-Doped Diamond Layers</b>	<b>149</b>
7.1	Phosphorus-Doped Diamond Layer Growth <i>(Results presented in [243])</i> . . . . .	150
7.1.1	Interaction between $\text{PH}_3$ and $\text{CH}_4$ in a hydrogen plasma . . . . .	150
7.1.2	Growth Conditions . . . . .	153
7.1.3	Growth Rate Measurements . . . . .	155
7.1.4	Scanning Electron Microscopy (SEM) Imaging . . . . .	156
7.2	PECVD Reactors Time Responses <i>(Results presented in [256])</i> . . . . .	158
7.2.1	Time Response Measurement Presentation . . . . .	158
7.2.2	Time Response Measurement Results . . . . .	159
7.2.3	MWPECVD Reactor Response Simulation . . . . .	164

7.3 Phosphorus-Doped Diamond Layers Characterization <i>(Results presented in [243])</i> . . . . .	169
7.3.1 Raman Spectroscopy Measurement . . . . .	169
7.3.2 Glow Discharge Optical Emission Spectroscopy Measurement	170
7.4 Conclusion . . . . .	174
<b>Conclusion and Perspectives</b>	<b>176</b>
<b>Bibliography</b>	<b>223</b>
<b>Appendix</b>	<b>224</b>

# List of Figures

1.1	Diamond crystalline structure . . . . .	28
1.2	Schottky diode fabricated on boron-doped diamond in <b>(a)</b> top and <b>(b)</b> cross section view [5] . . . . .	34
1.3	PiN diode fabricated on boron- and phosphorus-doped diamond [27]	34
1.4	Inversion mode MOSFET fabricated on boron- and phosphorus-doped diamond using a Al <sub>2</sub> O <sub>3</sub> gate [29] . . . . .	35
2.1	(P, T) diagram of carbon (inspired from the work of F. P. Bundy [40])	38
2.2	Tubular microwave plasma-assisted CVD reactor [55] . . . . .	42
2.3	ASTeX bell jar microwave plasma-assisted CVD reactor . . . . .	43
2.4	ASTeX high-pressure microwave source [57] . . . . .	45
2.5	Setup of the ellipsoidal reactor [60] . . . . .	46
2.6	Schematic drawing of linear antenna microwave plasma enhanced CVD system adapted for diamond deposition [62] . . . . .	47
2.7	Schematic illustrations of <b>(a)</b> a slot antenna, <b>(b)</b> a microwave launcher, <b>(c)</b> a large-area microwave antenna and <b>(d)</b> the large-area SWP apparatus developed in this work [64] . . . . .	48

2.8	View of <b>(a)</b> the 16 coaxial plasma sources inserted in a square metallic flange arranged in a 2D-matrix to constitute the Distributed Antenna Array (DAA), schematic view of <b>(b)</b> the design of a coaxial plasma source, view of <b>(c)</b> the ignited plasma sources inside the chamber [65] . . . . .	49
2.9	Evolution of the growth rate on (100)-oriented diamond substrate as a function of the $[\text{CH}_4]/[\text{H}_2]$ ratio for diamond layers grown under 3800 W (T. Teraji et al. [68]) and 750 W (D. Takeuchi et al. [69]) .	51
2.10	A simplified form of the Bachmann [87] atomic C–H–O diagram . .	55
2.11	Evolution of the growth rate on 100, 111, 110, and 113 planes as a function of the temperature under a pressure of 200 mbar, a microwave power of 3.5 kW and a methane $[\text{CH}_4]/[\text{H}_2]$ ratio of 4% [90]	56
2.12	Evolution of the growth rate on (100)-oriented diamond substrate as a function of the injected microwave power density at a temperature of 850 °C and a methane $[\text{CH}_4]/[\text{H}_2]$ ratio of 4% [72] . . . . .	57
2.13	Evolution of the growth rate on (100)-oriented diamond substrate as a function of the pressure for a microwave power of 3 kW, a temperature of 760 °C and a methane $[\text{CH}_4]/[\text{H}_2]$ ratio of 3% [95] .	59
3.1	ASTeX bell jar reactor used for the growth of single crystal boron-doped diamond layers . . . . .	71
3.2	NIRIM reactor used for the growth of polycrystalline phosphorus-doped diamond layers . . . . .	72
3.3	Time response measurement setup . . . . .	73

4.1	Schematic diagram of an atomic force microscope. <b>(1)</b> , Laser diode; <b>(2)</b> , cantilever; <b>(3)</b> , mirror; <b>(4)</b> , position-sensitive photodetector; <b>(5)</b> , electronics; and <b>(6)</b> , scanner with sample [162] . . . . .	77
4.2	AFM setup . . . . .	78
4.3	Schematic diagram of a scanning electron microscope [166] . . . . .	80
4.4	SEM setup . . . . .	81
4.5	The principle of secondary-ion mass spectrometry [167] . . . . .	82
4.6	Evolution of the voltage as a function of the current between two electrodes during an electric discharge [175] . . . . .	84
4.7	Schematic diagram of a Grimm-type GD source [176] . . . . .	85
4.8	Sputtering and light emission mechanism in GDOES [176] . . . . .	86
4.9	Six-contact Hall bar geometry . . . . .	87
4.10	Ti/Au Van der Pauw contacts on a boron doped diamond . . . . .	88
4.11	Hall measurement setup <b>(a)</b> and sample holder <b>(b)</b> . . . . .	91
4.12	Sectional view of the coaxial cable . . . . .	93
4.13	Theoretical representation of the coaxial cable . . . . .	93
4.14	TLP generator electrical scheme . . . . .	95
4.15	TLP current-voltage measurement setup. The legend for the different letters is given in Table 4.1 . . . . .	99
4.16	Homemade circuit board containing the reed relay . . . . .	101
4.17	Pick-off tee schematic . . . . .	102
4.18	Probe holder and micropositioner . . . . .	102
4.19	Phase shift induced by self-heating between a reference (left) and a probe laser beam (right) . . . . .	104
4.20	TIM setup schematic [187] . . . . .	105

4.21	TIM setup in TU Wien . . . . .	107
4.22	Sample holder for TLP setup <b>(a)</b> view from the front, <b>(b)</b> from the back, and <b>(c)</b> close-up from the back . . . . .	108
4.23	Jablonski diagram representing the energy transfer during a Stokes and anti-Stokes Raman scattering event [190] . . . . .	109
4.24	Example of Raman spectrum recorded on an undoped polycrystalline diamond layer [194]. The fitting was done using Lorentzian and Gaussian profiles . . . . .	111
4.25	Raman spectroscopy measurement setup . . . . .	112
5.1	AFM image of the surface of the diamond sample used for TIM measurement . . . . .	116
5.2	Different types of electrodes used for electrical characterizations: schematics and images of <b>(a)</b> <b>(c)</b> circular electrodes for pulsed I-V measurements, <b>(b)</b> <b>(d)</b> parallel electrodes for TIM measurements . . . . .	117
5.3	Boron concentration measured by SIMS as a function of the boron concentration in the gas phase during the CVD growth. The red line is a linear fit . . . . .	120
5.4	Hall mobility (black squares) and resistivity (red squares) measured by Hall measurement, and modeled mobility (white squares) as a function of the boron concentration on (100) boron-doped diamond samples at room temperature ( $T = 300$ K) . . . . .	121

5.5 Evolution of the Hall mobility (black squares) and resistivity (red squares) as a function of temperature for samples with a boron content of **(a)**  $6.3 \times 10^{19} \text{ cm}^{-3}$  and **(b)**  $9.4 \times 10^{19} \text{ cm}^{-3}$ . The black line represents the fitting function described in equation (5.1) . . . 122

6.1 Measured **(a)** voltage and **(b)** current waveform of sample B ( $[B] = 3.8 \times 10^{19} \text{ cm}^{-3}$ ) for different charging voltage  $V_{ch}$ , and I-V characteristics **(c)** calculated for different averaging periods in the voltage **(a)** and current **(b)** waveforms. The initial peak of current in **(b)** and small voltage steps in **(a)** are artifacts due to different spatial position of voltage and current probes and reflections. The lines in **(c)** are for eye-guiding . . . . . 125

6.2 Current-voltage characteristic of studied devices in linear **(a)** and semi-logarithmic **(b)** scales. In sample D, two measurement conditions (50 mA and 250 mA) at which TIM measurements were performed are indicated by pink arrows and crosses. . . . . 128

6.3 Phase shift measurement on sample D ( $[B] = 3.8 \times 10^{19} \text{ cm}^{-3}$ ) along a scanning line parallel to the electrodes for different times and a current of **(a)** 0.05 A and **(b)** 0.25 A. **(c)** is the evolution of the phase shift distribution along a scanning line perpendicular to the electrodes, in the center of the device, for currents of 0.25 A with a positive polarity on the right electrode. The photographs are backside infrared images of the device active area including the scanning direction (black bold line) . . . . . 130

6.4	Experimental [221] and calculated hole drift velocity as a function of the electric field . . . . .	134
6.5	Dispersion of activation energy with the boron concentration . . . .	135
6.6	Schematic representation of the PATE for a donor impurity level . .	136
6.7	Experimental (symbols) and simulated (lines and dashed lines) pulsed I-V characteristics using a combination of PATE, PFE, III, and SHE ( $t = 100$ ns) for <b>(a)</b> sample A, <b>(b)</b> B, and <b>(c)</b> C. . . . .	137
6.8	Schematic representation of the PTE for a donor impurity level. The black curve represents the potential well without electric field and the red one represents the potential well with an electric field applied.	138
6.9	Ionization rate $\alpha$ as a function of the reciprocal electric field. . . .	140
6.10	Simulated hole concentration as a function of voltage <b>(a)</b> and maximum temperature as a function of power <b>(b)</b> in samples A, B and C. . . . .	143
6.11	Simulated voltage <b>(a)</b> , current <b>(b)</b> waveforms, and maximum temperature <b>(c)</b> in sample B for an increasing amplitude of $V_{ch}$ . . . .	145
6.12	Simulated temperature <b>(a)</b> and phase shift <b>(b)</b> distribution along a scanning line perpendicular to the electrodes for sample D at a current of 0.25 A and temperature distribution for sample B at a current of 2.4 A ( $V_{ch} = 237.5$ V) <b>(c)</b> . The temperature is given at the surface of the sample ( $Z = 0$ $\mu\text{m}$ ) and for a depth of 10 $\mu\text{m}$ in the diamond ( $Z = 10$ $\mu\text{m}$ ). The time instant is $t = 100$ ns. . . . .	147

7.1	Time dependence of the intensity of the hydrogen-alpha, atomic phosphorus, PH radical, and CH radical optical emission lines during a period of five minutes with a one-minute-long CH <sub>4</sub> pulsed injection [249] . . . . .	151
7.2	Comparison of the time dependence of the CH radical optical emission line intensity with the intensity ratio of the PH and CH radicals optical emission lines a period of five minutes of one-minute-long CH <sub>4</sub> pulsed injection (Inset: Variation of the intensity ratio of the PH and CH radicals optical emission lines as a function of the CH radical optical emission line intensity) [249] . . . . .	152
7.3	Growth rate for the different layers as a function of the microwave power for <b>(a)</b> intrinsic polycrystalline diamond layers and <b>(b)</b> phosphorus-doped polycrystalline diamond layers . . . . .	156
7.4	Evolution of <b>(a)</b> the emission spectra as a function of time upon the injection of a N <sub>2</sub> gas pulse for a pressure of 110 mbar and a total gas flow of 200 sccm and <b>(b)</b> ) experimental normalized intensity of the NH emission line (336.9 nm) as a function of time upon the injection of a N <sub>2</sub> gas pulse (dots) and fitting curves (solid lines) measured on the NIRIM reactor for a pressure of 110 mbar and different total gas flows. For better readability, each curve is separated by an offset of 500 counts in <b>(a)</b> and 1 arb. unit in <b>(b)</b> . . . . .	160
7.5	Parameter $\tau$ as a function of the total gas flow and the pressure in the Seki reactor for a pulse of <b>(a)</b> N <sub>2</sub> , <b>(b)</b> CH <sub>4</sub> , and <b>(c)</b> O <sub>2</sub> . The solid lines represent fitting curves given by equation 7.3 . . . . .	161

7.6 Time position of the peak intensity of the dynamic pulse responses  $\tau m$  as a function of the total gas flow and the pressure in the Seki reactor for a pulse of **(a)** N<sub>2</sub>, **(b)** CH<sub>4</sub>, and **(c)** O<sub>2</sub>. The solid lines represent fitting curves given by equation (7.5) . . . . . 163

7.7 Parameter  $\tau$  as a function of the total gas flow and the pressure in the NIRIM reactor for a pulse of **(a)** N<sub>2</sub>, **(b)** CH<sub>4</sub>, and **(c)** O<sub>2</sub>. The solid lines represent fitting curves given by equation (7.3) . . . . . 165

7.8 Time position of the peak intensity of the dynamic pulse responses  $\tau m$  as a function of the total gas flow and the pressure in the NIRIM reactor for a pulse of **(a)** N<sub>2</sub>, **(b)** CH<sub>4</sub>, and **(c)** O<sub>2</sub>. The solid lines represent fitting curves given by equation (7.5) . . . . . 166

7.9 Experimental dynamic response to a O<sub>2</sub> gas pulse (connected dots) and fitting curves (solid lines) measured on the NIRIM reactor for a pressure of 110 mbar and a total gas flow of 800 sccm . . . . . 167

7.10 Fitting parameter  $k$  in equation 7.3 as a function of the volume of the reactors for an injection of N<sub>2</sub>, CH<sub>4</sub>, and O<sub>2</sub> . . . . . 167

7.11 Recorded and calculated response of the NIRIM reactor to a one-minute-long, square shaped flow of N<sub>2</sub> with an amplitude of 2 sccm using a pressure of 70 mbar and a total gas flow of 200 sccm . . . . . 168

7.12 Raman spectra of layers grown under 370 W and 50 mbar using the diamond ZCP peak as a reference value for normalization . . . . . 170

7.13  $sp^3/sp^2$  ratio calculated from Raman spectra measured on the different series of samples . . . . . 171

7.14 Phosphorus content calculated from GDOES measurements for phosphorus-doped diamond layers grown using continuous and pulsed flow of CH <sub>4</sub> . . . . .	172
7.15 Atomic fraction recorded as a function of time using GDOES for two phosphorus-doped diamond layers grown under 370 W and 50 mbar of pressure in <b>(a)</b> continuous and <b>(b)</b> pulsed CH <sub>4</sub> injection. The numbers between parentheses are scaling factors and $q$ is the sputtering rate as resulting from the quantification algorithm described in reference [177] . . . . .	173

# List of Tables

1.1	Physical properties of diamond . . . . .	30
1.2	Physical properties of diamond compared to SiC and GaN . . . . .	32
2.1	Parts highlighted within Figure 2.3 . . . . .	44
4.1	Parts highlighted within Figure 4.15 . . . . .	99
5.1	Growth conditions used for epitaxial growth on (100) diamond substrates . . . . .	115
5.2	Coating conditions for positive and negative photoresists . . . . .	118
5.3	Exposure conditions for positive and negative photoresists . . . . .	118
5.4	Developing conditions for positive and negative photoresists . . . . .	118
6.1	Physical characteristics of diamond samples and simulation parame- ters used in the finite element method simulation . . . . .	127
6.2	Default values of tolerance used in the Silvaco Atlas finite element simulation [215] . . . . .	132
6.3	Fitting parameters for the mobility model [14] . . . . .	133

6.4	Relaxation times calculated for neutral impurity scattering ( $\tau_{NI}$ ), ionized impurity scattering ( $\tau_{II}$ ), acoustic phonon scattering ( $\tau_{AC}$ ), and optical phonon scattering ( $\tau_{OP}$ ) for samples A, B, and C for minimum and maximum applied power. . . . .	144
7.1	Growth conditions for undoped and phosphorus-doped polycrystalline diamond layers grown using a continuous and pulsed $\text{CH}_4$ gas flow . . . . .	154
7.2	Combinations of microwave power, pressure, and distance between substrate and plasma used for the growth of polycrystalline diamond layers . . . . .	154
7.3	SEM images of diamond layers grown using continuous and pulsed flow of $\text{CH}_4$ , with a $[\text{P}]/[\text{C}]$ ratio of 200000 ppm in the gas phase, for different values of pressure, microwave power, and distance $D$ between the substrate's surface and the center of the plasma ball. $T$ is the thickness of the deposited polycrystalline diamond layer . . .	157
7.4	Fitting parameters $k$ and $k'$ and the calculated error on their value	162
7.5	Contributions to the work presented in this thesis with the respective list of contributors . . . . .	232

# Aims of the Thesis

The aim of this thesis is to study the growth of doped diamond layers and their high electric field conduction mechanism, more specifically the impurity impact ionization avalanche phenomenon which is poorly understood in diamond. In order to achieve this, this thesis aims at growing both boron- and phosphorus-doped diamond layers by microwave plasma enhanced chemical vapor deposition, and designing and fabricating test devices for conventional electrical characterization methods and high electric field characterization methods based on a transmission line pulsed generator which are developed as part of this work. In addition to a better knowledge of impurity impact ionization effect in diamond, the results of this study are expected to enable the optimization of existing designs of diamond high voltage electronic devices, and the creation of different and new electronic devices on doped diamond.

# Introduction

Diamond is a material with exceptionally high thermal conductivity, carrier mobility, and breakdown field [1] which potentially designates it as the best semiconductor for high power applications [2]. Those promising perspectives motivated the creation of different research groups all around the world, for example in the National Institute for Materials Science (NIMS) in Japan or in the Néel Institute in France. The development of diamond-based electronic devices is nowadays supported by the steady progress in n-type and p-type doping and hetero-epitaxial diamond growth. These achievements have enabled the demonstration of various types of diodes [3–5] and transistors [6, 7] for high power, high temperature applications. However, the behavior of diamond under high electric fields is not well understood yet and this knowledge is crucial for the design and fabrication of diamond-based power electronic devices.

In this thesis, the growth and electrical characterization of doped diamond layers have been studied. Epitaxial p-type boron-doped diamond layers were grown by MicroWave Plasma Enhanced Chemical Vapor Deposition (MWPECVD) and characterized under high electric field using a pulsed measurement setup which allows the application of high voltages on test devices while minimizing their degradation. The recorded thermal and electrical data were simulated using finite

element method. With the goal of conducting the same kind of experiment on n-type diamond, polycrystalline phosphorus-doped diamond layers were also grown by MWPECVD. A novel technique using pulsed gas flow during the growth was developed to increase the phosphorus incorporation in diamond. In order to better understand the gas dynamic in MWPECVD reactors and optimize the growth conditions of phosphorus-doped diamond layers using pulsed gas flows, the dynamic pulse responses of different MWPECVD reactors to the injection of small quantity of gas were recorded and analyzed.

In chapter 1, a general introduction to the diamond is given. Its main physical and electrical properties are presented, along with the classification of the different types of diamond.

In chapter 2, we focus on the synthesis of diamond. The phase diagram of carbon and its application to the different growth methods are presented. Among them, the accent is put on the Plasma Enhancement Chemical Vapor Deposition (PECVD), which was used to grow the diamond layers in this work.

In chapter 3, the PECVD reactors used for the growth of boron-doped and phosphorus-doped diamond are presented along with the optical characterization setup used for the study of gas dynamics in the reactor chambers.

In chapter 4, the different methods used to characterize the surface morphology of the diamond layers but also their thermal and electrical properties are presented. Atomic Force Microscopy (AFM) and Scanning Electron Microscopy (SEM) were used to obtain images of the diamond surface. The incorporation of dopants in the layers was measured using Secondary Ion-Mass Spectroscopy (SIMS) and Glow Discharge Optical Emission Spectroscopy (GDOES). A Transmission Line Pulse (TLP) generator was used to obtain the current-voltage (I-V) curves of

the different doped diamond devices at high electric field. The dissipation of the thermal energy was studied using Transient Interferometric Mapping (TIM). Other characterization techniques like Raman spectroscopy or Hall effect measurement were used to characterize the doped diamond layers.

In chapter 5, the conditions used for the PECVD growth of the epitaxial boron-doped diamond layers are detailed. The boron concentration in the grown layers was assessed using Secondary Ion Mass Spectroscopy (SIMS). The electrical properties of the layers such as hole mobility and resistivity were measured by Hall effect.

In chapter 6, the epitaxial boron-doped diamond layers were characterized using the TLP setup. The recorded I-V curves show a characteristic super-linear behavior which ultimately leads to a breakdown. In order to reveal the potential role of thermal effects in this behavior, TIM measurements were also performed. Finally, the experimental results from TLP and TIM measurements have been simulated taking into account the Impurity Impact Ionization (III) phenomenon and Self-Heating Effect (SHE) in order to explain the super-linear behavior of the measured I-V curves.

In chapter 7, the conditions used for the PECVD growth of the polycrystalline phosphorus-doped diamond layers using the pulsed  $\text{CH}_4$  injection method are detailed along with the dynamic pulse responses of different MWPECVD reactors to the injection of a small quantity of gas. The phosphorus content in the diamond layers was determined by Glow Discharge Optical Emission Spectroscopy (GDOES) and their crystalline quality was evaluated using Raman spectroscopy and Scanning Electron Microscopy (SEM).

# Part I

## STATE OF THE ART

# Chapter 1

## Diamond Material

In this chapter, the electrical, thermal and mechanical properties of the diamond material are presented, including some examples of electronic diamond devices.

### 1.1 Diamond Structure

Carbon has three crystalline allotropic forms which can be found in nature: graphite, lonsdealite, and diamond.

- Graphite is arranged in a hexagonal structure. It can be interpreted as a stacking of layers so called graphene although graphene and graphite have different properties. In a graphene layer, carbon atoms are linked by covalent bonds, making it a particularly strong materials with a tensile strength of 125 GPa and a Young modulus of  $1.1 \times 10^3$  GPa [8]. On the other hand, bonding between graphene layers is due to weak van der Waals bonds, making graphite a rather soft material. Graphene also has a very high thermal conductivity ( $5 \times 10^1$  W.cm<sup>-1</sup>.K<sup>-1</sup>) and electron mobility ( $2 \times 10^5$  cm<sup>2</sup>.V<sup>-1</sup>.s<sup>-1</sup>) [8].

- Lonsdaleite, also called hexagonal diamond, is formed when a meteorite containing graphite hits Earth. The heat and stress of the impact change the crystalline structure of graphite into something close to the one of diamond while retaining the hexagonal arrangement of graphite.
- Diamond, which is the material studied in this work, is composed of carbon atoms organized along a face centered cubic (fcc) Bravais lattice. Each carbon atom is linked to four carbon atoms by single  $\sigma$  bonds (0.154 nm) with an equal angle between each other of  $109.5^\circ$  forming a tetrahedron. The combination of each tetrahedron with four other tetrahedrons results in a very tight covalent crystal with a very high hardness and Young modulus (Table 1.1). The length of the covalent bonds is 1.54 Å and the lattice constant is 3.56 Å. Its primitive cell can be seen as two fcc substructures shifted from each other along the diagonal of the cubic cell (Figure 1.1). It has an atomic packing factor of 0.34 which is significantly smaller compared to the atomic packing factor of the body-centered cubic and face-centered cubic lattices and a density of  $3.52 \text{ g.cm}^{-3}$ .

## 1.2 Classification of Diamond

The classification of diamonds, that is currently being used, originates from 1934 [9]. It divides diamonds in two main categories according to their nitrogen content. Those two categories are also divided in subcategories that are detailed below.

- Type I: It is the most common type of natural diamond. 74% of natural diamonds belong to this class. They are classified depending on how the

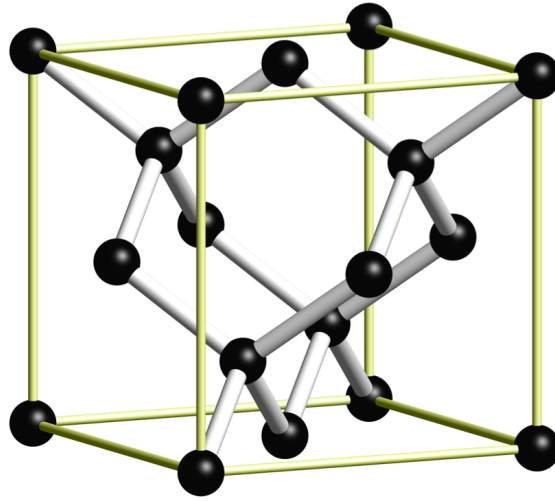


Figure 1.1: Diamond crystalline structure

nitrogen atoms are aggregated inside the crystalline lattice.

- Type Ia: In order to be classified Ia, a diamond should contain less than  $10^{16} \text{ cm}^{-3}$  of single substitutional nitrogen impurities [10]. This type of diamond is classified in three subcategories IaA, IaB, and IaB' depending on the type of nitrogen aggregates they contain. The IaA type contains A-centers which are two neighboring nitrogen atoms. When four nitrogen atoms surround a vacancy, they form a B-center. Diamonds which have this kind of defects are of the IaB type. Finally, the IaB' type contains nitrogen-containing platelets which are extended planar defects.
- Type Ib: These diamonds contain single substitutional nitrogen impurities. They are not common in the nature but most synthetic diamonds made under High Pressure High Temperature (HPHT) conditions belong to this category. They show the paramagnetic signal of substitutional nitrogen observed in Electron Paramagnetic Resonance (EPR) spec-

troscopy. The nitrogen impurities form a deep donor level, with an activation energy of 1.7 eV [11], which makes them unsuitable for electronic applications in single crystal diamond. They usually have a yellow color.

- Type II: This type of diamond contains no measurable nitrogen impurities. The diamonds containing less than  $10^{17} \text{ cm}^{-3}$  of nitrogen belong to this category. They are divided in two different classes.
  - Type IIa: It is the purest form of diamond. They are the most transparent type of diamond and they are very appreciated in jewelry for that reason.
  - Type IIb: This type of diamond contains boron as its main impurity which gives it p-type conductivity properties. The boron impurities have an activation energy of 0.37 eV. They are very rare in the nature with a maximum boron content of  $10^{17} \text{ cm}^{-3}$ . However, it is possible to grow them artificially using HPHT or Chemical Vapor Deposition (CVD) techniques and reach a boron content up to  $10^{22} \text{ cm}^{-3}$  in superconducting diamonds [12, 13]. Because of their boron content, diamonds of the IIb type have a blue color.

### 1.3 Properties

Diamond is the hardest material with a hardness of 10 on the Mohs scale and has a high Young modulus above 1000 GPa. Thanks to those properties, diamond is

Table 1.1: Physical properties of diamond

<b>Properties of diamond</b>	<b>Values</b>
Resistivity ( $\Omega\cdot\text{cm}^{-1}$ )	$10^{16}$
Relative permittivity	5.5
Thermal conductivity (at 300 K) ( $\text{W}\cdot\text{cm}^{-1}\cdot\text{K}^{-1}$ )	22
Volumetric heat capacity ( $\text{J}\cdot\text{cm}^{-3}\cdot\text{K}^{-1}$ )	1.83
Hardness on the Mohs scale	10
Young modulus (GPa)	$1.1 \times 10^3$
Transparency	From 225 nm to far IR
Refraction index	2.4
Melting point (K)	$3.8 \times 10^3$
Chemical reactivity	Inert

broadly employed in mechanical applications, it is for example used in polishing pastes and in cutting or milling tools.

Diamond is chemically inert for temperature below 900 K, which means it can withstand harsh chemical treatments. However, in an atmosphere of pure oxygen gas, diamond will burn for a temperature around 1000 K. This low chemical reactivity is also one of the reasons why diamond has a good biocompatibility, making it a promising material for medical applications. Diamond can also endure radiation exposition without suffering significant damages.

Wide Band Gap Semiconductors (WBGs), like SiC and GaN, are materials which have a larger band gap compared to conventional semiconductors like silicon (band gaps usually over 2 eV compared to 1.1 eV for Si). Their electrical properties fall in between those of conventional semiconductors and insulators and are well adapted to High Power (HP) and High Frequency (HF) applications. When HP or HF is being used, more energy is dissipated and the temperature tends to increase in the semiconductor material. If the energy is high enough, some charge carriers can directly jump from the valence band to the conduction band, altering

the semiconductor properties of the material. Thanks to their wide band gap, those transitions are more difficult in WBGs, and less sensitive to an elevation of temperature. From an electronic point of view, diamond is part of the WBG family. Its thermal conductivity is also more than six times higher than the one of SiC and GaN (Table 1.2) which makes it better at dissipating thermal energy from Joule heating. Combined with the wide band gap property, it makes the operation at high temperature possible. Diamond is a particularly promising material for high power application because it also has some other interesting properties that set it apart from SiC and GaN (Table 1.2): its breakdown electric field is twice higher compared to GaN and more than ten times higher compared to SiC and it also has significantly higher hole mobility which is a great advantage for the design of more compact and energy efficient devices.

However, diamond also comes with some downsides. First, although the growth of heteroepitaxial diamond [16, 17] and the fabrication of electronic devices on such substrate [18, 19] have been demonstrated in laboratories, the production of large diamond wafers for industrial use at reasonable prices is still a challenge. Then, even though the fabrication of p-type diamond layers is nowadays well understood, the production of high quality n-type phosphorous doped diamond layers is, on the other hand, not mastered yet.

Finally, another peculiarity of diamond is that, due to the high activation energy of its dopants, only a small part of them is ionized at room temperature which makes the doped diamond layers highly resistive in comparison to conventional semiconductors and can lead to particular electrical effects like super-linear increase of current at high electric field [20], a phenomena which has not been studied in details until now.

Table 1.2: Physical properties of diamond compared to SiC and GaN

<b>Properties</b>	<b>Diamond</b>	<b>SiC (3C polytype)</b>	<b>GaN (Wurtzite)</b>
Breakdown electric field (MV.cm <sup>-1</sup> )	>10	≈ 1	≈ 5
Band gap (eV)	5.47	2.36	3.39
Hole mobility (at 300 K) (cm <sup>2</sup> .V <sup>-1</sup> .s <sup>-1</sup> )	1870 [14]	320	200
Electron mobility (at 300 K) (cm <sup>2</sup> .V <sup>-1</sup> .s <sup>-1</sup> )	700 [15]	800	1000
Hole saturation velocity (cm.s <sup>-1</sup> )	1.1 × 10 <sup>7</sup>	1.0 × 10 <sup>7</sup>	6.6 × 10 <sup>6</sup>
Electron saturation velocity (cm.s <sup>-1</sup> )	2.0 × 10 <sup>7</sup>	2.0 × 10 <sup>7</sup>	1.4 × 10 <sup>7</sup>
Acceptor activation energy (eV)	0.37 (B)	0.26 (Al)	0.14 (Mg)
Donor activation energy (eV)	0.57 (P)	0.06 (N)	0.02 (Si)
Thermal conductivity (at 300 K) (W.cm <sup>-1</sup> .K <sup>-1</sup> )	22	3.6	1.3
Volumetric heat capacity (J.cm <sup>-3</sup> .K <sup>-1</sup> )	1.83	2.21	3.01

## 1.4 Diamond Devices

Due to its attractive properties for high power applications, various diamond-based electronic devices have been developed.

Schottky diodes (Figure 1.2) have been principally made on boron-doped p-type diamond since phosphorous dopants have a low incorporation and a higher activation energy (Table 1.2). In 1987, M. W. Geis et al. reported the first Schottky diodes fabricated on synthetic boron-doped diamond [21]. While Ti is the most used metal to make ohmic contacts on diamond, a wide range of metals have been used for Schottky contacts such as Al [22], Zr [5], Au [4], Ni [23], W [24], Cr [25]. Those diodes have a high breakdown voltage which can be as high as 7 kV [25]. Their forward current density can be over  $100 \text{ A.cm}^{-2}$  at 2 V [26] while their rectification ratio can reach values around  $1.7 \times 10^5$  for  $\pm 10 \text{ V}$  [23].

Bipolar PiN diamond have also been investigated using phosphorous- and boron-doped diamond (Figure 1.3). They can reach a forward current around  $140 \text{ A.cm}^{-2}$  at 40 V [27] and can have an extremely high breakdown voltage over 11 kV [28]. However, their development is hindered by their high built-in voltage which causes a significant forward voltage drop, and the lack of carrier lifetime control, reproducibility, and uniformity [29].

The first FET transistor made on boron-doped diamond was reported by H. Shiomi et al. in 1989 [30]. Regarding MOS transistors, the most used oxide for the gate is  $\text{Al}_2\text{O}_3$  (Figure 1.4) as it has a high energy barrier for holes (around 5 eV) due to its alignment with diamond energy bands. It also gives the best performance when combined to O-terminated diamond [29]. However, the lack of native oxides for diamond results in highly defective interfaces. H-terminated diamond surfaces

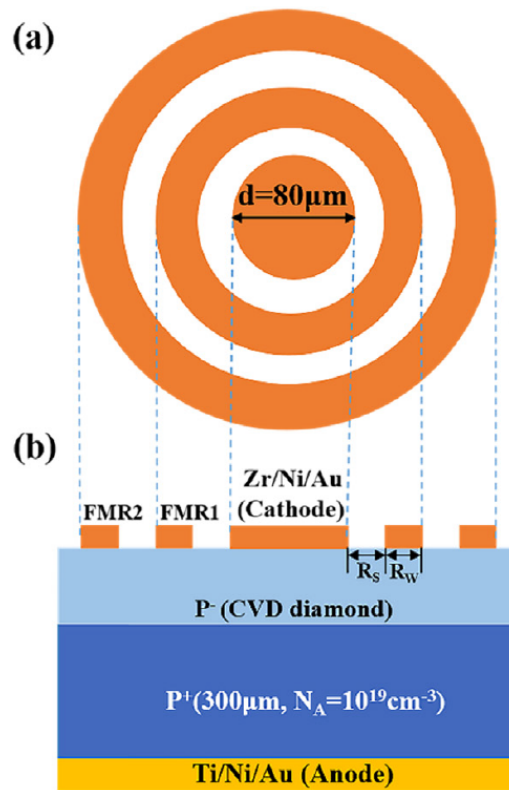


Figure 1.2: Schottky diode fabricated on boron-doped diamond in (a) top and (b) cross section view [5]

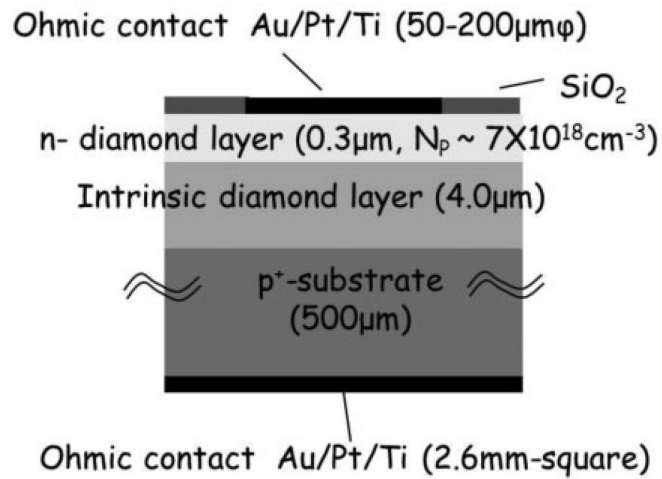


Figure 1.3: PiN diode fabricated on boron- and phosphorus-doped diamond [27]

are also widely used in the fabrication of FETs due to their p-type conductivity properties. Z. Ren et al. [7] used H-terminated diamond coated with gold to make the source and the drain of an accumulation mode FET while using O-terminated diamond coated with  $\text{Al}_2\text{O}_3$  and Al as the gate. Reported values of current density are about  $I_D = -51.6 \text{ mA}\cdot\text{mm}^{-1}$  at  $V_{GS} = V_{DS} = -4.5 \text{ V}$ .

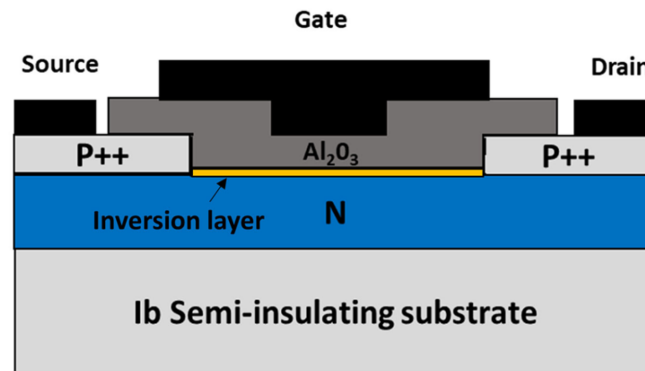


Figure 1.4: Inversion mode MOSFET fabricated on boron- and phosphorus-doped diamond using a  $\text{Al}_2\text{O}_3$  gate [29]

T. Matsumoto et al. brought the proof of concept for an inversion channel MOSFET made on (111) diamond using boron-doped diamond (p-type) as the source and the drain, and phosphorous-doped diamond (n-type) coated with  $\text{Al}_2\text{O}_3$  as the gate. A current density of  $I_D = -1.6 \text{ mA}\cdot\text{mm}^{-1}$  was obtained at  $V_{GS} = -12 \text{ V}$  and  $V_{DS} = -5 \text{ V}$ .

MESFET and JFET transistors are highly reliable for power electronics applications due to the absence of the gate oxide layer, which can generate defects at the interface between the oxide and the diamond. For MESFETs, various metals were used as a Schottky gate contact such as Al, Mo, or Pt [31]. S. Russel et al. [32] managed to attain a current density of  $I_D = 225 \text{ mA}\cdot\text{mm}^{-1}$  for  $V_{GS} = 0 \text{ V}$  and  $V_{DS} = -5 \text{ V}$  and a cut-off frequency of 53 GHz. MESFET devices have also been

made on polycrystalline diamond [33] which is cheaper compared to single crystal diamond and can be produced in large wafers.

Diamond JFET were investigated by T. Iwasaki et al. [34] using a p-type boron-doped channel and n-type gate made of n-type phosphorous-doped diamond. A maximum current density of  $I_D = -25 \text{ A.cm}^{-2}$  was obtained for  $V_{GS} = -5 \text{ V}$  and  $V_{DS} = -20 \text{ V}$  at 300 K in unipolar mode. Using bipolar mode, i.e. by injecting electrons through the gate, it was possible to enhance the current density  $I_D$  by a factor 4. At 500 K, it was still possible to operate the transistor in bipolar mode with current densities up to  $I_D = 3700 \text{ A.cm}^{-2}$ .

Recently, the development of diamond-based electronic devices have been focused on the use of different crystalline orientations such as the (113) orientation [35], heteroepitaxial diamond [36, 37], and H-terminated diamond [38, 39].

## 1.5 Conclusion

As a conclusion, diamond is a promising material for HP applications because of its wide band gap, and high thermal conductivity, breakdown electric field, high hole mobility. PiN and Schottky diodes have already been demonstrated along with FET. However, its behavior at high electric field is not fully understood yet.

# Chapter 2

## Diamond Growth

In this chapter, we focus on the synthesis of diamond. The PECVD growth method is presented and the role of the different gas precursor and growth parameters are discussed.

### 2.1 Carbon Pressure-Temperature Diagram

In order to fabricate diamond devices and control their properties, it is necessary to produce high quality diamond, both doped and undoped. The knowledge of the different phases of carbon and their equilibrium conditions is crucial to understand diamond growth. There are six main regions in the (P, T) phase diagram of carbon in Figure 2.1:

- The first one is the “*Graphite*” region, in which carbon spontaneously forms graphite which is the stable allotropic form of carbon at room temperature and atmospheric pressure. However, the conversion rate from diamond to graphite is so slow that there is no observable effect under normal conditions

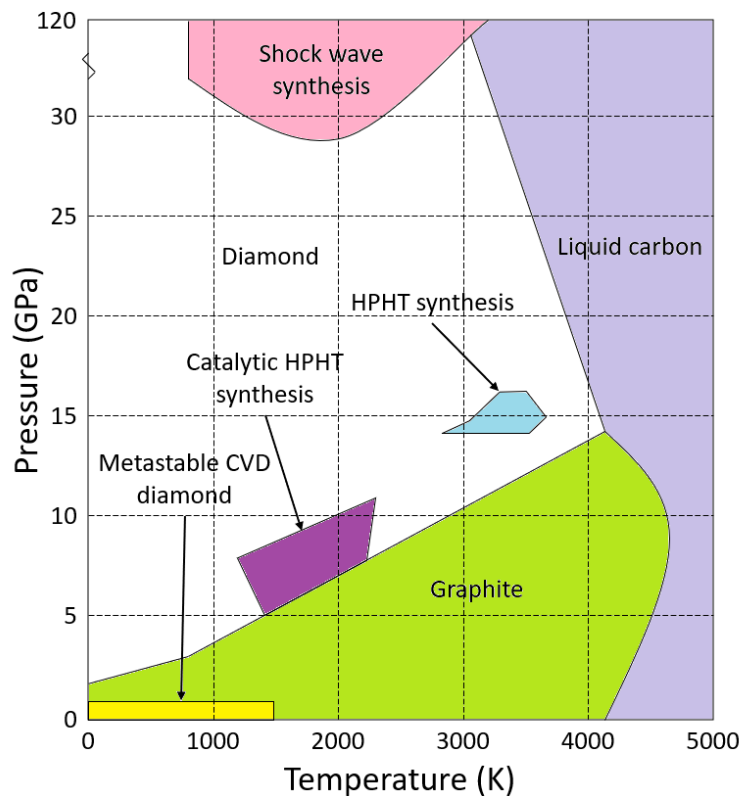


Figure 2.1: (P, T) diagram of carbon (inspired from the work of F. P. Bundy [40])

which means that diamond is kinetically metastable at room temperature and atmospheric pressure.

- The second region is the “*Liquid Carbon*” region. Under these temperature and pressure conditions, it is possible to obtain carbon in a liquid form.
- In the “*Shock Wave synthesis*” region, hexagonal graphite is converted into cubic diamond. Those conditions are used to produce nanodiamond by detonating an explosive carbon source within an enclosed explosion chamber [41]. The advantage of detonation nanodiamonds is their relatively low production cost and the uniformity of their shape and size.

- The “*HPHT synthesis*” region corresponds to the conditions used for HPHT diamond growth. This growth technique is based on the imitation of the circumstances under which diamond is formed in nature. In order to produce diamond with this technique, carbon should be put under a pressure around 15 GPa and a temperature over 3000 K. However, this process is very slow and therefore not economically viable.
- The “*Catalytic HPHT synthesis*” region describes another method for diamond synthesis from graphite. This method was first discovered by F. P. Bundy in 1955 [42]. In order to form diamond, graphite is mixed with a molten metallic solvent, like Ni, Co, or Fe, and pressed using a hydraulic press [43, 44]. The graphite is heated up by driving an electric current through it. Thanks to this technique, it is possible to grow diamond at a pressure between 5 GPa and 10 GPa and a temperature between 1500 K and 2300 K. This growth method is still used today to make industrial monocrystalline diamond substrates which are used as substrate for MWPECVD diamond growth and commercial applications (mechanical).
- Finally, the “*Metastable CVD Diamond*” gives the conditions of pressure and temperature for diamond growth by Chemical Vapor Deposition (CVD) method which will be discussed next.

## 2.2 Chemical Vapor Deposition (CVD)

The first diamond growth using the CVD method was reported in 1962 by W. G. Eversole [45] who discovered that it was possible to deposit diamond on a substrate

using a hydrocarbon gas or a CO/CO<sub>2</sub> mixture as a precursor at low pressure and temperatures where the diamond is metastable with respect to graphite (see Figure 2.1). In the following years, the scientific groups of B. V. Derjaguin [46] from the former USSR and J. C. Angus [47], in the US, worked independently on this subject and they both managed to co-deposit graphite and diamond on diamond crystal seeds. Their work led to the discovery of the crucial role of atomic hydrogen which preferentially etches away graphite and allows a much higher deposition rate [48]. From the 1970s, various scientific programs were led in Japan, especially in NIRIM [49] (now NIMS) leading to various CVD techniques to deposit thin diamond films on diamond and also non-diamond substrates.

A lot of different CVD techniques exists [44] depending on how the hydrocarbon precursor is decomposed. The ones that are the most used today are the Hot-Filament CVD (HFCVD) and the Plasma-Enhanced CVD (PECVD). However, the big disadvantage of HFCVD is the high risk of polluting the grown diamond layers with metallic impurities coming from the oxidation or vaporization of the hot filament used to decompose the hydrocarbon precursor. The amount of oxygen or methane also have to be restricted to minimize filament burning or degradation, respectively. PECVD offers a better control on the impurity content and the defects in the diamond layers that are produced. That is why in this work, the PECVD technique was used to produce boron-doped epitaxial and phosphorus-doped polycrystalline diamond layers.

### **2.2.1 Microwave Plasma Enhanced Chemical Vapor Deposition (MWPECVD)**

MWPECVD is a very popular method to grow diamond films. This technique does not rely on any electrode hence no impurities coming from it can contaminate the samples during the growth. However, contaminants can be generated by etching the reactor construction material, therefore, the deposition conditions have to be carefully chosen in order to minimize the contact between the plasma and the walls of the chamber [50]. MWPECVD provides high quality diamond films while being relatively easy to implement in a laboratory environment. MWPECVD reactors are generally more compact compared to their HPHT counterpart, simpler to operated since they don't require high pressure, and can deposit diamond over a large area.

In MWPECVD system, diamonds are generally grown using  $\text{CH}_4$  and molecular  $\text{H}_2$  but other carbon sources were also investigated such as  $\text{CO}$  [51],  $\text{CHF}_3$  [52] or even graphite [53]. The carbon precursor molecules are excited by a 2.45 GHz microwave generator. The plasma is formed by the collisions between high-temperature electrons and the relatively cold gas molecules resulting in the formation of precursors  $\text{CH}_3$  and atomic  $\text{H}$  [54] necessary to the diamond growth. There are several different MWPECVD reactor designs available on the market today.

#### **Tubular (NIRIM-type) reactor**

This type of reactor, presented in Figure 2.2 was developed in the early 1980s by Kamo et al. [49]. Precursor gases, a mixture of hydrocarbon and hydrogen gases, are dissociated by the 2.45 GHz microwave energy into a quartz tube inserted through a rectangular waveguide. A plunger is attached to the end of the waveguide

to minimize the reflected power and control the position of the plasma inside the discharge tube. The samples are inserted from the bottom of the chamber and placed at the intersection of the rectangular waveguide and the discharge tube. This type of setup has a power range from 100 W to 1.5 kW and a maximum operating pressure of about 130 mbar. The tubular reactor is compact and has a relatively low construction cost. However, this design limits the size of the sample to about 1 cm due to the diameter of the quartz tube (4.5 cm). For the MWPECVD growth of polycrystalline phosphorus-doped diamond layers presented in this work, a NIRIM-type reactor was used.

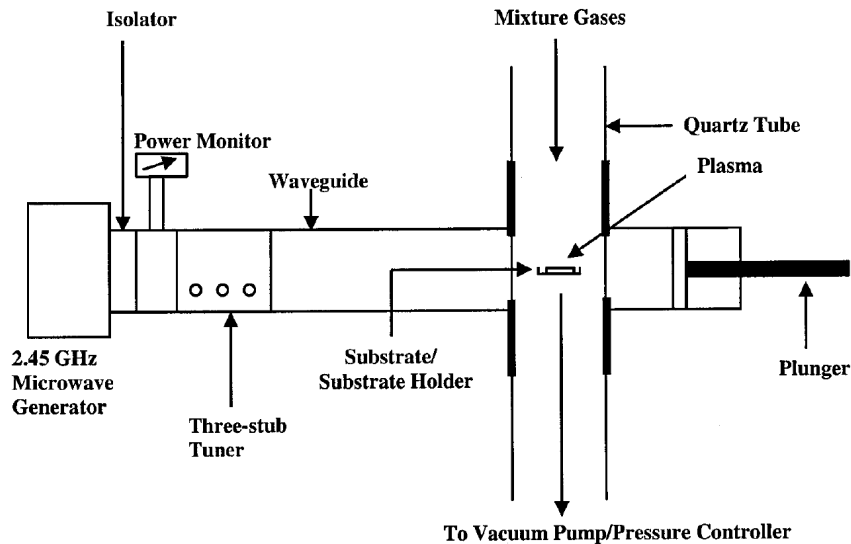


Figure 2.2: Tubular microwave plasma-assisted CVD reactor [55]

### Bell jar (ASTeX-type) reactor

The bell jar microwave CVD reactor, initially developed in 1987 [56, 57], and then commercialized by Applied Science and Technology, Inc. (ASTeX), is presented in Figure 2.3. In this design, the plasma is confined into a 10 cm inner diameter quartz

bell jar. The substrate holder, which is 7.5 cm in diameter, can accommodate larger samples compared to the NIRIM-type reactor. The microwave energy, provided by a magnetron connected to a 2.45 GHz power supply, is transmitted to the reactor using a rectangular waveguide. An antenna couples the energy from the waveguide into the cylindrical reactor. This model has a power range of 1.5 kW and an operating pressure 10 and 200 mbar. The position of the substrate holder is usually fixed. In this work, the MWPECVD growth of boron-doped diamond epitaxial layers was done using this type of reactor [58, 59].

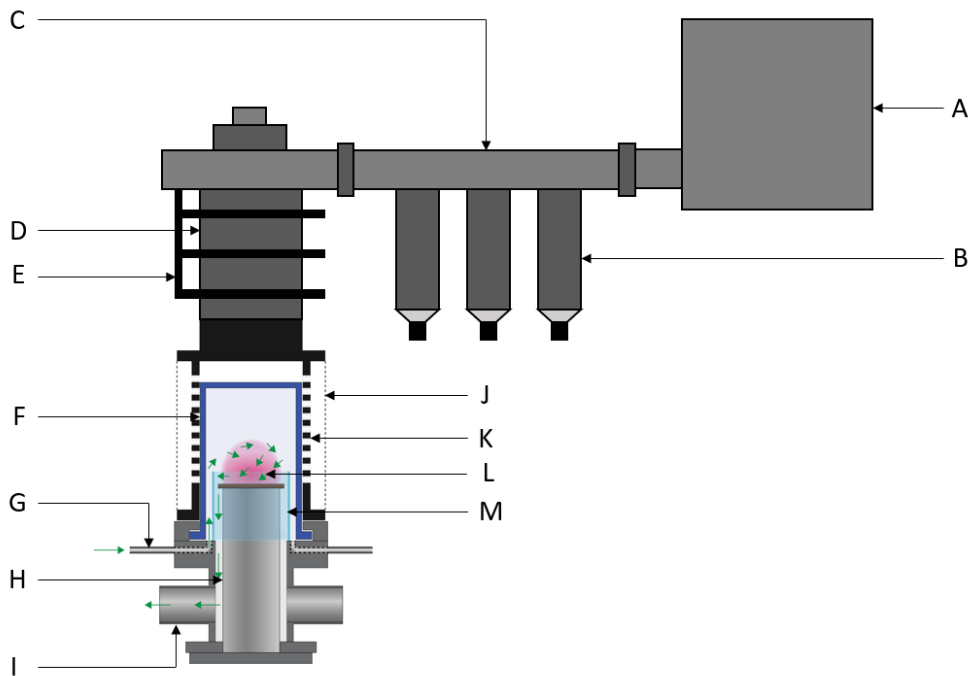


Figure 2.3: ASTeX bell jar microwave plasma-assisted CVD reactor

In 1992, ASTeX developed an improved version of the bell jar reactor called the ASTeX High Pressure Microwave Source (HPMS) [57] presented in Figure 2.4. The most notable difference with the previous model is the replacement of the quartz bell jar by a silica microwave window. The position of the substrate holder

Table 2.1: Parts highlighted within Figure 2.3

<b>Reference</b>	<b>Part name</b>
A	Microwave generator
B	Tuning stubs
C	Rectangular waveguide
D	Circular waveguide
E	Water-cooling system
F	Quartz bell jar
G	Gas input
H	Substrate holder
I	Gas output
J	Metallic grid
K	Coarse metallic grid
L	Plasma ball
M	Quartz tube

can now be adjusted, and the substrate can also be cooled or heated if necessary. The HPMS ASTeX system can be used with pressure values above 160 mbar and a maximum microwave power of 8 kW at 2.45 GHz. ASTeX also designed a 915 MHz system that permitted the use of higher power 30 – 60 kW magnetron power supplies [57] and the diamond growth on substrates with a diameter over 30 cm.

### **Ellipsoidal MWPECVD reactor**

This type of reactor, which was developed by M. Fünner et al. [60], is shown in Figure 2.5. Similarly to the ASTeX reactor, the microwave energy from the rectangular waveguide is coupled to the reactor cavity using a probe antenna. The peculiarity of this type of reactor comes from the ellipsoidal shape of the microwave cavity which is designed to maximize the microwave electric field strength at the location where the plasma is desired, i.e. just above the substrate. This reactor configuration was constructed at both 2.45 GHz and 915 MHz. The 2.45 GHz

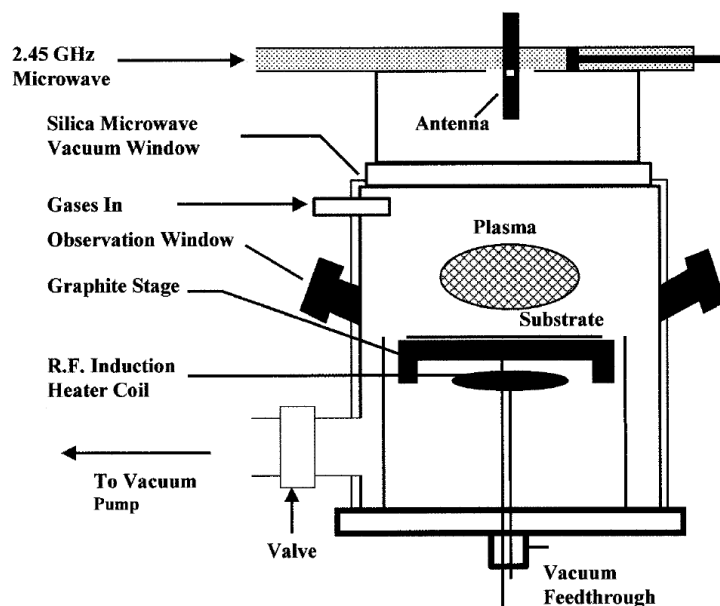


Figure 2.4: ASTeX high-pressure microwave source [57]

system used up to 6 kW of power for operation in the pressure range from 50 to 200 mbar with a maximum substrate size of 7.5 cm. The 915 MHz system was used to deposit diamond on substrates with a diameter up to 15 cm. The power for the 915 MHz system was up to 60 kW and the operating pressure was the same as the 2.45 GHz version [60].

### Surface wave plasma MWPECVD reactor

Diamond deposition over a large area is important for industrial applications such as the production of large-area protective coatings, and electrodes for electrochemical processes or waste-water treatment. However, scaling up to larger deposition areas is particularly difficult and costly for resonant cavity microwave systems and the HFCVD method which was originally used for this purpose has major drawbacks (see subsection 2.2). On top of that, those two techniques can cause

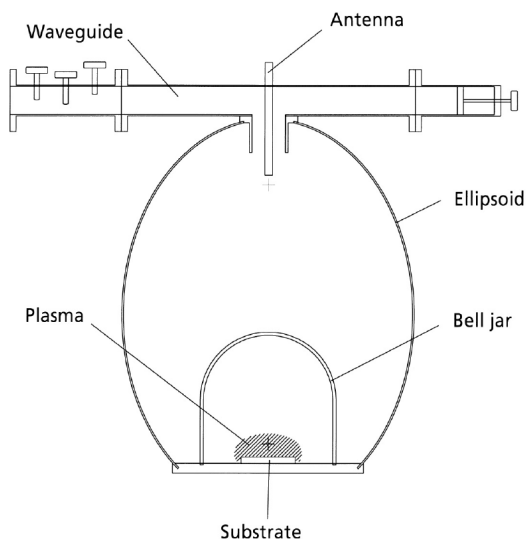


Figure 2.5: Setup of the ellipsoidal reactor [60]

substrate damage during deposition as the substrate temperature can easily be above 800 °C. In order to face those issues, K. Tsugawa et al. proposed in 2006 an alternative method for the growth of diamond using a MWPECVD process based on Surface Wave Plasma (SWP) in a linear antenna arrangement [61]. In this MWPECVD reactor presented in Figure 4, two microwave power supplies operating at a frequency of 2.45 GHz apply a maximum power of 20 kW to a set of linear antennas encased in quartz tubes. The plasma generated along the quartz tubes reaches the substrates placed on a stage below the antennas by diffusion. Compared to reactors using a plasma resonant cavity, the linear antenna system operates at a much lower pressure of around 1 mbar which limits the substrate temperature between 100 to 500 °C. The setup developed by K. Tsugawa et al. used two sets of eight parallel coaxial antennas which can cover substrates with an area up to  $30 \times 30 \text{ cm}^2$ . However, because of the scalability of the equipment, nanodiamond diamond coatings using this method are possible on much larger area

by increasing the number of electrodes.

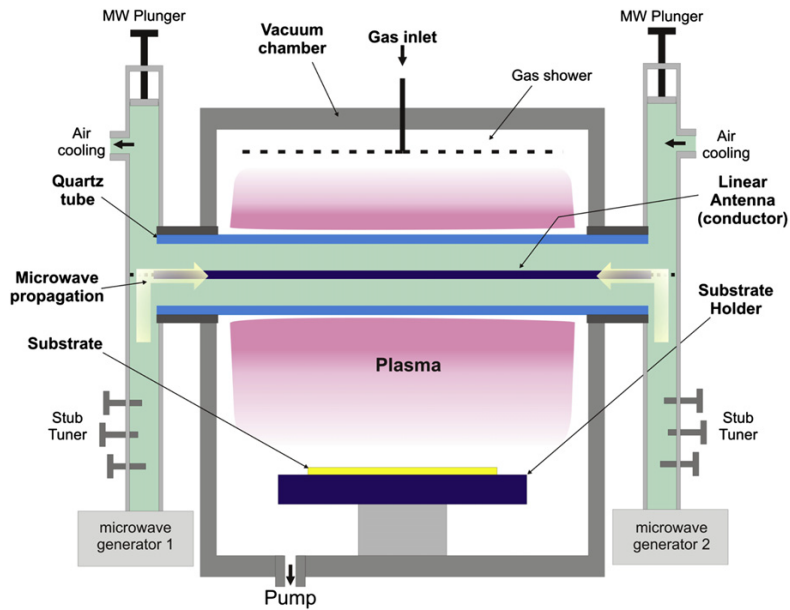


Figure 2.6: Schematic drawing of linear antenna microwave plasma enhanced CVD system adapted for diamond deposition [62]

In 2007, J. Kim et al. developed another MWPECVD setup for the growth of nanocrystalline diamond based on surface waves using multi-slotted antennas [63] which operate at a maximum power of 5 kW (see Figure 2.7). Smooth nanocrystalline diamond coatings were successfully deposited on a  $30 \times 30 \text{ cm}^2$  borosilicate glass plate under a pressure of 0.05 mbar and a temperature of  $500 \text{ }^\circ\text{C}$  [64].

### Distributed antenna array MWPECVD reactor

In 2014, H.-A. Mehedi et al. proposed a new reactor design for the deposition of diamond on large area [65]. In the Distributed Antenna Array (DAA) reactor, the plasma is formed in the reactor chamber using an array of 16 coaxial plasma sources inserted in a square metallic flange arranged in a  $4 \times 4$  matrix fed by a

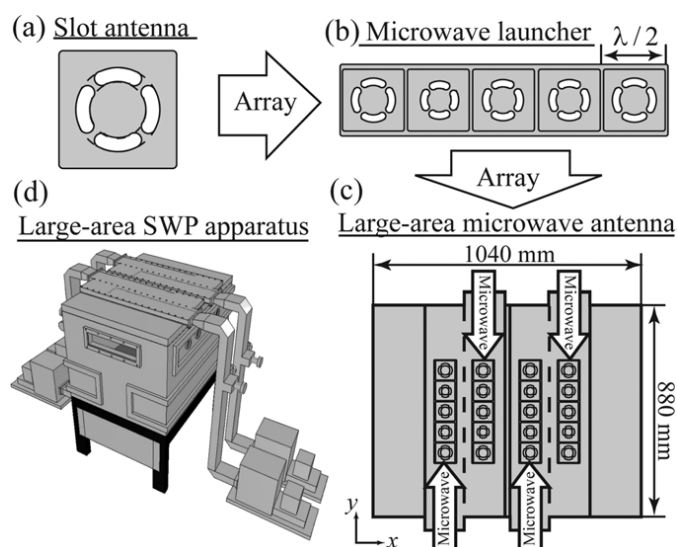


Figure 2.7: Schematic illustrations of (a) a slot antenna, (b) a microwave launcher, (c) a large-area microwave antenna and (d) the large-area SWP apparatus developed in this work [64]

6 kW (375 W per electrode) power generator (see Figure 2.8). After the ignition of the plasma around each electrode, the increase of the microwave power causes the localized plasmas to expand and meet to form a uniform plasma sheet. The operating pressure for this system is around 1 mbar which limits the substrate temperature to 300 - 500 °C. The number of sources can be increased to cover larger surfaces and a 3D arrangement of sources can theoretically be used to cover more complex shapes. The DAA design also offers a higher plasma density of  $10^{12}$  electrons. $\text{cm}^{-3}$  compared to the SWP reactors which will lead, for similar microwave power, to a more efficient chemical species production. Moreover, the DAA reactor does not use microwave applicators with large silica surfaces which, due to the use of hydrogen plasma, can be etched and lead to film contamination in SWP reactor designs.

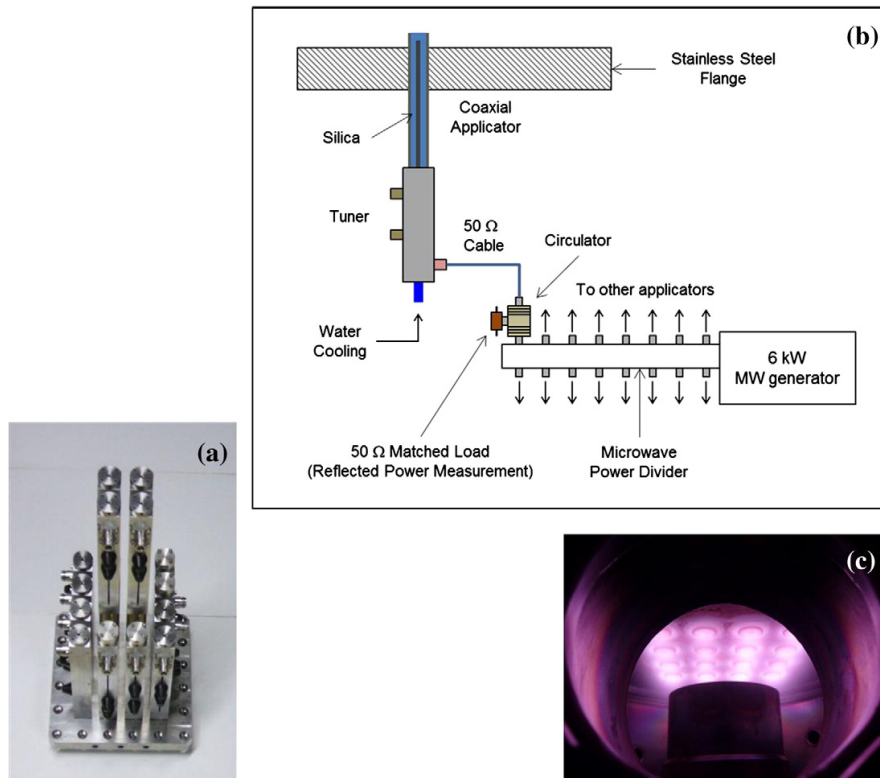


Figure 2.8: View of (a) the 16 coaxial plasma sources inserted in a square metallic flange arranged in a 2D-matrix to constitute the Distributed Antenna Array (DAA), schematic view of (b) the design of a coaxial plasma source, view of (c) the ignited plasma sources inside the chamber [65]

## 2.2.2 Role of the Different Precursor Gases

### Role of hydrogen

Hydrogen is the main component of the plasma. In its atomic form, it has different crucial roles in the growth of diamond using the MWPECVD method:

- It primarily contributes to the dissociation of carbon containing species in the gas phase into  $\text{CH}_x$  (with  $x = 1$  to 3) radicals [66].
- It etches non-diamond carbonated structures like graphite from the surface of the diamond substrate [47].

- It stabilizes the diamond surface by saturating the dangling bonds and thus favors the formation of  $sp^3$  carbon instead of  $sp^2$  carbon [66].
- It generates growth sites on the diamond surface by H-atom abstraction which can react with  $CH_3$  radicals and form C-C bonds necessary to the diamond growth [67].
- It prohibits the formation of aromatic hydrocarbons such as benzene, which can lead to non-diamond phase formation [66].

### **Role of methane**

Methane is the source of carbon for the diamond growth. Its concentration is given as a fraction of the total gas flow in the reactor. However, considering that hydrogen is by far the gas with the highest concentration in the plasma, the methane concentration is usually given as a fraction of the dihydrogen concentration  $[CH_4]/[H_2]$ . The growth rate increases with the fraction of methane in the gas phase [68–70] (see Figure 2.9). Depending on the methane concentration in the MWPECVD reactor, the type of diamond growth will also change:

- At low fraction  $[CH_4]/[H_2]$ , the epitaxial diamond layers obtained by MWPECVD growth are rough and defective. The formation of etch pits on the surface is attributed to the competition between diamond growth and diamond etching by the hydrogen plasma [71]. The limit of methane concentration under which this regime appears depends on the microwave power density used during the growth [72].
- At moderate fraction  $[CH_4]/[H_2]$  ( $[CH_4]/[H_2]$  ratio above 1% in a NIRIM-type

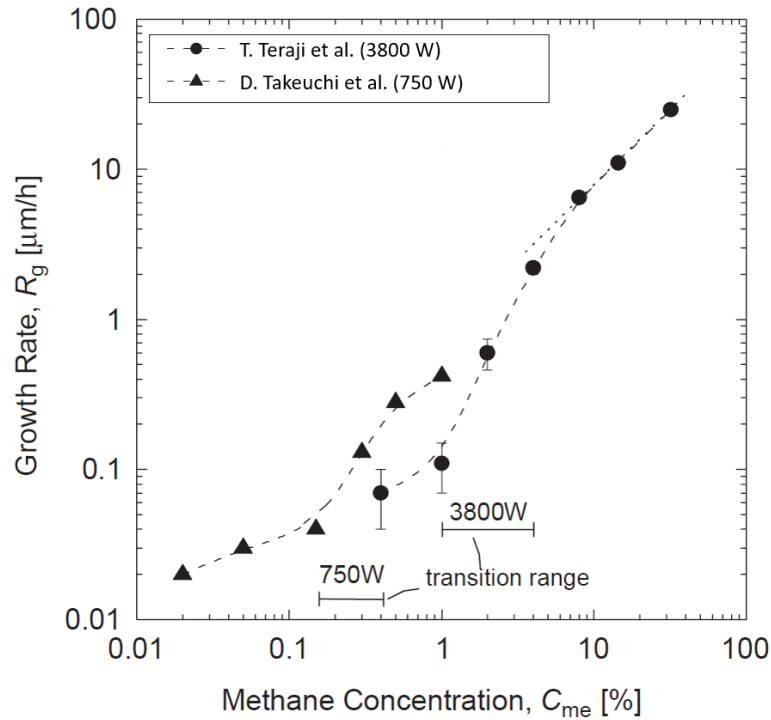


Figure 2.9: Evolution of the growth rate on (100)-oriented diamond substrate as a function of the  $[\text{CH}_4]/[\text{H}_2]$  ratio for diamond layers grown under 3800 W (T. Teraji et al. [68]) and 750 W (D. Takeuchi et al. [69])

reactor at 875 °C under 105 mbar of pressure [73]), the step-flow type of growth tends to dominate. This growth type is also favored by the off-angle on (100) substrates since crystalline steps are more numerous on the diamond surface for high off-angle, and the nucleation happens at the edges of those steps [73]. The step-flow type of growth results in smooth diamond surfaces [69, 74].

- When the  $[\text{CH}_4]/[\text{H}_2]$  ratio is further increased, nucleation also happens on terrace creating growth hillocks, leading to a two-dimensional nucleation and a rougher grown surface [73, 74]. Step bunching can also appear [72], forming macro steps on the diamond surface. This phenomenon can be caused by

adsorbed impurities such as nitrogen which block the advancing steps [75, 76] but it can also happen when the velocity of an individual step becomes of the order of the velocity of the diffusing adatoms [77].

- At high fraction  $[\text{CH}_4]/[\text{H}_2]$  ( $[\text{CH}_4]/[\text{H}_2]$  ratio above 6% in a NIRIM-type reactor at 875 °C under 105 mbar of pressure [73]), the diamond layer show random growth features [73] with non-epitaxial crystallites and vacancies. The use of a higher power can limit the apparition of such defects [68].

### **Role of oxygen**

Hydrogen can be mixed with oxygen in the reactor. The addition of oxygen to the gas mixture reduces the concentration of acetylene [78]. Oxygen also reacts with hydrogen to form OH radicals which etches non-diamond impurities faster and contribute to a better crystalline quality of the diamond layer [79]. Contrary to hydrogen, oxygen does not promote the formation of  $\text{sp}^3$  carbon. J. Ruan et al. [80] also found that oxygen could decrease the incorporation of boron atoms in the diamond lattice which is detrimental to the production of highly-doped p-type diamond but could be used to produce p-type diamond layers with very low boron concentration [4]. However, this mechanism is not well understood yet.

### **Role of $\text{CO}_2$**

Q. Zhang et al. [81] reported that the addition of  $\text{CO}_2$  during the MWPECVD growth of single crystal diamond by enhances the growth rate while retaining the crystalline quality of the diamond layer. This phenomenon was attributed to the enhanced etching of  $\text{sp}^2$  carbon impurities due to the presence of oxygen and the

increased carbonaceous source by adding CO<sub>2</sub>. However, due to the competition between those two effect, there is an optimum CO<sub>2</sub> concentration to reach the maximum growth rate. A. Kromka et al. [62] observed a similar effect for the growth of polycrystalline diamond at a low pressure of 0.1 mbar. The addition of 10% of CO<sub>2</sub> in the gas mix during the MWPECVD growth increased the diamond quality evaluated by Raman spectroscopy as well as the growth rate. It was also found that the addition of CO<sub>2</sub> suppressed the renucleation process (repeated formation of seeds) resulting in a larger grain size.

### **Role of nitrogen**

The addition of nitrogen during the growth of single crystal diamond by MWPECVD promotes the growth on the (100)-oriented faces [82]. A. Chayahara et al. [83] recorded a growth rate enhanced by a factor 2 with the addition of nitrogen during the growth rate by MWPECVD. G. Z. Cao et al. [84] attributed this phenomenon to the nitrogen-related species breaking part of the dimers on the reconstructed (100)-oriented surface and enhancing the diamond growth rate of this face by the creation of additional kink sites at the growth steps. Nitrogen impurities also tend to favor the apparition of step bunching on the (100)-oriented diamond layers. At high nitrogen concentration, the growth rate saturates and the morphology of the diamond surface changes to two-dimensional growth which competes with step bunching leading to a non-uniformity in roughness and growth rate [83].

### **Role of argon**

The addition of argon in the MWPECVD reactor during the synthesis of polycrystalline diamond decreases the grain size of diamond crystals in the layer. D. Zhou

et al. [85] observed a transition from microcrystalline to nanocrystalline diamonds for a gas mix in the reactor containing above 80% of argon. This phenomenon was attributed to a change in the plasma chemistry initiating the process of renucleation [86].

### **C-H-O diagram**

Bachmann et al. [87] compiled the data of many diamond deposition experiments using different CVD methods (MWPECVD, hot filament CVD, etc.). They concluded that the exact composition of the precursor gases was unimportant in most cases and that, under typical process temperature and pressure, only the relative ratios of C, H, and O controlled the diamond growth. Figure 2.10 shows the diagram resulting from this study. Diamond deposition is only possible in a small area of the diagram located around the C-O tie line (i.e.  $[C] = [O]$ ). Below this limit, the concentration of  $\text{CH}_3$  radicals is too low to sustain diamond deposition and therefore, there is no growth. Above this limit, the concentration of  $\text{CH}_3$  radicals is too high and deposition outpaces the rate at which hydrogen can etch non-diamond phases [88].

As previously mentioned, the tertiary diagram in Figure 2.10 is true for most CVD techniques but exceptions exist. As an example, M. Varga et al. [89] managed to grow porous diamond layers in a linear antenna MWPECVD system with a fraction of  $\text{CO}_2$  above 40% in a  $\text{H}_2/\text{CH}_4$  gas mix.

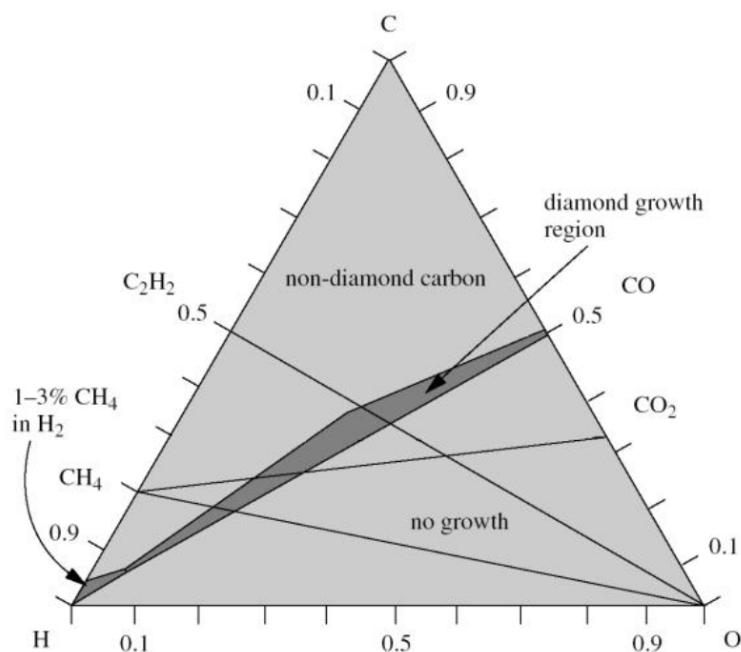


Figure 2.10: A simplified form of the Bachmann [87] atomic C–H–O diagram

### 2.2.3 Influence of the Growth Parameters

#### Influence of substrate temperature

Brinza et al. [90] studied the evolution of the growth rate of epitaxial layers as a function of the substrate temperature between 750 and 950 °C for (100)-, (111)-, (110)-, and (113)-oriented planes. The measured growth rates are reported in Figure 2.11 and they increase with the substrate temperature. This result is consistent with the fact that diamond is thermally activated and the growth rate follow an Arrhenius law [91]. It was also observed that layers grown at a low substrate temperature (around 750 °C) on (100)-oriented diamond had a rough surface with a high density of square pit defects on the surface [72, 92]. At higher substrate temperature, the surface mobility of the species increases and the step-flow type of growth is favored, resulting in higher growth rates and flatter surface [73]. However,

for temperature close to 1000 °C, the surface quality degrades, with the apparition of large pyramidal structures [72, 92]. A substrate temperature of 850 °C offers a good compromise between high growth rate and good surface quality [72, 92, 93].

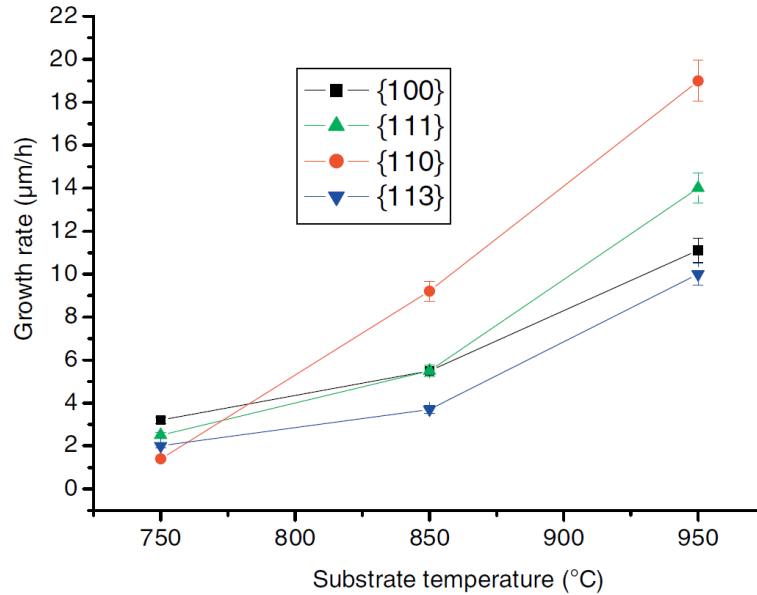


Figure 2.11: Evolution of the growth rate on 100, 111, 110, and 113 planes as a function of the temperature under a pressure of 200 mbar, a microwave power of 3.5 kW and a methane  $[\text{CH}_4]/[\text{H}_2]$  ratio of 4% [90]

### Influence of the microwave power density

The microwave power density is defined as the ratio as the ratio of the total injected power to the volume of the full plasma ball obtained in the absence of the substrate holder. C. Findeling-Dufour et al. [93] found that increasing the microwave power density from 12.5 to 17  $\text{W}\cdot\text{cm}^{-3}$  during the growth of (100) diamond layers at 850 °C in 2% of methane decreases the density of crystallites and the size of hillocks on their surface. This improvement of surface quality can be attributed to the promotion of the step-flow type of growth at high power density [68]. J. Achard

et al. [72] observed an increase in the growth rate from 3 to 8.5  $\mu\text{m}\cdot\text{h}^{-1}$  for (100) diamond layers grown at 850 °C in 4% of methane when the power density went from 75 to 130  $\text{W}\cdot\text{cm}^{-3}$  (see Figure 2.12) which was attributed to the higher concentration of  $\text{CH}_3$  radicals and atomic hydrogen in the reactor for higher power density. For a given pressure and temperature, increasing the microwave power density also increases the  $[\text{CH}_4]/[\text{H}_2]$  fraction above which non-diamond phases are deposited. This improvement in crystalline quality was attributed to the increase in atomic H density [94]. However, it was also observed that under high power density, diamond etching can compete with diamond growth and create etch pits on the surface if the methane concentration is too low [68, 72, 92].

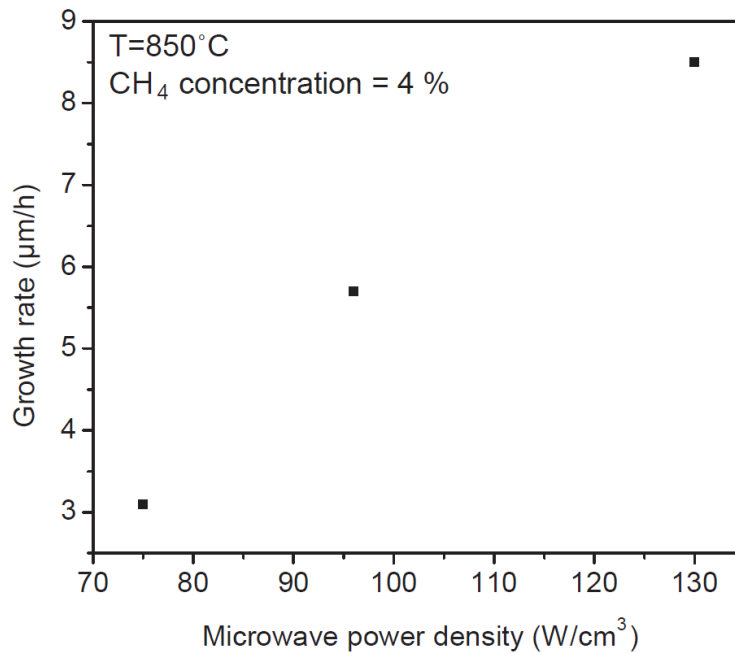


Figure 2.12: Evolution of the growth rate on (100)-oriented diamond substrate as a function of the injected microwave power density at a temperature of 850 °C and a methane  $[\text{CH}_4]/[\text{H}_2]$  ratio of 4% [72]

### **Influence of the pressure**

C. J. Widmann et al. [95] observed an increase in the growth rate on (100)-oriented diamond substrates when the pressure in the MWPECVD reactor during deposition increased from 250 to 400 mbar with a microwave power of 3 kW (see Figure 2.13). This behavior could be attributed to the increase in concentration of carbon species close to the diamond surface at higher pressure. A. L. Maslov et al. [96] conducted a similar study with a pressure varying from 293 mbar to 400 mbar and a higher microwave power of 4 kW. He observed that the growth rate increases from 7.6 to 27  $\mu\text{m}\cdot\text{h}^{-1}$  when the pressure goes from 293 to 347 mbar but then decreases to 10  $\mu\text{m}\cdot\text{h}^{-1}$  when the pressure further increases to 400 mbar. This difference could be attributed to the higher power used in this experiment compared to the one of C. J. Widmann et al. which causes diamond etching to compete with diamond growth as previously described. Indeed, at higher pressure, the microwave power density also increases due to a reduction of the plasma volume.

A Kromka et al. [62] reported on the growth of polycrystalline diamond under low pressure in the presence of  $\text{CO}_2$ . He observed that decreasing the pressure from 2 mbar to 0.1 mbar improved the growth rate. This phenomenon is attributed to the increase of the plasma molecular species mean free path and the extension of the plasma volume towards the substrate at lower pressure. Additionally, the presence of  $\text{CO}_2$  suppresses the development of non-diamond carbon phases and limits the renucleation process, resulting in a one order of magnitude increase in the size of the diamond crystals.

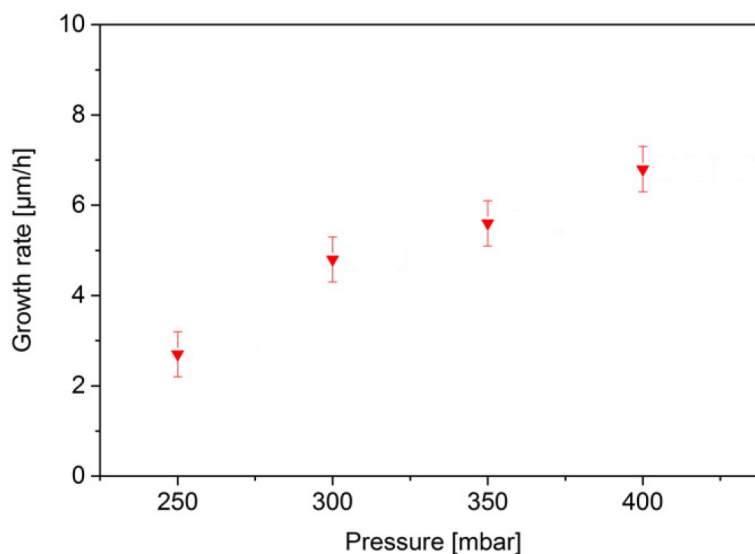


Figure 2.13: Evolution of the growth rate on (100)-oriented diamond substrate as a function of the pressure for a microwave power of 3 kW, a temperature of 760 °C and a methane  $[\text{CH}_4]/[\text{H}_2]$  ratio of 3% [95]

## 2.3 Diamond Doping

### 2.3.1 Diamond P-Type Doping

Even though aluminum was originally foreseen as being responsible for the p-type conductivity in diamond, it was demonstrated by A. T. Collins et al. [97] in 1971 that it was in fact due to boron impurities. These results were later confirmed by R. M. Chrenko [98] in 1973. Boron is the only dopant which can be incorporated with great reproducibility. Boron atoms are particularly adapted to p-type doping since their covalent radius (0.088 nm) is very close to the one of carbon atoms (0.077 nm) which favors their incorporation in substitutional sites. Initially, the doping was done by using diborane  $\text{B}_2\text{H}_6$  as a source of boron atoms, but nowadays, trimethylborane (TMB)  $\text{C}_3\text{H}_9\text{B}$  is preferred as it gives similar results while being less toxic.

Since the activation energy of boron in diamond is 0.37 eV, only a small fraction of boron atoms is ionized at room temperature. For boron concentrations below  $1 \times 10^{19} \text{ cm}^{-3}$ , only  $2 \times 10^{-3}$  holes are introduced in the valence band per boron atom [99]. For boron concentrations between  $1 \times 10^{19} \text{ cm}^{-3}$  and  $3 \times 10^{20} \text{ cm}^{-3}$  the boron impurities form a band in which the conduction is done by hopping between ionized and neutral impurities [100, 101]. For boron concentrations above  $3 \times 10^{20} \text{ cm}^{-3}$ , the activation energy decreases quickly. It is the Mott transition of diamond [102–104].

The growth of boron-doped homoepitaxial diamond has been investigated on various crystalline orientation, mostly on (100)- [105], (111)- [106], (110)- [107], and more recently on (113)- [108], (115)-, and (118)-oriented substrates [109].

### **Growth on (100)-oriented substrates**

The (100) orientation is the most popular for the growth of homoepitaxial boron-doped diamond. Boron-doping is possible within a wide range of concentrations from  $1 \times 10^{14}$  [110] up to  $1 \times 10^{21}$  [111]. The doped diamond layers grown on (100)-oriented substrates are smooth with values of RMS roughness as low as 0.2 nm even for a high boron concentration of  $1 \times 10^{20} \text{ cm}^{-3}$  [112]. V. Mortet et al. [113] observed that an increase in the misorientation angle from  $0^\circ$  to  $5^\circ$  caused a decrease in the RMS roughness from 1 nm to 0.3 nm and an increase in the growth rate from  $2 \mu\text{m.h}^{-1}$  to  $5 \mu\text{m.h}^{-1}$ . This phenomenon was attributed to the step flow growth which is predominant at larger misorientation angle due to the higher density of steps and produces atomically flat surfaces. The (100)-oriented boron-doped diamond layers also have good electrical properties with high hole mobility values: H. Okushi et al. [114] managed to reach a hole mobility of 1840

$\text{cm}^2.\text{V}^{-1}.\text{s}^{-1}$  at 290 K for a boron concentration of  $1 \times 10^{17} \text{ cm}^{-3}$ . Low compensation of boron acceptors by other impurities such as nitrogen can also be achieved with values as low as 0.01% [99]. Despite its qualities, the (100) orientation suffers from a relatively poor boron incorporation efficiency into the lattice compared to other crystalline orientations. V. Mortet et al. [113] reported an incorporation efficiency close to 30% for a boron to carbon ratio in the gas phase of 1000 ppm.

### **Growth on (111)-oriented substrates**

The (111) orientation offers a better incorporation efficiency of boron compared to the (100) orientation with reported values up 1000% [113]. A. Boussadi reported a high growth rate up to  $4.3 \mu\text{m}.\text{h}^{-1}$  and the growth of a thick  $100 \mu\text{m}$  layer free of non-epitaxial defects for a boron concentration of few  $10^{20} \text{ cm}^{-3}$ . H. Ye et al. also reported the growth of smooth (111) layers with a RMS roughness of 0.2 nm at a similar boron concentration. Above  $10^{20} \text{ cm}^{-3}$  of boron, however, the crystalline quality of the deposited layer tends to degrade [115] with the apparition of growth hillocks and stacking faults [116, 117] and above  $2 \times 10^{21} \text{ cm}^{-3}$  up to  $5 \times 10^{21}$  (which is the highest boron concentration reported in single crystal diamond), a phase separation between  $\text{sp}^3$  carbon,  $\text{sp}^2$  carbon, and boron is even observed [118]. The biggest flaw of the (111) orientation is the poor hole mobility in the layers. Reasonably high mobility values can be obtained in layers with low boron content: A. Lazea et al. [119] reported a hole mobility of  $556 \text{ cm}^2.\text{V}^{-1}.\text{s}^{-1}$  at a boron concentration of  $3 \times 10^{17} \text{ cm}^{-3}$ . S.-G. Ri et al. [120] also observed that increasing the  $[\text{CH}_4]/[\text{H}_2]$  ratio during the growth doesn't change the incorporation efficiency of boron in (111)-oriented diamond layers while it improves it in (100)-oriented layers. This result suggests a different boron doping mechanism between (100)-

and (111)-oriented diamond substrates.

### **Growth on (113)-oriented substrates**

The (113) orientation has a vicinal surface composed of monoatomic (100) and (111) steps. Boron-doped diamond layers grown on (113)-oriented substrates have a smooth surface with a RMS roughness of 1 nm comparable to what was measured on (100) diamond layers but without growth hillocks and also exhibit a uniform boron incorporation [121]. A growth rate of  $5 \mu\text{m.h}^{-1}$ , a boron incorporation efficiency up to 5 times higher compared to the (100) orientation [108], and a maximum hole mobility above  $1200 \text{ cm}^2.\text{V}^{-1}.\text{s}^{-1}$  were reported for boron-doped diamond layers grown on this orientation [122]. A. Tallaire et al. [108] reported that it was possible to grow boron-doped diamond on (113)-oriented substrates at temperature higher than  $1000 \text{ }^\circ\text{C}$  without experiencing unepitaxial defects. V. Mortet et al. [123] also reported that it was possible to grow heavily boron-doped diamond layers (boron concentration of  $10^{21} \text{ cm}^{-3}$ ) up to a thickness of  $3.5 \mu\text{m}$ . For thicker layers, cracks appear on the diamond surface which are attributed to the relaxation of the elastic energy stored in the epitaxial undoped layer due to the significant lattice mismatch between the undoped and highly boron-doped diamond layers. The (113) orientation offers a trade-off between the properties of the (100) and (111) orientation which is most likely due to the vicinal nature of its surface.

### **2.3.2 Diamond N-Type Doping**

Achieving n-type doping is a very important step in the manufacturing of electronic devices. However, contrary to the p-type doping which is relatively easy to achieve

and can even be found in natural diamonds, n-type doping is still a very challenging task.

Due to the rigidity of the diamond structure and the small size of the carbon atom, it is hard to find an appropriate dopant. Nitrogen forms a deep donor level at 1.7 eV under the conduction band [124] which is too deep to create n-type conductivity. Theoretical studies found that lithium, sodium, and sulfur could be potential candidates for n-type doping in diamond [125, 126]. Lithium and sodium were predicted to form donor levels at an energy of respectively 0.1 eV and 0.3 eV under the conduction band but they have a very poor solubility in diamond structure making doping by diffusion impossible [127]. Because of their preference to occupy interstitial positions in the diamond lattice, there is no competition with carbon atoms for substitutional sites and therefore it is possible to use ion-implantation to form n-type diamond. However, high dose of implanting ions causes irrecoverable graphitization [128] and it was also found that the donors are electrically inactive after annealing [125].

In the early 1990s, phosphorus was also considered as a potential dopant. However, at the time, theoretical studies were not consistent between each other and predicted a donor behavior at an energy ranging from 0.2 eV [129] to 1.09 eV [130] below the conduction band. A very low substitutional solubility was also predicted [131].

The first evidence of n-type conductivity measured on phosphorus-doped diamond was provided in 1995 by J. F. Prins et al. [132] on natural IIb diamonds implanted with a low dose of  $P^+$  ions. In 1997, S. Koizumi et al. [133] managed to produce the first n-type doped diamond using CVD and  $PH_3$  on (111)-oriented diamond samples. In 1999, another Japanese team claimed that they achieved

n-type doping on (100) diamond samples using CVD and H<sub>2</sub>S [134]. However, it was found later that the conduction was due to boron atoms which were unintentionally incorporated in the lattice [135]. Nowadays, phosphorus is considered as the main dopant to achieve n-type conductivity with an activation energy around 0.6 eV [136–138]. Recently some novel co-doping techniques have been developed using two different elements forming complexes in the diamond layer [139, 140]. New shallow donors could be found with this method.

The growth of phosphorus-doped diamond has been investigated on various crystalline orientations including (100), (111), and (113) lately.

### **Growth on (100)-oriented substrates**

As the production of p-type diamond layers grown on (100) oriented substrates was already well understood, effort were made to produce phosphorus-doped n-type layers using this orientation. H. Kato et al. [141] managed to produce n-type doped diamond layers with a controllable range of phosphorus concentration between  $5 \times 10^{17}$  and  $8 \times 10^{18} \text{ cm}^{-3}$ . An electron mobility of  $780 \text{ cm}^2 \cdot \text{V}^{-1} \cdot \text{s}^{-1}$  was reported [142]. However, phosphorus doping on (100) diamond substrates poses a number of problems. First, a very low doping efficiency of 0.05% was reported [141]. Second, the phosphorus donor fraction (the percentage of incorporated phosphorus atoms in the diamond lattice acting as donors) is less than 65% [143] and the compensation ratio is extremely high (from 50 to 80%) [144] which is detrimental to the electrical properties of the phosphorus-doped diamond layers.

### **Growth on (111)-oriented substrates**

The production of n-type diamond layers by MWPECVD was first demonstrated on the (111) orientation [133] and it is still the most documented crystalline orientation for the growth of phosphorus-doped diamond layers. Phosphorus concentrations up to  $1.5 \times 10^{20} \text{ cm}^{-3}$  with a maximum growth rate of  $1.25 \mu\text{m.h}^{-1}$  were reported [145] and electron mobilities up to  $660 \text{ cm}^2.\text{V}^{-1}.\text{s}^{-1}$  [146]. The doping efficiency of phosphorus is about 2% [141] which is between one and two orders of magnitude higher than the one reported for (100)-oriented layers. A phosphorus donor fraction over 90% [147] and a compensation ration about 10% [148] were also measured on (111) phosphorus-doped diamond layers. Despite their better incorporation of phosphorus compared to layers grown on (100) substrates, (111)-oriented layers tend to present cracks and structural defects.

### **Growth on (113)-oriented substrates**

The (113) orientation was recently investigated for the growth of n-type diamond layers as it has intermediate properties between the (100) and (111) orientations making it a promising candidate for both boron and phosphorus doping. M.-A. Pinault-Thaury et al. [149] developed a method combining MWPECVD and metal-organic CVD to produce phosphorus-doped diamond layers on (113)-oriented samples using tertiary butyl-phosphine (TBP:  $\text{C}_4\text{H}_{11}\text{P}$ ) vapor as a dopant source. A phosphorus concentration up to  $4.5 \times 10^{19} \text{ cm}^{-3}$  was obtained with a doping efficiency around 0.08% which is still low but about three times higher than what was obtained on (100) substrates. The phosphorus donor fraction was close to 100% for samples with a phosphorus concentration around  $10^{16} \text{ cm}^{-3}$ . A good

crystalline quality and a smooth surface with a RMS roughness as low as 7 nm were obtained over three decades of phosphorus content without pyramid hillocks and non-epitaxial crystallites. The measured growth rate was up to  $1.1 \mu\text{m}\cdot\text{h}^{-1}$  which is comparable to the one of (111) phosphorus-doped diamond layers. Finally, an electron mobility of  $355 \text{ cm}^2\cdot\text{V}^{-1}\cdot\text{s}^{-1}$  was obtained on a sample with a phosphorus content of  $2.0 \times 10^{18} \text{ cm}^{-3}$  which is a higher mobility value than the one of (100)- and (111)-oriented layers with a similar phosphorus concentration [150].

### 2.3.3 Surface Conductivity

In addition to these bulk doped p-type and n-type diamond, surface conductivity phenomena have also been observed.

Hydrogenated diamond surfaces exhibit p-type conductivity at room temperature. This type of surface can be obtained by oil polishing (a method originally used in jewelry), exposition to atomic hydrogen using hot filament or plasma [151], and it is also observed on as-grown epitaxial diamond after CVD processing [152]. This surface with p-type behavior has been observed on both (100) and (111) diamond samples with values of conductivity ranging from  $10^{-4}$  to  $10^{-5} \Omega^{-1}$  [153]. The reason for this conductivity is not well understood yet, but it is assumed that hydrogen termination is responsible for the accumulation of holes by creating a layer of unspecified acceptor defects about 30 nm under the surface [154]. A negative electron affinity of -1.3 eV was measured on the hydrogenated diamond surface by J. B. Cui et al. [155] with a Fermi level at 0.7 eV below the valence band maximum [156]. F. Maier et al. [153] showed that the hydrogenation of the surface is a necessary but not sufficient condition for surface conductivity and

made the hypothesis of the presence of a thin water layer on the surface of the sample which would provide the electron sink for the subsurface hole accumulation. The chemical potential of electrons in water being lower than the Fermi level  $E_F$  of the diamond, electrons are exchanged with water according to the reaction  $2H_3O^+ + 2e^- = 2H_2O + H_2$ , leaving holes in the valence band.

The diamond p-type surface conductivity can be problematic as it can interfere with the measurement of transport properties in doped diamond films. It is possible to remove the diamond surface conductivity due to hydrogenation by oxidizing its surface. F. Maier et al. [157] measured an electron affinity of 1.7 eV on oxidized diamond surfaces prepared by boiling the diamond sample in a concentrated solution of  $HNO_3/H_2SO_4$ . The Fermi level was 0.8 eV above the valence band maximum. A. Denisenko et al. [158] showed that the electronic barrier can be further modified by using anodic oxidation in KOH on diamond surfaces already oxidized by wet chemical treatment and obtained a Fermi level at 3.6 eV above the valence band maximum.

## 2.4 Conclusion

To conclude, the growth parameters such as the pressure, the temperature, the power density, the methane concentration, and the presence of other chemicals such as boron, phosphorus, nitrogen, and oxygen during the diamond growth by MWPECVD directly impact the growth rate and the quality of the deposited diamond layers. Additionally, one shall not forget that, in the case of epitaxial growth, the orientation of the diamond substrate is also a crucial parameter, the growth of boron-doped diamond is easier on the (100) orientation while the (111)

orientation is more favorable to phosphorus doping. That is why alternative orientations such as (113) have also been investigated in order to find a compromise between the properties of the (100) and (111) orientations.

## Part II

# EXPERIMENTAL

# Chapter 3

## MWPECVD Reactors

In this chapter, the two different reactors used for the growth of boron-doped and phosphorus-doped diamond layers are presented along with the time response measurement setup used for the study of gas dynamics in MWPECVD reactors.

### 3.1 Reactor Types

#### 3.1.1 Bell Jar (ASTeX-Type) Reactor

The reactor used for the epitaxial boron-doped diamond growth is a commercial ASTeX 5010 reactor (Seki Technotron, Japan). It is a bell jar reactor whose operating principle was already presented in subsection 2.2.1. A base pressure in the reactor chamber below  $10^{-6}$  mbar was achieved using a Pfeiffer Vacuum TMH-071 turbo-molecular pumping system. The microwave power was provided by an ASTeX S-1500 plasma source with a maximum power output of 1.5 kW. The PECVD system is shown in Figure 3.1.

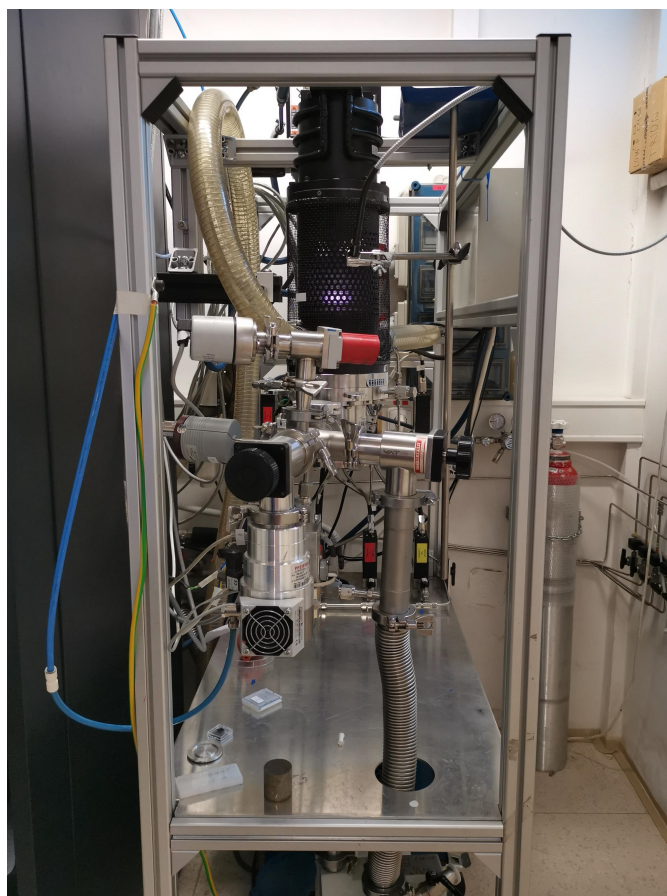


Figure 3.1: ASTeX bell jar reactor used for the growth of single crystal boron-doped diamond layers

### 3.1.2 Tubular (NIRIM-Type) Reactor

The reactor used for the growth of polycrystalline phosphorus-doped diamond layers is a lab-made tubular reactor whose operating principle was already presented in subsection 2.2.1. The reactor chamber was evacuated to a base pressure below  $10^{-6}$  mbar using a Agilent Turbo-V 301 Navigator turbo-molecular pumping system. The microwave power is provided by a WR340 downstream plasma source from SAIREM working at frequency of 2.45 GHz. The PECVD system is shown in Figure 3.2. Gas flows were regulated using MKS mass flow controllers while the

pressure was measured using a capacitive gauge during operation and regulated using an MKS 20000 sccm control valve and a type 250 controller together with a rotary vane pump DUO 20 M from Pfeiffer Vacuum.

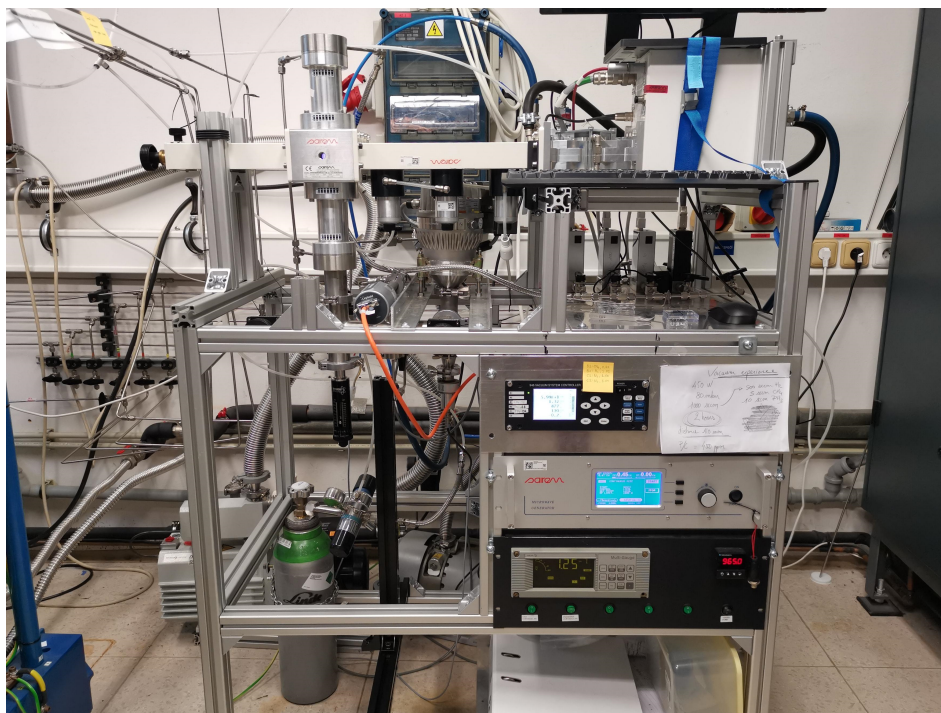


Figure 3.2: NIRIM reactor used for the growth of polycrystalline phosphorus-doped diamond layers

## 3.2 MWPECVD Reactor Time Response Measurement Setup

In order to study the gas dynamics in MWPECVD reactors, a setup recording the response of the plasma to the injection of a small quantity of gas in the two different reactors previously presented (see subsection 3.1.1 and 3.1.2) was designed.

The gases used in this study are  $H_2$  (N5.6),  $CH_4$  (N5.5),  $O_2$  (N4.5),  $N_2$  (N5.0).

The flow of gases was controlled using MKS mass flow controllers. The precursor gas pulses were generated using the gas trapped in a small volume at a constant pressure (2 bar) between two ball valves and released instantaneously in the reactor. The volume of trapped gas was about 1 mL. The setup is described in Figure 3.3. The emission lines of NH (336.9 nm [159], C<sub>2</sub> (517.0 nm [160]), and OH (311.4 nm [161])) were analyzed to study the effect of a pulse of N<sub>2</sub>, CH<sub>4</sub>, and O<sub>2</sub> in the plasma. Two different optical measurement systems were considered to record the time evolution of the emission lines characteristic of the precursor gases injected in the reactors.

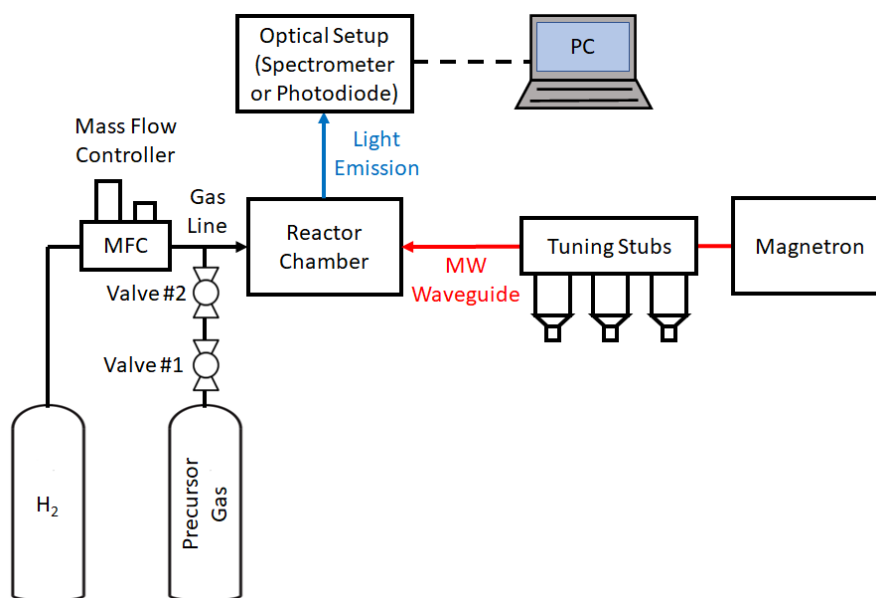


Figure 3.3: Time response measurement setup

At first, the emission lines were monitored using a Thorlabs SM05PD3A photodiode with a wavelength range from 320 to 1100 nm in combination with several Thorlabs band-pass filters centered around the wavelength of the emission line of interest. The photodiode voltage was recorded as a function of time using a

Keysight 34461A multimeter and saved on a computer using Keysight BenchVue software. A homemade brass holder was designed to combine the photodiode and filter in a closed package and isolate it from any parasitic light sources. The main advantages of this setup are its simplicity and its operation speed with a sampling rate of about 20 Hz. However, its major flaw is its poor selectivity as it is impossible to measure and remove possible variation of the continuous background light coming from the hydrogen plasma during the gas pulse, which can overshadow the variation of the measured emission line. This setup was abandoned as significant variation of the background light intensity were observed during the measurements.

It was then decided to use a Stellarnet BLACK-Comet-SR compact spectrometer, which has an acquisition range from 200 to 1100 nm, to record the dynamic gas pulse responses. In order to have enough points to correctly record the fast variations of the signal, an integration time of 25 ms was chosen. The acquired spectra were analyzed using an algorithm in Origin<sup>®</sup> software to remove the variation of the continuous background from the signal.

# Chapter 4

## Characterization Techniques

In this chapter, the different characterization techniques and experimental setups used in this thesis are presented. The surface morphology of the boron-doped and phosphorus-doped diamond layers was checked using AFM and SEM imaging respectively. The boron concentration in the epitaxial layers was obtained using SIMS measurement. The larger size of the Si substrates on which the phosphorus-doped diamond layers were deposited allowed us to use GDOES for the determination of the phosphorus concentration. The electrical properties of the boron-doped diamond layers were characterized using a TLP current-voltage setup and Hall effect measurement, and their thermal properties were characterized using TIM. Finally, Raman spectroscopy was used to evaluate the crystalline quality of the phosphorus-doped diamond layers.

## 4.1 Atomic Force Microscopy (AFM)

### 4.1.1 AFM Theory

AFM is a type of microscopy in which images are obtained by scanning the surface of the sample under study with a tip mounted at the end of a cantilever. The tip is brought in closest contact with the sample and the movements of the cantilever are recorded to create a topographic image of the sample's surface. In this thesis, AFM was used to obtain images of the epitaxial single crystal boron-doped diamond layers grown by PECVD.

Figure 4.1 shows a schematic representation of an AFM system. The tip and cantilever are usually made of silicon or silicon carbide. The position of the cantilever is monitored using a laser beam which is reflected from the backside of the cantilever into a position-sensitive photodetector consisting of two side-by-side photodiodes. In this arrangement, a small deflection of the cantilever will change the reflection angle of the laser beam and, therefore, the position of the laser spot on the photodetector. The difference in signal between the two photodiodes gives the position of the laser spot on the photodetector from which it is possible to calculate the deflection angle of the cantilever. This arrangement is called an optical lever [162].

Images are formed by recording the effects of the interaction forces between the tip and the surface as the cantilever is scanned over the sample. The cantilever is attached to a piezoelectric actuator connected to an electronic feedback circuit. This assembly forms, with the sample and the optical lever, a feedback loop which allows the system to maintain the tip at a constant force or at a constant height above the surface of the sample. In the constant force mode, the real time height

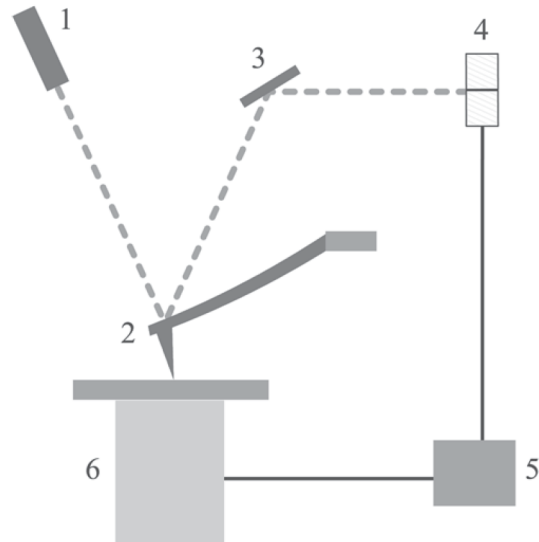


Figure 4.1: Schematic diagram of an atomic force microscope. (1), Laser diode; (2), cantilever; (3), mirror; (4), position-sensitive photodetector; (5), electronics; and (6), scanner with sample [162]

deviation of the tip is measured. In the constant height mode, the deflection force on the sample is recorded [163].

### 4.1.2 AFM Setup

In this thesis, the AFM images of the boron-doped diamond layers were done using a Dimension Icon from Bruker using in peak force tapping mode with Bruker ScanAsyst-Air tips. The setup is represented in Figure 4.2.

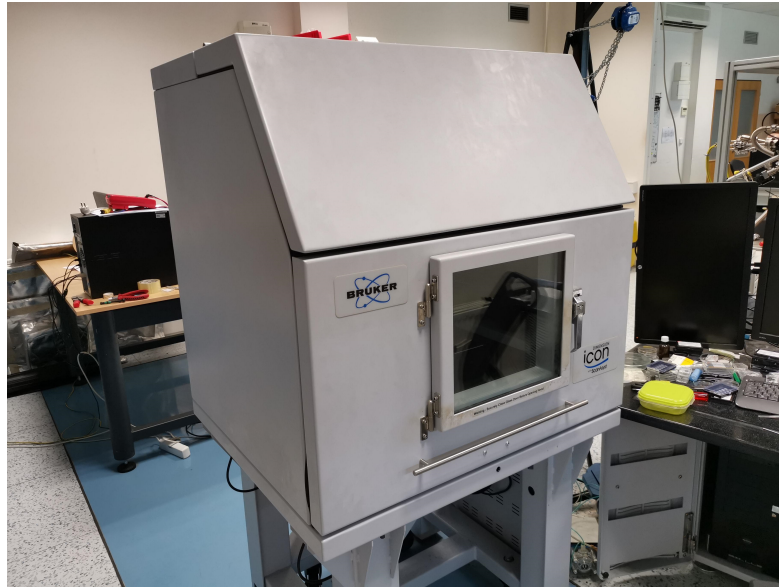


Figure 4.2: AFM setup

## 4.2 Scanning Electron Microscopy (SEM)

### 4.2.1 SEM Theory

SEM is a type of microscopy technique in which images are obtained by scanning the surface of the material under study with a focused beam of electrons. In this thesis, SEM was used to obtain images of the polycrystalline phosphorus-doped diamond layers grown by PECVD and check their morphology.

On principle, SEM is very similar to Optical Microscopy (OM), the main difference being that the first uses electron emission while the second uses light to form an image. The SEM has several advantages over OM [164]:

- It can reach a magnification of  $\times 1000000$  with a resolution down to 1 nm while conventional OM can only reach a magnification around  $\times 1000$ .
- It has a larger depth of field compared to OM allowing most of the surface of

the sample to be in focus even at high roughness.

- It can give more information than just the surface topology such as crystalline structure, chemical composition, and electrical properties.

Figure 4.3 shows a schematic representation of a SEM system. The two main types of electron emitter are the thermionic emission type composed of a heated filament (over 2500 °C) made of tungsten or lanthanum hexaboride, and the field emission type using a very high electric field applied on a fine tip until the emission of electrons by quantum mechanical tunneling occurs [164, 165]. The electron beam is then condensed and focused by a series of magnetic lenses composed of a coil wound around a soft iron core [165] before being used to scan the surface of the material under study using a scan coil.

There are two main types of signals used to create surface images of the sample under characterization [164, 165]:

- Secondary electrons: They correspond to electrons which escape from the sample with an energy about 50 eV. They are usually electrons to which a small quantity of energy has been transferred within a short distance of the surface. They are very abundant and are the most commonly signal in SEM. Because they come from a very shallow region near the surface, they provide images with high spatial resolution.
- Backscattered electrons: They correspond to primary electrons that left the surface of the sample before giving up all their energy. Compared to secondary electrons, they have a higher energy and they are also less numerous. They come from a slightly deeper region in the sample and therefore provide images with a slightly lower resolution

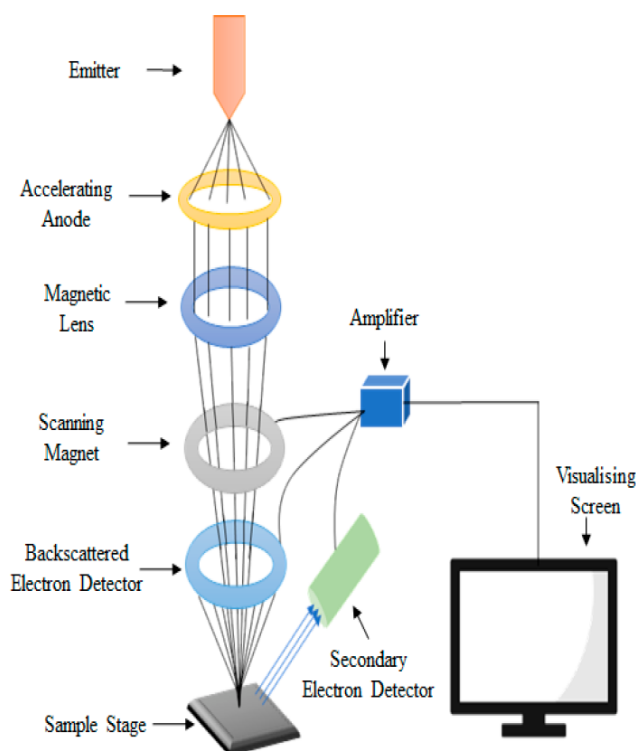


Figure 4.3: Schematic diagram of a scanning electron microscope [166]

Other signals can also be recorded such as cathodoluminescence and x-ray emission, which provide information on the chemical composition of the sample, and Auger electron emission, which give information on the surface chemistry.

### 4.2.2 SEM Setup

A TESCAN FERA3 GM microscope was used to make SEM images and assess the phosphorus-doped polycrystalline diamond layers' morphology. The images were obtained using a Everhart-Thornley secondary electron detector with an accelerating voltage of 5.0 kV. The SEM setup is shown in Figure 4.4.



Figure 4.4: SEM setup

## 4.3 Secondary Ion-Mass Spectroscopy (SIMS)

### 4.3.1 SIMS Theory

SIMS is a technique used to analyze the composition of solid surfaces and thin films. In this study, it was used to determine the boron concentration in single crystal boron-doped diamond layers grown by PECVD.

This technique relies on an ion beam to sputter the surface of the solid to be characterized into atoms and atomic clusters (Figure 4.5). A small fraction of those atoms is ionized and they can be analyzed using a mass spectrometer.

The principle of this technique was first discovered by J. J. Thomson in 1910 [168]. A first prototype was made by R. F. K. Herzog and F. P. Viehböck [169] in 1949. In the beginning of the 1960s, two SIMS setups were developed. The first one was developed in the United States of America by R. F. K. Herzog and

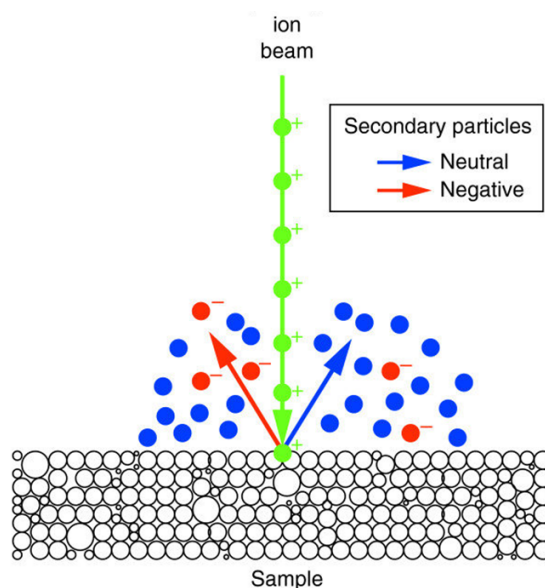


Figure 4.5: The principle of secondary-ion mass spectrometry [167]

F. P. Viehböck as part of a project sponsored by the NASA for the analysis of moon rocks. The other setup was developed in France, at the University of Paris-Sud by R. Castaing and G. Slodzian [170]. Both instruments were respectively commercialized by GCA Corp and CAMECA S.A.S. and both were using sector field mass spectrometers. This type of spectrometer uses a static electric or magnetic field to separate the ions based on their difference in inertia. In the beginning of the 1970s, a new type of setup was developed by K. Wittmaack [171] equipped with a quadrupole mass spectrometer which uses an oscillating electric field to filter the secondary ions. Around the same time, A. Benninghoven [172] introduced the method of static SIMS which is based on the use of time-of-flight mass spectrometers in which the ion beam is pulsed. With this method, only a very small part of the uppermost layer of the sample is analyzed with minimum disturbance to its composition and structure.

### 4.3.2 SIMS Setup

In this work, the SIMS measurements were used to determine the concentration of incorporated boron in the boron doped-diamond samples. The equipment used to perform the measurement is a CAMECA IMS 7f. The base pressure in the chamber is about  $3 \times 10^{-8}$  mbar.  $O_2^+$  primary ions were used with an impact energy of 10 keV, an impact angle of  $38^\circ$ , and a primary current of 100 nA. The exposed area on the sample is  $150 \times 150 \mu\text{m}^2$ . The secondary ions were extracted with a voltage of 5 kV and the analyzed area was  $63 \mu\text{m}^2$  in the middle of the crater. The setup was calibrated using a sample with a known boron concentration of  $10^{21} \text{ cm}^{-3}$ .

## 4.4 Glow Discharge Optical Emission Spectroscopy (GDOES)

### 4.4.1 GDOES Theory

Glow Discharge Optical Emission Spectroscopy (GDOES) is a spectroscopic method used for the characterization of metals, alloys, and other non-metallic solids. GDOES was used in this thesis to determine the phosphorus concentration in polycrystalline phosphorus-doped diamond layers grown by PECVD. Due to the large number of phosphorus-doped diamond layers to characterize, GDOES was preferred to SIMS as it is a faster and more affordable method.

Contrary to atomic spectroscopy, which is used to determine the surface of a material, GDOES gradually ablates layers of the sample under study and gives the composition of the material in his depth. GDOES is based on the use of a flat-cathode setup called the Grimm-type source [173] combined with a spectrometer,

which can either be a multi-channel polychromator with photomultipliers used as detectors or an instrument using Charge Coupled Device (CCD) detectors.

GDOES uses a Glow Discharge (GD) plasma which is a self-sustained weakly ionized plasma obtained at room temperature and low pressure in a carrier gas, usually argon [174]. Figure 4.6 shows the typical evolution of the voltage as a function of the current between two electrodes during an electric discharge. The **d** and **e** sections of the curve are corresponding to GD and abnormal GD respectively. In the abnormal GD the entire cathode surface is covered by the plasma and an increase of the voltage corresponds to an increase of the current. This is the functioning region used for GDOES [174].

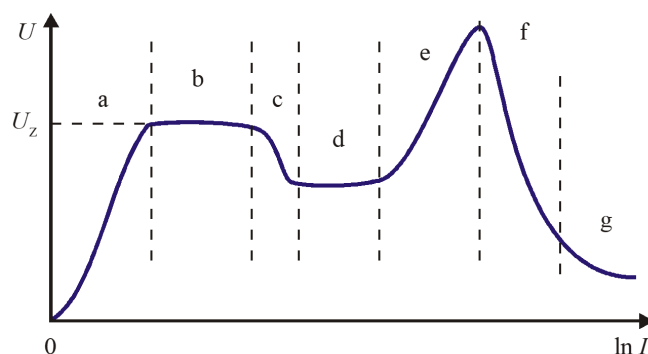


Figure 4.6: Evolution of the voltage as a function of the current between two electrodes during an electric discharge [175]

Figure 4.7 shows a schematic diagram of a Grimm-type GD source. The sample is used as the cathode and the discharge cavity is closed on the surface of the sample by a silicone O-ring which ensures an airtight seal. The property of the plasma strongly depends on the quality of the carrier gas and the presence of other gases such as hydrogen and nitrogen can alter the measured analytical results. The distance between the sample at the cathode and the tubular anode also changes

the impedance of the GD source and hence the nature of the plasma.

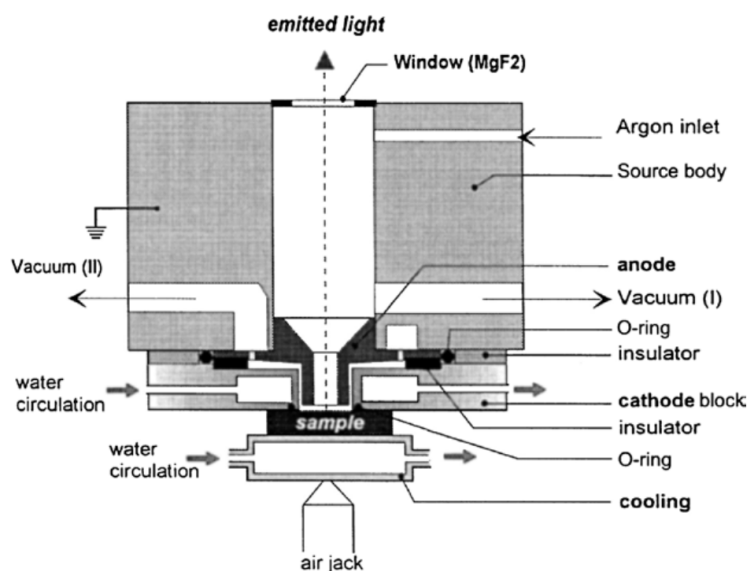


Figure 4.7: Schematic diagram of a Grimm-type GD source [176]

The sputtering and light emission mechanism of the GD source are presented in Figure 4.8. Ionized argon atoms bombard the surface of the cathode and cause the sputtering of atoms, ions and electrons from the sample at the cathode. Through various collisions in the plasma, those sputtered atoms and ions get excited and then de-excite by emitting photons in the negative glow region of the plasma. The emitted light can then be analyzed by the spectrometer.

#### 4.4.2 GDOES Setup

The phosphorus concentrations in the doped diamond layers grown using continuous and pulsed  $\text{CH}_4$  flow were determined using a GDA750HR spectrometer from Spectrumba GmbH for GDOES measurement (see Figure 7.14). The P I emission line at 178.284 nm was used for phosphorus analysis. Its background was measured by analyzing boron-doped diamond layers (free of phosphorus) and its emission

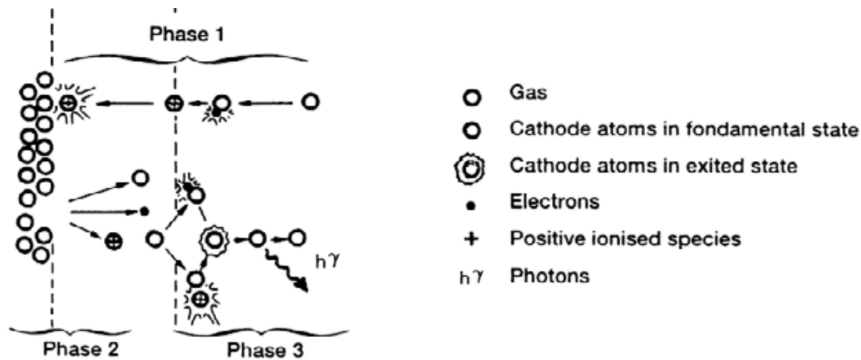


Figure 4.8: Sputtering and light emission mechanism in GDOES [176]

yield was established by sputter-rate corrected calibration [177], based on certified reference materials of steel and cast iron with phosphorus concentrations up to 0.16%. In conformity with the work from C. Schubert et al. [178], sputtering rates of the analyzed layers were found to be 40 to 50 times lower than that of steel, hence, the phosphorus signal matched well the calibration range.

## 4.5 Hall Effect Measurement Method

### 4.5.1 Hall Effect Measurement Theory

Hall effect measurements were carried out to determine the resistivity, the mobility and the carrier density inside a material using the Lorentz force. In this work, this technique was used to characterize the electrical properties of single crystal boron-doped diamond layers grown by PECVD.

When an electron (or a hole) moves perpendicularly to a magnetic field, it experiences a force both normal to the electron's direction of movement and the magnetic field. This force is given by:

$$\vec{F} = q\vec{E} + q\vec{v} \times \vec{B} \quad (4.1)$$

Where  $q$  is the charge of the carrier,  $\vec{v}$  is the carrier velocity.  $\vec{E}$  is the electric field and  $\vec{B}$  the magnetic field. If a current is going through a semiconductive layer and a magnetic field is applied perpendicularly to the surface of the layer. The Lorentz force will induce a deviation of the charge carrier flow and induce an electric field normal to the current flow and the magnetic field. Current density is determined from the total excitation current and the sample's geometry. Electric fields are determined by measuring voltage differences between electrical contacts on the sample surface.

One of the most common devices used to make Hall effect measurement is the Hall bar presented in Figure 4.9. A constant current density flows between contacts 5 and 6 while a perpendicular external magnetic field is applied and the side contacts 1, 2, 3, and 4 are used for voltage measurements.

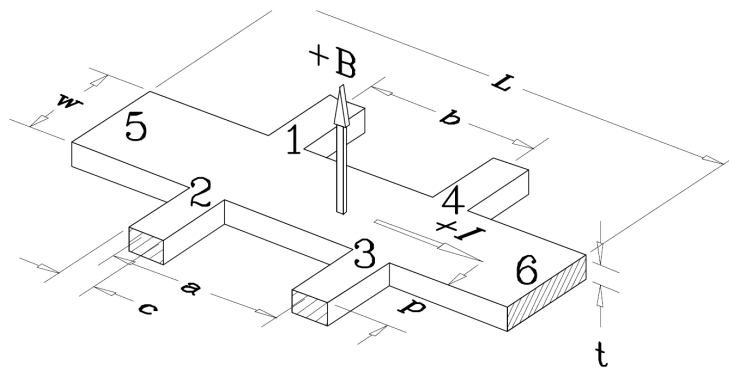


Figure 4.9: Six-contact Hall bar geometry

The main disadvantage of this geometry is the requirement of a mesa etching around the Hall bar to avoid current leakage. Because of this, Hall bars are difficult

to fabricate and are also destructive for the diamond layer.

For those reasons, the use of the van der Pauw method, which doesn't require mesa etching and allows the Hall effect measurement on a sample of arbitrary shape, was preferred. To use this method, several conditions have to be fulfilled:

- The contacts are at the circumference of the sample.
- The contacts are sufficiently small.
- The sample is homogeneous in thickness.
- The surface is singly connected, i.e., the sample does not have isolated holes.

Taking those conditions into consideration, the contacts configuration presented in Figure 4.10 was chosen for the Hall effect measurements on the boron-doped diamond samples. The contacts were placed in the corners of the diamond sample so that it would be easier to connect them to the Hall effect measurement setup.

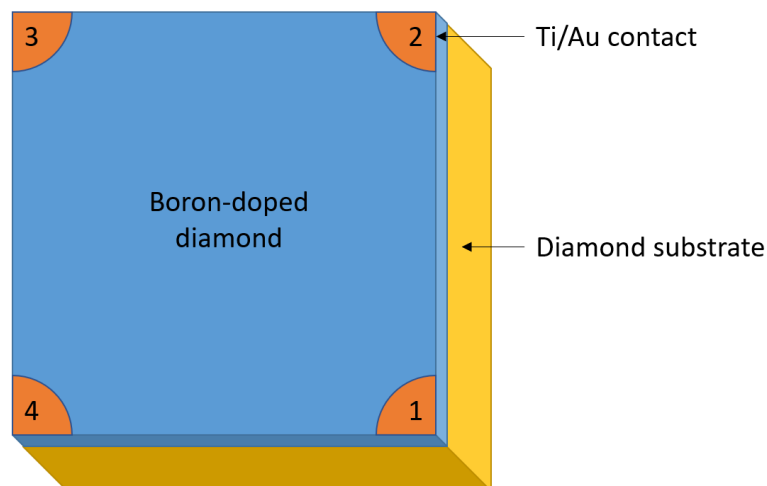


Figure 4.10: Ti/Au Van der Pauw contacts on a boron doped diamond

First, a preliminary resistivity measurement is done without any external magnetic field applied to the sample. An electric current is applied between two contacts along one edge of the sample and the voltage is measured between the two contacts on the other side. For example:

$$R_{12,43} = \frac{V_{43}}{I_{12}} \quad (4.2)$$

where  $I_{12}$  is a positive current flowing from electrode 1 to electrode 2 and  $V_{43}$  is the voltage measured between 4 and 3 using the electrode numbering defined in Figure 4.10. Using the set of conditions previously presented, L. J. van der Pauw [179] demonstrated the following equation:

$$\exp\left(-\frac{\pi t}{\rho} R_{12,43}\right) + \exp\left(-\frac{\pi t}{\rho} R_{24,31}\right) = 1 \quad (4.3)$$

where  $t$  is the thickness of the doped diamond layer and  $\rho$  is the resistivity. However, because of the symmetries of the square boron-dope diamond samples, we have:

$$R_{12,43} = R_{24,31} \quad (4.4)$$

And therefore, the resistivity  $\rho$  can be expressed like this:

$$\rho = \frac{\pi t R_{12,43}}{\ln(2)} \quad (4.5)$$

To further improve the precision of the resistance value, four different measurements are done at different position on the sample and then averaged:

$$R = \frac{R_{12,43} + R_{23,14} + R_{34,21} + R_{41,32}}{4} \quad (4.6)$$

Therefore, the resistivity can also be expressed as such:

$$\rho = \frac{\pi t R}{\ln(2)} \quad (4.7)$$

In order to determine the Hall mobility, a current was applied between electrodes 1 and 3 while the transverse voltage is measured between electrodes 4 and 2. A magnetic field  $B$  is applied perpendicularly to the sample surface. The measurement of the current and voltage are first done with the magnetic field in one direction and a second time with the magnetic field in the opposite direction. The Hall coefficient  $R_H$  is given by:

$$R_H = \frac{t}{B} \cdot \frac{V_{42}(B_+) - V_{42}(B_-)}{I_{31}(B_+) - I_{31}(B_-)} \quad (4.8)$$

Finally, the Hall mobility can be obtained using the following formula:

$$\mu_H = \frac{|R_H|}{\rho} \quad (4.9)$$

The carrier concentration can also be obtained from the Hall effect measurement. In p-type boron-doped diamond, holes are the majority carriers, therefore, we have:

$$p = \frac{1}{\rho q \mu_H} \quad (4.10)$$

where  $q$  is the elementary charge.

### 4.5.2 Hall Effect Measurement Setup

A picture of the Hall measurement setup used in this work is shown in Figure 4.11a. A tube-shaped cryostat is placed between the two poles of an electromagnet. The sample is fixed at the end of a rod with four metallic tips shown in Figure 4.11b which are also used to make connect to the Ti/Au van der Pauw contacts at the edge of the sample. The rod is then slid into the cryostat so that the sample is in the middle of the electromagnet with its surface perpendicular to the magnetic field. The applied magnetic field for Hall coefficient measurement was about 0.3 T.

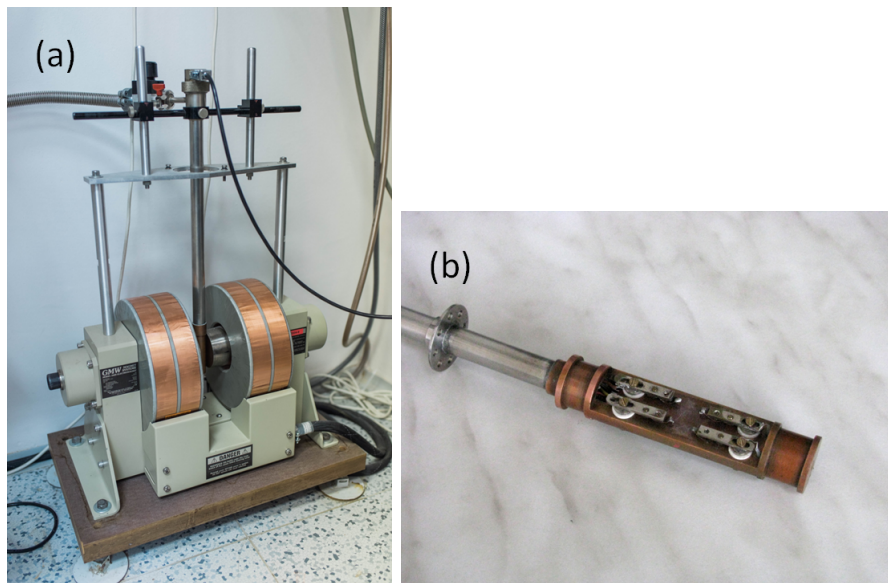


Figure 4.11: Hall measurement setup **(a)** and sample holder **(b)**

The resistivity and Hall coefficient have been calculated using the delta method [180] in order to limit errors due do thermoelectric effects. Parasitic thermoelectric voltages appear when the temperature inside the material is non-uniform. To counter this effect, several measurements of the same voltage are made while the current is alternated about 5 to 10 times per second. About a hundred

measurements are made and they are then averaged in order to get the final value of voltage and resistance.

## 4.6 Transmission Line Pulse (TLP) Current-Voltage Measurement

The Transmission Line Pulse (TLP) generator is a voltage pulse generator based on a simple coaxial cable usually used to simulate electrostatic discharge events in electronic devices. In this thesis, a measurement setup based on a TLP voltage pulse generator was designed to test boron-doped diamond devices under high electric fields up to  $1.8 \times 10^5 \text{ V.cm}^{-1}$  and obtain their I-V characteristics. Compared to a continuous applied voltage, the short voltage pulses generated by the TLP generator limit the thermal effects which would otherwise destroy the test devices.

The TLP generator was first presented by T. J. Maloney in 1985 [181] and it addresses this problem by the application of short voltage pulses on the nanosecond scale which limit the amount of energy dissipated in the devices and prevent any subsequent damage. This device uses the charge and discharge of a transmission line to generate rectangular voltage pulses.

### 4.6.1 TLP Current-Voltage Measurement Theory

#### Transmission Line Model

The coaxial cable is the most common type of transmission line that is be the main topic of this chapter.

- The three main components of the coaxial cable are: the inner conductor (a

copper wire), the external conductor (a copper mesh) and finally the insulator between them,

- The five main parameters of a coaxial cable are: the radius of the inner conductor  $a$ , the radius of the external hollow conductor  $b$ , the length of the cable  $D$ , and finally the permittivity  $\epsilon$ , and the permeability  $\mu$  of the insulator (Figure 4.12),

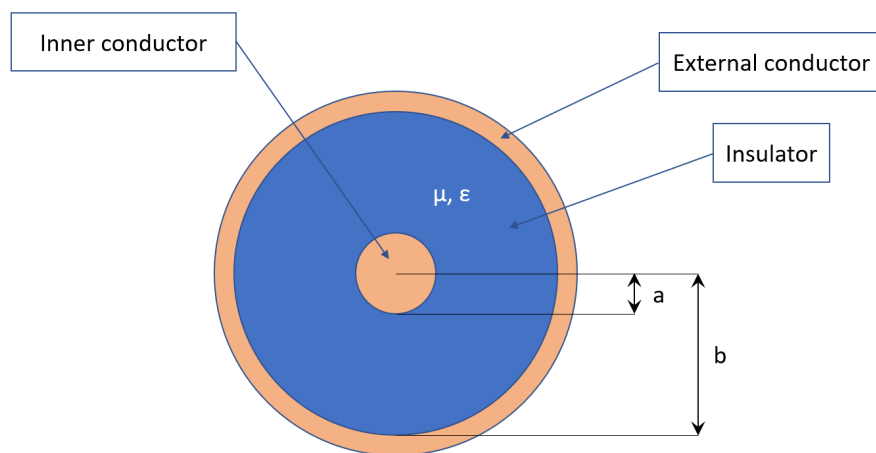


Figure 4.12: Sectional view of the coaxial cable

A theoretical representation of the coaxial cable is presented in Figure 4.13. It is depicted as a succession of inductors and capacitors. It shall be underlined that this model does not consider the resistive propagation losses in the cable.

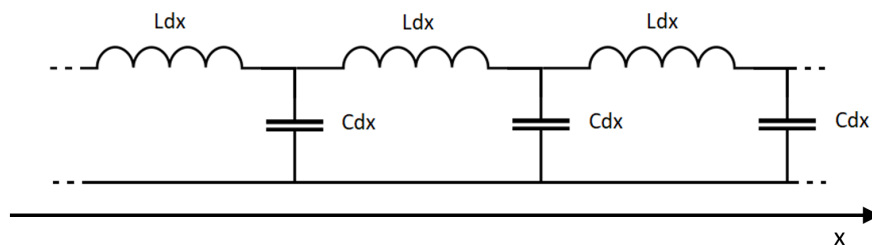


Figure 4.13: Theoretical representation of the coaxial cable

From this representation, the following equations of the voltage and current in the coaxial cable can be determined:

$$\frac{\partial V}{\partial x} = -L \frac{\partial I}{\partial t} \quad (4.11)$$

$$\frac{\partial I}{\partial x} = -C \frac{\partial V}{\partial t} \quad (4.12)$$

Equations (4.11) and (4.12) are the “Telegrapher’s Equations”. These equations may be combined to form two propagation wave equations, one for voltage and one for current:

$$\frac{\partial^2 V}{\partial x^2} = -v_p^2 \frac{\partial^2 V}{\partial t^2} \quad (4.13)$$

$$\frac{\partial^2 I}{\partial x^2} = -v_p^2 \frac{\partial^2 I}{\partial t^2} \quad (4.14)$$

$$\text{With } v_p = \frac{1}{\sqrt{LV}} \quad (4.15)$$

Where  $v_p$  is the speed of waves in the coaxial cable.

The lineic inductance  $L$  and capacitance  $C$  are expressed as a function of the physical parameters of the coaxial cable defined previously as follows:

$$L = \frac{\mu}{2\pi} \ln \left( \frac{b}{a} \right) \quad (4.16)$$

$$C = \frac{2\pi\epsilon}{\ln \left( \frac{b}{a} \right)} \quad (4.17)$$

Finally, the characteristic impedance of the coaxial cable  $Z_0$  is expressed as follows:

$$Z_0 = \sqrt{\frac{L}{C}} = \frac{1}{2\pi} \ln\left(\frac{b}{a}\right) \sqrt{\frac{\mu}{\epsilon}} \quad (4.18)$$

$v_p$  may also be expressed differently thanks to (4.16) and (4.17) as follows:

$$v_p = \frac{1}{\sqrt{LC}} = \frac{1}{\sqrt{\mu\epsilon}} \quad (4.19)$$

### Principle of Operation of the TLP Generator

This TLP generator uses the wave propagation properties of the coaxial cable in order to generate voltage pulses across the Device Under Test (DUT) [182, 183].

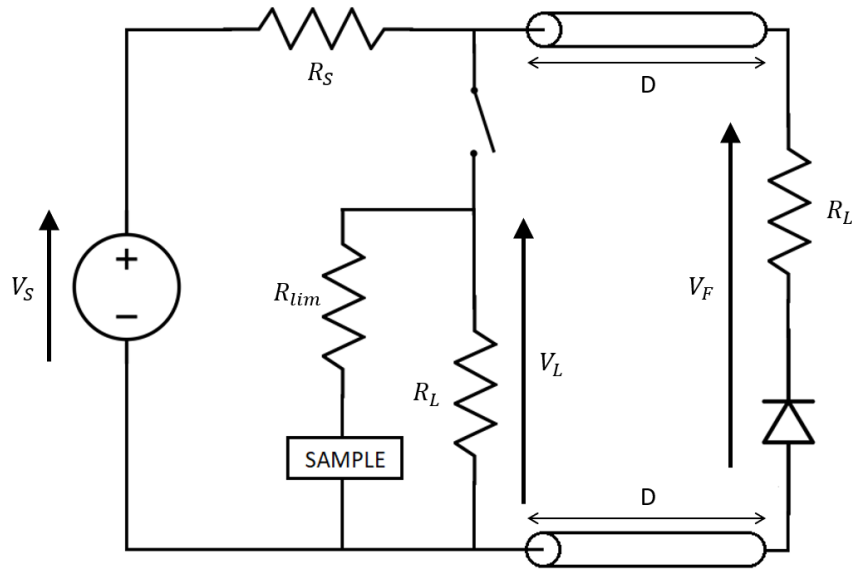


Figure 4.14: TLP generator electrical scheme

The structure of the TLP setup used in this work is shown in Figure 4.14 which is similar to the one used by N. Mauran [184]. In this setup, we have:

- the two conductors of length  $D$  represent the coaxial cable. The top one in the figure is the inner conductor while the bottom one is the outer mesh connected to the ground,
- $R_S$  must have a very high value compared to the characteristic impedance of the cable  $Z_0 = 50 \Omega$ . It isolates the voltage generator from the rest of the circuit during the voltage pulse,
- $R_L = Z_0 = 50 \Omega$ : on the generator side, its role is to adapt the sample to the coaxial cable impedance. Indeed, calculating the equivalent impedance of the set made of  $R_L$  and  $Z_{sample}$ , the sample impedance, the following formula is obtained:

$$Z_{tot} = \frac{Z_{sample} \cdot R_L}{Z_{sample} + R_L} \quad (4.20)$$

Since the impedance of the boron doped diamond device is supposed to be much higher than  $R_L$ ,  $Z_{tot}$  becomes:

$$Z_{tot} = \frac{Z_{sample} \cdot R_L}{Z_{sample}} = R_L = 50 \Omega \quad (4.21)$$

- $R_L$  and the diode: the role of  $R_L$  at the end of the cable is different, its purpose is to absorb any negative reflections in the cable. In case of positive voltage, the diode will be in blocking mode which means that the coaxial cable will end on an open circuit. In case of negative voltage however, the diode will act as a short circuit and the voltage wave will be absorbed by the resistor  $R_L$ . The diode also limits the maximum voltage in the coaxial cable

to avoid damage,

- $V_s$  is the voltage applied by the power supply.

Initially, the electrical relay is open, the voltage source charges the line as described previously described. In normal use, there should be no negative reflections at the end of the line, this way the diode should act as an open circuit with an infinite impedance  $Z_F$ . Once the coaxial cable is fully charged, the voltage at the end of the line is  $V_F = V_S = 100$  V.  $V^+$  and  $V^-$  are the forward and backward waves in the coaxial cable.  $V^+$  travels from the generator to the load and  $V^-$  travels from the load to the generator. We can calculate them thanks to these formulas:

$$V^+ = \frac{V_F \left(1 + \frac{Z_0}{Z_F}\right)}{2} = \frac{V_S}{2} = 50 \text{ V} \quad (4.22)$$

$$V^- = \frac{V_F \left(1 - \frac{Z_0}{Z_F}\right)}{2} = \frac{V_S}{2} = 50 \text{ V} \quad (4.23)$$

In the first step of the voltage pulse generation, the electrical relay is closed. The voltage source is now isolated from the rest of the circuit due to the high electrical resistance  $R_S$ . Hence, the circuit can be considered as a combination of  $R_L$  and  $Z_{sample}$ , the impedance of the sample connected to the transmission line. For simplification purpose, the combination of  $Z_{sample}$  and  $R_L$  can be reduced to  $R_L$  as long as  $Z_{sample}$  is much higher than  $R_L$ .

$$\frac{Z_{sample} \cdot R_L}{Z_{sample}} \approx R_L \quad (4.24)$$

Which means that the value of  $\Gamma_L$ , the reflection coefficient on this side of the

line has also changed to:

$$\Gamma_L = \frac{R_L - Z_0}{R_L + Z_0} = \frac{50 - 50}{50 + 50} = 0 \quad (4.25)$$

Therefore, we can calculate the new value of  $V^+$ ,

$$V^+ = \Gamma_L \cdot V^- = 0 \text{ V} \quad (4.26)$$

From (4.23) and (4.26), we also have:

$$V_L = V^- + V^+ = \frac{V_S}{2} = 50 \text{ V} \quad (4.27)$$

The forward wave  $V^+$  will travel through the line at a  $v_p$  speed. When it will reach the end of the line, there will be a total reflection as  $Z_F = \text{inf}$ , in other words  $\Gamma_F = 1$  and thus:

$$V^- = \Gamma_F \cdot V^+ = 0 \text{ V} \quad (4.28)$$

This backward wave  $V^-$  will travel through the line at a  $v_p$  avalanche. When it will reach the input, (4.26) and (4.28) will give:

$$V_L = V^- + V^+ = 0 \text{ V} \quad (4.29)$$

As a result, this circuit has created a  $\frac{V_S}{2}$  pulse that lasted for  $2T$ , where  $T$  is the time needed for a wave to travel from one end to the other end of the cable:

$$T = \frac{D}{v_p} \quad (4.30)$$

Table 4.1: Parts highlighted within Figure 4.15

Reference	Part Name
A	BNC cable
B	Voltage sources
C	Function generator
D	Oscilloscope
E	Reed relay box
F	Probe holder and micropositioner

$D$  is the length of the cable and  $v_p$  is the speed of waves in the coaxial cable.

### 4.6.2 TLP Current-Voltage Measurement Setup

The lab-made TLP current-voltage measurement setup used in this work is shown in Figure 4.15 and it has the same structure as in Figure 4.14 with:

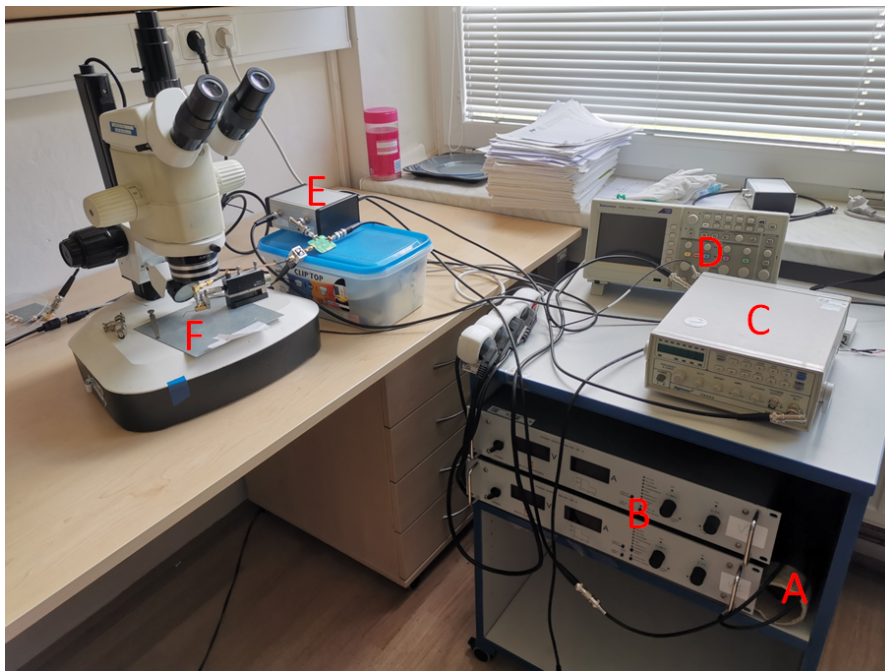


Figure 4.15: TLP current-voltage measurement setup. The legend for the different letters is given in Table 4.1

- $D = 10$  m, the length of the line: this value can be adjusted to modify the duration of the impulse. In this setup, the coaxial cable is a RG58C/U with Bayonet Neill–Concelman (BNC) connectors (**A** in Figure 4.15), a standard and cheap cable very common in laboratories. If we consider the speed of an electric signal in the cable to be  $v_p = 2.0 \times 10^8$  m.s<sup>-1</sup>, we obtain that  $T = 50$  ns from equation (4.30). Which means the generated voltage pulse across the DUT will be 100 ns long,
- $R_S = 4.7$  M $\Omega$ : as mentioned in section 4.6  $R_S \gg Z_0 = 50$   $\Omega$ ,
- $R_L$  is a MP930 from Caddock which can resist up to 30 W,
- $V_s$  can vary from 0 to 800 V on our TLP setup. The voltage source is composed of two SM 400-AR-8 voltage supplies of 400 V each which are connected in series (**B** in Figure 4.15). The voltage value is controlled through a NI USB-6009 piloted by a LabVIEW program. In the following example,  $V_s$  will be set to 100 V for calculations,
- Originally, a SHV05-1A85-78D3K lead-free reed relay from Standex-Meder Electronics was used. However, frequent failures forced us to upgrade this component to a 5503-05-1 reed relay from Coto Technology (Figure 4.16). This component can switch voltages up to 3.5 kV and current up to 3 A. The maximum operating power is 200 W which is well-suited for our high voltage setup. It is controlled by a FG303 function generator from Digimess (**C** in Figure 4.15) using a square wave signal with a 5 V amplitude and a 0.1 Hz frequency,
- For the measurements acquisition, a Tektronix TDS2004C oscilloscope is used

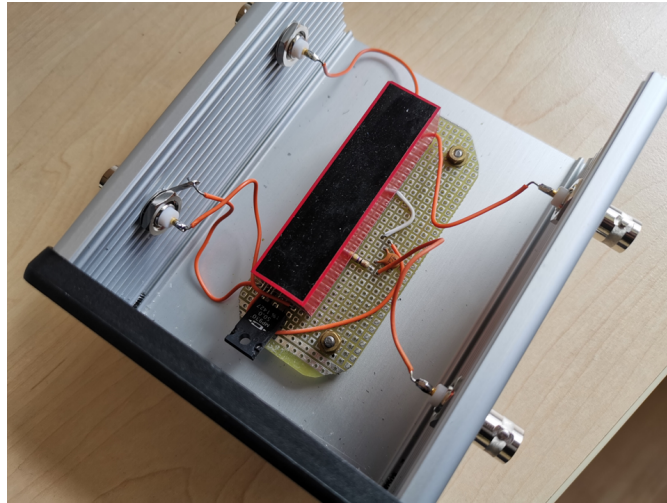


Figure 4.16: Homemade circuit board containing the reed relay

(**D** in Figure 4.15). It allows single shot acquisition and the transfer of the data to a computer,

- A Tektronix CT-1 current probe is used to measure current. The probe has a hole through which a current carrying conductor is inserted during circuit assembly. The probe converts the current into a voltage which is measured by the oscilloscope. This probe has a sensitivity of  $5 \text{ mV} \cdot \text{mA}^{-1}$ ,
- For voltage measurement, a pick-off tee is used (Figure 4.17). It is simply a resistor that is connected between the transmission line and the oscilloscope. The resistor should have a high value compare to  $Z_0 = 50 \Omega$ , the impedance of the cable. In our case, its resistance is  $500 \Omega$ ,
- The electrodes on the sample are connected to the TLP generator with a 74CJ-APT-KS-100GP/50 Probe Holder with a  $100 \mu\text{m}$  pitch from American Probe via a DPP105-PTH micropositioner from Cascade Microtech (Figure 4.18).

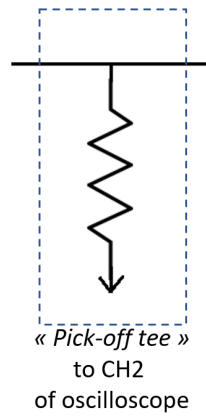


Figure 4.17: Pick-off tee schematic

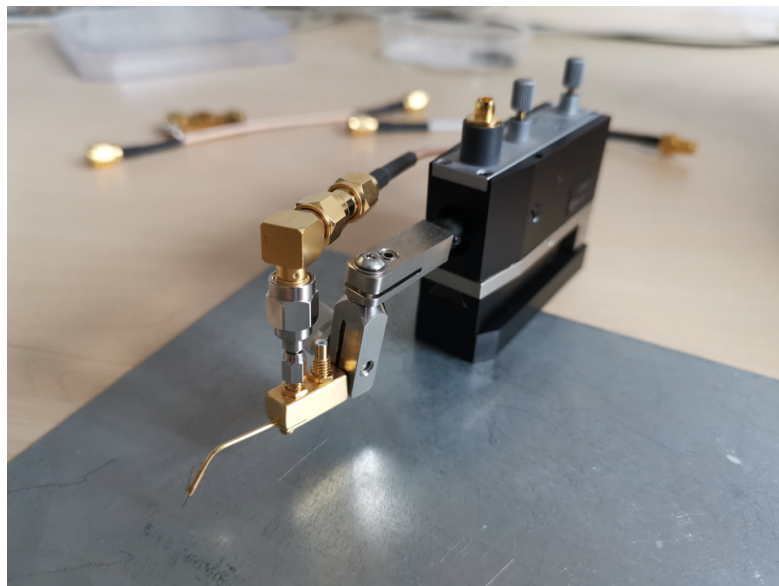


Figure 4.18: Probe holder and micropositioner

## 4.7 Transient Interferometric Mapping (TIM)

### 4.7.1 TIM Theory

Transient Interferometric Mapping (TIM) is an optical method used to obtain a 2-D map of the thermal dissipation in a semiconductor material. It was used in this work to study the thermal energy dissipation in single crystal boron-doped diamond layers stressed under pulsed high voltage. The measurements were made in Austria at the Technische Universität (TU) Wien thanks to Ass. Prof. Dionyz Pogany, Dr. Hasan Karaca, and Dr. Clément Fleury.

This technique is based on the measurement of the refraction index change due to the variation in temperature or carrier concentration (Figure 4.19). The biggest advantage of this method is that it can be performed in single shot mode, providing information on thermal energy and charge carrier density during a single stress pulse [185]. This measurement is performed using a heterodyne interferometer presented in Figure 4.20 where the probe beam goes through the polished backside of the sample. The use of a  $1.3 \mu\text{m}$  wavelength ensures that semiconductors with a band gap larger than  $0.95 \text{ eV}$  (which is the case for diamond cf. Table 1.1) are transparent to the probe beam, provided they are low-doped. The voltage stress pulse is generated using a TLP setup similar to the one described in the previous chapter.

The phase shift variation due to the change in the refraction index is given by the following equation [186]:

$$\Delta\varphi(x, y, t) = 2 \cdot \frac{2\pi}{\lambda} \int_0^d (\Delta n_T(x, y, z, t) + \Delta n_e(x, y, z, t) + \Delta n_h(x, y, z, t)) dz \quad (4.31)$$

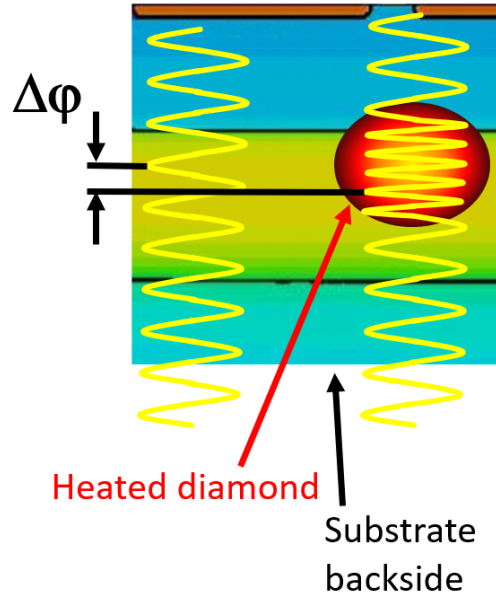


Figure 4.19: Phase shift induced by self-heating between a reference (left) and a probe laser beam (right)

Where  $\Delta n_T$  is the change in refraction index due to the change in temperature,  $\Delta n_e$  and  $\Delta n_h$  are the change in refraction index due to the variation in electron and hole concentration respectively. The thermo-optical and plasma-optical effects have opposite contribution. This allows the distinction between thermally (positive) and plasma-induced (negative) phase shift. The factor 2 appears in the equation because the probe beam goes through the sample twice since it is reflected on the top side. If the influence of the carrier density on the phase shift is negligible compared to the one due to the temperature change, then the phase shift can be expressed as a function of the thermal energy density  $E_{3D}$ :

$$\Delta\varphi(x, y, t) = \frac{4\pi}{\lambda} \cdot \frac{dn}{dT} \int_0^d \frac{\Delta E_{3D}(x, y, z, t)}{c_v} dz \quad (4.32)$$

Where  $c_v$  is the volume specific heat and  $\lambda$  is the wavelength of the probe beam.

If  $c_v$  is constant, (4.32) becomes:

$$\Delta\varphi(x, y, t) = \frac{4\pi}{\lambda c_v} \cdot \frac{dn}{dT} E_{2D}(x, y, t) \quad (4.33)$$

Where  $E_{2D} = \int_0^d E_{3D} dz$  is the 2-D thermal energy density. From (4.33) we can see that the phase shift is proportional to  $E_{2D}$ . Therefore, the phase shift  $\Delta\varphi$  is a direct measure of the 2-D thermal energy density stored in the semiconductor device.

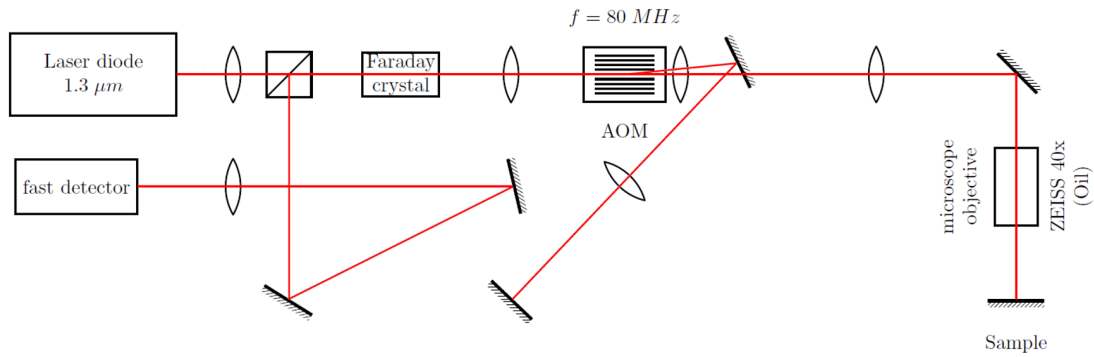


Figure 4.20: TIM setup schematic [187]

The measurement of the phase shift is done using a heterodyne interferometer shown in Figure 4.20. This interferometer is called heterodyne because the probe beam is mixed with an intermediate frequency of  $\omega_{mix} = 80$  MHz in an Acoustical-Optical Modulator (AOM). Since the probe beam goes twice through the AOM, it ends up being shifted by 160 MHz compared to the reference beam. The reference and probe beam interfere at the infrared detector to give a detector signal  $S(t)$  of the form:

$$S(t) = I_P(t) + I_R(t) + 2\sqrt{I_P(t)I_R(t)} \cdot \cos(2 \cdot \Delta\omega \cdot t + \Delta\varphi(t)) \quad (4.34)$$

Where  $I_P(t)$  and  $I_R(t)$  are respectively the intensity of the probe and reference beams,  $2\Delta\omega = 2\omega_{mix} = 160$  MHz is the beating frequency, and  $\Delta\varphi(t) = \varphi_P(t) - \varphi_R(t)$  is the phase shift difference between the phase of the probe  $\varphi_P$  and the reference beam  $\varphi_R$ . The factor 2 comes from the double passing through the AOM. The detector signal  $S(t)$  is then transferred from the time to the frequency domain  $S'(u)$  using Fast Fourier Transform (FFT).  $S'(u)$  is filtered in order to eliminate the low frequency disturbances due to  $I_P(t)$  and  $I_R(t)$ . The resulting signal is finally transferred back to the time domain and the phase shift  $\Delta\varphi(t)$  is extracted using an unwrapping algorithm.

### 4.7.2 TIM Setup

The TIM setup used in this thesis is the one from Technische Universität (TU) Wien and it is shown in Figure 4.21. The binocular microscope is used to position the probe needles on the parallel electrodes (Figure 5.2d). The Zeiss objective used for optical measurements in Figure 4.20 is positioned under the sample. In order to have the best light transmission and avoid parasitic reflections, the backside of the diamond sample was polished and a layer of grease was used as an interface between the sample and the microscope objective.

Due to the small dimensions of the diamond samples, a special holder had to be designed (Figure 4.22). The sample is placed in the holder from the back and held in place by drops of glue placed at each corner of the diamond sample (Figure 4.22c). The glue can be easily removed using acetone. The machining around the square window in Figure 4.22a is designed to make room for the probe needles so that it is easier to contact the electrodes on the surface of the sample.

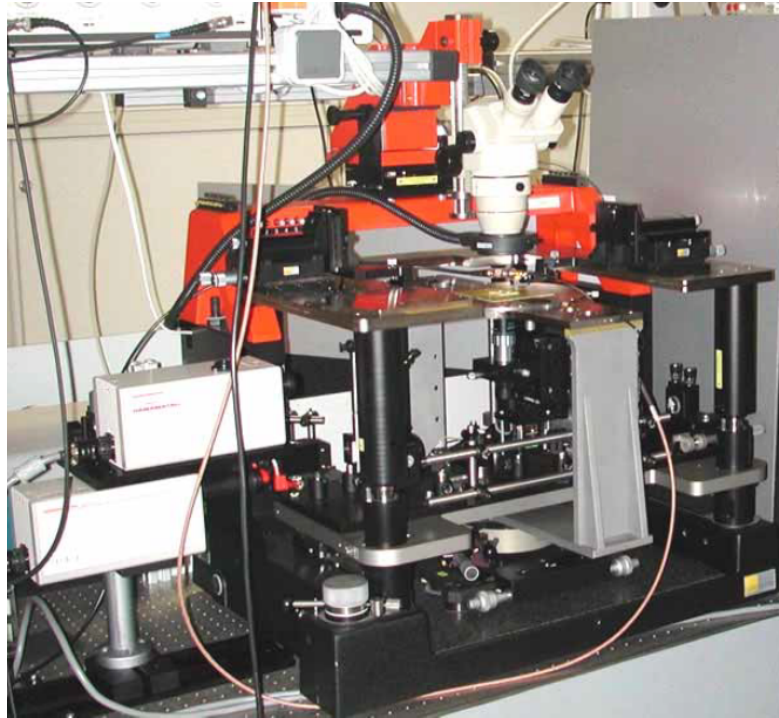


Figure 4.21: TIM setup in TU Wien

## 4.8 Raman Spectroscopy

### 4.8.1 Raman Spectroscopy Theory

Raman spectroscopy is an analytical technique where scattered light is used to measure the vibrational energy modes of a sample which can give some information on its structure and chemical composition. This spectroscopic technique was used as an additional way to determine the boron concentration in single crystal boron-doped diamond layers and to compare the crystalline quality of polycrystalline phosphorus-doped diamond layers by calculating their  $sp^3/sp^2$  carbon ratio.

Raman scattering is a type of inelastic scattering of light which means that the wavelength of the scattered light is different from the wavelength of the incident light (contrary to elastic or Rayleigh scattering). Raman scattering was first predicted

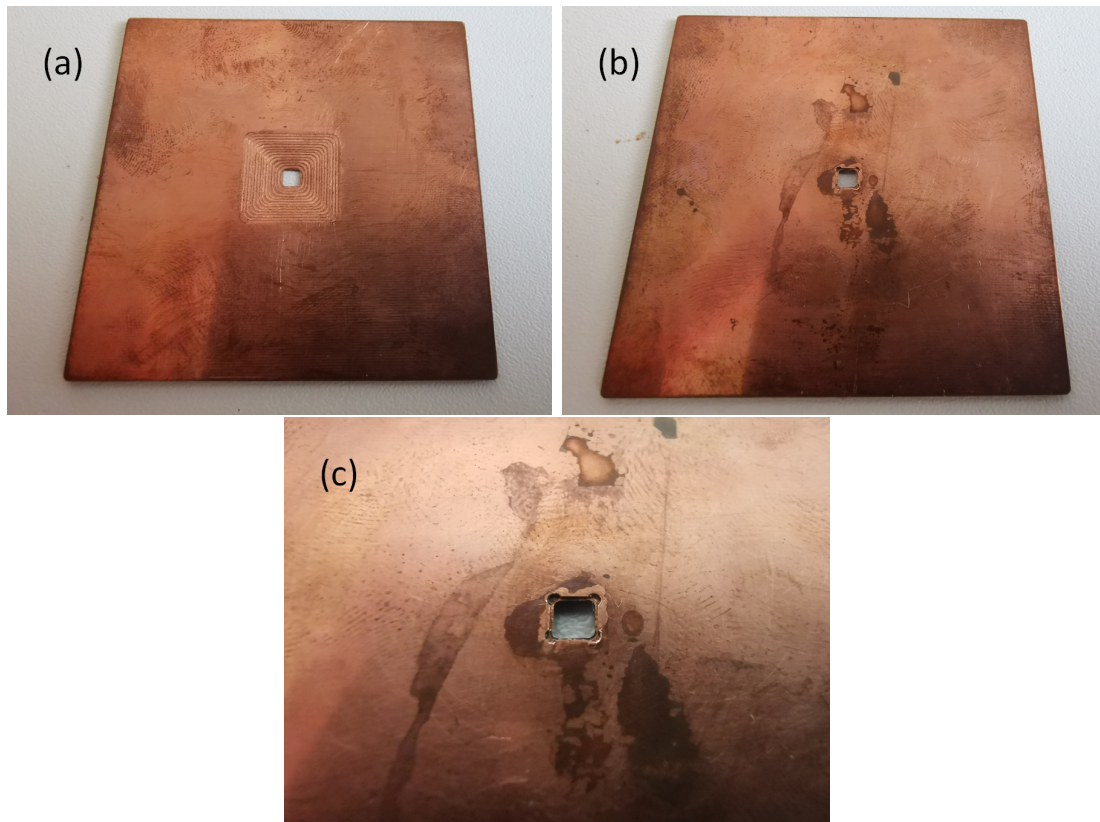


Figure 4.22: Sample holder for TLP setup **(a)** view from the front, **(b)** from the back, and **(c)** close-up from the back

by A. Smekal in 1923 [188] using classical quantum theory and then experimentally observed by C. V. Raman and K. S. Krishnan in 1928 [189]. The frequency of the scattered light follows the equation:

$$\omega_S = \omega_p \pm \omega_{osc} \quad (4.35)$$

Where  $\omega_S$  is the scattered photon frequency,  $\omega_p$  is the frequency of the incident photon, also called pump photon, and  $\omega_{osc}$  is the frequency of the lattice or molecule vibrational mode. When  $\omega_S$  is smaller than  $\omega_p$ , the Raman scattering is said to be Stokes Raman, and when  $\omega_S$  is larger than  $\omega_p$ , it is an anti-Stokes Raman

scattering event. Stokes and anti-Stokes Raman scattering are presented in a Jablonski diagram in Figure 4.23.

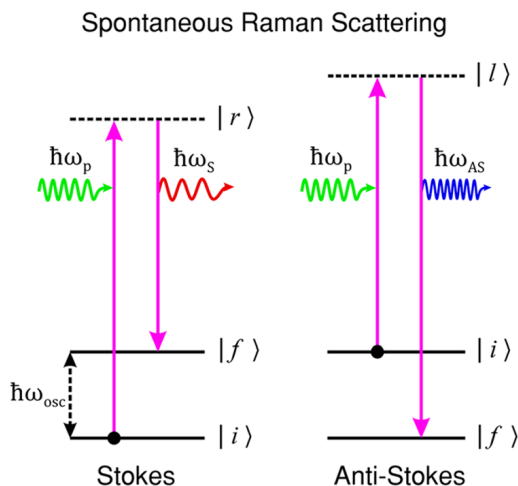


Figure 4.23: Jablonski diagram representing the energy transfer during a Stokes and anti-Stokes Raman scattering event [190]

Raman spectroscopy is a technique based on the measurement of the energy shift of the outgoing photon. The shift in energy is attributed to the excitation and relaxation of vibrational modes which cause a change in the polarizability of the molecules or in the dielectric susceptibility in the case of a crystal. This shift is specific to the chemical composition of the molecules responsible for scattering, making Raman spectroscopy suitable for chemical characterization.

In the case of spontaneous Raman, the Raman effect is relatively weak with about 1 out of  $10^8$  incident radiation being affected by Raman scattering [191]. In order to obtain a stronger signal compared to spontaneous Raman, additional techniques were developed such as Stimulated Raman Scattering (SRS) [190, 192] and Coherent Anti-Stokes Raman Scattering (CARS) [190, 193]. Both of these techniques rely on the use of additional photons to excite specific vibrational states

of the molecule or lattice and resonantly enhance the Raman effect.

When studying diamond layers, Raman spectroscopy gives useful information regarding the crystalline quality and the doping. An example of Raman spectrum recorded on a polycrystalline diamond layer is presented in Figure 4.24. Several peaks are visible [194]:

- The peak located around  $1333\text{ cm}^{-1}$  called the Zone Center Phonon (ZCP) peak is attributed to the  $\text{sp}^3$  diamond lattice.
- The band at  $1355\text{ cm}^{-1}$  is the D-band assigned to distorted  $\text{sp}^3$  and  $\text{sp}^2$ .
- The band at  $1440\text{-}1480\text{ cm}^{-1}$  is attributed to C-H bending and transpolyacetylene.
- The band at  $1560\text{ cm}^{-1}$  is the G-band attributed to amorphous  $\text{sp}^2$  carbon and graphite.

By calculating the ratio between the area under the curve of the signal attributed to  $\text{sp}^3$  carbon at  $1333\text{ cm}^{-1}$  to the ones attributed to  $\text{sp}^2$  carbon, it is possible to obtain the  $\text{sp}^3/\text{sp}^2$  carbon ratio in the diamond layer giving valuable information on its crystalline quality [195].

In the presence of boron and phosphorus impurities, the ZCP diamond peak tends to be redshifted [196, 197]. When boron is present in the diamond layer, additional peaks appear in the spectrum at  $500\text{ cm}^{-1}$  and  $1200\text{ cm}^{-1}$  [196]. For boron doping above the Mott transition, the ZCP diamond peak switches from a Lorentzian shape to a N-shaped Fano profile [198]. V. Mortet et al. also showed that it is possible to calculate the boron concentration in an epitaxial doped diamond

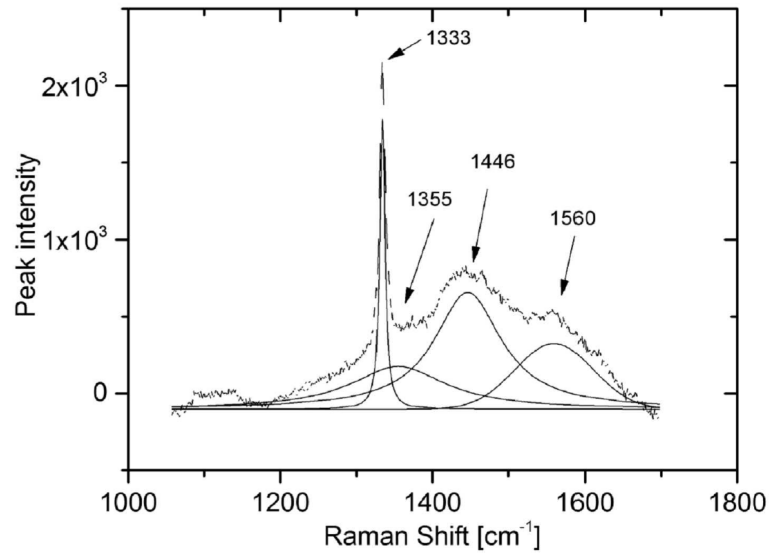


Figure 4.24: Example of Raman spectrum recorded on an undoped polycrystalline diamond layer [194]. The fitting was done using Lorentzian and Gaussian profiles

layer from the unperturbed position or the width of the Fano-shaped ZCP diamond peak.

### 4.8.2 Raman Spectroscopy Setup

Raman spectra were measured using a Renishaw InVia Raman Microscope with a argon-ion laser with an excitation wavelength of 488 nm with an output power of 50 mW. A  $2400 \text{ l.mm}^{-1}$  grating was used to separate the constituent wavelengths of the collected Raman scatter onto different pixels of a Renishaw CCD 1024 chip for detection. The Raman spectroscopy setup is presented in Figure 4.25.



Figure 4.25: Raman spectroscopy measurement setup

**Part III**

**RESULTS**

# Chapter 5

## Boron-Doped Diamond Layers

In this chapter, the growth conditions of the epitaxial diamond layers studied in this thesis are presented along with the microfabrication of electrodes used for TLP current-voltage characterization and TIM. The boron concentration and electrical properties, obtained from SIMS and Hall effect measurement respectively, are also discussed.

### 5.1 Boron-Doped Diamond Layer Growth

#### 5.1.1 Growth Conditions

The boron-doped diamond layers used in this work were grown on (100) oriented diamond substrates by PECVD with various boron concentration from 50 ppm to 1000 ppm in the gas phase. The (100) single crystal diamond substrates were first cleaned in a hot oxidizing mixture of  $\text{H}_2\text{SO}_4$  and  $\text{KNO}_3$  for 10 min. The samples were then washed in hot deionized water, ultrasonically cleaned in acetone and isopropyl alcohol and finally dried with cleaned dry air.

Table 5.1: Growth conditions used for epitaxial growth on (100) diamond substrates

Step	Process gas composition	Pressure (mbar)	MW Power (W)	Time (min)
1	H <sub>2</sub>	100	500	10
2	O <sub>2</sub> (1%) - H <sub>2</sub> (99%)	100	700	10
3	H <sub>2</sub>	100	700	10
4	H <sub>2</sub> (~ 99%) - CH <sub>4</sub> (~ 1%) - B <sub>2</sub> H <sub>6</sub> (50-1000 ppm)	100	700	120

The epitaxial boron-doped diamond layers were grown in a bell jar reactor described in subsection 3.1.1. Prior to the deposition, the samples were etched in a H<sub>2</sub>/O<sub>2</sub> plasma in order to remove subsurface defects. The epitaxial layers on (100) substrate were then grown in a mixture of dihydrogen H<sub>2</sub> and methane CH<sub>4</sub> with a total gas flow of 700 sccm. The boron doping was achieved using diborane B<sub>2</sub>H<sub>6</sub> diluted at 7500 ppm in H<sub>2</sub>. The detailed growth conditions are summarized in Table 5.1. A deposition rate of about 1.7  $\mu\text{m}\cdot\text{h}^{-1}$  was calculated by measuring the mass of the samples before and after the epitaxial growth using a high precision ME5 microbalance. After the growth, the samples were cleaned again using the same technique as prior deposition. Figure 5.1 shows the AFM image of the surface of the diamond sample used for TIM measurement. The AFM setup is presented in subsection 4.1.2. The surface of the diamond is smooth with a Root Mean Square (RMS) roughness of 0.3 nm.

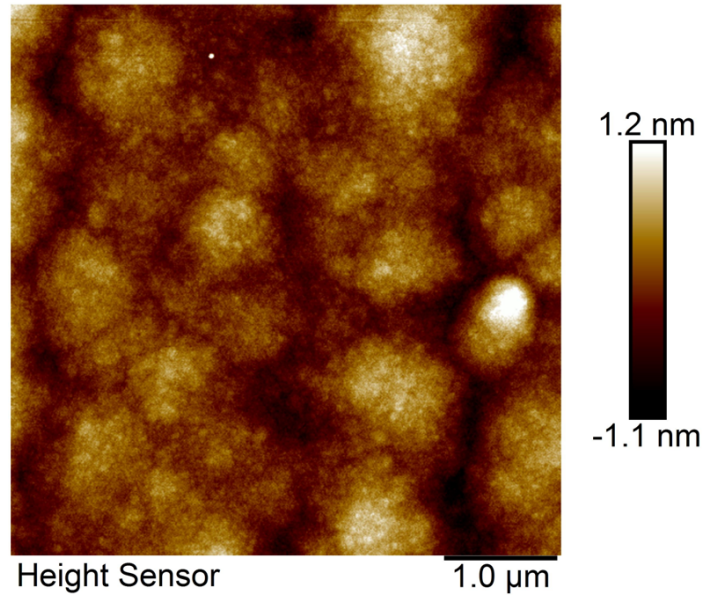


Figure 5.1: AFM image of the surface of the diamond sample used for TIM measurement

### 5.1.2 Electrical Contacts Microfabrication

Electrodes are ohmic contacts made of a Ti (10 nm) and Au (200 nm) deposited by e-beam evaporation in an Edwards Auto 500 vacuum coater and annealed at 450 °C for 20 minutes [199]. Ti is a good metal to make ohmic contacts as it forms a carbide at the interface with diamond which decreases the contact resistance [200].

Two types of electrodes were patterned on the surface of the samples: ring-disk electrodes used for pulsed current-voltage (I-V) measurements (Figure 5.2a) (which are also often used for contact resistance determination) and parallel electrodes used for Transient Interferometric Mapping (TIM) (Figure 5.2b). The ring-disk electrodes were chosen to avoid edge effects and their circular symmetry makes them easier to model. As it is not possible to do TIM measurement along a line parallel to the electrodes in the ring-disk configuration, parallel electrodes were used for this purpose instead.

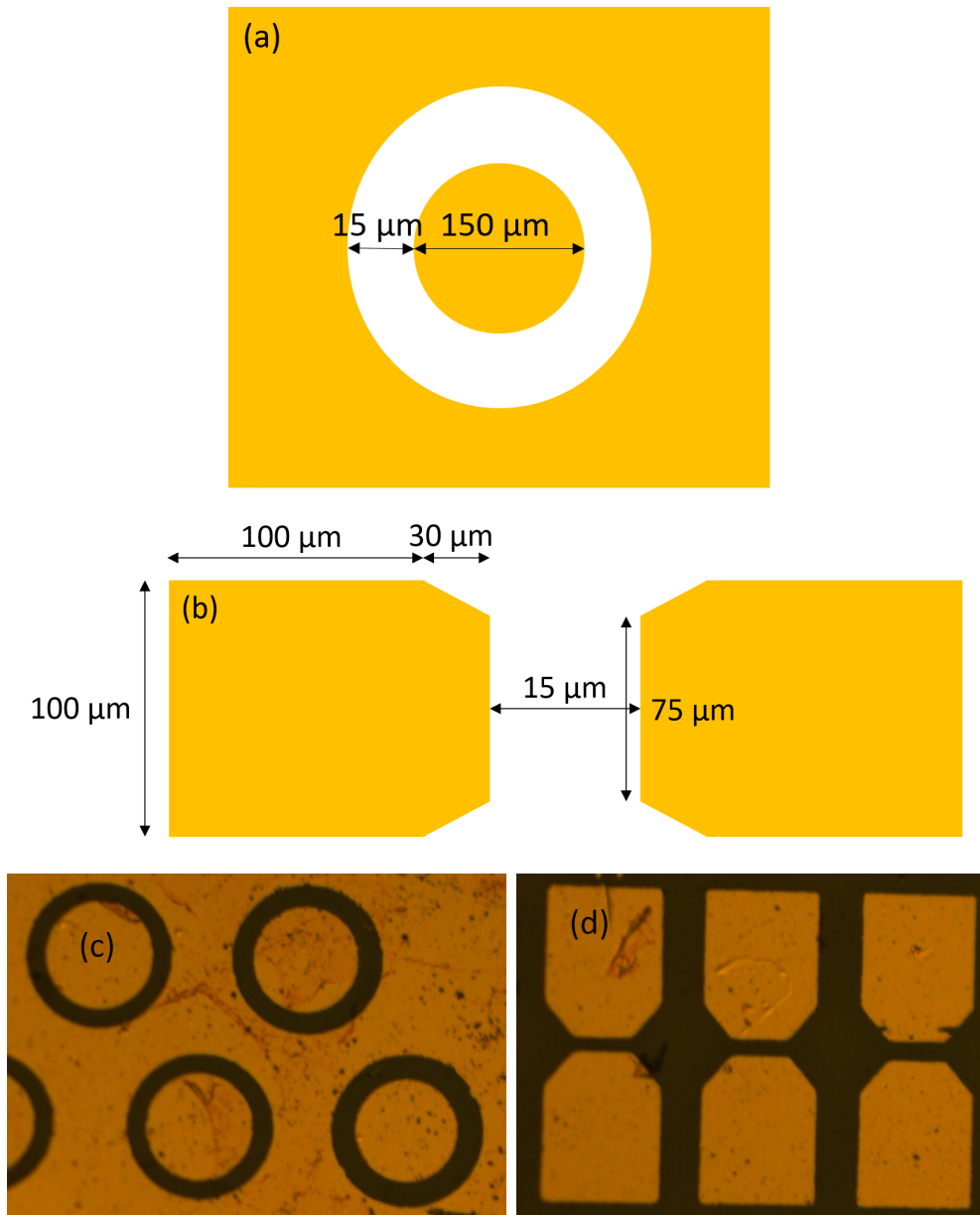


Figure 5.2: Different types of electrodes used for electrical characterizations: schematics and images of **(a)** **(c)** circular electrodes for pulsed I-V measurements, **(b)** **(d)** parallel electrodes for TIM measurements

Both types of electrodes were patterned by photolithography and wet etching techniques. A  $1\ \mu\text{m}$ -thick photoresist layer (positive for ring-disk electrodes and

Table 5.2: Coating conditions for positive and negative photoresists

Photoresist type	Coating speed (rpm)	Process duration (s)	Baking temperature (°C)	Baking duration (s)
Positive (ma-P 1210)	3000	30	110	90
Negative (ma-N 1410)	3000	30	110	120

Table 5.3: Exposure conditions for positive and negative photoresists

Photoresist type	Laser energy (mJ.cm <sup>2</sup> )	Dose correction factor	Focus correction factor
Positive (ma-P 1210)	150	0.6	0.4
Negative (ma-N 1410)	250	1.2	0.4

negative for parallel electrodes) from Micro Resist Technology was deposited by spin-coating on the surface of the diamond samples, and then baked on a hot plate. The photoresist layer was then exposed using a direct-write photolithography machine equipped with a 405 nm laser (MicroWriter ML2 from Durham Magneto Optics) and developed using the appropriate chemical developer. The conditions used for the coating, exposition, and developing of the photoresist layers are presented in Table 5.2, Table 5.3, and Table 5.4. Finally, the electrodes were obtained by wet chemical etching using KI/I<sub>2</sub> and diluted HF (0.1%) as etchants for Au and Ti, respectively.

Table 5.4: Developing conditions for positive and negative photoresists

Photoresist type	Developer type	Developing time (s)
Positive (ma-P 1210)	mr-D 526/S	30
Negative (ma-N 1410)	ma-D 533/S	30

## 5.2 Boron-Doped Diamond Layers Characterization

### 5.2.1 Secondary Ion-Mass Spectroscopy Measurement

The boron concentration  $[B]$  of the layers, which ranges from  $3.2 \times 10^{18} \text{ cm}^{-3}$  to  $6.3 \times 10^{19} \text{ cm}^{-3}$  (details are given in Table 6.1), was calculated from the incorporation ratio determined from SIMS measurements of boron-doped diamonds samples from reference [20]. The SIMS setup used for those measurements is presented in subsection 4.3.2. An incorporation ratio of 0.369 with an error of 0.002 was determined by fitting the SIMS data using a linear function as presented in Figure 5.3. The incorporation ratio decreases at low boron concentration in the gas phase. This behavior was also observed by K. Ushizawa et al. [201] on the (100)-oriented facets of a doped polycrystalline diamond layer. The calculated boron incorporation ratio is comparable with the one reported by K. Ushizawa et al. [201] and V. Mortet et al. [113].

### 5.2.2 Hall Effect Measurement

Hall measurement was used to determine the resistivity and hole mobility in boron-doped diamond samples. The results are presented in Figure 5.4. They were made on diamond samples grown with boron concentrations in the gas phase ranging from 10 to 1500 ppm which translates to  $6.5 \times 10^{17}$  to  $9.4 \times 10^{19} \text{ cm}^{-3}$  in the diamond layer according to the SIMS measurement made in section 5.2.1. Apart from the sample containing  $3.2 \times 10^{18} \text{ cm}^{-3}$  of boron, the modeled mobility is much higher compared to the Hall mobility. This can be attributed to the hopping

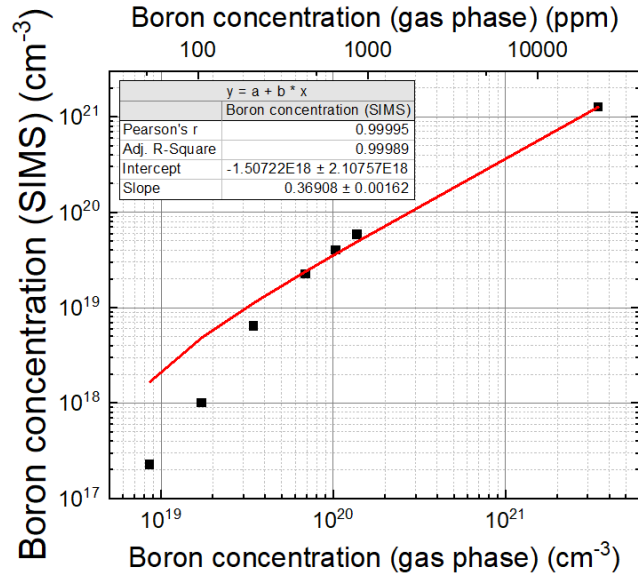


Figure 5.3: Boron concentration measured by SIMS as a function of the boron concentration in the gas phase during the CVD growth. The red line is a linear fit

mechanism, already observed in highly doped diamond [101, 104, 202], which is not taken into account in the mobility model presented by S. Kagamihara et al. [203]. The transition to hopping conductivity seems to happen for a boron concentration close to  $2 \times 10^{19} \text{ cm}^{-3}$ . M. Grünwald et al. [204] found that in hopping regime, the Hall mobility evolution with temperature obeys the following equation,

$$\ln \mu_h \propto -\frac{3}{8} \left( \frac{T_0}{T} \right)^{\frac{1}{4}} \quad (5.1)$$

with

$$T_0 = 18 \frac{\alpha^3}{k_B N_0} \quad (5.2)$$

where  $N_0$  is the site density and  $\alpha^{-1}$  is the decay length of the wave function at the localized sites.

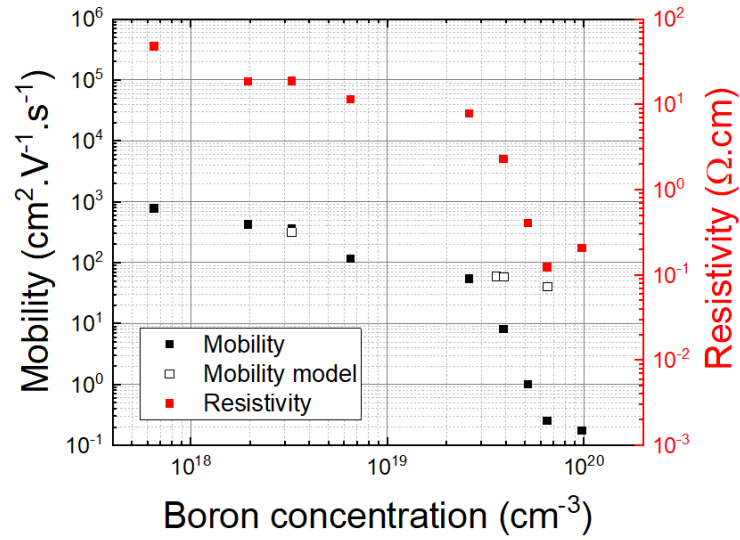


Figure 5.4: Hall mobility (black squares) and resistivity (red squares) measured by Hall measurement, and modeled mobility (white squares) as a function of the boron concentration on (100) boron-doped diamond samples at room temperature ( $T = 300$  K)

The Hall mobility and the resistivity were measured as a function of the temperature for the samples containing  $6.3 \times 10^{19} \text{ cm}^{-3}$  (1000 ppm in the gas phase) and  $9.4 \times 10^{19} \text{ cm}^{-3}$  (1500 ppm in the gas phase) of boron. The values of resistivity are decreasing with the temperature which is consistent with the results obtained by D. M. Malta et al. [205]. The mobility values were fitted using equation (5.1) in Figure 5.5. Equation (5.1) offers a good fit of the experimental data which confirms the hopping conductivity in samples with high boron content.

### 5.3 Conclusion

Epitaxial boron-doped diamond layers were grown and Ti/Au electrodes were made using wet chemical etching for TLP current-voltage and TIM characterization. A

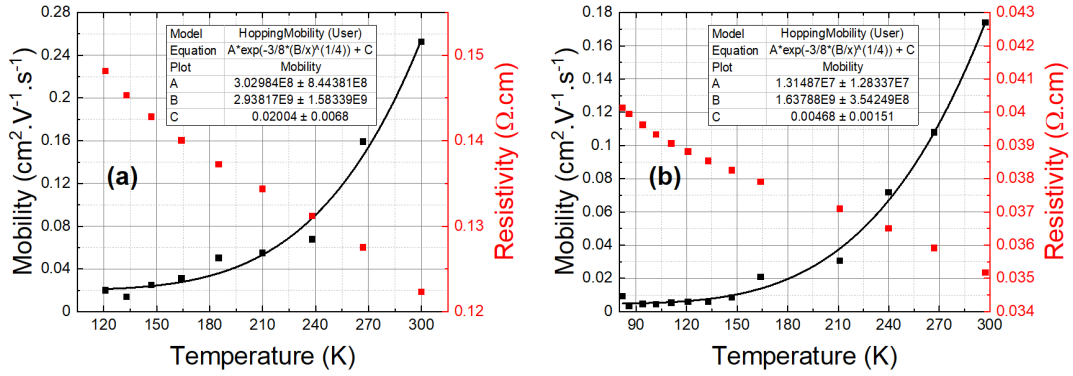


Figure 5.5: Evolution of the Hall mobility (black squares) and resistivity (red squares) as a function of temperature for samples with a boron content of (a)  $6.3 \times 10^{19} \text{ cm}^{-3}$  and (b)  $9.4 \times 10^{19} \text{ cm}^{-3}$ . The black line represents the fitting function described in equation (5.1)

boron concentration ranging from  $3.2 \times 10^{18} \text{ cm}^{-3}$  to  $6.3 \times 10^{19} \text{ cm}^{-3}$  was obtained from SIMS measurements. Hall effect measurements reveal the apparition of hopping conductivity in the boron-doped diamond layer with the highest boron concentration.

## Chapter 6

# Electronic Transport under High Electric Fields

In this chapter, four different samples were considered in this study. Their characteristics are summarized in Table 6.1. The TLP current-voltage and TIM setup were used to characterize electrically and thermally the different samples. The measured current-voltage characteristics were finally simulated using finite element method taking into account the Self-Heating Effect (SHE) and Impurity Impact Ionization (III) processes.

## 6.1 Transmission Line Pulse (TLP) Measurements

*(Results presented in [206])*

TLP current-voltage measurements were done using the lab-made setup described in subsection 4.6.2. Figure 6.1 shows typical characteristic voltage and current waveforms of boron-doped diamond sample B ( $[B] = 3.8 \times 10^{19} \text{ cm}^{-3}$ ) during voltage pulses with different charging voltages  $V_{ch}$ . At applied voltages lower than 100 V, the voltage and current waveforms are nearly flat during the 100 ns pulse, which indicates that there is no significant heating and temperature variation in the device. At larger applied voltages, both the voltage and current vary in time, which is characteristic of thermal runaway due to SHE and the current intensity further increases with the increasing  $V_{ch}$  until catastrophic breakdown. This phenomenon is also visible in Figure 6.1c in which I-V curves have been plotted for four different averaging periods during the voltage pulse. For a voltage lower than 100 V, the I-V curves are very similar while a divergence is observed for a voltage higher than 100 V. The later the averaging is done during the pulse, the higher the resulting current is. A Negative Differential Resistance (NDR) region in the I-V curve also emerges for longer times at currents above 1 A. The spike at the beginning of the current pulse (observed in Figure 6.1b) is an artifact due to the propagation of the signal in the cable between the probe and the sample.

Figure 6.2 shows quasi-static I-V characteristics for all samples in linear and semi-logarithmic scale determined from waveforms with different  $V_{ch}$  (cf. also Figure 6.1). The average value of voltage and current were calculated at the end of

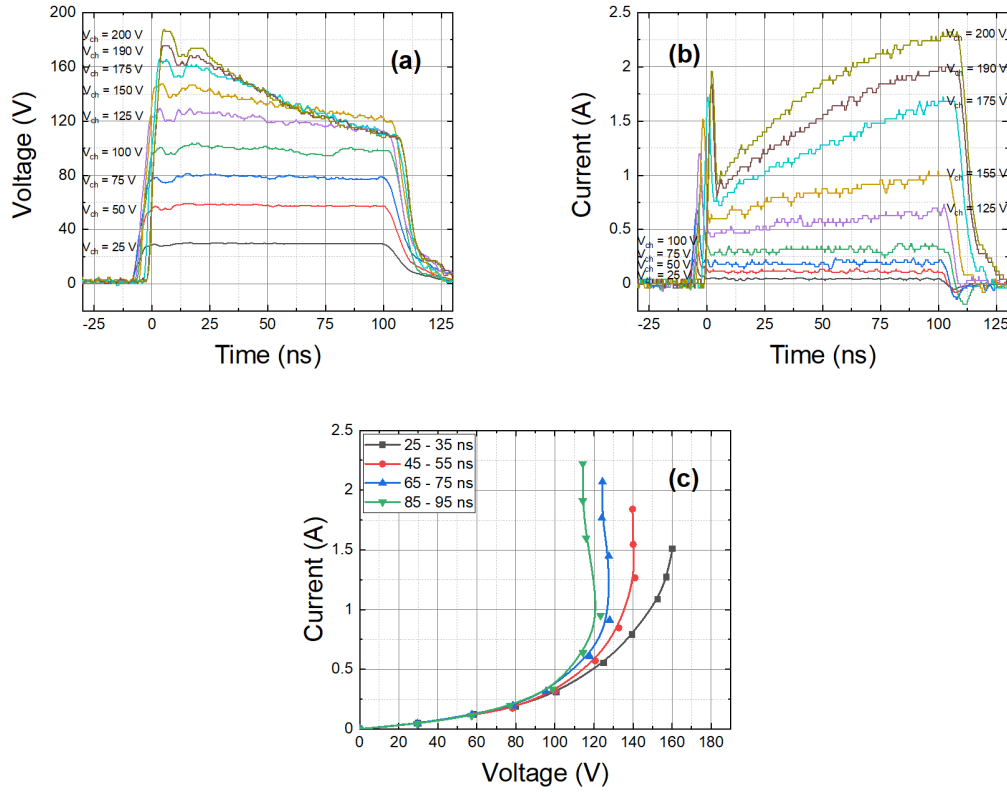


Figure 6.1: Measured (a) voltage and (b) current waveform of sample B ( $[B] = 3.8 \times 10^{19} \text{ cm}^{-3}$ ) for different charging voltage  $V_{ch}$ , and I-V characteristics (c) calculated for different averaging periods in the voltage (a) and current (b) waveforms. The initial peak of current in (b) and small voltage steps in (a) are artifacts due to different spatial position of voltage and current probes and reflections. The lines in (c) are for eye-guiding

each pulse, i.e. between 85 ns and 95 ns from the beginning of each pulse. Each curve exhibits a short linear part up to approximately 50 V which transitions to an exponential behavior as the voltage increases. Finally, the current increases even further with a super-exponential evolution until the breakdown voltage ( $V_{bd}$ ) indicated by dashed lines in Figure 6.2. The breakdown electric field for each sample was calculated by dividing the breakdown voltage by the inter-electrode gap and is reported in Table 6.1. For samples A, B, and C the breakdown electric field

decreases with the boron concentration in the diamond layers which contradicts results obtained on p-type and n-type germanium [207]. However, it is consistent with results reported by V. I. Sankin et al. on aluminum-doped p-type SiC [208]. The authors attributed this behavior to the decrease of the dopant activation energy and the compensation ratio with the dopant concentration. The values of breakdown electric field obtained for each diamond sample are also comparable with the ones reported by V. Mortet et al. [20, 209]. Sample B shows a NDR region at currents above 1.0 A, i.e. for  $V_{ch}$  superior to 150 V (cf. also Figure 6.1c). The instantaneous voltage decreases rapidly while the instantaneous current increases (Figure 6.1), causing the NDR.

Besides the III effect, the origin of the non-linear increase in current, especially the NDR regime, and the following breakdown observed in I-V characteristics could be attributed to SHE. Indeed, SHE is known to cause NDR behavior in electronic devices such PIN diodes [211] or MOSFET transistors [212]. Therefore, TIM measurements were carried-out on boron-doped diamond layers with parallel electrodes to investigate the possible self-heating effect. Thermal energy distribution maps were obtained through multiple pulsed measurements. Since repeated pulses in the NDR regime gradually degrade the electrodes, TIM measurements were performed below and at the onset of the NDR region.

Table 6.1: Physical characteristics of diamond samples and simulation parameters used in the finite element method simulation

	Sample A	Sample B	Sample C	Sample D
<i>Growth conditions</i>				
$[B]/[C]$ gas phase (ppm)	50	550	1000	600
<i>Physical characteristics</i>				
Geometry of electrodes	Circular	Circular	Circular	Parallel
Inter-electrode gap ( $\mu\text{m}$ )	16.6	12.8	14.8	14.3
Boron concentration - SIMS ( $\text{cm}^{-3}$ )	$3.2 \times 10^{18}$	$3.6 \times 10^{19}$	$6.3 \times 10^{19}$	$3.8 \times 10^{19}$
Breakdown voltage (V)	215	125	110	255
Breakdown electric field ( $\text{kV}\cdot\text{cm}^{-1}$ )	130	98	74	157
<i>Simulation parameters</i>				
Carrier lifetime (s)		$1.2 \times 10^{-11}$ [210]		
Carrier capture cross section ( $\text{cm}^{-2}$ )		$10^{-14}$ [210]		
Donor concentration ( $\text{cm}^{-3}$ )	$3.1 \times 10^{16}$	$3.0 \times 10^{18}$	$3.5 \times 10^{18}$	$1.9 \times 10^{18}$
$A_\alpha$ ( $\text{cm}^{-1}$ )	$1.4 \times 10^3$	$1.2 \times 10^3$	$1.0 \times 10^3$	$1.2 \times 10^3$
$B_\alpha$ ( $\text{V}\cdot\text{cm}^{-1}$ )	$8.4 \times 10^5$	$4.6 \times 10^4$	$6.2 \times 10^5$	$4.6 \times 10^4$
$A_{cv}$ ( $\text{J}\cdot\text{cm}^{-3}\cdot\text{K}^{-1}$ )		$4.0 \times 10^{-1}$		
$B_{cv}$ ( $\text{J}\cdot\text{cm}^{-3}\cdot\text{K}^{-2}$ )		$1.0 \times 10^{-2}$		
$C_{cv}$ ( $\text{J}\cdot\text{cm}^{-3}\cdot\text{K}^{-3}$ )		$-4.0 \times 10^{-6}$		
$D_{cv}$ ( $\text{J}\cdot\text{K}\cdot\text{cm}^{-3}$ )		$-1.1 \times 10^5$		
$v_{sat}$ ( $\text{cm}\cdot\text{s}^{-1}$ )		$1.1 \times 10^7$		
$\beta_{sat}$		$9.5 \times 10^{-1}$		

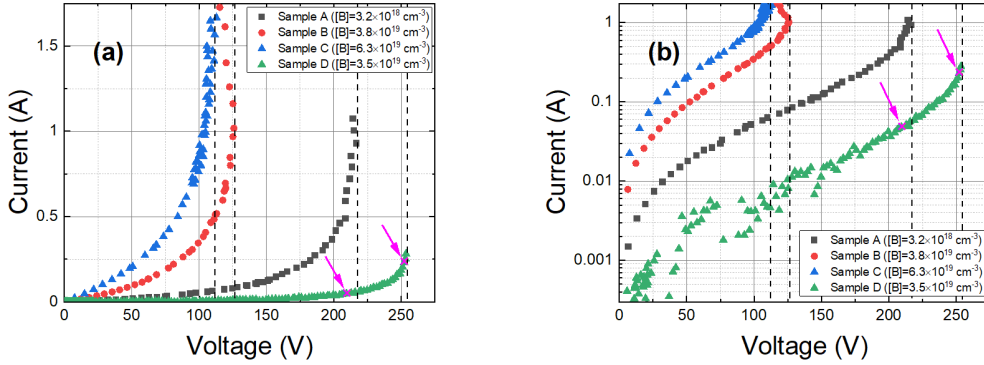


Figure 6.2: Current-voltage characteristic of studied devices in linear (a) and semi-logarithmic (b) scales. In sample D, two measurement conditions (50 mA and 250 mA) at which TIM measurements were performed are indicated by pink arrows and crosses.

## 6.2 Transient Interferometric Mapping (TIM)

### Measurements

#### *(Results presented in [206])*

TIM measurements were carried out on sample D in TU Wien using the setup described in subsection 4.7.2. Figure 6.3a shows the phase shift distribution in the inter-electrode gap space below the NDR regime's onset, i.e. at a constant (final) current of 50 mA in the exponential region. This condition is indicated by the pink arrow in the I-V curve of sample D in Figure 6.2. The phase shift increases non-linearly with time until the end of the pulse ( $t = 100$  ns), where it is at maximum (0.05 rad) and then decreases. The uniform phase shift along the device's electrodes width (X-direction) demonstrates a uniform current distribution. Figure 6.3b shows TIM measurement made at the onset of the NDR, i.e. at a current of 250 mA (see the right arrow label in the I-V curve of sample D in Figure 6.2).

While the phase shift at  $t = 50$  ns is still homogeneous along the X-axis, it becomes non-uniform at longer times and forms two peaks at the end of the pulse with a maximum value of approximately 0.24 rad. The two peaks are attributed to the formation of two hot spots, which are narrow regions of concentrated current and elevated temperature, between the electrodes. Those hot spots are due to excessive dissipated power. The positive feedback between the increase in current density and the elevation of temperature would ultimately lead to current filamentation and thermal runaway [213].

Figure 6.3c represents the measured phase shift between the electrodes along the electric current path, i.e. perpendicularly to the electrodes, for the current of 0.25 A and positive polarity on the right electrode. The heat distribution reaches its maximum in the region between the electrodes. The phase shift distribution is nearly identical when the electrodes are polarized the opposite way. The sharp negative peaks of the phase shift at the electrodes edge (i.e. at  $Y = 3$  and  $Y = 17$   $\mu\text{m}$ ) are optical artifacts. Unfortunately, they are at the positions where the phase shift distribution has the largest gradient and therefore prohibit establishing its exact shape.

The spreading of phase shift with time and its apparent increase after the end of the pulse outside the spatial limits of the inter-electrode gap are due to thermal diffusion. The diffusion length in Figure 6.3c is estimated as the distance from the edge of the electrode for which the temperature decreases by around 90% and it is consistent with the diamond diffusion length ( $L_{th} = 11$   $\mu\text{m}$  for  $t = 100$  ns) as estimated from:

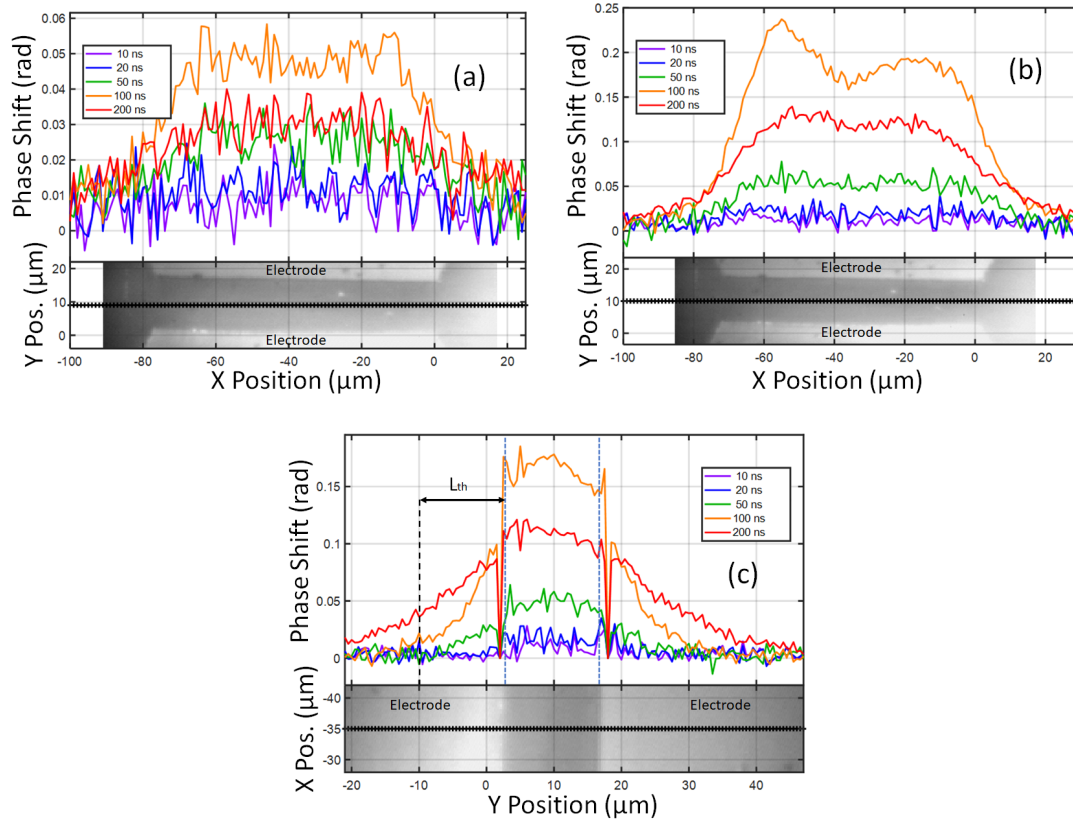


Figure 6.3: Phase shift measurement on sample D ( $[B] = 3.8 \times 10^{19} \text{ cm}^{-3}$ ) along a scanning line parallel to the electrodes for different times and a current of **(a)** 0.05 A and **(b)** 0.25 A. **(c)** is the evolution of the phase shift distribution along a scanning line perpendicular to the electrodes, in the center of the device, for currents of 0.25 A with a positive polarity on the right electrode. The photographs are backside infrared images of the device active area including the scanning direction (black bold line)

$$L_{th} = \sqrt{\frac{k_T}{c_v} t} \quad (6.1)$$

with the thermal conductivity ( $k_T = 22 \text{ W.cm}^{-1}.\text{K}^{-1}$ ) [214], the volumetric heat capacity ( $c_V = 1.83 \text{ J.cm}^{-3}.\text{K}^{-1}$ ) and the time ( $t$ ).

## 6.3 Modeling of Boron-Doped Diamond under High Electric Fields

*(Results presented in [206])*

### 6.3.1 Presentation

The I-V characteristics, and voltage/current transient waveforms were modeled by finite element method (Atlas by Silvaco) using the drift diffusion and thermodynamic approach (i.e. drift diffusion model with thermal equation) based on the dependences of transport parameters and hole concentration on the electric field and the temperature. The concentric electrodes with their cylindrical geometry simplify the simulations to a two-dimensional problem in space. A substrate depth of 100  $\mu\text{m}$  has been considered. A 50  $\Omega$  resistor has been used between the simulated device and voltage source to emulate the 50  $\Omega$  internal resistance of the TLP generator's equivalent circuit. The simulated area is a rectangle with a height of 150  $\mu\text{m}$  and a width of 100  $\mu\text{m}$  with two ohmic contacts on top of it. The mesh size was set to 0.1  $\mu\text{m}$  between the electrodes and the limit of the doped diamond layer and progressively set to 5  $\mu\text{m}$  at the end of the simulated area. The default values of tolerance from the Atlas software (Silvaco) [215] were used for the simulations (see Table 6.2).

As the super-linearity is observed at voltages for which no significant heating is expected, additional mechanisms have to be considered to explain this behavior: Phonon-Assisted Tunneling Effect (PATE), Poole-Frenkel Effect (PFE) [216, 217], and Impurity Impact Ionization (III) [218, 219]. The simulation parameters used for each model are reported in Table 6.1.

Table 6.2: Default values of tolerance used in the Silvaco Atlas finite element simulation [215]

<b>PX.TOL</b>	Relative tolerance for the potential equation	$10^{-5}$
<b>PR.TOL</b>	Absolute tolerance for the Poisson equation	$10^{-26}$
<b>CX.TOL</b>	Relative tolerance for the continuity equation	$10^{-5}$
<b>CR.TOL</b>	Absolute tolerance for the continuity equation	$5 \times 10^{-18}$
<b>TCX.TOL</b>	Relative tolerance for convergence of the carrier temperature equations	$10^{-5}$
<b>TLX.TOL</b>	Relative tolerance for convergence of the lattice temperature equation	$10^{-5}$
<b>TCR.TOL</b>	Absolute tolerance for convergence of the carrier temperature equations	100
<b>TLR.TOL</b>	Absolute tolerance for convergence of the lattice temperature equation	100
<b>IX.TOL</b>	Relative current convergence criteria	$5 \times 10^{-4}$
<b>IR.TOL</b>	Absolute current convergence criteria	$5 \times 10^{-11}$

### 6.3.2 Mobility Modeling

Prior to modeling, it is crucial to know the hole mobility  $\mu_h$  and activation energy  $E_a$  dispersion with temperature and dopant concentration.

The temperature and impurity concentration dependence of the hole mobility was modeled using the equations derived by S. Kagamihara et al. [203] from the work of D. M. Caughey and R. E. Thomas [220] (see equations (6.2) to (6.5)):

$$\mu_{h0}(T, N_{imp}) = \mu_h(T_{amb}, N_{imp}) \left( \frac{T}{T_{amb}} \right)^{-\beta N_{imp}} \quad (6.2)$$

$$\mu_{h0}(T_{amb}, N_{imp}) = \mu^{min} + \frac{\mu^{max} - \mu^{min}}{1 + \left( \frac{N_{imp}}{N_\mu} \right)^{\gamma_\mu}} \quad (6.3)$$

$$\beta_{h0}(N_{imp}) = \beta^{min} + \frac{\beta^{max} - \beta^{min}}{1 + \left( \frac{N_{imp}}{N_\beta} \right)^{\gamma_\beta}} \quad (6.4)$$

Table 6.3: Fitting parameters for the mobility model [14]

$\mu^{min}$ ( $\text{cm}^2 \cdot \text{V}^{-1} \cdot \text{s}^{-1}$ )	0	$\beta^{min}$	0
$\mu^{max}$ ( $\text{cm}^2 \cdot \text{V}^{-1} \cdot \text{s}^{-1}$ )	2016	$\beta^{max}$	3.11
$\gamma_\mu$ $N_\mu$ ( $\text{cm}^{-3}$ )	0.73 $3.25 \times 10^{17}$	$\gamma_\beta$ $N_\beta$	0.617 $4.1 \times 10^{18}$

$$N_{imp} = N_A + N_D \quad (6.5)$$

where  $N_A$  and  $N_D$  are the acceptor and the donor concentrations respectively, and  $T_{amb} = 300$  K. The  $\beta^{min}$ ,  $\beta^{max}$ ,  $\gamma_\beta$ ,  $N_\beta$ ,  $\mu^{min}$ ,  $\mu^{max}$ ,  $\gamma_\mu$ , and  $N_{mu}$  parameters based on [14] are reported in Table 6.3.

The dependence of the mobility on the electric field  $E$  and the saturation velocity  $v_{sat}$  is given in (see [220]):

$$\mu_h(E, T, N_{imp}) = \mu_{h0}(T, N_{imp}) \left( \frac{1}{1 + \left( \frac{\mu_{h0}(T, N_{imp})E}{v_{sat}} \right)^{\beta_{sat}}} \right) \quad (6.6)$$

The drift velocity for holes is then given by:

$$v_d(E, T, N_{imp}) = \mu_h(E, T, N_{imp})E \quad (6.7)$$

$v_{sat}$  and  $\beta_{sat}$  were obtained by fitting the hole-drift velocity data from [221] measured on (100) diamond samples at 300 K using equations (6.6) and (6.7). The resulting fitting is given in Figure 6.4.

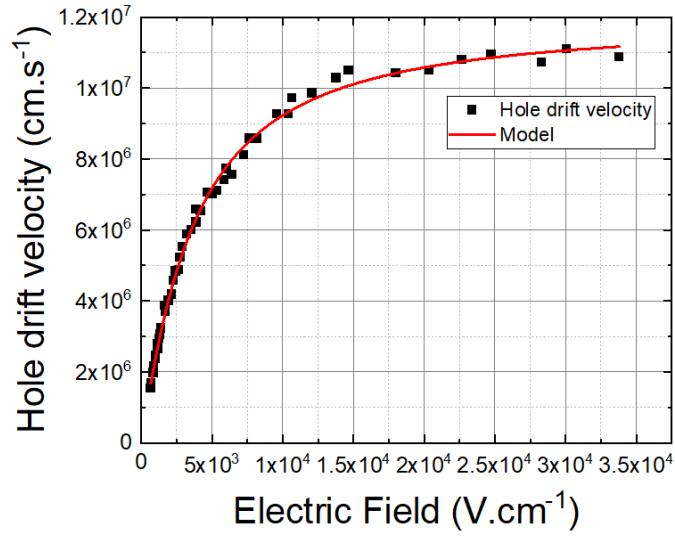


Figure 6.4: Experimental [221] and calculated hole drift velocity as a function of the electric field

### 6.3.3 Activation Energy Modeling

The activation energy  $E_a$  of boron acceptors decreases with increasing doping concentration due to the interaction between carriers and ionized impurities [222].

In this work, we used a modified Pearson and Bardeen [223] model, see equation (6.8), which fits the experimental data better:

$$E_a(N_A) = E_I - aN_A^b \quad (6.8)$$

with  $E_I = 0.37$  eV. The coefficients  $a$  ( $1.2 \times 10^{-10}$  eV.cm<sup>3/2.15</sup>) and  $b$  (1/2.15) were determined by fitting experimental values from the literature [105, 107, 205, 224–228] using the least square method. In the original Pearson and Bardeen model, only  $a$  is used as a fitting parameter and  $b = 1/3$ . Figure 6.5 shows that the modified model clearly offers a better fit of the experimental data compared

to the original model and gives boron activation energy with a root mean square error of  $7 \times 10^{-3}$  eV.

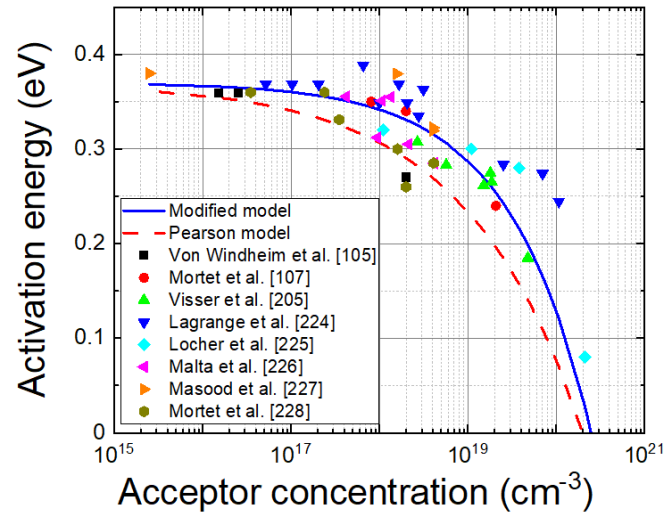


Figure 6.5: Dispersion of activation energy with the boron concentration

### 6.3.4 Super-linear Behavior Discussion

#### Phonon-Assisted Tunneling Effect (PATE)

PATE is a type of field emission due to the absorption of phonons by electrons or holes trapped at an impurity level. The mechanism is described in Figure 6.6. Thanks to the energy acquired from the phonon absorption and under the influence of an external electric field, the trapped carriers can tunnel through the energy barrier and reach the conduction or valence band. PATE is described by the equations presented in [229]. The comparison between experimental data and simulated I-V curves using PATE model is shown in Figure 6.7 (black dashed lines). The simulated I-V characteristics do not match the experimental data. The

exponential behavior is not observed and the simulated I-V curve barely deviates from a classic linear ohmic model. Therefore, we can conclude that PATE alone cannot explain the behavior of the I-V characteristics of the studied boron-doped diamond samples.

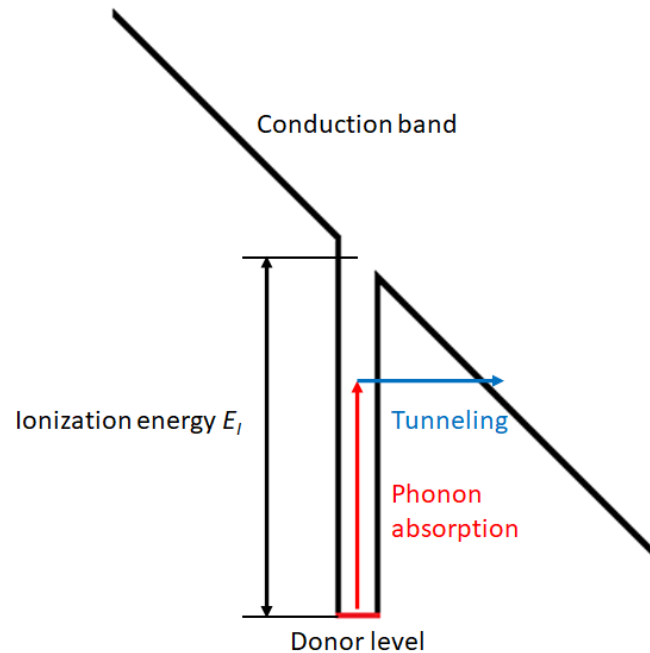


Figure 6.6: Schematic representation of the PATE for a donor impurity level

### Poole-Frenkel Effect (PFE)

Besides PATE, PFE might also contribute to the non-linearity of the I-V characteristics. The mechanism of PFE is presented in Figure 6.8. The energy barrier of a charged acceptor (or donor) energy level and the valence (or conduction) band decreases because of the dissymmetry in the impurity potential well in the external electric field and facilitates carrier emission by PATE. PFE has been previously reported in undoped diamond [216]. Since the boron impurities in diamond are,

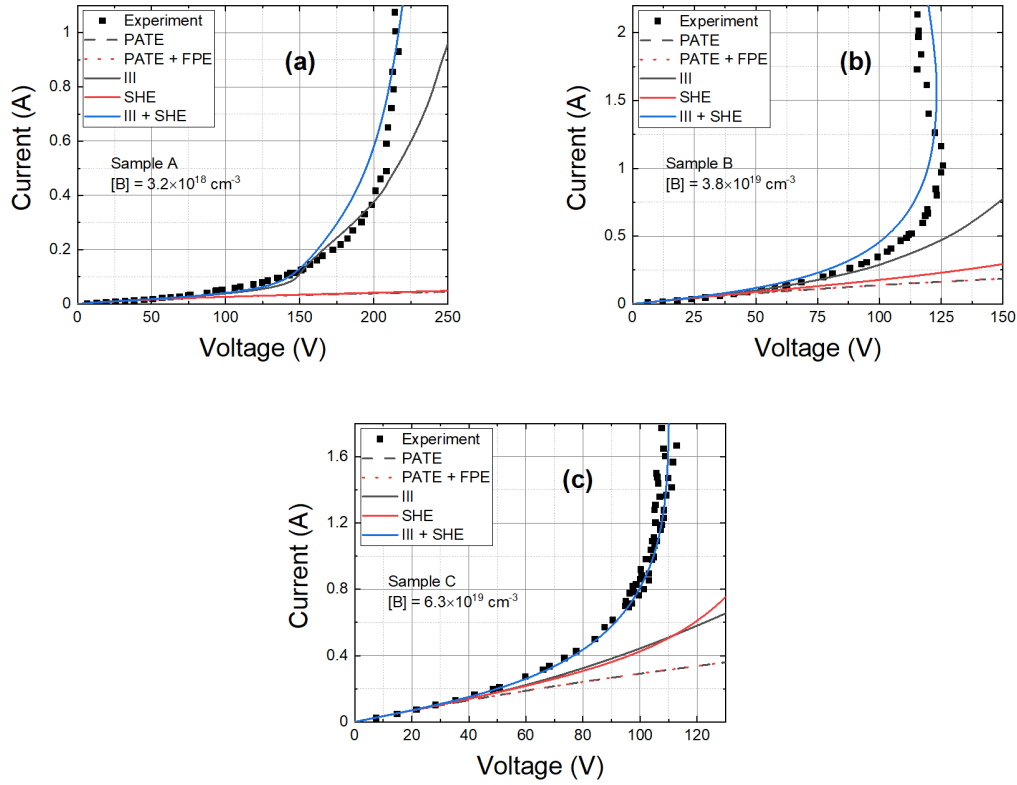


Figure 6.7: Experimental (symbols) and simulated (lines and dashed lines) pulsed I-V characteristics using a combination of PATE, PFE, III, and SHE ( $t = 100 \text{ ns}$ ) for (a) sample A, (b) B, and (c) C.

for the most part, not ionized at room temperature, PFE should not have a large influence on the I-V characteristics.

The modeled I-V characteristics, including PFE and PATE, are reported in Figure 6.7 (red dashed lines). PFE has been included in the simulation using the model embedded in the finite element simulator Atlas (Silvaco). These new simulated I-V characteristics are nearly identical to the one including PATE only and they show that PFE and PATE have a limited influence on the non-linear I-V characteristic of boron-doped diamond at high electric field. This result is also consistent with the study of A.K. Jonscher [230], which shows the negligible

contribution of PFE effect in electrical conductivity in crystalline semiconductors.

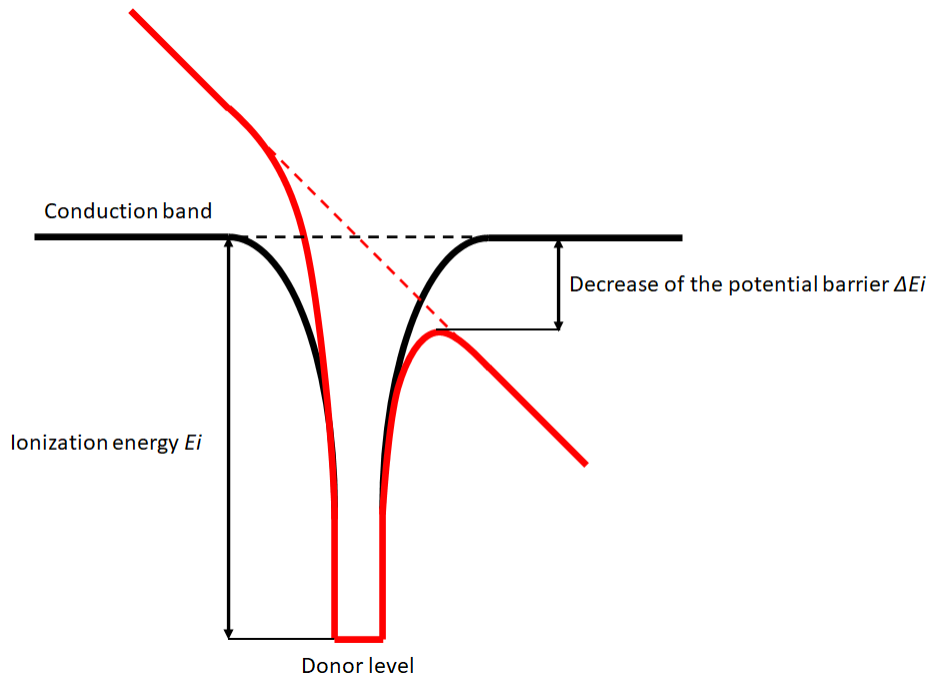


Figure 6.8: Schematic representation of the PTE for a donor impurity level. The black curve represents the potential well without electric field and the red one represents the potential well with an electric field applied.

### Impurity Impact Ionization (III) Effect

Impurity Impact Ionization (III) is a freeze-out regime effect which has been also reported for germanium and silicon carbide [208, 231]. When submitted to a strong enough electric field, some hot carriers can get enough kinetic energy to ionize other impurities in the crystal by knocking them.

To determine the impact of III on the electrical properties of boron-doped diamond, we followed the same approach as in [219] using the classical band-to-band impact ionization equations to model the current multiplication from the boron acceptor.

In this case, the current multiplication coefficient is given by:

$$M = \frac{1}{1 - \int_0^L \alpha_p \exp[-\int_0^x dx'(\alpha_p - \alpha_n)] dx} \quad (6.9)$$

where  $L$  is the distance between the electrodes and  $\alpha_p$  and  $\alpha_n$  are the ionization rate for holes and electrons respectively. We assume  $\alpha_p = \alpha_n = \alpha$  (see [232]) for simplification. The ionization rate  $\alpha$ , which reflects the number of ionization events per unit of length is given by (see [233]):

$$\alpha(E) = A_\alpha \exp\left(-\frac{B_\alpha}{E}\right) \quad (6.10)$$

where  $E = U/L$  is the electric field,  $U$  is the voltage difference between the two electrodes, and  $A$  and  $B$  are fitting parameters. This simplification leads to a new expression of the current multiplication coefficient given in:

$$M = \frac{1}{1 - L\alpha(U)} \quad (6.11)$$

This model does not take into account the temperature dependence of the ionization rate observed in Si and Ge [234]. However, L. Tirino et al. [235] studied the influence of temperature for various wide band gap semiconductors and reached the conclusion that the temperature dependence of the ionization rate is mainly due to the temperature dependence of the phonon scattering rates. He also found out that the higher the optical phonon energy is, the less sensitive to temperature the impact ionization coefficients will be. For example, 3C-SiC has an optical phonon energy of 120 meV and its ionization rate was found to be almost insensitive to temperature variations from 300 to 500 K. As a comparison, J. Pernot et al.

[110] calculated an optical phonon energy of 165 meV for diamond from the data reported in [236]. Therefore, the ionization rate in diamond has been assumed to be independent of temperature.

Ionization rates were determined by fitting the I-V curves using Eqs. (6.6), (6.10), and (6.11) in the region of negligible SHE, i.e. without temperature variation during the pulses (e.g. between 0 and 100 V for sample B). To simplify the calculation, the electric field was assumed to be constant between the electrodes, i.e. the edge effects due to the electrodes are neglected. Figure 6.9 shows the determined ionization rate as a function of the inverse electric field for boron-doped diamond samples A, B, and C. Although there is no clear variation with boron concentration, the variation of the determined ionization rate is consistent for all boron concentrations, i.e. it increases and saturates at values of ca.  $10^3 \text{ cm}^{-1}$  for voltages (electric fields) superior to 100 V ( $70 \text{ kV}\cdot\text{cm}^{-1}$ ).

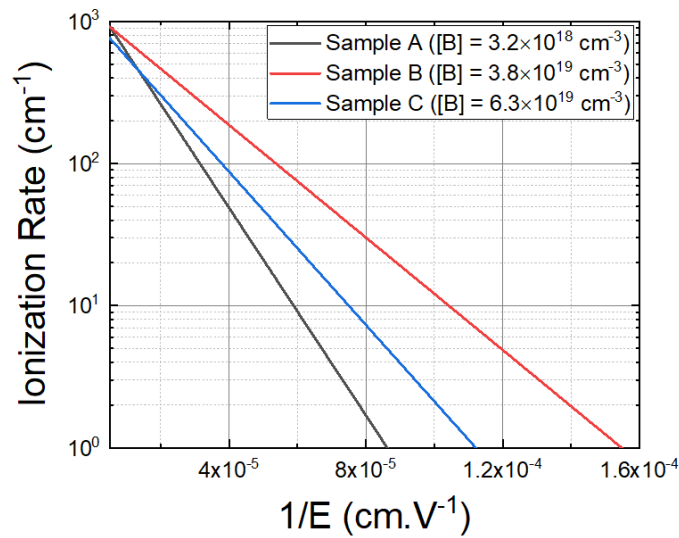


Figure 6.9: Ionization rate  $\alpha$  as a function of the reciprocal electric field.

The finite element simulated currents due to the III effect using the determined ionization rates are compared to the experimental I-V curves in Figure 6.7 (black lines). They reproduce correctly the exponential behavior of the current at low voltage, but are unable to reproduce its steep increase at high voltage, which is attributed to thermal runaway as indicated by TIM measurements.

### Impurity Impact Ionization (III) and Self-Heating Effect (SHE)

To model the SHE, we used temperature dependent thermal conductivity (see [215]) and volumetric heat capacity given respectively by

$$k_T(T) = k_T(300 \text{ K}) \left( \frac{T}{300} \right)^{-m} \quad (6.12)$$

with  $m = 1$ , and

$$c_V(T) = A_{c_V} + B_{c_V}T + C_{c_V}T^2 + \frac{D_{c_V}}{T^2} \quad (6.13)$$

The parameters  $A_{c_V}$ ,  $B_{c_V}$ ,  $C_{c_V}$ , and  $D_{c_V}$  were determined by fitting the experimental values of volumetric heat capacity as a function of the temperature from [237]. The heat generation  $H$  term is given by

$$H = (\vec{J}_n + \vec{J}_p) \cdot \vec{E} \quad (6.14)$$

where  $J_n$  and  $J_p$  are respectively the electron (negligible) and hole current density and  $E$  is the electric field. The concentration of donors is adjusted so that the simulated and experimental I-V curves have the same resistance between electrodes at low voltage. The resulting simulated I-V curves using a combination

of III and SHE satisfactorily model the experimental non-linear current increase and the NDR for all samples as shown on Figure 6.7 (blue lines).

In order to confirm the significant role of the III effect, I-V characteristics have been modeled using only SHE (see the red lines in Figure 6.7), i.e. without the III effect. Although the simulated characteristic fits correctly the initial linear part, the current increases at a lower rate compared to the experimental I-V characteristic. This result shows that SHE is not accountable alone for the observed I-V characteristic, even though it has a predominant effect at high electric field.

Figure 6.10a shows the evolution of the simulated hole concentration at  $t = 100$  ns as a function of voltage for samples A, B and C. The hole concentration exhibits super linear behavior, which is consistent with the I-V characteristics shown in Figure 6.7. Sample A shows a slowdown of the hole multiplication above 165 V, which can be attributed to saturation of the carrier velocity described in equation (6.6). Figure 6.10b shows the corresponding evolution of the maximum temperature as a function of the dissipated power. The temperature increases proportionally with the dissipated power for sample B and C. The temperature evolution in sample A on the other hand has a sub-linear behavior. The difference might be explained by the more dominant impact of saturation velocity in sample A due to the higher mobility of holes in this sample.

As mentioned previously, the empirical model presented by S. Kagamihara et al. [203] was used to calculate the hole mobility. The main condition for this model to be applicable is that the evolution of the mobility should be dominated by phonon scattering. In order to make sure this is true in the case of this study, the temperature and hole concentration from Figure 6.10a and Figure 6.10b were used to calculate the relaxation time, i.e. the time between scattering events, for

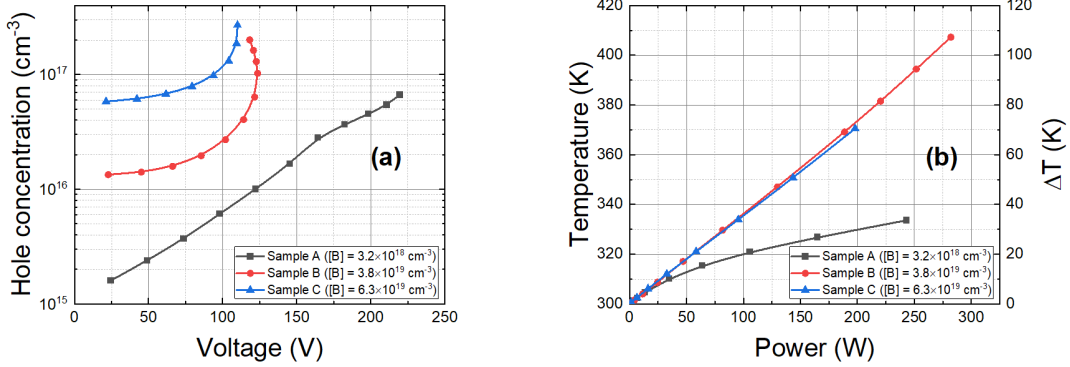


Figure 6.10: Simulated hole concentration as a function of voltage **(a)** and maximum temperature as a function of power **(b)** in samples A, B and C.

neutral impurity scattering, ionized impurity scattering, acoustic phonon scattering, and optical phonon scattering. The calculation was done for both the minimum and maximum power (i.e. the first and last point) of each simulated curve in Figure 6.10a and Figure 6.10b. The formulas used for the calculation are presented in the work of J. Pernot et al. [110], and D. M. Caughey and R. E. Thomas [220]. The results are presented in Table 6.4. The phonon scattering events have a relaxation time which is about four orders of magnitude smaller than the ones of neutral and ionized impurities for minimum and maximum power. It means that the evolution of the mobility is largely dominated by phonon scattering at low applied power but also for high power despite the increase in the number of ionized impurities due to III and SHE. It also confirms the validity of the mobility model used for the simulation.

Figure 6.11a and Figure 6.11b show respectively the simulated voltage and current waveforms for sample B for different values of  $V_{ch}$ . Figure 6.11c shows the corresponding evolution of the maximal temperature. For device voltages less than 110 V (i.e.  $V_{ch} < 125$  V), the voltage waveform is nearly flat over time, which is

Table 6.4: Relaxation times calculated for neutral impurity scattering ( $\tau_{NI}$ ), ionized impurity scattering ( $\tau_{II}$ ), acoustic phonon scattering ( $\tau_{AC}$ ), and optical phonon scattering ( $\tau_{OP}$ ) for samples A, B, and C for minimum and maximum applied power.

	Sample A	Sample B	Sample C
Relaxation Times (Minimum Power)			
<b>Neutral impurity</b> $\tau_{NI}$ (s)	$4.4 \times 10^{-7}$	$3.9 \times 10^{-8}$	$2.4 \times 10^{-8}$
<b>Ionized impurity</b> $\tau_{II}$ (s)	$8.4 \times 10^{-8}$	$2.3 \times 10^{-9}$	$1.1 \times 10^{-9}$
<b>Acoustic phonon</b> $\tau_{AC}$ (s)	$5.2 \times 10^{-12}$	$5.2 \times 10^{-12}$	$5.2 \times 10^{-12}$
<b>Optical phonon</b> $\tau_{OP}$ (s)	$1.5 \times 10^{-12}$	$1.5 \times 10^{-12}$	$1.5 \times 10^{-12}$
Relaxation Times (Maximum Power)			
<b>Neutral impurity</b> $\tau_{NI}$ (s)	$4.6 \times 10^{-7}$	$4.1 \times 10^{-8}$	$2.4 \times 10^{-8}$
<b>Ionized impurity</b> $\tau_{II}$ (s)	$6.0 \times 10^{-8}$	$3.4 \times 10^{-9}$	$1.4 \times 10^{-9}$
<b>Acoustic phonon</b> $\tau_{AC}$ (s)	$4.5 \times 10^{-13}$	$3.3 \times 10^{-13}$	$3.8 \times 10^{-13}$
<b>Optical phonon</b> $\tau_{OP}$ (s)	$7.5 \times 10^{-13}$	$2.5 \times 10^{-13}$	$4.1 \times 10^{-13}$

consistent with the assumption used for the calculation of the ionization rate  $\alpha$ , that the temperature has little influence on the shape of the I-V characteristic at low voltage. However, for higher initial device voltage (i.e.  $V_{ch} > 125$  V), the voltage is decreasing with time, due to thermal ionization of boron acceptor impurities, which decreases the resistivity of the sample during the pulse. For pulses with a starting voltage value over 200 V, the voltage value at the end of the pulse decreases when the starting voltage increases. On the other hand, in Figure 6.11b, the value of the current at the end of the pulse increases steadily when the loading DC voltage increases. The combination of the decrease of the instantaneous voltage and increase of the instantaneous current is responsible for the appearance of the NDR regime in sample B for high loading DC voltage visible in Figure 6.10b. A similar behavior is observed in experimental waveforms measured on sample B in Figure 6.1 and it is attributed to SHE, which causes an increase in temperature with time and with  $V_{ch}$ , evidenced by TIM measurements in Figure 6.3 and confirmed by

simulation in Figure 6.11c for sample B. The simulation shows that temperature reaches a maximum value of 407 K for  $V_{ch} = 237.5$  V.

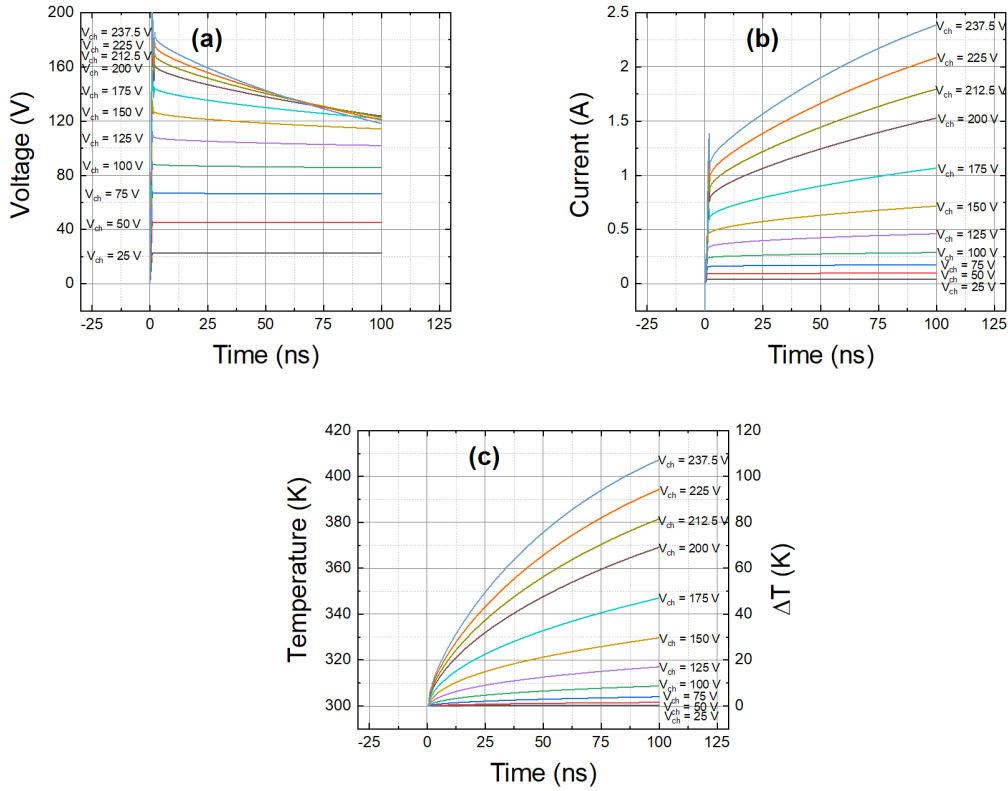


Figure 6.11: Simulated voltage (a), current (b) waveforms, and maximum temperature (c) in sample B for an increasing amplitude of  $V_{ch}$ .

Figure 6.12a shows the simulated temperature distribution for sample D under conditions similar to the ones used for TIM measurements in Figure 6.3c (i.e. for a current of 0.25 A) at  $t = 100$  ns for two different depths: black squares represent the surface temperature distribution and the red dots the temperature for a distance of  $10 \mu\text{m}$  from the surface. The vertical dashed lines represent the limits of the electrodes. Due to the stripe layout of samples used for TIM, in this case, the simulation was performed in 2-D rectangular geometry which

is still a good approach for the use of short pulses. One can observe that the surface temperature peaks at the right electrode edge (the ground electrode) with a maximum value of about 440 K. The temperature distribution in the depth is smeared. The phase shift distribution from the 2-D temperature profile was also calculated using equations in [186] and taking into account diamond thermo-optical coefficient from the work of V. Y. Yurov et al. [238]. In brief, the phase shift is the integral of temperature along the laser beam path weighted by the thermo-optical coefficient [185, 186]. The phase shift distribution at  $t = 100$  ns is plotted in Figure 6.12b. The peak phase shift value near 0.14 rad is within the experimental error to the experiment in Figure 6.3c. The calculated phase shift maximum in Figure 6.12b is also shifted toward the right electrode but is smeared due to significant temperature contribution from the bulk. This shift in the phase shift distribution is however not distinguishable in experiment in Figure 6.3c which can be attributed to experimental uncertainty [186] and/or model imperfection. Figure 6.12c shows the simulated temperature distribution for sample B (electrodes with cylindrical geometry) for a current of 2.4 A (i.e.  $V_{ch} = 237.5$  V) and give similar results to what was observed with sample D. The surface temperature peaks at the positive electrode with a maximum value of 407 K. This maximum is consistent with the temperature value for the same condition at the pulse end (see top curve in Figure 6.11c). The temperature distribution in the depth is smeared and the peak is shifted toward the middle of the inter-electrode gap.

The relatively good quantitative agreement between our experiments and simulations indicates that our model describes the charge transport quite satisfactorily. It means that hot carrier effects [239–242], like possible differences between hot hole and lattice temperature does not need to be included explicitly. In particular,

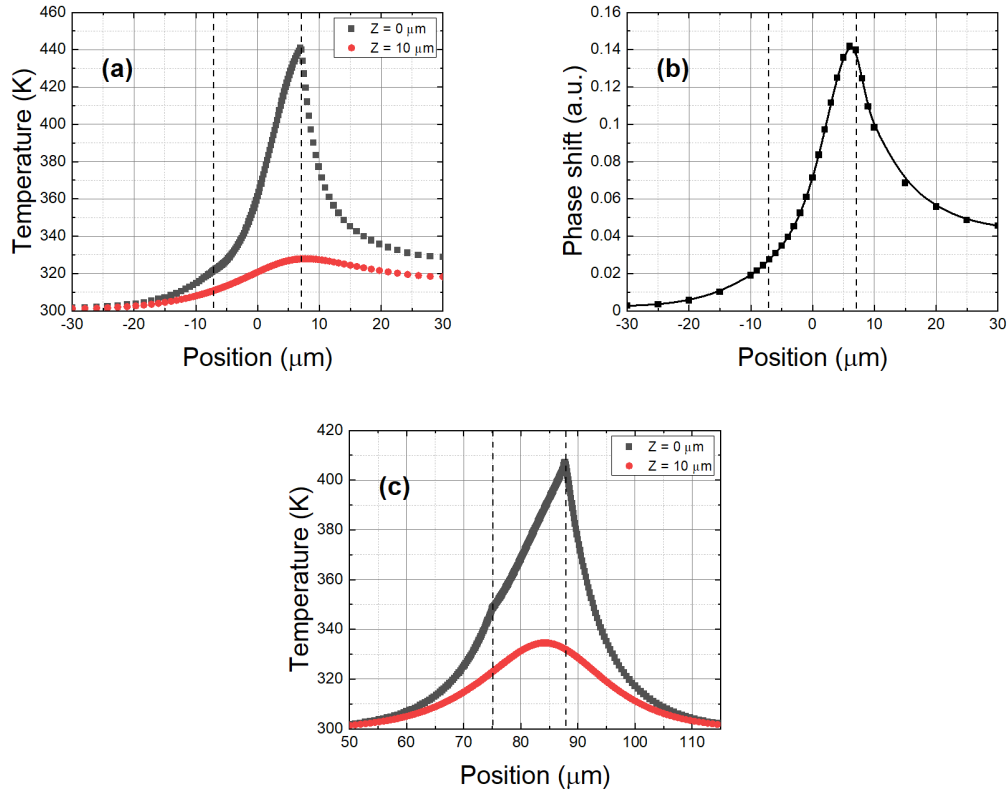


Figure 6.12: Simulated temperature (a) and phase shift (b) distribution along a scanning line perpendicular to the electrodes for sample D at a current of 0.25 A and temperature distribution for sample B at a current of 2.4 A ( $V_{ch} = 237.5 \text{ V}$ ) (c). The temperature is given at the surface of the sample ( $Z = 0 \mu\text{m}$ ) and for a depth of  $10 \mu\text{m}$  in the diamond ( $Z = 10 \mu\text{m}$ ). The time instant is  $t = 100 \text{ ns}$ .

the carrier thermalization (energy relaxation) time constant in diamond is in the order of tens of ps [242], which is much shorter than the time scale of 10-100 ns considered in this study. The hot carrier effects are, however, included implicitly in our model since impurity impact ionization and velocity saturation are in fact due to hot carriers.

## 6.4 Conclusion

The pulsed current-voltage I-V characteristics measured with the TLP setup on boron-doped diamond layers showed a non-linear multiplication of current and even a NDR regime when the applied voltage on the electrodes is high enough. TIM measurements revealed a thermal runaway phenomenon which can partially explain the current multiplication in the TLP measurements. The finite element method simulation, taking into account self-heating effect and III accurately reproduced the observed current multiplication and even NDR regime observed in the I-V characteristics measured on the boron-doped diamond layers.

## Chapter 7

# Phosphorus-Doped Diamond Layers

In this chapter, the growth of phosphorus-doped diamond layers and the interaction between  $\text{PH}_3$  and  $\text{CH}_4$  during PECVD diamond growth are discussed. In order to limit this interaction and improve the incorporation of phosphorus in diamond, a new growth method using pulsed  $\text{CH}_4$ , was developed and used to grow polycrystalline phosphorus-doped diamond layers. The gas dynamics in different MWPECVD reactors was also studied using OES. Finally, the grown layers were characterized by GDOES, SEM, and Raman spectroscopy.

## 7.1 Phosphorus-Doped Diamond Layer Growth

*(Results presented in [243])*

### 7.1.1 Interaction between PH<sub>3</sub> and CH<sub>4</sub> in a hydrogen plasma

The interaction between PH<sub>3</sub> and CH<sub>4</sub> was investigated by Optical Emission Spectroscopy (OES) in a lab-made NIRIM type reactor [49] presented in subsection 3.1.2. In this study, the MWPECVD reactor has been operated at constant total gas flow of 1000 sccm, pressure of 80 mbar, microwave power of 450 W. CH<sub>4</sub> (N5.5) was used as a source of carbon and PH<sub>3</sub> (N5.0, diluted at 6000 ppm in N5.6 H<sub>2</sub>) as a source of phosphorus dopant in a H<sub>2</sub> microwave plasma (N5.6).

Time-dependent OES measurements were carried out using an imaging spectrometer Jobin Yvon with 500 mm focal length and a 1200 g.mm<sup>-1</sup> diffraction grating (blazed 550 nm). The light was collected by an optic fiber placed perpendicularly through the microwave wave guide opening along the z-axis. Diffracted light was detected by a Peltier-cooled CCD detector (1024 × 512 pixels) over a spectral region from 200 nm to 800 nm. OES and optical path parameters were kept constant for all measurements.

Figure 7.1 shows the time-dependent variation of the intensity of the emission lines of the atomic hydrogen-alpha at 656.5 nm, atomic phosphorous at 253.5 nm, PH radical at 341.9 nm, and CH radical at 431.4 nm of a hydrogen-phosphine (16 ppm) plasma with a 1 sccm CH<sub>4</sub> pulse for one minute over a period of five minutes. The injection of CH<sub>4</sub> has an immediate effect on the chemistry of the plasma. The CH line intensity quickly increases while the PH and atomic phosphorus

intensities decreases rapidly. The phenomenon was already observed by Loabaev et al. [244] and it is attributed to the formation of methylphosphine [245] and methinophosphide [246] in the plasma which most likely do not participate in the synthesis of phosphorus-doped diamond. After the end of the  $\text{CH}_4$  pulse the CH, PH, and atomic phosphorus lines slowly recover the intensity they had before the  $\text{CH}_4$  pulse. When methane is injected, we observed a transient peak of the hydrogen-alpha line emission. Such an increase in hydrogen emission line has already been observed [247, 248], and it is due to the presence of carbon species. The decrease of the hydrogen-alpha line intensity is attributed to the reactions of carbon species with P species. The consumption of carbon species by the phosphorous species likely decreases the number of carbon species responsible for the increase of the hydrogen line intensity.

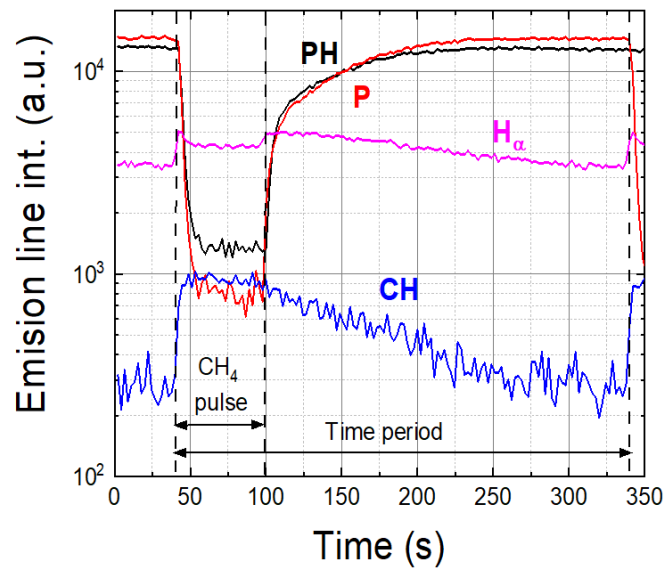


Figure 7.1: Time dependence of the intensity of the hydrogen-alpha, atomic phosphorus, PH radical, and CH radical optical emission lines during a period of five minutes with a one-minute-long  $\text{CH}_4$  pulsed injection [249]

Figure 7.2 compares the time variation of the emission line intensity of the CH radical with the intensity ratio of the PH radical and the CH radical emission lines. Assuming PH and CH radicals are representative of the species responsible for phosphorous incorporation and diamond growth, the optimal chemical composition of the plasma, that maximize phosphorous incorporation and diamond growth, are in the transient time after the methane flow is stopped. The inset of Figure 7.2 shows in a semi-log plot the exponential decay of the ratio of the PH and the CH lines intensity as a function of the varying CH line intensity after the methane flow is stopped. The exponential decay shows that diamond growth and phosphorous incorporation in diamond are antagonist processes with the addition of methane in the plasma.

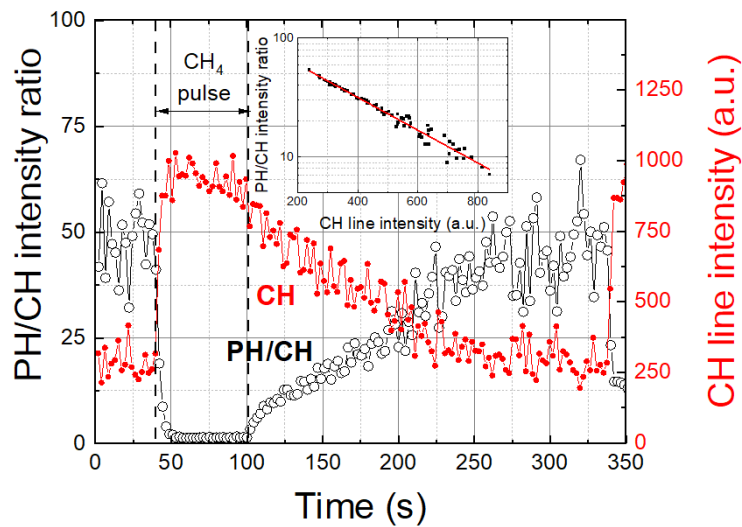


Figure 7.2: Comparison of the time dependence of the CH radical optical emission line intensity with the intensity ratio of the PH and CH radicals optical emission lines a period of five minutes of one-minute-long  $\text{CH}_4$  pulsed injection (Inset: Variation of the intensity ratio of the PH and CH radicals optical emission lines as a function of the CH radical optical emission line intensity) [249]

### 7.1.2 Growth Conditions

In order to reduce the unwanted cross reaction between carbon and phosphorous species shown in subsection 7.1.1 and therefore enhance the phosphorus incorporation ratio in the diamond layer during the MWPECVD growth, specific growth conditions using pulsed  $\text{CH}_4$  were tested. The pulsed  $\text{CH}_4$  regime was already investigated by G. Frangieh et al. [250] for the fabrication of diamond layers doped with arsenic with an incorporation ratio more than twice higher compared to conventional continuous growth procedure.

Polycrystalline undoped and phosphorus-doped diamond layers were grown on (100) p-type boron-doped polished Si substrates with a resistivity between  $2.5 \times 10^{-3}$  and  $4.0 \times 10^{-3} \Omega\cdot\text{m}$ . Those substrates were first cleaned in a piranha solution to remove organic residues from their surfaces. They were then rinsed in deionized water and cleaned in acetone and isopropyl alcohol in an ultrasonic bath. An aqueous seeding solution containing nano-diamonds [251] was spread on the surface of the substrates using a spin coater to ensure nucleation. The spin coater was set to run at 1500 rpm for 5 seconds followed by a 5 seconds acceleration phase and finally 3800 rpm for 30 seconds. Polycrystalline diamond layers were grown in a lab-made NIRIM type reactor using microwave plasma which is presented in subsection 7.1.1. Four series of five polycrystalline diamond layers were grown on Si substrates using pulsed or continuous  $\text{CH}_4$  and with or without  $\text{PH}_3$  (see Table 7.1 and Table 7.2).

During growths in pulsed  $\text{CH}_4$  flow mode, the  $\text{CH}_4$  gas line was open for 1 minute and then closed for 4 minutes in 5 minutes cycles. The  $\text{H}_2$  and  $\text{PH}_3$  gas lines were left open during the growth. The duration of a cycle was adjusted

Table 7.1: Growth conditions for undoped and phosphorus-doped polycrystalline diamond layers grown using a continuous and pulsed CH<sub>4</sub> gas flow

<b>CH<sub>4</sub> gas flow</b>	<b>Deposition time (h)</b>	<b>[CH<sub>4</sub>]/[H<sub>2</sub>] (%)</b>	<b>Total gas flow (sccm)</b>	<b>Substrate tempera- ture (°C)</b>	<b>[P]/[C]<sub>gas</sub> ratio (ppm)</b>
Continuous	6	0.10	1000	1000	0
Pulsed	6	0.25	1000	1000	0
Continuous	6	0.10	1000	1000	200000
Pulsed	6	0.25	1000	1000	200000

Table 7.2: Combinations of microwave power, pressure, and distance between substrate and plasma used for the growth of polycrystalline diamond layers

<b>MW Power (W)</b>	<b>Pressure (mbar)</b>	<b>Distance substrate/plasma (mm)</b>
280	30	3
370	50	14
500	70	20
640	90	23
780	110	26

to match the residency time of CH radicals in the reactor measured by Optical Emission Spectroscopy (OES) in Figure 7.1. The different microwave power and pressure conditions used in this work were chosen to keep the size of the plasma ball constant. The distance between the substrate and the center of the plasma ball was adjusted for each combination of pressure and microwave power to set the substrate's temperature at 1000 °C during the diamond growth [252]. The temperature was measured from the reactor top window using a Williamson Pro 92-38 dual-wavelength infrared pyrometer. The combinations of pressure, microwave power and distance between the substrate and the plasma used for diamond growth are detailed in Table 7.2.

### 7.1.3 Growth Rate Measurements

The thickness of the polycrystalline diamond layer was measured by profilometry in a groove formed in an unseeded line on the substrate. The measured growth rate (see Figure 7.3) decreases with the applied microwave power, and consequently with the distance between the substrate and the center of the plasma ball, for all the polycrystalline diamond layers. This phenomenon was already observed for both polycrystalline [253] and single crystal [254] diamond growth and is attributed to the decrease in the concentration of atomic hydrogen close to the substrate's surface. Both undoped and phosphorus-doped diamond layers grown using a pulsed CH<sub>4</sub> flow exhibit a larger variation of growth rate between low and high power compared to diamond layers grown using a continuous CH<sub>4</sub> flow. The growth rate at low power and using a pulsed CH<sub>4</sub> flow is higher than the one of layers grown in continuous flow of CH<sub>4</sub> despite an average lower CH<sub>4</sub> concentration in

the reactor. This difference might be attributed to an inhomogeneous distribution of carbon species in the reactor induced by the intermittent  $\text{CH}_4$  flow, with more carbon species being present in the vicinity of the plasma. The maximum growth rate recorded is  $440 \text{ nm}\cdot\text{h}^{-1}$  for a phosphorus-doped polycrystalline diamond layer grown at 280 W and 30 mbar using a pulsed flow of  $\text{CH}_4$ .

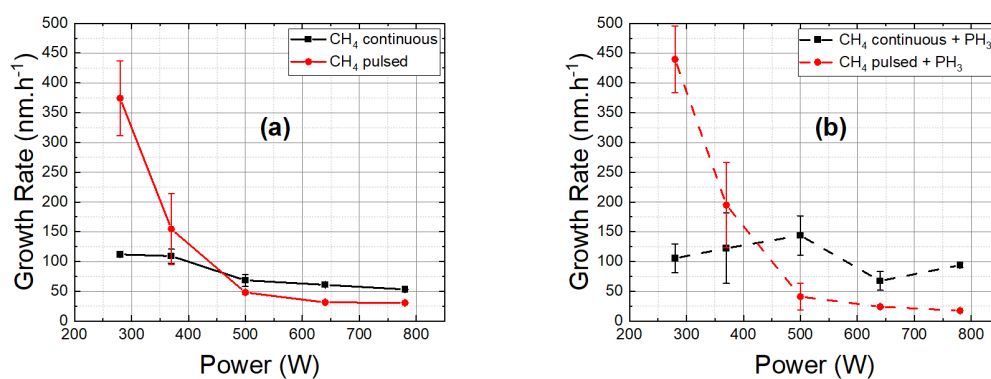
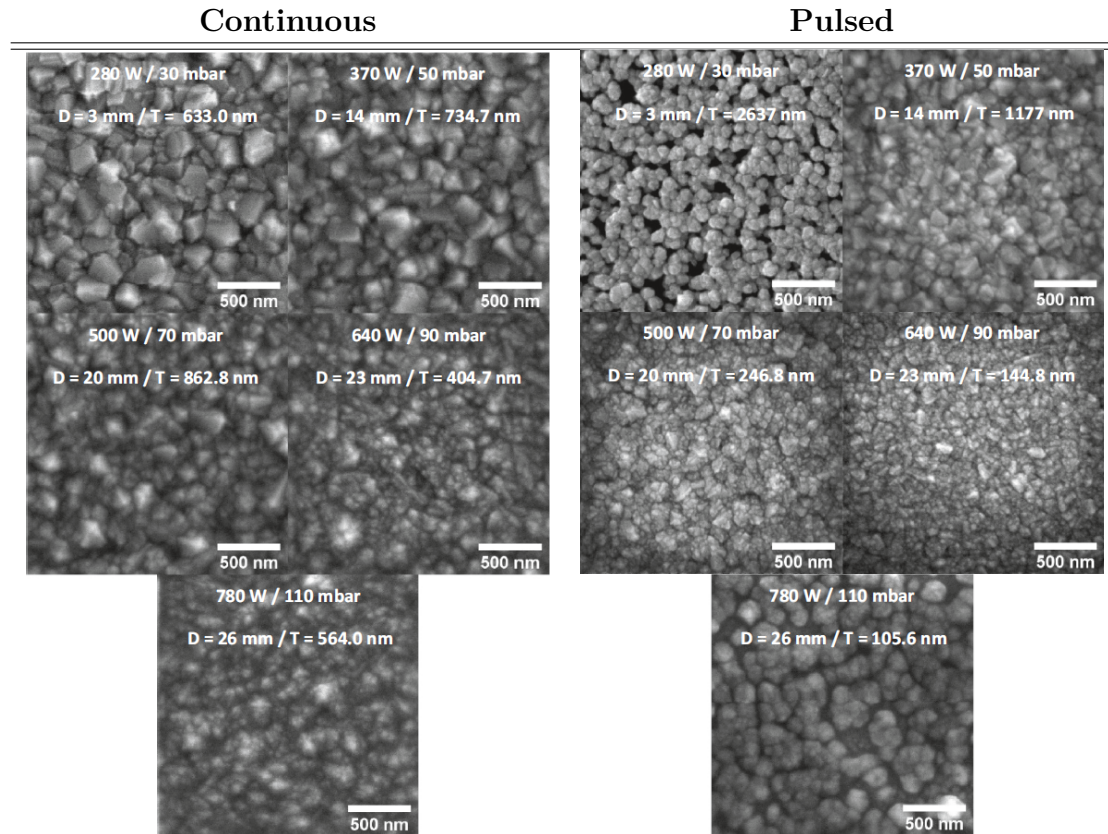


Figure 7.3: Growth rate for the different layers as a function of the microwave power for (a) intrinsic polycrystalline diamond layers and (b) phosphorus-doped polycrystalline diamond layers

### 7.1.4 Scanning Electron Microscopy (SEM) Imaging

SEM images of the phosphorus-doped diamond layers surface were made using the setup described in subsection 4.2.2. Well faceted diamond crystals are visible on the surface of the phosphorus-doped diamond samples grown using pulsed and continuous  $\text{CH}_4$  flow. The size of the diamond crystals increases (see Table 7.3) when the applied power and pressure decrease with the exception of the phosphorus-doped layer grown in pulsed gas conditions under 280 W and 30 mbar which has smaller crystals and gaps between the grains. The bigger diamond crystals observed at lower applied power and lower pressure are consistent with

Table 7.3: SEM images of diamond layers grown using continuous and pulsed flow of CH<sub>4</sub>, with a [P]/[C] ratio of 200000 ppm in the gas phase, for different values of pressure, microwave power, and distance D between the substrate's surface and the center of the plasma ball. T is the thickness of the deposited polycrystalline diamond layer



the higher growth rate but could also be attributed to a switch from diamond re-nucleation to lateral diamond growth at lower operating pressure [255]. The samples grown using continuous CH<sub>4</sub> flow have slightly larger crystals which are more uniform in size compared to samples grown in pulsed gas conditions. The growth conditions of 370 W and 50 mbar offers the best crystalline quality for the phosphorus-doped layers grown using the pulsed gas method with large diamond crystals which are homogeneous in size.

## 7.2 PECVD Reactors Time Responses

*(Results presented in [256])*

### 7.2.1 Time Response Measurement Presentation

In order to optimize the growth parameters for the deposition of phosphorus-doped diamond layers, particularly the duration of CH<sub>4</sub> pulses and the frequency at which they should be repeated, it is necessary to understand the gas dynamic of the MWPECVD reactors. We studied the dynamic response using different gases (N<sub>2</sub>, CH<sub>4</sub>, and O<sub>2</sub>) impulse in hydrogen plasma of two different MWPECVD reactors for different conditions of pressure and total gas flow. The MWPECVD reactors considered in this study are: the commercial reactor AX5010 from Seki Diamond Systems (presented in subsection 3.1.1) and a lab-made NIRIM type reactor (presented in subsection 3.1.2). The Seki and the NIRIM reactor used a total gas flow between 200 and 600 sccm and 200 and 1000 sccm respectively. Both reactors were operated at a pressure between 30 and 110 mbar. The limits of total gas flow and pressure range investigated in this work were chosen in accordance with the optimal operation conditions of each reactor. The main difference between the two reactors is their volume which is 1.4 L for the NIRIM system and 3.2 L for the Seki system.

The experimental time responses were recorded using the setup presented in section 3.2 and were then fitted using the impulse response equation proposed by H. Pendar et al. [257].

$$f(t) = \alpha t^m e^{-t/\tau} \quad (7.1)$$

where  $t$  is the time and  $\alpha$ ,  $m$ , and  $\tau$  are fitting parameters.  $\tau$  is the characteristic time of the exponential decay of the signal which dominates for large values of  $t$  while  $m$  characterizes the rising portion of the signal for small value of  $t$ . The curve reaches its maximum at  $t = \tau m$  with a maximum value of:

$$f(\tau m) = \alpha(\tau m)^m e^{-m} \quad (7.2)$$

### 7.2.2 Time Response Measurement Results

Figure 7.4a shows the evolution of the emission spectra as a function of time upon the injection of a N<sub>2</sub> gas pulse for a total gas flow of 200 sccm and a pressure of 110 mbar in the NIRIM reactor. At  $t = 0$  s, N<sub>2</sub> is released into the reactor chamber and the intensity of the emission line of NH increases before gradually decreasing as the gas species are removed from the reactor by the pumping system. Figure 7.4b shows the dynamic pulse responses to a N<sub>2</sub> gas pulse in a pure hydrogen plasma recorded on the NIRIM reactor for different total gas flows and a pressure of 110 mbar. The time position of maximum intensity,  $\tau m$ , is indicated on the figure for the signal recorded with a total gas flow of 200 sccm. The normalized intensity of the emission line of NH was recorded as a function of time with the spectrometer and fitted using equation (7.1) which offers a good fit to the experimental curves. The rising and decay times become shorter when the total gas flow increases which is consistent with a faster circulation of gases in the reactor.

Figure 7.5a shows the evolution of the parameter  $\tau$  in the Seki reactor as a function of total gas flow and pressure for a pulse of N<sub>2</sub>. Data points of the same color were recorded at the same total gas flow. The parameter  $\tau$ , which reflects

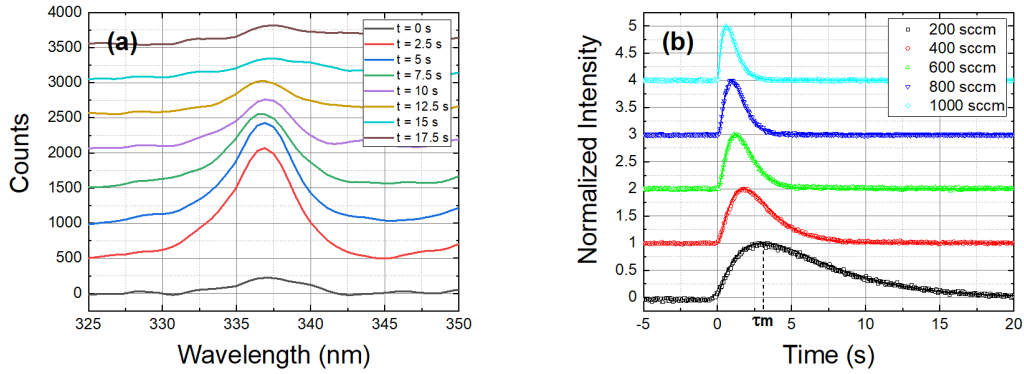


Figure 7.4: Evolution of **(a)** the emission spectra as a function of time upon the injection of a N<sub>2</sub> gas pulse for a pressure of 110 mbar and a total gas flow of 200 sccm and **(b)** experimental normalized intensity of the NH emission line (336.9 nm) as a function of time upon the injection of a N<sub>2</sub> gas pulse (dots) and fitting curves (solid lines) measured on the NIRIM reactor for a pressure of 110 mbar and different total gas flows. For better readability, each curve is separated by an offset of 500 counts in **(a)** and 1 arb. unit in **(b)**

the residency time of the precursor species inside the reactor, decreases with the total gas flow. This behavior is consistent with what was observed in Figure 7.4, a higher flow rate increases the circulation speed of gas in the reactor and decreases the residency time of precursor species. The parameter  $\tau$  also increases with the pressure. Indeed, an increase in pressure translates to an increase in the quantity of gas molecules present in the reactor, therefore, for a same total gas flow, it will take longer to remove the precursor specie from the chamber. The following equation was used to fit the evolution of the parameter  $\tau$  as a function of the total gas flow and the pressure:

$$\tau = \frac{kP}{F} \quad (7.3)$$

Where  $P$  is the pressure in mbar,  $F$  is the total gas flow under standard

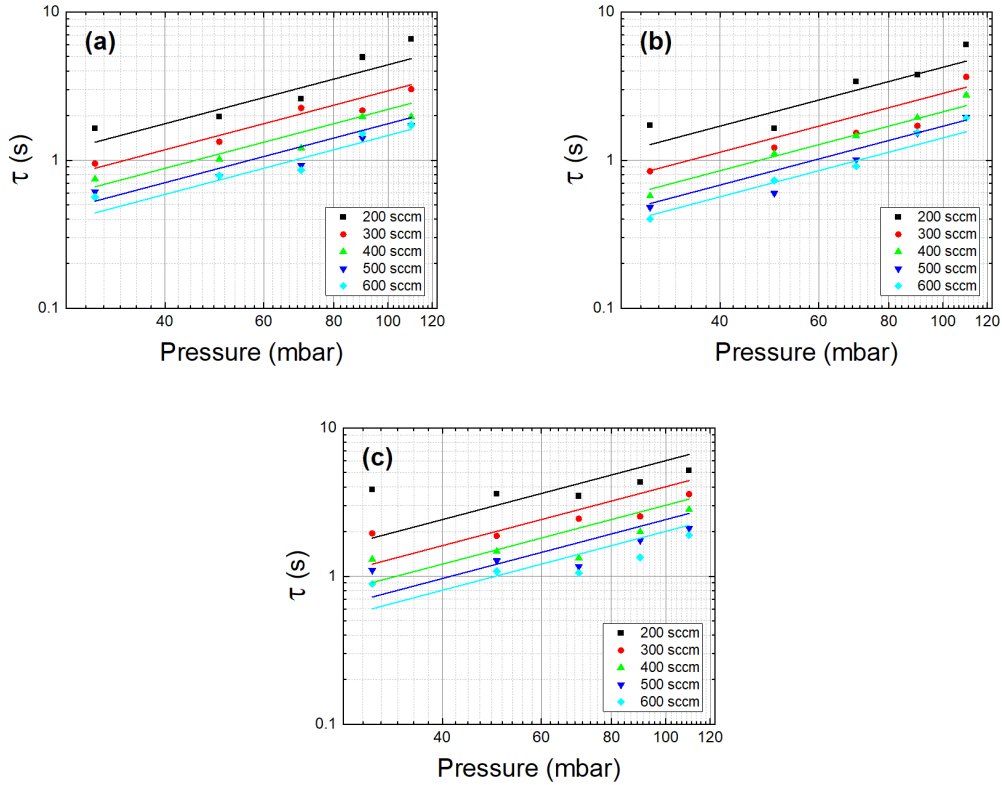


Figure 7.5: Parameter  $\tau$  as a function of the total gas flow and the pressure in the Seki reactor for a pulse of (a)  $\text{N}_2$ , (b)  $\text{CH}_4$ , and (c)  $\text{O}_2$ . The solid lines represent fitting curves given by equation 7.3

conditions of pressure and temperature ( $P_0 = 1.01$  bar and  $T_0 = 20$  °C), and  $k$  is a constant. The parameter  $k$  was obtained by averaging the value of  $\frac{\tau F}{P}$  over each condition of pressure and total gas flow used in the OES measurement. The calculated values of  $k$  are summarized in Table 7.4. In Figure 7.5a, the fitting curves represented by the solid lines are given by equation (7.3) with  $k = 1.47 \times 10^{-4}$  L.mbar $^{-1}$  which matches well the evolution of  $\tau$ . This result is consistent with the simple impulse response model presented by G. A. Bartholomew et al. [258], where the value of  $\tau$  is given by:

Table 7.4: Fitting parameters  $k$  and  $k'$  and the calculated error on their value

Reactor type	Gas	$k$ (L.mbar <sup>-1</sup> )	$k$ error (%)	$k'$ (L.mbar <sup>-1</sup> )	$k'$ error (%)
Seki	N <sub>2</sub>	$1.47 \times 10^{-4}$	17.2	$9.88 \times 10^{-5}$	23.8
	CH <sub>4</sub>	$1.41 \times 10^{-4}$	17.8	$9.29 \times 10^{-5}$	20.0
	O <sub>2</sub>	$2.01 \times 10^{-4}$	36.4	$9.82 \times 10^{-5}$	14.6
NIRIM	N <sub>2</sub>	$6.82 \times 10^{-5}$	25.4	$1.36 \times 10^{-4}$	30.5
	CH <sub>4</sub>	$6.04 \times 10^{-5}$	25.5	$1.13 \times 10^{-4}$	19.8
	O <sub>2</sub>	$1.01 \times 10^{-4}$	67.0	$2.33 \times 10^{-4}$	66.4

$$\tau = \frac{V}{\dot{V}} = \frac{VP}{P_0 F} \quad (7.4)$$

Where  $V$  is the volume of the chamber,  $\dot{V}$  is the gas flow rate, and  $P_0$  is the standard pressure. Figure 7.5b and Figure 7.5c present the results of similar experiments done on the Seki system for a pulse of CH<sub>4</sub> and O<sub>2</sub> respectively. The evolution of the parameter  $\tau$  is close to what was observed for N<sub>2</sub> with  $k = 1.41 \times 10^{-4}$  L.mbar<sup>-1</sup> for CH<sub>4</sub> and  $k = 2.01 \times 10^{-4}$  L.mbar<sup>-1</sup> for O<sub>2</sub>.

Figure 7.6 shows the evolution of  $\tau m$ , the time to reach the peak intensity of the dynamic pulse response, as a function of the total gas flow in the Seki reactor. The position of the maximum intensity is inversely proportional to the total gas flow which can be attributed to the higher circulation speed of gas species in the reactor at higher flow rate. The time to reach the maximum intensity increases with the pressure which can be explained by the additional collisions between gas molecules which slow down the diffusion of the gas in the reactor when the pressure increases. A similar equation to equation 7.3 was used to fit the experimental values of  $\tau m$ :

$$\tau m = \frac{k'P}{F} \quad (7.5)$$

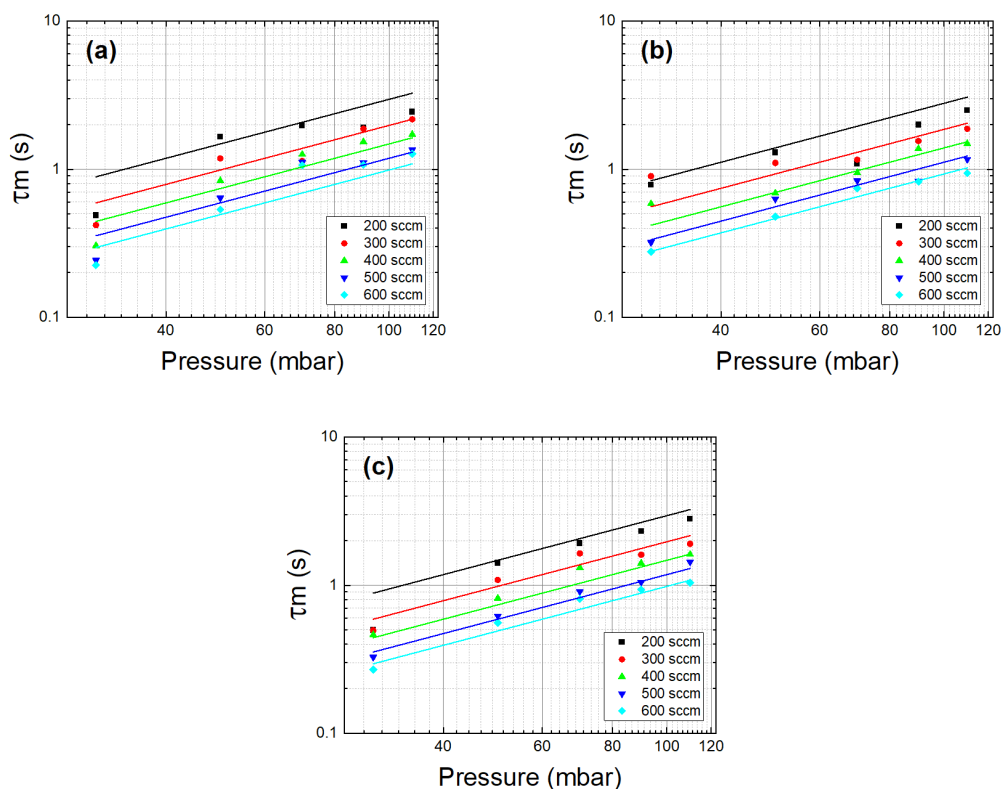


Figure 7.6: Time position of the peak intensity of the dynamic pulse responses  $\tau m$  as a function of the total gas flow and the pressure in the Seki reactor for a pulse of (a)  $\text{N}_2$ , (b)  $\text{CH}_4$ , and (c)  $\text{O}_2$ . The solid lines represent fitting curves given by equation (7.5)

Where  $P$  is the pressure in mbar,  $F$  is the total gas flow under standard conditions of pressure and temperature, and  $k'$  is a constant. The parameter  $k'$  was obtained using the same method used to obtain  $k$  in equation (7.3). The calculated values of  $k'$  are summarized in Table 7.4. This equation offers a good fit of the value of  $\tau m$  for the measurements done with  $\text{N}_2$ ,  $\text{CH}_4$ , and  $\text{O}_2$  with a  $k'$  of  $9.88 \times 10^{-5} \text{ L.mbar}^{-1}$ ,  $9.29 \times 10^{-5} \text{ L.mbar}^{-1}$ , and  $9.82 \times 10^{-5} \text{ L.mbar}^{-1}$  respectively. In general, the values of  $k$  and  $k'$  are similar for all three gases.

Similar measurements were done in the NIRIM reactor. Equation (7.3) and (7.5)

fit well the evolution of the parameter  $\tau$  and the position of the time to reach the peak intensity  $\tau m$  respectively for pulses of  $N_2$  and  $CH_4$  as shown in Figure 7.7 and Figure 7.8. The intensity of the  $C_2$  line could not be measured for a pressure below 70 mbar because the signal was too weak. In the case of  $O_2$ , equation (7.3) and (7.5) don't match well the evolution of the  $\tau$  and  $\tau m$  respectively. Figure 7.9 shows the dynamic response of the NIRIM system to a pulse of  $O_2$  for a pressure of 110 mbar and a gas flow of 800 sccm. Shortly after the gas pulse is released at  $t = 0$  s, a sharp peak in the signal is observed at  $t = 0.6$  s which interferes with the dynamic response. The origin of this parasitic signal is not fully understood but could be attributed to the reaction between  $O_2$  and phosphorous impurities deposited on the walls of the NIRIM reactor chamber during previous phosphorus-doped diamond growth.

Figure 7.10 shows the evolution of the fitting parameter  $k$  as a function of the volume of the reactors for an injection of  $N_2$ ,  $CH_4$ , and  $O_2$ . The parameter  $\tau$  increases with the volume of the reactor which can also be attributed to the larger quantity of gas molecules present in the reactor at larger volume. In equation (7.4) proposed by Bartholomew et al. [258], the parameter  $\tau$  is proportional to the volume of the chamber in which the gas is injected. Even though it is not possible to confirm this result with measurements from only two different reactors, the results presented in Figure 7.10 are in agreement with equation (7.4).

### 7.2.3 MWPECVD Reactor Response Simulation

Using linear system theory, it is possible to determine the time response of the reactors to an arbitrary shaped gas flow input from its pulse response [259, 260].

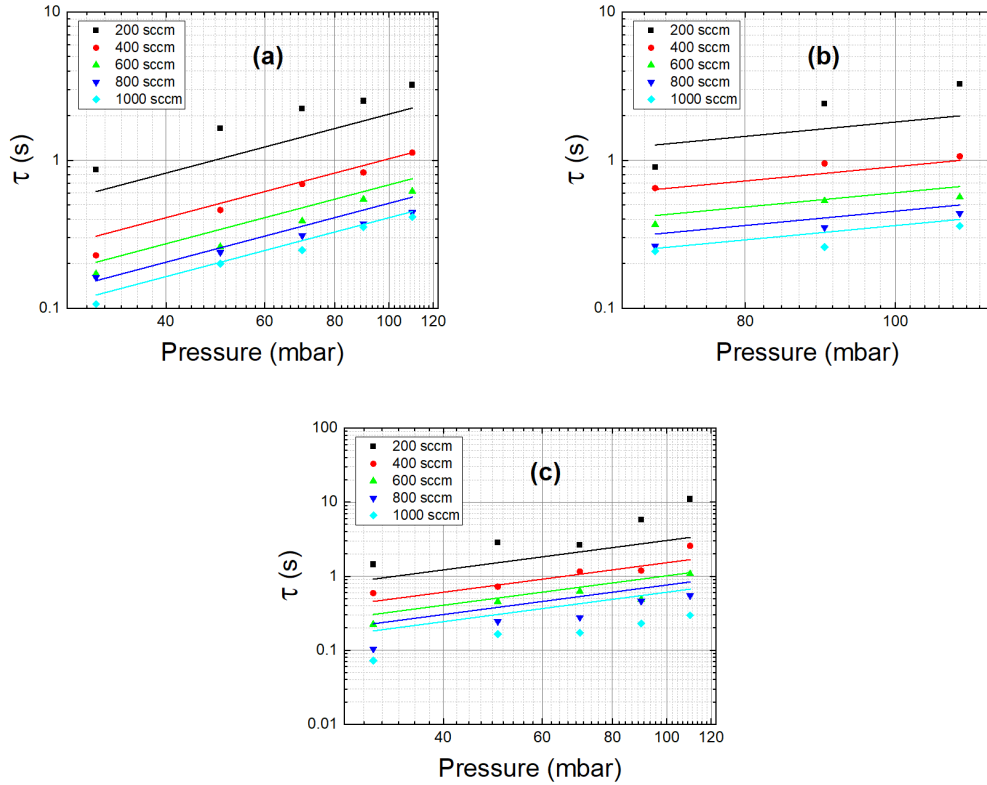


Figure 7.7: Parameter  $\tau$  as a function of the total gas flow and the pressure in the NIRIM reactor for a pulse of **(a)**  $\text{N}_2$ , **(b)**  $\text{CH}_4$ , and **(c)**  $\text{O}_2$ . The solid lines represent fitting curves given by equation (7.3)

The dynamic response is given by the convolution between the arbitrary input signal  $u(t)$  and the impulse time response of the reactor  $h(t)$  :

$$c(t) = \int_0^t u(\tau)h(t - \tau)d\tau \quad (7.6)$$

In order to test this model, the experimental time response of the NIRIM reactor to a one-minute-long, square shaped flow of  $\text{N}_2$  with an amplitude of 2 sccm, injected into the hydrogen plasma using a MKS mass flow controller, was recorded using the Stellarnet BLACK-Comet-SR compact spectrometer. For this experiment,

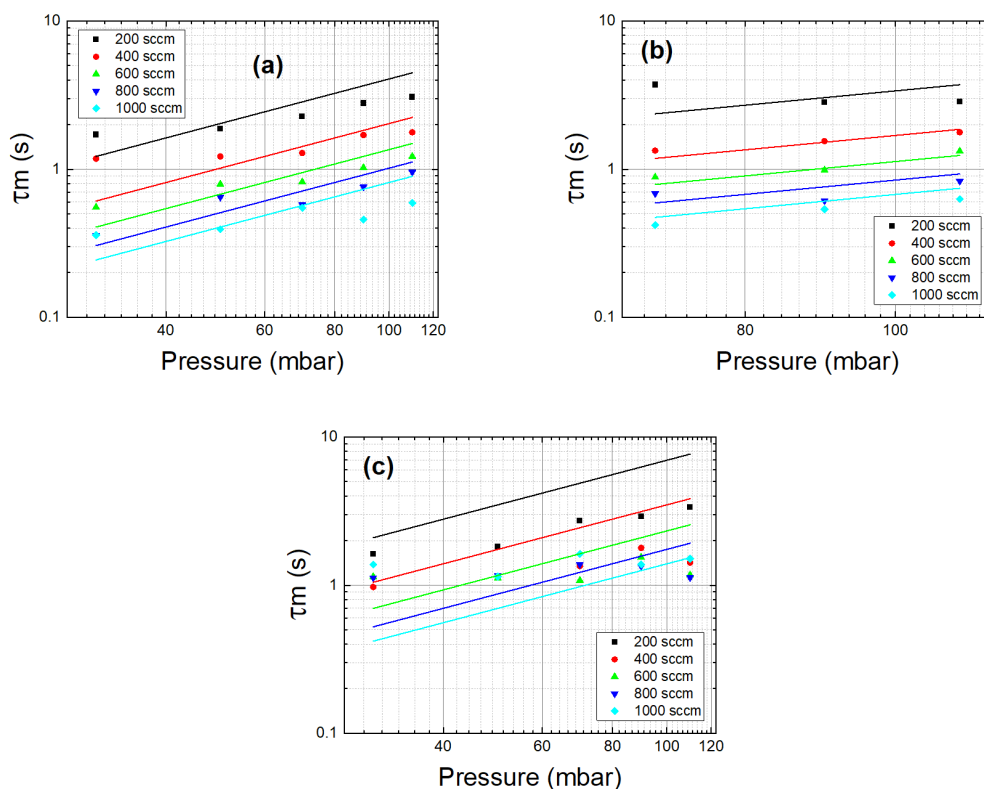


Figure 7.8: Time position of the peak intensity of the dynamic pulse responses  $\tau m$  as a function of the total gas flow and the pressure in the NIRIM reactor for a pulse of (a)  $\text{N}_2$ , (b)  $\text{CH}_4$ , and (c)  $\text{O}_2$ . The solid lines represent fitting curves given by equation (7.5)

the pressure in the reactor chamber was set to 70 mbar and a total gas flow of 200 sccm was used. This experimental signal was then compared to the calculated dynamic response obtained using equation (7.1), the impulse response (7.6), and the fitting parameters  $\tau$  and  $m$  from Figure 7.7 and 7.8. The experimental and calculated responses are presented in Figure 7.11. The calculated response offers a good fit to the experimental data. The discrepancy observed in the rising part of the curve is attributed to the slow response time of the mass flow controller which can be up to 750 ms.

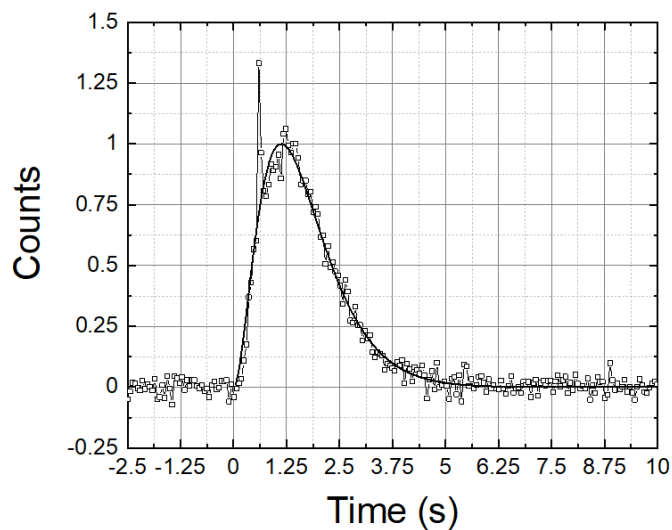


Figure 7.9: Experimental dynamic response to a O<sub>2</sub> gas pulse (connected dots) and fitting curves (solid lines) measured on the NIRIM reactor for a pressure of 110 mbar and a total gas flow of 800 sccm

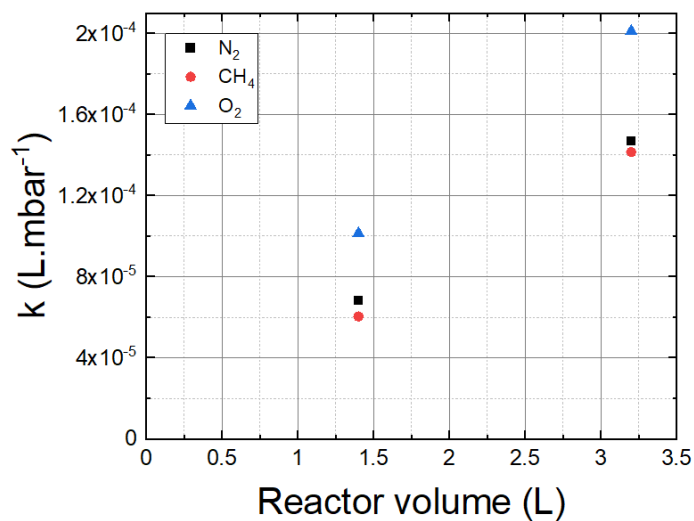


Figure 7.10: Fitting parameter  $k$  in equation 7.3 as a function of the volume of the reactors for an injection of N<sub>2</sub>, CH<sub>4</sub>, and O<sub>2</sub>

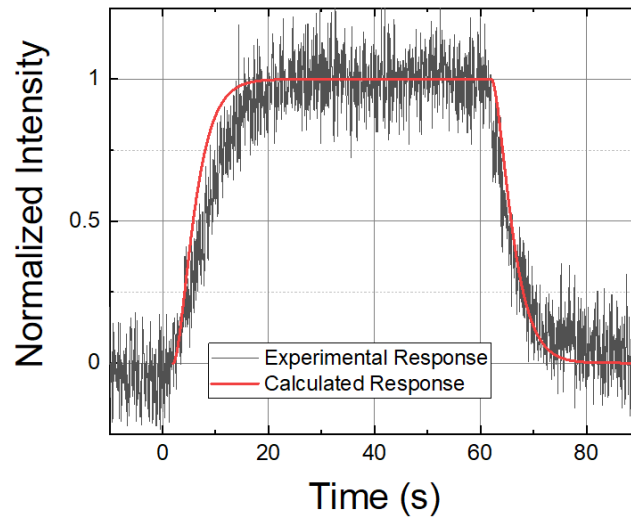


Figure 7.11: Recorded and calculated response of the NIRIM reactor to a one-minute-long, square shaped flow of  $N_2$  with an amplitude of 2 sccm using a pressure of 70 mbar and a total gas flow of 200 sccm

Using this method, it is possible to predict the residency time of precursor species in the reactor, which is a crucial parameter for the optimization of the growth conditions when using MWPECVD with pulsed gas flow as presented in section 7.1.

## 7.3 Phosphorus-Doped Diamond Layers Characterization

*(Results presented in [243])*

### 7.3.1 Raman Spectroscopy Measurement

Raman spectroscopy measurements were performed on the phosphorus-doped diamond layers using the setup presented in subsection 4.8.2 in order to assess the crystalline quality of the layers. Figure 7.12 shows the Raman spectra of undoped and phosphorus-doped polycrystalline diamond layers grown at 370 W and 50 mbar. All the spectra exhibit a sharp peak around  $1330\text{ cm}^{-1}$  which is attributed to the diamond ZCP line which is characteristic of diamond. For both polycrystalline undoped diamond layers, the ZCP line is centered at  $1333\text{ cm}^{-1}$  while a shift to lower wavenumber values is observed for phosphorus-doped layers grown using a continuous and a pulsed flow of  $\text{CH}_4$ , centered at  $1331.6\text{ cm}^{-1}$  and  $1330.1\text{ cm}^{-1}$  respectively. This observation is consistent with the results obtained by M. Mermoux et al. [197] on (111) epitaxial phosphorus-doped diamond layers.

Both phosphorus doping and the pulsed  $\text{CH}_4$  injection during the growth result in an increase of intensity of the "non-diamond" band centered around  $1520\text{ cm}^{-1}$  [195]. In particular, the spectrum of the undoped layer grown using a pulsed  $\text{CH}_4$  flow shows the appearance of a prominent band centered around  $1480\text{ cm}^{-1}$  which is attributed to C-H bending and transpolyacetylene [194], while the G-band, attributed to graphite, is also visible around  $1600\text{ cm}^{-1}$  [195, 261].

The  $\text{sp}^3/\text{sp}^2$  ratio calculated from Raman spectra [195] (see Figure 7.13) also shows that with the addition of  $\text{PH}_3$ , the concentration of non-diamond carbon

species increases in the polycrystalline diamond layers grown in both continuous and pulsed  $\text{CH}_4$  flows. To a lesser extent, the use of pulsed  $\text{CH}_4$  conditions during the diamond growth also increases the fraction of non-diamond carbon species in the polycrystalline layers compared to continuous  $\text{CH}_4$  conditions. Overall, all layers have a quality factor above 75%.

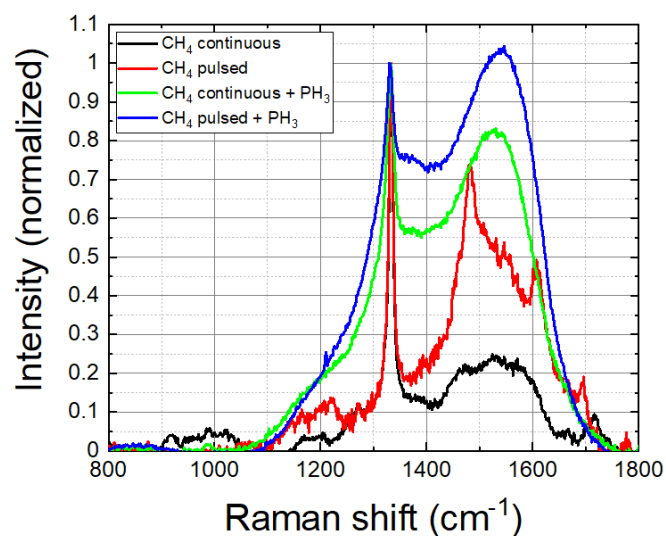


Figure 7.12: Raman spectra of layers grown under 370 W and 50 mbar using the diamond ZCP peak as a reference value for normalization

### 7.3.2 Glow Discharge Optical Emission Spectroscopy Measurement

The phosphorus concentration in the doped diamond layers grown using continuous and pulsed  $\text{CH}_4$  flow were determined using the GDOES setup described in subsection 4.4.2. The results are presented in Figure 7.14. The estimated combined standard uncertainty of the phosphorus analysis was about 10 to 20% (relative),

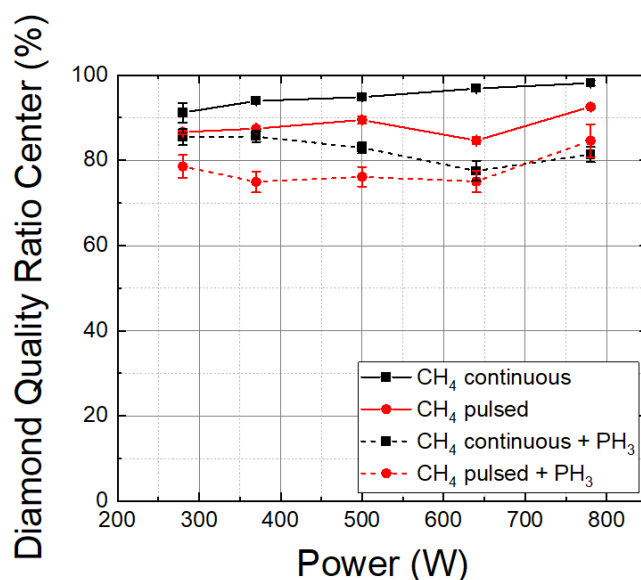


Figure 7.13:  $sp^3/sp^2$  ratio calculated from Raman spectra measured on the different series of samples

whilst its major component was the uncertainty of the calibration model [177]. The estimated random uncertainty of the phosphorus content is by an order of magnitude lower. Hence, prospective error of the results shown in Figure 7.14 would be largely a systematic one, i.e. the same bias for all the results presented, on relative basis.

The doped polycrystalline diamond layers grown using pulsed  $CH_4$  have a phosphorus content at least twice as high as the ones grown using continuous gas flow which is comparable with the results obtained by G. Frangieh et al. [250] using a similar growth method for the production of arsenic-doped diamond. The maximum phosphorus concentration recorded is  $7.1 \times 10^{20} \text{ cm}^{-3}$  which is remarkably higher than the maximum phosphorus incorporation of  $5.0 \times 10^{20} \text{ cm}^{-3}$  reported in nano-crystalline diamond layers [262]. The higher phosphorus concentration in layers grown in pulsed  $CH_4$  flow is coincident with the lower quality factor.

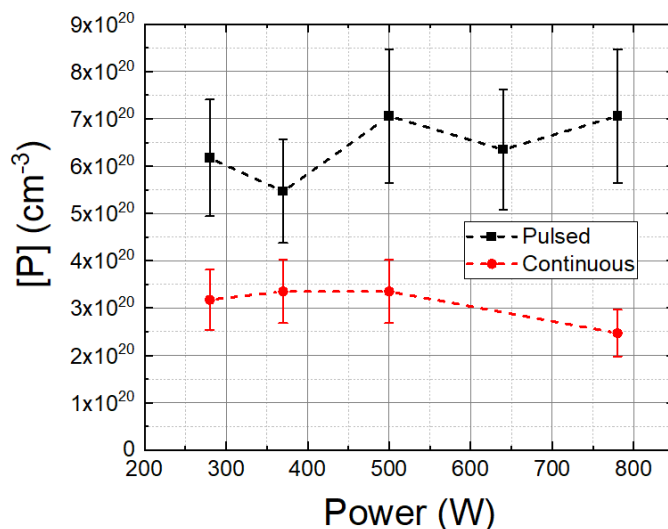


Figure 7.14: Phosphorus content calculated from GDOES measurements for phosphorus-doped diamond layers grown using continuous and pulsed flow of  $\text{CH}_4$

Phosphorus atoms distort the diamond lattice and cause the apparition of defects in the diamond crystals when they are incorporated due to their larger size compared to carbon [263, 264]. Therefore, the deterioration in crystalline quality observed for doped polycrystalline diamond layers grown in pulsed  $\text{CH}_4$  flow is consistent with their higher incorporation of phosphorus compared to samples grown in a continuous flow of  $\text{CH}_4$ . Figure 7.15 shows the atomic fractions for P, C, Si, and B as a function of time recorded by GDOES on two phosphorus-doped polycrystalline diamond layers grown at 370 W and 50 mbar using a continuous and a pulsed flow of  $\text{CH}_4$ . The time coordinate on the x-axis is not proportional to the depth in the sample as the sputtering rate  $q$  is about ten times higher for Si compared to diamond. Scaling factors, specified in the legend, were applied to the atomic fractions to match the ordinate scaling. As expected, the concentration of P goes

down to zero in the Si substrate. The atomic fraction of P is also inhomogeneous in the depth of the layer when pulsed  $\text{CH}_4$  conditions are used for the growth and it reaches its maximum at the interface between the polycrystalline diamond layer and the Si substrate. H. Spicka et al. [265] attributed the maximum phosphorus incorporation at the interface between the diamond layer and the substrate to the incorporation of phosphorus in grain boundaries as it is the case for B atoms [205] because of impurity segregation. In the early growth stage, diamond crystals are smaller which results in a larger grain boundary area and a potential higher phosphorus incorporation. However, W. Janssen et al. [266] also demonstrated the incorporation of P atoms in substitutional sites in polycrystalline diamond using cathodoluminescence while obtaining a phosphorus incorporation profile similar to the one shown in Figure 7.15b.

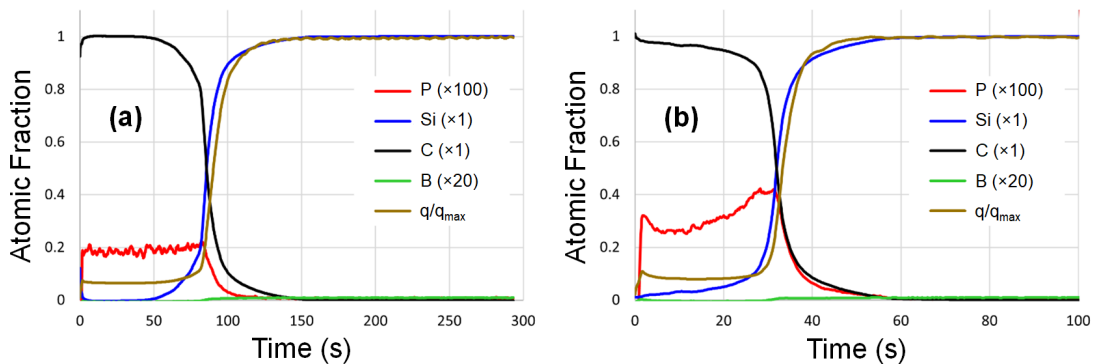


Figure 7.15: Atomic fraction recorded as a function of time using GDOES for two phosphorus-doped diamond layers grown under 370 W and 50 mbar of pressure in (a) continuous and (b) pulsed  $\text{CH}_4$  injection. The numbers between parentheses are scaling factors and  $q$  is the sputtering rate as resulting from the quantification algorithm described in reference [177]

The pulsed  $\text{CH}_4$  method was also experimented to grow phosphorus-doped

diamond layers on single crystal diamond substrates. A multilayer phosphorus-doped diamond layer was grown on a (111)-oriented diamond substrate using both continuous and pulsed  $\text{CH}_4$  flow and different  $\text{PH}_3$  concentration in the gas phase [249]. Preliminary results show an increase in the incorporation of phosphorus up to 90% compared to layers obtained using a continuous  $\text{CH}_4$  flow and a maximum phosphorus content in the layer up to  $6.0 \times 10^{20} \text{ cm}^{-3}$  which is also higher than the maximum phosphorus incorporation of  $2.2 \times 10^{20} \text{ cm}^{-3}$  previously reported on (111)-oriented diamond crystals [267]. The further development of phosphorus doping on single crystal diamond using pulsed  $\text{CH}_4$  would also allow electrical characterization such as Hall effect or TLP measurements and could be compared to results already obtained on epitaxial boron-doped diamond layers. This type of measurement couldn't be carried out on phosphorus-doped polycrystalline diamond layers because of the conductive nature of the Si substrate. Other substrates such as fused silica were investigated but the poor adhesion of the diamond layer made them unusable.

## 7.4 Conclusion

The phosphorus-doped diamond layers grown using the pulsed  $\text{CH}_4$  method have a phosphorus incorporation at least twice higher compared to layers grown using a continuous  $\text{CH}_4$  flow while retaining a good crystalline quality. In order to better understand the gas dynamics during the diamond growth using pulsed  $\text{CH}_4$ , the response of the Seki (see subsection 3.1.1) and NIRIM (see subsection 3.1.2) reactors to short pulse of  $\text{N}_2$ ,  $\text{CH}_4$ , and  $\text{O}_2$  was recorded by OES. It was found that the residency time of the precursor species decreases with the total flow rate

and increases with the pressure. Using linear system theory, it was also possible to predict the response of a reactor to an arbitrary shapes gas flow input from its pulse response. Finally, the pulsed gas growth method was also experimented for the growth of single crystal phosphorus-doped diamond on a (111)-oriented diamond substrate. Preliminary results show an improvement in phosphorus incorporation similar to what was observed on polycrystalline diamond layers.

# Conclusion and Perspectives

## Conclusion

In this thesis, the electronic properties of boron-doped diamond layers grown by MWPECVD were studied under high electric field. A TLP generator was specifically developed as part of this work in order to record quasi-static I-V characteristics at high voltage without damaging the test devices. The recorded I-V curves showed a characteristic super-linear behavior which ultimately leads to a breakdown. Additionally, the dissipation of thermal energy in the diamond was studied using TIM, revealing a non-uniform temperature distribution between the electrodes at high electric fields attributed to thermal runaway which could explain the super-linear behavior of the I-V curves.

In order to have a better understanding of the physics behind the characteristic shape of the recorded I-V curves, the experimental results were simulated using finite element method. A proper fit of the experimental data was obtained considering thermal effects, as suggested by TIM measurements, and III [218]. The super-linear I-V behavior at low currents and electric field is attributed to III whereas the I-V shape with NDR at high currents and electric field can only be explained by additional SHE.

With the objective of conducting similar electrical characterization on n-type diamond layers, the growth of phosphorus-doped diamond was also studied. In order to improve the low phosphorus incorporation in diamond, a new growth method involving pulsed injection of  $\text{CH}_4$  during the growth by MWPECVD was developed. Highly phosphorus-doped polycrystalline diamond layers were grown on (100)-oriented Si substrates using both pulsed and continuous injection of  $\text{CH}_4$ . Despite the addition of  $\text{PH}_3$ , all layers had a good crystalline quality with a  $\text{sp}^3/\text{sp}^2$  carbon ration determined by Raman spectroscopy over 75%. Most importantly, GDOES measurements revealed a improvement of the phosphorus incorporation by a factor 2 for layers grown using pulsed  $\text{CH}_4$  injection compared to continuous injection and a maximum phosphorus concentration of  $7.1 \times 10^{20} \text{ cm}^{-3}$  was obtained which is higher than the maximum value previously reported in nanocrystalline diamond layers [262]. The pulsed gas growth method was also tested for the growth of single crystal phosphorus-doped diamond on a (111)-oriented diamond substrate resulting in an improvement of the phosphorus incorporation compared to growth conditions using continuous gas flow and a maximum phosphorus concentration in the layer of  $6.0 \times 10^{20} \text{ cm}^{-3}$ .

## Perspectives

In outlook, the growth conditions of the gas pulsed PECVD method will be optimized using the temporal parameters extracted from the dynamic gas pulse response analysis of the MWPECVD reactors. The goal will be to produce highly phosphorus-doped single crystal diamond which could then be electrically characterized using the TLP generator and Hall effect measurement.

The thesis thereby provides foundation for further research on the development and fabrication of high power diamond devices. Preliminary results were obtained with the fabrication of ohmic contacts on (113) boron-doped diamond layers using Ti/Au, Zr/Au, and Mo/Au. Mo/Au and Zr/Au contacts on highly boron-doped layers ( $[B] \approx 10^{21} \text{ cm}^{-3}$ ) showed excellent ohmic contact properties when annealed at 700 °C, and therefore can be considered as improved candidates for ohmic contacts for diamond-based high-temperature power electronics compared to the classic Ti/Au contact system [268]. Pseudo-vertical Schottky diodes were also fabricated on (113) boron-doped diamond. Mo/Au was used to form ohmic contacts on highly-doped diamond ( $[B] \approx 10^{21} \text{ cm}^{-3}$ ) and Schottky contacts on low-doped diamond ( $[B] \approx 10^{21} \text{ cm}^{-3}$ ) [35]. At 180 °C, an ideality factor of 1.23, a Schottky barrier height of 1.71 eV, a specific on-resistance of  $1.3 \text{ m}\Omega.\text{cm}^2$ , a reverse current density below  $10^{-8} \text{ A.cm}^{-2}$ , and a rectification ratio of  $10^{11}$  were achieved. Those characteristics are comparable to state-of-the-art Schottky diodes produced on (100) and (111) boron-doped diamond [269–271].

# Bibliography

- [1] “Semiconductor diamond,” en, in *Ultra-Wide Bandgap Semiconductor Materials*, DOI: 10.1016/B978-0-12-815468-7.00002-0, Elsevier, 2019, pp. 111–261, ISBN: 978-0-12-815468-7. [Online]. Available: <https://linkinghub.elsevier.com/retrieve/pii/B9780128154687000020>.
- [2] S. Koizumi, H. Umezawa, J. Pernot, and M. Suzuki, *Power Electronics Device Applications of Diamond Semiconductors*. English. San Diego: Elsevier Science & Technology, 2018, OCLC: 1043603825, ISBN: 978-0-08-102184-2. [Online]. Available: <https://public.ebookcentral.proquest.com/choice/publicfullrecord.aspx?p=5438686>.
- [3] H. Umezawa, S.-i. Shikata, and T. Funaki, “Diamond schottky barrier diode for high-temperature, high-power, and fast switching applications,” *Japanese Journal of Applied Physics*, vol. 53, no. 5S1, 05FP06, May 1, 2014, ISSN: 0021-4922, 1347-4065. DOI: 10.7567/JJAP.53.05FP06.
- [4] P.-N. Volpe *et al.*, “High breakdown voltage schottky diodes synthesized on p-type cvd diamond layer,” en, *physica status solidi (a)*, vol. 207, no. 9, pp. 2088–2092, Sep. 2010, ISSN: 18626300. DOI: 10.1002/pssa.201000055.

- [5] J. Wang *et al.*, “Diamond schottky barrier diodes with floating metal rings for high breakdown voltage,” en, *Materials Science in Semiconductor Processing*, vol. 97, pp. 101–105, Jul. 2019, ISSN: 13698001. DOI: 10.1016/j.mssp.2019.03.004.
- [6] T. Matsumoto *et al.*, “Inversion channel diamond metal-oxide-semiconductor field-effect transistor with normally off characteristics,” en, *Scientific Reports*, vol. 6, no. 1, Oct. 2016, [Online; accessed 2018-03-30], ISSN: 2045-2322. DOI: 10.1038/srep31585. [Online]. Available: <http://www.nature.com/articles/srep31585>.
- [7] Z. Ren *et al.*, “High performance single crystalline diamond normally-off field effect transistors,” *IEEE Journal of the Electron Devices Society*, vol. 7, pp. 82–87, 2019, ISSN: 2168-6734. DOI: 10.1109/JEDS.2018.2880005.
- [8] V. B. Mbayachi, E. Ndayiragije, T. Sammani, S. Taj, E. R. Mbuta, and u. A. khan ullah ullah ullah ullah ullah ullah, “Graphene synthesis, characterization and its applications: A review,” en, *Results in Chemistry*, vol. 3, p. 100163, Jan. 2021, ISSN: 22117156. DOI: 10.1016/j.rechem.2021.100163.
- [9] R. Robertson, J. J. Fox, and A. E. Martin, “Two types of diamond,” en, *Philosophical Transactions of the Royal Society A: Mathematical, Physical and Engineering Sciences*, vol. 232, no. 707-720, pp. 463–535, Jan. 1, 1934, ISSN: 1364-503X, 1471-2962. DOI: 10.1098/rsta.1934.0013.
- [10] A. Zaitsev, *Optical Properties of Diamond: a Data Handbook*, English. Berlin, Heidelberg: Springer Berlin Heidelberg, 2001, OCLC: 851379989, ISBN: 978-3-

- 662-04548-0. [Online]. Available: <http://public.ebookcentral.proquest.com/choice/publicfullrecord.aspx?p=3097059>.
- [11] J. Walker, "Optical absorption and luminescence in diamond," *Reports on Progress in Physics*, vol. 42, no. 10, pp. 1605–1659, Oct. 1, 1979, ISSN: 0034-4885, 1361-6633. DOI: 10.1088/0034-4885/42/10/001.
- [12] S. N. Polyakov *et al.*, "Formation of boron-carbon nanosheets and bilayers in boron-doped diamond: Origin of metallicity and superconductivity," en, *Nanoscale Research Letters*, vol. 11, no. 1, p. 11, Dec. 2016, ISSN: 1931-7573, 1556-276X. DOI: 10.1186/s11671-015-1215-6.
- [13] T. Kageura *et al.*, "Superconductivity in nano- and micro-patterned high quality single crystalline boron-doped diamond films," en, *Diamond and Related Materials*, vol. 90, pp. 181–187, Nov. 2018, ISSN: 09259635. DOI: 10.1016/j.diamond.2018.10.013.
- [14] P.-N. Volpe, J. Pernot, P. Muret, and F. Omnès, "High hole mobility in boron doped diamond for power device applications," en, *Applied Physics Letters*, vol. 94, no. 9, p. 092 102, Mar. 2, 2009, ISSN: 0003-6951, 1077-3118. DOI: 10.1063/1.3086397.
- [15] J. Pernot and S. Koizumi, "Electron mobility in phosphorous doped {111} homoepitaxial diamond," en, *Applied Physics Letters*, vol. 93, no. 5, p. 052 105, Aug. 4, 2008, ISSN: 0003-6951, 1077-3118. DOI: 10.1063/1.2969066.
- [16] C. Bednarski, Z. Dai, A.-P. Li, and B. Golding, "Studies of heteroepitaxial growth of diamond," en, *Diamond and Related Materials*, vol. 12, no. 3-7, pp. 241–245, Mar. 2003, ISSN: 09259635. DOI: 10.1016/S0925-9635(02)00287-X.

- [17] K. Ichikawa, K. Kurone, H. Kodama, K. Suzuki, and A. Sawabe, “High crystalline quality heteroepitaxial diamond using grid-patterned nucleation and growth on ir,” en, *Diamond and Related Materials*, vol. 94, pp. 92–100, Apr. 2019, ISSN: 09259635. DOI: 10.1016/j.diamond.2019.01.027.
- [18] M. Syamsul, N. Oi, S. Okubo, T. Kageura, and H. Kawarada, “Heteroepitaxial diamond field-effect transistor for high voltage applications,” *IEEE Electron Device Letters*, vol. 39, no. 1, pp. 51–54, Jan. 2018, ISSN: 0741-3106, 1558-0563. DOI: 10.1109/LED.2017.2774290.
- [19] U. Choi, T. Kwak, S. Han, S.-W. Kim, and O. Nam, “High breakdown voltage of boron-doped diamond metal semiconductor field effect transistor grown on freestanding heteroepitaxial diamond substrate,” en, *Diamond and Related Materials*, vol. 121, p. 108 782, Jan. 2022, ISSN: 09259635. DOI: 10.1016/j.diamond.2021.108782.
- [20] V. Mortet *et al.*, “Conductivity of boron-doped diamond at high electrical field,” en, *Diamond and Related Materials*, vol. 98, p. 107 476, Oct. 2019, ISSN: 09259635. DOI: 10.1016/j.diamond.2019.107476.
- [21] M. Geis, D. Rathman, D. Ehrlich, R. Murphy, and W. Lindley, “High-temperature point-contact transistors and schottky diodes formed on synthetic boron-doped diamond,” *IEEE Electron Device Letters*, vol. 8, no. 8, pp. 341–343, Aug. 1987, ISSN: 0741-3106. DOI: 10.1109/EDL.1987.26653.
- [22] H. Shiomi, Y. Nishibayashi, and N. Fujimori, “High-voltage schottky diodes on boron-doped diamond epitaxial films,” en, *Japanese Journal of Applied Physics*, vol. 29, no. Part 2, No. 12, pp. L2163–L2164, Dec. 20, 1990, ISSN: 0021-4922. DOI: 10.1143/JJAP.29.L2163.

- [23] M. Suzuki, H. Yoshida, N. Sakuma, T. Ono, T. Sakai, and S. Koizumi, “Electrical characterization of phosphorus-doped  $n$ -type homoepitaxial diamond layers by schottky barrier diodes,” en, *Applied Physics Letters*, vol. 84, no. 13, pp. 2349–2351, Mar. 29, 2004, ISSN: 0003-6951, 1077-3118. DOI: 10.1063/1.1695206.
- [24] J. Alvarez, F. Houzé, J. Kleider, M. Liao, and Y. Koide, “Electrical characterization of schottky diodes based on boron doped homoepitaxial diamond films by conducting probe atomic force microscopy,” en, *Superlattices and Microstructures*, vol. 40, no. 4-6, pp. 343–349, Oct. 2006, ISSN: 07496036. DOI: 10.1016/j.spmi.2006.07.027.
- [25] J. E. Butler *et al.*, “Exceptionally high voltage schottky diamond diodes and low boron doping,” *Semiconductor Science and Technology*, vol. 18, no. 3, S67–S71, Mar. 1, 2003, ISSN: 0268-1242. DOI: 10.1088/0268-1242/18/3/309.
- [26] V. Bormashov *et al.*, “Thin large area vertical schottky barrier diamond diodes with low on-resistance made by ion-beam assisted lift-off technique,” en, *Diamond and Related Materials*, vol. 75, pp. 78–84, May 2017, ISSN: 09259635. DOI: 10.1016/j.diamond.2017.02.006.
- [27] M. Suzuki *et al.*, “Electrical characterization of diamond pin diodes for high voltage applications: Electrical characterization of diamond pin diodes,” en, *physica status solidi (a)*, vol. 210, no. 10, pp. 2035–2039, Oct. 2013, ISSN: 18626300. DOI: 10.1002/pssa.201300051.
- [28] M. Suzuki, “High voltage diamond pin diodes: Feasibility study on ultimate properties of diamond toward ultimate power devices,” en, *Oyo Buturi*,

- vol. 85, no. 3, pp. 218–222, 2016, ISSN: 2188-2290. DOI: 10.11470/oubutsu.85.3\_218.
- [29] N. Donato, N. Rouger, J. Pernot, G. Longobardi, and F. Udrea, “Diamond power devices: State of the art, modelling, figures of merit and future perspective,” *Journal of Physics D: Applied Physics*, vol. 53, no. 9, p. 093001, Feb. 27, 2020, ISSN: 0022-3727, 1361-6463. DOI: 10.1088/1361-6463/ab4eab.
- [30] H. Shiomi, Y. Nishibayashi, and N. Fujimori, “Field-effect transistors using boron-doped diamond epitaxial films,” en, *Japanese Journal of Applied Physics*, vol. 28, no. Part 2, No. 12, pp. L2153–L2154, Dec. 20, 1989, ISSN: 0021-4922. DOI: 10.1143/JJAP.28.L2153.
- [31] H. Umezawa, T. Matsumoto, and S.-I. Shikata, “Diamond metal-semiconductor field-effect transistor with breakdown voltage over 1.5 kv,” *IEEE Electron Device Letters*, vol. 35, no. 11, pp. 1112–1114, Nov. 2014, ISSN: 0741-3106, 1558-0563. DOI: 10.1109/LED.2014.2356191.
- [32] S. A. O. Russell, S. Sharabi, A. Tallaire, and D. A. J. Moran, “Hydrogen-terminated diamond field-effect transistors with cutoff frequency of 53 ghz,” *IEEE Electron Device Letters*, vol. 33, no. 10, pp. 1471–1473, Oct. 2012, ISSN: 0741-3106, 1558-0563. DOI: 10.1109/LED.2012.2210020.
- [33] K. Ueda *et al.*, “Diamond fet using high-quality polycrystalline diamond with  $f_{\text{sub t/}}$  of 45 ghz and  $f_{\text{sub max/}}$  of 120 ghz,” *IEEE Electron Device Letters*, vol. 27, no. 7, pp. 570–572, Jul. 2006, ISSN: 0741-3106. DOI: 10.1109/LED.2006.876325.

- [34] T. Iwasaki *et al.*, “Current enhancement by conductivity modulation in diamond jfets for next generation low-loss power devices,” [Online; accessed 2020-05-18], 2015 IEEE 27th International Symposium on Power Semiconductor Devices and IC’s (ISPSD), Hong Kong, China: IEEE, May 2015, pp. 77–80, ISBN: 978-1-4799-6259-4. DOI: 10.1109/ISPSD.2015.7123393. [Online]. Available: <http://ieeexplore.ieee.org/document/7123393/>.
- [35] P. Hazdra *et al.*, “Pseudo-vertical mo/au schottky diodes on {113} oriented boron doped homoepitaxial diamond layers,” en, *Diamond and Related Materials*, vol. 126, p. 109 088, Jun. 2022, ISSN: 09259635. DOI: 10.1016/j.diamond.2022.109088.
- [36] J. Arnault *et al.*, “Epitaxial diamond on ir/ sr tio3/si (001): From sequential material characterizations to fabrication of lateral schottky diodes,” en, *Diamond and Related Materials*, vol. 105, p. 107 768, May 2020, ISSN: 09259635. DOI: 10.1016/j.diamond.2020.107768.
- [37] T. Kwak *et al.*, “Diamond schottky barrier diodes fabricated on sapphire-based freestanding heteroepitaxial diamond substrate,” en, *Diamond and Related Materials*, vol. 114, p. 108 335, Apr. 2021, ISSN: 09259635. DOI: 10.1016/j.diamond.2021.108335.
- [38] H. N. Abbasi, Y.-F. Wang, W. Wang, J. Hussain, and H.-X. Wang, “Diamond field effect transistors using bilayer dielectrics yb2tio5/al2o3 on hydrogen-terminated diamond,” en, *Diamond and Related Materials*, vol. 106, p. 107 866, Jun. 2020, ISSN: 09259635. DOI: 10.1016/j.diamond.2020.107866.

- [39] M. Zhang *et al.*, “Normally-off hydrogen-terminated diamond field effect transistor with yttrium gate,” en, *Carbon*, vol. 176, pp. 307–312, May 2021, ISSN: 00086223. DOI: 10.1016/j.carbon.2021.01.121.
- [40] F. Bundy, “Pressure-temperature phase diagram of elemental carbon,” en, *Physica A: Statistical Mechanics and its Applications*, vol. 156, no. 1, pp. 169–178, Mar. 1989, ISSN: 03784371. DOI: 10.1016/0378-4371(89)90115-5.
- [41] K. Hanada, “Detonation nanodiamond: Perspective and applications,” en, *Surface Engineering*, vol. 25, no. 7, pp. 487–489, Oct. 2009, ISSN: 0267-0844, 1743-2944. DOI: 10.1179/174329409X433939.
- [42] F. P. Bundy, H. T. Hall, H. M. Strong, and R. H. Wentorfjun., “Man-made diamonds,” en, *Nature*, vol. 176, no. 4471, pp. 51–55, Jul. 1955, ISSN: 0028-0836, 1476-4687. DOI: 10.1038/176051a0.
- [43] F. P. Bundy, “Diamond synthesis with non-conventional catalyst-solvents,” en, *Nature*, vol. 241, no. 5385, pp. 116–118, Jan. 1973, ISSN: 0028-0836, 1476-4687. DOI: 10.1038/241116a0.
- [44] H. Liu and D. S. Dandy, *Diamond chemical vapor deposition: nucleation and early growth stages*. Park Ridge, N.J: Noyes Publications, 1995, ISBN: 978-0-8155-1380-3.
- [45] W. G. Eversole, “Synthesis of diamond,” Apr. 17, 1962.
- [46] B. Derjaguin, D. Fedoseev, V. Lukyanovich, B. Spitzin, V. Ryabov, and A. Lavrentyev, “Filamentary diamond crystals,” en, *Journal of Crystal Growth*, vol. 2, no. 6, pp. 380–384, Dec. 1968, ISSN: 00220248. DOI: 10.1016/0022-0248(68)90033-X.

- [47] J. C. Angus, H. A. Will, and W. S. Stanko, “Growth of diamond seed crystals by vapor deposition,” en, *Journal of Applied Physics*, vol. 39, no. 6, pp. 2915–2922, May 1968, ISSN: 0021-8979, 1089-7550. DOI: 10.1063/1.1656693.
- [48] R. C. DeVries, “Synthesis of diamond under metastable conditions,” en, *Annual Review of Materials Science*, vol. 17, no. 1, pp. 161–187, Aug. 1987, ISSN: 0084-6600. DOI: 10.1146/annurev.ms.17.080187.001113.
- [49] M. Kamo, Y. Sato, S. Matsumoto, and N. Setaka, “Diamond synthesis from gas phase in microwave plasma,” en, *Journal of Crystal Growth*, vol. 62, no. 3, pp. 642–644, Aug. 1983, ISSN: 00220248. DOI: 10.1016/0022-0248(83)90411-6.
- [50] E. L. H. Thomas, L. Ginés, S. Mandal, G. M. Klemencic, and O. A. Williams, “A simple, space constrained nirim type reactor for chemical vapour deposition of diamond,” en, *AIP Advances*, vol. 8, no. 3, p. 035 325, Mar. 2018, ISSN: 2158-3226. DOI: 10.1063/1.5009182.
- [51] F. Cerio, W. Weimer, and C. Johnson, “Diamond growth using carbon monoxide as a carbon source,” en, *Journal of Materials Research*, vol. 7, no. 5, pp. 1195–1203, May 1992, ISSN: 0884-2914, 2044-5326. DOI: 10.1557/JMR.1992.1195.
- [52] I. Schmidt, F. Hentschel, and C. Benndorf, “Low temperature diamond growth using fluorinated hydrocarbons,” en, *Diamond and Related Materials*, vol. 5, no. 11, pp. 1318–1322, Nov. 1996, ISSN: 09259635. DOI: 10.1016/0925-9635(96)00542-0.

- [53] S. Jou, H. J. Doerr, and R. F. Bunshah, “Diamond coatings from a solid carbon source,” en, *Thin Solid Films*, vol. 253, no. 1-2, pp. 95–102, Dec. 1994, ISSN: 00406090. DOI: 10.1016/0040-6090(94)90301-8.
- [54] J. E. Butler, Y. A. Mankelevich, A. Cheesman, J. Ma, and M. N. R. Ashfold, “Understanding the chemical vapor deposition of diamond: Recent progress,” *Journal of Physics: Condensed Matter*, vol. 21, no. 36, p. 364 201, Sep. 9, 2009, ISSN: 0953-8984, 1361-648X. DOI: 10.1088/0953-8984/21/36/364201.
- [55] J. Asmussen and D. K. Reinhard, Eds., *Diamond films handbook*. New York: Marcel Dekker, 2002, ISBN: 978-0-8247-9577-1.
- [56] P. K. Bachmann and H. Lydtin, “Diamond forming discharges,” en, *MRS Proceedings*, vol. 165, p. 181, 1989, ISSN: 0272-9172, 1946-4274. DOI: 10.1557/PROC-165-181.
- [57] M. A. Prelas, G. Popovici, and L. K. Bigelow, Eds., *Handbook of industrial diamonds and diamond films*. New York: Marcel Dekker, 1998, ISBN: 978-0-8247-9994-6.
- [58] K. Kobashi, *Diamond films: chemical vapor deposition for oriented and heteroepitaxial growth*, eng. Amsterdam: Elsevier, 2005, OCLC: 254696946, ISBN: 978-0-08-044723-0.
- [59] B. Dischler and C. Wild, *Low-Pressure Synthetic Diamond: Manufacturing and Applications*, English. 1998, OCLC: 1113082526, ISBN: 978-3-642-71992-9.

- [60] M. Fünér, C. Wild, and P. Koidl, “Novel microwave plasma reactor for diamond synthesis,” en, *Applied Physics Letters*, vol. 72, no. 10, pp. 1149–1151, Mar. 9, 1998, ISSN: 0003-6951, 1077-3118. DOI: 10.1063/1.120997.
- [61] K. Tsugawa, M. Ishihara, J. Kim, M. Hasegawa, and Y. Koga, “Large-area and low-temperature nanodiamond coating by microwave plasma chemical vapor deposition,” en, vol. 16, no. 6, pp. 337–346, Mar. 19, 2007.
- [62] A. Kromka, O. Babchenko, T. Izak, K. Hruška, and B. Rezek, “Linear antenna microwave plasma cvd deposition of diamond films over large areas,” en, vol. 86, pp. 776–779, 2012.
- [63] J. Kim and M. Katsurai, “Control of plasma space potentials and chemical vapor deposition of nanocrystalline diamond films in surface-wave excited low-pressure plasmas,” en, *Journal of Applied Physics*, vol. 101, no. 2, p. 023301, Jan. 15, 2007, ISSN: 0021-8979, 1089-7550. DOI: 10.1063/1.2409761.
- [64] J. Kim, K. Tsugawa, M. Ishihara, Y. Koga, and M. Hasegawa, “Large-area surface wave plasmas using microwave multi-slot antennas for nanocrystalline diamond film deposition,” *Plasma Sources Science and Technology*, vol. 19, no. 1, p. 015003, Feb. 1, 2010, ISSN: 0963-0252, 1361-6595. DOI: 10.1088/0963-0252/19/1/015003.
- [65] H.-A. Mehedi *et al.*, “Low temperature and large area deposition of nanocrystalline diamond films with distributed antenna array microwave-plasma reactor,” en, *Diamond and Related Materials*, vol. 47, pp. 58–65, Aug. 2014, ISSN: 09259635. DOI: 10.1016/j.diamond.2014.05.004.

- [66] A. Gicquel, K. Hassouni, F. Silva, and J. Achard, “Cvd diamond films: From growth to applications,” en, *Current Applied Physics*, vol. 1, no. 6, pp. 479–496, Dec. 2001, ISSN: 15671739. DOI: 10.1016/S1567-1739(01)00061-X.
- [67] M. Page and D. W. Brenner, “Hydrogen abstraction from a diamond surface. ab initio quantum chemical study with constrained isobutane as a model,” en, *Journal of the American Chemical Society*, vol. 113, no. 9, pp. 3270–3274, Apr. 1991, ISSN: 0002-7863, 1520-5126. DOI: 10.1021/ja00009a008.
- [68] T. Teraji and T. Ito, “Homoepitaxial diamond growth by high-power microwave-plasma chemical vapor deposition,” en, *Journal of Crystal Growth*, vol. 271, no. 3-4, pp. 409–419, Nov. 2004, ISSN: 00220248. DOI: 10.1016/j.jcrysgro.2004.08.005.
- [69] D. Takeuchi, H. Watanabe, S. Yamanaka, H. Okushi, and K. Kajimura, “Defects in device grade homoepitaxial diamond thin films grown with ultra-low ch<sub>4</sub>/h<sub>2</sub> conditions by microwave-plasma chemical vapor deposition,” *physica status solidi (a)*, vol. 174, no. 1, pp. 101–115, 1999. DOI: 10.1002/(SICI)1521-396X(199907)174:1<101::AID-PSSA101>3.0.CO;2-0.
- [70] C. J. Chu, R. H. Hauge, J. L. Margrave, and M. P. D’Evelyn, “Growth kinetics of (100), (110), and (111) homoepitaxial diamond films,” en, *Applied Physics Letters*, vol. 61, no. 12, pp. 1393–1395, Sep. 21, 1992, ISSN: 0003-6951, 1077-3118. DOI: 10.1063/1.107548.
- [71] T. Teraji, S. Mitani, and T. Ito, “High rate growth and luminescence properties of high-quality homoepitaxial diamond (100) films,” en, *physica status solidi (a)*, vol. 198, no. 2, pp. 395–406, Aug. 2003, ISSN: 0031-8965, 1521-396X. DOI: 10.1002/pssa.200306615.

- [72] J. Achard, A. Tallaire, R. Sussmann, F. Silva, and A. Gicquel, “The control of growth parameters in the synthesis of high-quality single crystalline diamond by cvd,” en, *Journal of Crystal Growth*, vol. 284, no. 3-4, pp. 396–405, Nov. 2005, ISSN: 00220248. DOI: 10.1016/j.jcrysgro.2005.07.046.
- [73] N. Lee and A. Badzian, “A study on surface morphologies of (001) homoepitaxial diamond films,” en, *Diamond and Related Materials*, vol. 6, no. 1, pp. 130–145, Jan. 1997, ISSN: 09259635. DOI: 10.1016/S0925-9635(96)00698-X.
- [74] T. Tsuno, H. Shiomi, Y. Kumazawa, S.-i. Shikata, and S.-i. Akai, “Growth rate and surface morphology of diamond homoepitaxial films on misoriented (001) substrates,” en, *Japanese Journal of Applied Physics*, vol. 35, no. Part 1, No. 9A, pp. 4724–4727, Sep. 15, 1996, ISSN: 0021-4922, 1347-4065. DOI: 10.1143/JJAP.35.4724.
- [75] W. van Enkevort, A. van der Berg, K. Kreuwel, A. Derksen, and M. Couto, “Impurity blocking of growth steps: Experiments and theory,” en, *Journal of Crystal Growth*, vol. 166, no. 1-4, pp. 156–161, Sep. 1996, ISSN: 00220248. DOI: 10.1016/0022-0248(96)00136-4.
- [76] F. de Theije, J. Schermer, and W. van Enkevort, “Effects of nitrogen impurities on the cvd growth of diamond: Step bunching in theory and experiment,” en, *Diamond and Related Materials*, vol. 9, no. 8, pp. 1439–1449, Aug. 2000, ISSN: 09259635. DOI: 10.1016/S0925-9635(00)00261-2.
- [77] P. van der Putte, W. van Enkevort, L. Giling, and J. Bloem, “Surface morphology of hcl etched silicon wafers,” en, *Journal of Crystal Growth*,

- vol. 43, no. 6, pp. 659–675, Jul. 1978, ISSN: 00220248. DOI: 10.1016/0022-0248(78)90145-8.
- [78] T. Kawato and K.-i. Kondo, “Effects of oxygen on cvd diamond synthesis,” en, *Japanese Journal of Applied Physics*, vol. 26, no. Part 1, No. 9, pp. 1429–1432, Sep. 20, 1987, ISSN: 0021-4922, 1347-4065. DOI: 10.1143/JJAP.26.1429.
- [79] S. J. Harris and A. M. Weiner, “Effects of oxygen on diamond growth,” en, *Applied Physics Letters*, vol. 55, no. 21, pp. 2179–2181, Nov. 20, 1989, ISSN: 0003-6951, 1077-3118. DOI: 10.1063/1.102350.
- [80] J. Ruan, K. Kobashi, and W. J. Choyke, “Effect of oxygen on boron doping in chemical vapor deposition of diamond as deduced from cathodoluminescence studies,” en, *Applied Physics Letters*, vol. 60, no. 15, pp. 1884–1886, Apr. 13, 1992, ISSN: 0003-6951, 1077-3118. DOI: 10.1063/1.107143.
- [81] Q. Zhang *et al.*, “The effect of co2 on the high-rate homoepitaxial growth of cvd single crystal diamonds,” en, *Diamond and Related Materials*, vol. 20, no. 4, pp. 496–500, Apr. 2011, ISSN: 09259635. DOI: 10.1016/j.diamond.2011.02.001.
- [82] J.-C. Tung, T.-C. Li, Y.-J. Teseng, and P.-L. Liu, “Effect of nitrogen on the growth of (100)-, (110)-, and (111)-oriented diamond films,” en, *Applied Sciences*, vol. 11, no. 1, p. 126, Dec. 24, 2020, ISSN: 2076-3417. DOI: 10.3390/app11010126.
- [83] A. Chayahara *et al.*, “The effect of nitrogen addition during high-rate homoepitaxial growth of diamond by microwave plasma cvd,” en, *Diamond and Related Materials*, vol. 13, no. 11-12, pp. 1954–1958, Nov. 2004, ISSN: 09259635. DOI: 10.1016/j.diamond.2004.07.007.

- [84] G. Z. Cao, J. J. Schermer, W. J. P. van Enkevort, W. A. L. M. Elst, and L. J. Giling, “Growth of {100} textured diamond films by the addition of nitrogen,” en, *Journal of Applied Physics*, vol. 79, no. 3, pp. 1357–1364, Feb. 1996, ISSN: 0021-8979, 1089-7550. DOI: 10.1063/1.361033.
- [85] D. Zhou, D. M. Gruen, L. C. Qin, T. G. McCauley, and A. R. Krauss, “Control of diamond film microstructure by ar additions to ch<sub>4</sub>/h<sub>2</sub> microwave plasmas,” en, *Journal of Applied Physics*, vol. 84, no. 4, pp. 1981–1989, Aug. 15, 1998, ISSN: 0021-8979, 1089-7550. DOI: 10.1063/1.368331.
- [86] A. Vikharev, A. Gorbachev, A. Kozlov, D. Radishev, and A. Muchnikov, “Microcrystalline diamond growth in presence of argon in millimeter-wave plasma-assisted cvd reactor,” en, *Diamond and Related Materials*, vol. 17, no. 7-10, pp. 1055–1061, Jul. 2008, ISSN: 09259635. DOI: 10.1016/j.diamond.2008.01.050.
- [87] P. K. Bachmann, D. Leers, and H. Lydtin, “Towards a general concept of diamond chemical vapour deposition,” en, *Diamond and Related Materials*, vol. 1, no. 1, pp. 1–12, Aug. 1991, ISSN: 09259635. DOI: 10.1016/0925-9635(91)90005-U.
- [88] J. R. Petherbridge, P. W. May, and M. N. R. Ashfold, “Modeling of the gas-phase chemistry in c–h–o gas mixtures for diamond chemical vapor deposition,” en, *Journal of Applied Physics*, vol. 89, no. 9, pp. 5219–5223, May 2001, ISSN: 0021-8979, 1089-7550. DOI: 10.1063/1.1360221.
- [89] M. Varga, Š. Potocký, M. Domonkos, T. Ižák, O. Babčenko, and A. Kromka, “Great variety of man-made porous diamond structures: Pulsed microwave cold plasma system with a linear antenna arrangement,” en, *ACS Omega*,

- vol. 4, no. 5, pp. 8441–8450, May 31, 2019, ISSN: 2470-1343, 2470-1343. DOI: 10.1021/acsomega.9b00323.
- [90] O. Brinza *et al.*, “Dependence of cvd diamond growth rate on substrate orientation as a function of process parameters in the high microwave power density regime,” en, *physica status solidi (a)*, vol. 205, no. 9, pp. 2114–2120, Sep. 2008, ISSN: 18626300, 18626319. DOI: 10.1002/pssa.200879716.
- [91] K. A. Snail and C. M. Marks, “*In situ* diamond growth rate measurement using emission interferometry,” en, *Applied Physics Letters*, vol. 60, no. 25, pp. 3135–3137, Jun. 22, 1992, ISSN: 0003-6951, 1077-3118. DOI: 10.1063/1.106747.
- [92] A. Tallaire, J. Achard, F. Silva, R. Sussmann, and A. Gicquel, “Homoepitaxial deposition of high-quality thick diamond films: Effect of growth parameters,” en, *Diamond and Related Materials*, vol. 14, no. 3-7, pp. 249–254, Mar. 2005, ISSN: 09259635. DOI: 10.1016/j.diamond.2004.10.037.
- [93] C. Findeling-Dufour, A. Vignes, and A. Gicquel, “Mwpacvd diamond homoepitaxial growth: Role of the plasma and the substrate parameters,” en, *Diamond and Related Materials*, vol. 4, no. 4, pp. 429–434, Apr. 1995, ISSN: 09259635. DOI: 10.1016/0925-9635(94)05316-2.
- [94] A. Gicquel, F. Silva, and K. Hassouni, “Diamond growth mechanisms in various environments,” en, *Journal of The Electrochemical Society*, vol. 147, no. 6, p. 2218, 2000, ISSN: 00134651. DOI: 10.1149/1.1393510.
- [95] C. Widmann, W. Müller-Sebert, N. Lang, and C. Nebel, “Homoepitaxial growth of single crystalline cvd-diamond,” en, *Diamond and Related Mate-*

- rials*, vol. 64, pp. 1–7, Apr. 2016, ISSN: 09259635. DOI: 10.1016/j.diamond.2015.12.016.
- [96] A. L. Maslov, N. I. Polushin, A. I. Laptev, T. V. Martynova, and A. M. Grechikhina, “Impact of cvd-synthesis parameters and film thickness on growth rate of single-crystal diamond,” *IOP Conference Series: Materials Science and Engineering*, vol. 1047, no. 1, p. 012 181, Feb. 1, 2021, ISSN: 1757-8981, 1757-899X. DOI: 10.1088/1757-899X/1047/1/012181.
- [97] A. T. Collins and A. W. S. Williams, “The nature of the acceptor centre in semiconducting diamond,” *Journal of Physics C: Solid State Physics*, vol. 4, no. 13, pp. 1789–1800, Sep. 17, 1971, ISSN: 0022-3719. DOI: 10.1088/0022-3719/4/13/030.
- [98] R. M. Chrenko, “Boron, the dominant acceptor in semiconducting diamond,” en, *Physical Review B*, vol. 7, no. 10, pp. 4560–4567, May 15, 1973, ISSN: 0556-2805. DOI: 10.1103/PhysRevB.7.4560.
- [99] M. Gabrysch *et al.*, “Compensation in boron-doped cvd diamond,” en, *physica status solidi (a)*, vol. 205, no. 9, pp. 2190–2194, Sep. 2008, ISSN: 18626300, 18626319. DOI: 10.1002/pssa.200879711.
- [100] M. Werner, R. Locher, W. Kohly, D. Holmes, S. Klose, and H. Fecht, “The diamond irvin curve,” en, *Diamond and Related Materials*, vol. 6, no. 2-4, pp. 308–313, Mar. 1997, ISSN: 09259635. DOI: 10.1016/S0925-9635(96)00683-8.
- [101] K. Thonke, “The boron acceptor in diamond,” *Semiconductor Science and Technology*, vol. 18, no. 3, S20–S26, Mar. 1, 2003, ISSN: 0268-1242. DOI: 10.1088/0268-1242/18/3/303.

- [102] J.-P. Lagrange, A. Deneuve, and E. Gheeraert, “Activation energy in low compensated homoepitaxial boron-doped diamond films,” en, *Diamond and Related Materials*, vol. 7, no. 9, pp. 1390–1393, Sep. 1998, ISSN: 09259635. DOI: 10.1016/S0925-9635(98)00225-8.
- [103] T. H. Borst and O. Weis, “Boron-doped homoepitaxial diamond layers: Fabrication, characterization, and electronic applications,” en, *Physica Status Solidi (a)*, vol. 154, no. 1, pp. 423–444, Mar. 16, 1996, ISSN: 00318965, 1521396X. DOI: 10.1002/pssa.2211540130.
- [104] T. Klein *et al.*, “Metal-insulator transition and superconductivity in boron-doped diamond,” en, *Physical Review B*, vol. 75, no. 16, p. 165313, Apr. 17, 2007, ISSN: 1098-0121, 1550-235X. DOI: 10.1103/PhysRevB.75.165313.
- [105] J.-P. Lagrange, A. Deneuve, and E. Gheeraert, “A large range of boron doping with low compensation ratio for homoepitaxial diamond films,” en, *Carbon*, vol. 37, no. 5, pp. 807–810, Apr. 1999, ISSN: 00086223. DOI: 10.1016/S0008-6223(98)00275-9.
- [106] M. Mermoux, F. Jomard, C. Tavarès, F. Omnès, and E. Bustarret, “Raman characterization of boron-doped {111} homoepitaxial diamond layers,” en, *Diamond and Related Materials*, vol. 15, no. 4-8, pp. 572–576, Apr. 2006, ISSN: 09259635. DOI: 10.1016/j.diamond.2005.11.035.
- [107] V. Mortet *et al.*, “Properties of boron-doped epitaxial diamond layers grown on (110) oriented single crystal substrates,” en, *Diamond and Related Materials*, vol. 53, pp. 29–34, Mar. 2015, ISSN: 09259635. DOI: 10.1016/j.diamond.2015.01.006.

- [108] A. Tallaire *et al.*, “Growth of thick and heavily boron-doped (113)-oriented cvd diamond films,” en, *Diamond and Related Materials*, vol. 66, pp. 61–66, Jun. 2016, ISSN: 09259635. DOI: 10.1016/j.diamond.2016.03.020.
- [109] A. Taylor *et al.*, “Growth and comparison of high-quality mw pecvd grown b doped diamond layers on {118}, {115} and {113} single crystal diamond substrates,” en, *Diamond and Related Materials*, vol. 123, p. 108 815, Mar. 2022, ISSN: 09259635. DOI: 10.1016/j.diamond.2021.108815.
- [110] J. Pernot *et al.*, “Hall hole mobility in boron-doped homoepitaxial diamond,” en, *Physical Review B*, vol. 81, no. 20, May 7, 2010, [Online; accessed 2019-02-10], ISSN: 1098-0121, 1550-235X. DOI: 10.1103/PhysRevB.81.205203. [Online]. Available: <https://link.aps.org/doi/10.1103/PhysRevB.81.205203>.
- [111] P.-N. Volpe *et al.*, “Boron incorporation issues in diamond when tmb is used as precursor: Toward extreme doping levels,” en, *Diamond and Related Materials*, vol. 22, pp. 136–141, Feb. 2012, ISSN: 09259635. DOI: 10.1016/j.diamond.2011.12.019.
- [112] M. Aono, O. Maida, and T. Ito, “Hall data analysis of heavily boron-doped cvd diamond films using a model considering an impurity band well separated from valence bands,” en, *Diamond and Related Materials*, vol. 20, no. 10, pp. 1357–1362, Nov. 2011, ISSN: 09259635. DOI: 10.1016/j.diamond.2011.08.008.
- [113] V. Mortet *et al.*, “Effect of substrate crystalline orientation on boron-doped homoepitaxial diamond growth,” en, *Diamond and Related Materials*,

- vol. 122, p. 108 887, Feb. 2022, ISSN: 09259635. DOI: 10.1016/j.diamond.2022.108887.
- [114] H. Okushi, “High quality homoepitaxial cvd diamond for electronic devices,” en, *Diamond and Related Materials*, vol. 10, no. 3-7, pp. 281–288, Mar. 2001, ISSN: 09259635. DOI: 10.1016/S0925-9635(00)00399-X.
- [115] C. Tavares, F. Omnès, J. Pernot, and E. Bustarret, “Electronic properties of boron-doped {111}-oriented homoepitaxial diamond layers,” en, *Diamond and Related Materials*, vol. 15, no. 4-8, pp. 582–585, Apr. 2006, ISSN: 09259635. DOI: 10.1016/j.diamond.2005.11.034.
- [116] H. Ye *et al.*, “Electronic properties of homoepitaxial (111) highly boron-doped diamond films,” en, *Journal of Applied Physics*, vol. 103, no. 5, p. 054 503, Mar. 2008, ISSN: 0021-8979, 1089-7550. DOI: 10.1063/1.2837114.
- [117] M. Kasu, T. Makimoto, W. Ebert, and E. Kohn, “Formation of stacking faults containing microtwins in (111) chemical-vapor-deposited diamond homoepitaxial layers,” en, *Applied Physics Letters*, vol. 83, no. 17, pp. 3465–3467, Oct. 27, 2003, ISSN: 0003-6951, 1077-3118. DOI: 10.1063/1.1622105.
- [118] S. Ghodbane, F. Omnès, and C. Agnès, “A cathodoluminescence study of boron doped {111}-homoepitaxial diamond films,” en, *Diamond and Related Materials*, vol. 19, no. 4, pp. 273–278, Apr. 2010, ISSN: 09259635. DOI: 10.1016/j.diamond.2009.11.003.
- [119] A. Lazea, Y. Garino, T. Teraji, and S. Koizumi, “High quality p-type chemical vapor deposited {111}-oriented diamonds: Growth and fabrication of related electrical devices,” en, *physica status solidi (a)*, vol. 209, no. 10, pp. 1978–1981, Oct. 2012, ISSN: 18626300. DOI: 10.1002/pssa.201228162.

- [120] S.-G. Ri *et al.*, “Electrical and optical characterization of boron-doped (111) homoepitaxial diamond films,” en, *Diamond and Related Materials*, vol. 14, no. 11-12, pp. 1964–1968, Nov. 2005, ISSN: 09259635. DOI: 10.1016/j.diamond.2005.06.032.
- [121] J. Voves *et al.*, “Effect of the substrate crystalline orientation on the surface morphology and boron incorporation into epitaxial diamond layers,” [Online; accessed 2022-06-16], NANOCON 2020, 2020, pp. 98–102. DOI: 10.37904/nanocon.2020.3683. [Online]. Available: <https://www.confer.cz/nanocon/2020/3683-effect-of-the-substrate-crystalline-orientation-on-the-surface-morphology-and-boron-incorporation-into-epitaxial-diamond-layers>.
- [122] V. Mortet *et al.*, “Properties of boron-doped (113) oriented homoepitaxial diamond layers,” en, *Diamond and Related Materials*, vol. 111, p. 108 223, Jan. 2021, ISSN: 09259635. DOI: 10.1016/j.diamond.2020.108223.
- [123] V. Mortet, L. Klimsa, N. Lambert, M. Davydova, J. Kopecek, and S. Ignacova Sedlakova, “Study of cracks formation in highly – low boron-doped epitaxial (113) diamond bilayers,” [Online; accessed 2022-08-04], 2021, pp. 65–68. DOI: 10.37904/nanocon.2021.4326. [Online]. Available: <https://www.confer.cz/nanocon/2021/4326-study-of-cracks-formation-in-p-p-epitaxial-113-boron-doped-diamond-bilayers>.
- [124] B. B. Li, M. C. Tosin, A. C. Peterlevitz, and V. Baranauskas, “Measurement of the substitutional nitrogen activation energy in diamond films,” en, *Applied Physics Letters*, vol. 73, no. 6, pp. 812–814, Aug. 10, 1998, ISSN: 0003-6951, 1077-3118. DOI: 10.1063/1.122010.

- [125] S. A. Kajihara, A. Antonelli, and J. Bernholc, “N-type doping and diffusion of impurities in diamond,” en, *MRS Proceedings*, vol. 162, p. 315, 1989, ISSN: 0272-9172, 1946-4274. DOI: 10.1557/PROC-162-315.
- [126] T. Miyazaki and H. Okushi, “A theoretical study of a sulfur impurity in diamond,” en, *Diamond and Related Materials*, vol. 10, no. 3-7, pp. 449–452, Mar. 2001, ISSN: 09259635. DOI: 10.1016/S0925-9635(00)00582-3.
- [127] C. Uzan-Saguy, C. Cytermann, B. Fizegeer, V. Richter, R. Brenner, and R. Kalish, “Diffusion of lithium in diamond,” *physica status solidi (a)*, vol. 193, no. 3, pp. 508–516, 2002. DOI: 10.1002/1521-396X(200210)193:3<508::AID-PSSA508>3.0.CO;2-H.
- [128] J. F. Prins, “Onset of hopping conduction in carbon-ion-implanted diamond,” en, *Physical Review B*, vol. 31, no. 4, pp. 2472–2478, Feb. 15, 1985, ISSN: 0163-1829. DOI: 10.1103/PhysRevB.31.2472.
- [129] S. Kajihara, A. Antonelli, and J. Bernholc, “Impurity incorporation and doping of diamond,” en, *Physica B: Condensed Matter*, vol. 185, no. 1-4, pp. 144–149, Apr. 1993, ISSN: 09214526. DOI: 10.1016/0921-4526(93)90228-X.
- [130] K. Jackson, M. R. Pederson, and J. G. Harrison, “Donor levels and impurity-atom relaxation in nitrogen- and phosphorus-doped diamond,” en, *Physical Review B*, vol. 41, no. 18, pp. 12 641–12 649, Jun. 15, 1990, ISSN: 0163-1829, 1095-3795. DOI: 10.1103/PhysRevB.41.12641.
- [131] A. B. Anderson and S. P. Mehandru, “ $n$ -type dopants and conduction-band electrons in diamond: Cluster molecular-orbital theory,” en, *Physical Review*

- B*, vol. 48, no. 7, pp. 4423–4427, Aug. 15, 1993, ISSN: 0163-1829, 1095-3795. DOI: 10.1103/PhysRevB.48.4423.
- [132] J. F. Prins, “Ion-implanted n-type diamond: Electrical evidence,” en, *Diamond and Related Materials*, vol. 4, no. 5-6, pp. 580–585, May 1995, ISSN: 09259635. DOI: 10.1016/0925-9635(94)05261-1.
- [133] S. Koizumi, M. Kamo, Y. Sato, H. Ozaki, and T. Inuzuka, “Growth and characterization of phosphorous doped {111} homoepitaxial diamond thin films,” en, *Applied Physics Letters*, vol. 71, no. 8, pp. 1065–1067, Aug. 25, 1997, ISSN: 0003-6951, 1077-3118. DOI: 10.1063/1.119729.
- [134] I. Sakaguchi *et al.*, “Sulfur: A donor dopant for *n*-type diamond semiconductors,” en, *Physical Review B*, vol. 60, no. 4, R2139–R2141, Jul. 15, 1999, ISSN: 0163-1829, 1095-3795. DOI: 10.1103/PhysRevB.60.R2139.
- [135] R. Kalish, A. Reznik, C. Uzan-Saguy, and C. Cytermann, “Is sulfur a donor in diamond?” en, *Applied Physics Letters*, vol. 76, no. 6, pp. 757–759, Feb. 7, 2000, ISSN: 0003-6951, 1077-3118. DOI: 10.1063/1.125885.
- [136] M. Nesládek, K. Meykens, K. Haenen, L. M. Stals, T. Teraji, and S. Koizumi, “Low-temperature spectroscopic study of *n*-type diamond,” en, *Physical Review B*, vol. 59, no. 23, pp. 14 852–14 855, Jun. 15, 1999, ISSN: 0163-1829, 1095-3795. DOI: 10.1103/PhysRevB.59.14852.
- [137] E. Gheeraert, S. Koizumi, T. Teraji, H. Kanda, and M. Nesládek, “Electronic states of boron and phosphorus in diamond,” en, *physica status solidi (a)*, vol. 174, no. 1, pp. 39–51, Jul. 1999, ISSN: 00318965, 1521396X. DOI: 10.1002/(SICI)1521-396X(199907)174:1<39::AID-PSSA39>3.0.CO;2-E.

- [138] H. Sternschulte, K. Thonke, R. Sauer, and S. Koizumi, “Optical evidence for 630-mev phosphorus donor in synthetic diamond,” en, *Physical Review B*, vol. 59, no. 20, pp. 12 924–12 927, May 15, 1999, ISSN: 0163-1829, 1095-3795. DOI: 10.1103/PhysRevB.59.12924.
- [139] H. Katayama-Yoshida, T. Nishimatsu, T. Yamamoto, and N. Orita, “Codoping method for the fabrication of low-resistivity wide band-gap semiconductors in p-type gan, p-type aln and n-type diamond: Prediction versus experiment,” *Journal of Physics: Condensed Matter*, vol. 13, no. 40, pp. 8901–8914, Oct. 8, 2001, ISSN: 0953-8984, 1361-648X. DOI: 10.1088/0953-8984/13/40/304.
- [140] T. Miyazaki, H. Okushi, and T. Uda, “Theoretical study of sulfur-hydrogen-vacancy complex in diamond,” en, *Applied Physics Letters*, vol. 78, no. 25, pp. 3977–3979, Jun. 18, 2001, ISSN: 0003-6951, 1077-3118. DOI: 10.1063/1.1381041.
- [141] H. Kato, S. Yamasaki, and H. Okushi, “Carrier compensation in (001) n-type diamond by phosphorus doping,” en, *Diamond and Related Materials*, vol. 16, no. 4-7, pp. 796–799, Apr. 2007, ISSN: 09259635. DOI: 10.1016/j.diamond.2006.11.085.
- [142] H. Kato, T. Makino, S. Yamasaki, and H. Okushi, “N-type diamond growth by phosphorus doping,” en, *MRS Proceedings*, vol. 1039, 1039–P05-01, 2007, ISSN: 0272-9172, 1946-4274. DOI: 10.1557/PROC-1039-P05-01.
- [143] H. Kato, D. Takeuchi, N. Tokuda, H. Umezawa, S. Yamasaki, and H. Okushi, “Electrical activity of doped phosphorus atoms in (001) n-type diamond,”

- en, *physica status solidi (a)*, vol. 205, no. 9, pp. 2195–2199, Sep. 2008, ISSN: 18626300, 18626319. DOI: 10.1002/pssa.200879722.
- [144] H. Kato, S. Yamasaki, and H. Okushi, “N-type doping of (001)-oriented single-crystalline diamond by phosphorus,” en, *Applied Physics Letters*, vol. 86, no. 22, p. 222 111, May 30, 2005, ISSN: 0003-6951, 1077-3118. DOI: 10.1063/1.1944228.
- [145] T. Grotjohn, D. Tran, M. Yaran, S. Demlow, and T. Schuelke, “Heavy phosphorus doping by epitaxial growth on the (111) diamond surface,” en, *Diamond and Related Materials*, vol. 44, pp. 129–133, Apr. 2014, ISSN: 09259635. DOI: 10.1016/j.diamond.2014.02.009.
- [146] M. Katagiri, J. Isoya, S. Koizumi, and H. Kanda, “Lightly phosphorus-doped homoepitaxial diamond films grown by chemical vapor deposition,” en, *Applied Physics Letters*, vol. 85, no. 26, pp. 6365–6367, Dec. 27, 2004, ISSN: 0003-6951, 1077-3118. DOI: 10.1063/1.1840119.
- [147] M. Hasegawa, T. Teraji, and S. Koizumi, “Lattice location of phosphorus in *n*-type homoepitaxial diamond films grown by chemical-vapor deposition,” en, *Applied Physics Letters*, vol. 79, no. 19, pp. 3068–3070, Nov. 5, 2001, ISSN: 0003-6951, 1077-3118. DOI: 10.1063/1.1417514.
- [148] M.-A. Pinault-Thaury *et al.*, “Phosphorus donor incorporation in (1 0 0) homoepitaxial diamond: Role of the lateral growth,” en, *Journal of Crystal Growth*, vol. 335, no. 1, pp. 31–36, Nov. 2011, ISSN: 00220248. DOI: 10.1016/j.jcrysgro.2011.06.007.
- [149] M.-A. Pinault-Thaury *et al.*, “Phosphorus-doped (113) cvd diamond: A breakthrough towards bipolar diamond devices,” en, *Applied Physics Letters*,

- vol. 114, no. 11, p. 112 106, Mar. 18, 2019, ISSN: 0003-6951, 1077-3118. DOI: 10.1063/1.5079924.
- [150] M.-A. Pinault-Thaury *et al.*, “Attractive electron mobility in (113) n-type phosphorus-doped homoepitaxial diamond,” en, *Carbon*, vol. 175, pp. 254–258, Apr. 2021, ISSN: 00086223. DOI: 10.1016/j.carbon.2021.01.011.
- [151] B. D. Thoms, M. S. Owens, J. E. Butler, and C. Spiro, “Production and characterization of smooth, hydrogen-terminated diamond c(100),” en, *Applied Physics Letters*, vol. 65, no. 23, pp. 2957–2959, Dec. 5, 1994, ISSN: 0003-6951, 1077-3118. DOI: 10.1063/1.112503.
- [152] H. Kawarada, “Hydrogen-terminated diamond surfaces and interfaces,” en, *Surface Science Reports*, vol. 26, no. 7, pp. 205–206, 1996, ISSN: 01675729. DOI: 10.1016/S0167-5729(97)80002-7.
- [153] F. Maier, M. Riedel, B. Mantel, J. Ristein, and L. Ley, “Origin of surface conductivity in diamond,” en, *Physical Review Letters*, vol. 85, no. 16, pp. 3472–3475, Oct. 16, 2000, ISSN: 0031-9007, 1079-7114. DOI: 10.1103/PhysRevLett.85.3472.
- [154] A. Denisenko, A. Aleksov, A. Pribil, P. Gluche, W. Ebert, and E. Kohn, “Hypothesis on the conductivity mechanism in hydrogen terminated diamond films,” en, *Diamond and Related Materials*, vol. 9, no. 3-6, pp. 1138–1142, Apr. 2000, ISSN: 09259635. DOI: 10.1016/S0925-9635(99)00317-9.
- [155] J. B. Cui, J. Ristein, and L. Ley, “Electron affinity of the bare and hydrogen covered single crystal diamond (111) surface,” en, *Physical Review Letters*, vol. 81, no. 2, pp. 429–432, Jul. 13, 1998, ISSN: 0031-9007, 1079-7114. DOI: 10.1103/PhysRevLett.81.429.

- [156] B. Rezek *et al.*, “Fermi level on hydrogen terminated diamond surfaces,” en, *Applied Physics Letters*, vol. 82, no. 14, pp. 2266–2268, Apr. 7, 2003, ISSN: 0003-6951, 1077-3118. DOI: 10.1063/1.1564293.
- [157] F. Maier, J. Ristein, and L. Ley, “Electron affinity of plasma-hydrogenated and chemically oxidized diamond (100) surfaces,” en, *Physical Review B*, vol. 64, no. 16, p. 165 411, Oct. 5, 2001, ISSN: 0163-1829, 1095-3795. DOI: 10.1103/PhysRevB.64.165411.
- [158] A. Denisenko, C. Pietzka, A. Romanyuk, H. El-Hajj, and E. Kohn, “The electronic surface barrier of boron-doped diamond by anodic oxidation,” en, *Journal of Applied Physics*, vol. 103, no. 1, p. 014 904, Jan. 2008, ISSN: 0021-8979, 1089-7550. DOI: 10.1063/1.2827481.
- [159] M. Nur, N. Bonifaci, A. Denat, and V. M. Atrazhev, “Nh and cn radical emission from corona post discharge region in high density nitrogen plasma,” *IOP Conference Series: Materials Science and Engineering*, vol. 509, p. 012 084, May 3, 2019, ISSN: 1757-899X. DOI: 10.1088/1757-899X/509/1/012084.
- [160] M. Hiramatsu, K. Kato, C. Lau, J. Foord, and M. Hori, “Measurement of c2 radical density in microwave methane/hydrogen plasma used for nanocrystalline diamond film formation,” en, *Diamond and Related Materials*, vol. 12, no. 3-7, pp. 365–368, Mar. 2003, ISSN: 09259635. DOI: 10.1016/S0925-9635(02)00216-9.
- [161] C. Huang, C.-Y. Tsai, and R.-S. Juang, “Surface modification and characterization of an h2/o2 plasma-treated polypropylene membrane,” en, *Journal of Applied Polymer Science*, vol. 124, no. S1, E108–E115, Jun. 25, 2012, ISSN: 00218995. DOI: 10.1002/app.34049.

- [162] P. C. Braga and D. Ricci, Eds., *Atomic force microscopy: biomedical methods and applications* (Methods in molecular biology). Totowa, N.J: Humana Press, 2004, ISBN: 978-1-58829-094-6.
- [163] N. Jalili and K. Laxminarayana, “A review of atomic force microscopy imaging systems: Application to molecular metrology and biological sciences,” en, *Mechatronics*, vol. 14, no. 8, pp. 907–945, Oct. 2004, ISSN: 09574158. DOI: 10.1016/j.mechatronics.2004.04.005.
- [164] K. Vernon-Parry, “Scanning electron microscopy: An introduction,” en, *III-Vs Review*, vol. 13, no. 4, pp. 40–44, Jul. 2000, ISSN: 09611290. DOI: 10.1016/S0961-1290(00)80006-X.
- [165] P. J. Goodhew, F. J. Humphreys, and R. Beanland, *Electron microscopy and analysis*, 3rd ed. London ; New York: Taylor & Francis, 2001, ISBN: 978-0-7484-0968-6.
- [166] S. Sharma, S. Jaiswal, B. Duffy, and A. Jaiswal, “Nanostructured materials for food applications: Spectroscopy, microscopy and physical properties,” en, *Bioengineering*, vol. 6, no. 1, p. 26, Mar. 19, 2019, ISSN: 2306-5354. DOI: 10.3390/bioengineering6010026.
- [167] C. Lechene *et al.*, “High-resolution quantitative imaging of mammalian and bacterial cells using stable isotope mass spectrometry,” *Journal of Biology*, vol. 5, no. 6, p. 20, 2006, ISSN: 14754924. DOI: 10.1186/jbiol142.
- [168] J. Thomson, “Lxxxiii. Rays of positive electricity,” en, *The London, Edinburgh, and Dublin Philosophical Magazine and Journal of Science*, vol. 20, no. 118, pp. 752–767, Oct. 1910, ISSN: 1941-5982, 1941-5990. DOI: 10.1080/14786441008636962.

- [169] R. F. K. Herzog and F. P. Viehböck, “Ion source for mass spectrography,” en, *Physical Review*, vol. 76, no. 6, pp. 855–856, Sep. 15, 1949, ISSN: 0031-899X. DOI: 10.1103/PhysRev.76.855.
- [170] R. Castaing and G. J. Slodzian, “Optique corpusculaire—premiers essais de microanalyse par emission ionique secondaire,” fr, *Microscopie*, vol. 1, pp. 395–399, 1962.
- [171] K. Wittmaack, “Pre-equilibrium variation of the secondary ion yield,” en, *International Journal of Mass Spectrometry and Ion Physics*, vol. 17, no. 1, pp. 39–50, May 1975, ISSN: 00207381. DOI: 10.1016/0020-7381(75)80005-2.
- [172] A. Benninghoven, “Analysis of submonolayers on silver by negative secondary ion emission,” de, *physica status solidi (b)*, vol. 34, no. 2, K169–K171, 1969, ISSN: 03701972, 15213951. DOI: 10.1002/pssb.19690340267.
- [173] W. Grimm, “Eine neue glimmentladungslampe für die optische emissionsspektralanalyse,” de, *Spectrochimica Acta Part B: Atomic Spectroscopy*, vol. 23, no. 7, pp. 443–454, Jun. 1968, ISSN: 05848547. DOI: 10.1016/0584-8547(68)80023-0.
- [174] T. Nelis and R. Payling, *Glow discharge optical emission spectroscopy: a practical guide* (RSC analytical spectroscopy monographs). Cambridge, UK: Royal Society of Chemistry, 2003, OCLC: ocm54494212, ISBN: 978-0-85404-521-1.
- [175] C. F. Gallo, “Coronas and gas discharges in electrophotography: A review,” *IEEE Transactions on Industry Applications*, vol. IA-11, no. 6, pp. 739–748, Nov. 1975, ISSN: 0093-9994. DOI: 10.1109/TIA.1975.349370.

- [176] R. Payling, D. G. Jones, and A. Bengtson, Eds., *Glow discharge optical emission spectrometry*. Chichester: New York : J. Wiley, 1997, ISBN: 978-0-471-96683-8.
- [177] Z. Weiss, “Calibration methods in glow discharge optical emission spectroscopy: A tutorial review,” en, *Journal of Analytical Atomic Spectrometry*, vol. 30, no. 5, pp. 1038–1049, 2015, ISSN: 0267-9477, 1364-5544. DOI: 10.1039/C4JA00482E.
- [178] C. Schubert *et al.*, “Compositional depth profiling of diamond-like carbon layers by glow discharge optical emission spectroscopy,” en, *Journal of Analytical Atomic Spectrometry*, vol. 31, no. 11, pp. 2207–2212, 2016, ISSN: 0267-9477, 1364-5544. DOI: 10.1039/C6JA00251J.
- [179] L. Van der Pauw, “A method of measuring the resistivity and hall coefficient on lamellae of arbitrary shape,” en, *Philips Technical Review*, vol. 20, pp. 220–224, 1958.
- [180] B. Gómez-Ferrer, *Resistivity Recovery in Fe and FeCr alloys*, English. Springer International Publishing., 2016, OCLC: 1113689201, ISBN: 978-3-319-38857-1. [Online]. Available: <https://doi.org/10.1007/978-3-319-38857-1>.
- [181] T. J. Maloney and N. Khurana, “Transmission line pulse technique for circuit modeling and esd phenomena,” en, EOS/ESD Symposium, 1985, pp. 49–54.
- [182] G. Durgin, *Tdt03: Dc pulses on transmission lines*, en, 2012. [Online]. Available: <https://www.youtube.com/watch?v=B86rV5FdKpU>.

- [183] N. Lambert, “Creation of a test bench for i and v measurements under high electric field,” en, Ph.D. dissertation, France, Sep. 2017.
- [184] N. Mauran, “Conception et réalisation d’un banc de caractérisation sous pointes pour mesures impulsionnelles haute énergie,” fr, Ph.D. dissertation, 2003.
- [185] M. Litzenberger, C. Furbock, S. Bychikhin, D. Pogany, and E. Gornik, “Scanning heterodyne interferometer setup for the time-resolved thermal and free-carrier mapping in semiconductor devices,” en, *IEEE Transactions on Instrumentation and Measurement*, vol. 54, no. 6, pp. 2438–2445, Dec. 2005, ISSN: 0018-9456. DOI: 10.1109/TIM.2005.858121.
- [186] D. Pogany *et al.*, “Quantitative internal thermal energy mapping of semiconductor devices under short current stress using backside laser interferometry,” en, *IEEE Transactions on Electron Devices*, vol. 49, no. 11, pp. 2070–2079, Nov. 2002, ISSN: 0018-9383. DOI: 10.1109/TED.2002.804724.
- [187] C. Fleury, “Behavior of silicon and gallium nitride devices under electrical overstress conditions,” en, Ph.D. dissertation, Vienna, Austria, Dec. 2017.
- [188] A. Smekal, “Zur quantentheorie der dispersion,” de, *Die Naturwissenschaften*, vol. 11, no. 43, pp. 873–875, Oct. 1923, ISSN: 0028-1042, 1432-1904. DOI: 10.1007/BF01576902.
- [189] C. V. Raman and K. S. Krishnan, “A new type of secondary radiation,” en, *Nature*, vol. 121, no. 3048, pp. 501–502, Mar. 1928, ISSN: 0028-0836, 1476-4687. DOI: 10.1038/121501c0.

- [190] R. R. Jones, D. C. Hooper, L. Zhang, D. Wolverson, and V. K. Valev, “Raman techniques: Fundamentals and frontiers,” en, *Nanoscale Research Letters*, vol. 14, no. 1, p. 231, Dec. 2019, ISSN: 1931-7573, 1556-276X. DOI: 10.1186/s11671-019-3039-2.
- [191] D. J. Gardiner and H. J. Bowley, Eds., *Practical Raman spectroscopy: with 11 tables*, eng. Berlin Heidelberg: Springer, 1989, ISBN: 978-3-540-50254-8.
- [192] T. T. Basiev, A. A. Sobol, P. G. Zverev, V. V. Osiko, and R. C. Powell, “Comparative spontaneous raman spectroscopy of crystals for raman lasers,” en, *Applied Optics*, vol. 38, no. 3, p. 594, Jan. 20, 1999, ISSN: 0003-6935, 1539-4522. DOI: 10.1364/AO.38.000594.
- [193] A. Zumbusch, G. R. Holtom, and X. S. Xie, “Three-dimensional vibrational imaging by coherent anti-stokes raman scattering,” en, *Physical Review Letters*, vol. 82, no. 20, pp. 4142–4145, May 17, 1999, ISSN: 0031-9007, 1079-7114. DOI: 10.1103/PhysRevLett.82.4142.
- [194] L. Golunski *et al.*, “Optimization of polycrystalline cvd diamond seeding with the use of  $sp^3/sp^2$  raman band ratio,” en, *Acta Physica Polonica A*, vol. 128, no. 1, pp. 136–140, Jul. 2015, ISSN: 0587-4246, 1898-794X. DOI: 10.12693/APhysPolA.128.136.
- [195] W. Fortunato, A. J. Chiquito, J. C. Galzerani, and J. R. Moro, “Crystalline quality and phase purity of cvd diamond films studied by raman spectroscopy,” en, *Journal of Materials Science*, vol. 42, no. 17, pp. 7331–7336, Jun. 29, 2007, ISSN: 0022-2461, 1573-4803. DOI: 10.1007/s10853-007-1575-0.

- [196] V. Mortet *et al.*, “Insight into boron-doped diamond raman spectra characteristic features,” en, *Carbon*, vol. 115, pp. 279–284, May 2017, ISSN: 00086223. DOI: 10.1016/j.carbon.2017.01.022.
- [197] M. Mermoux, B. Marcus, A. Crisci, A. Tajani, E. Gheeraert, and E. Bustarret, “Micro-raman scattering from undoped and phosphorous-doped (111) homoepitaxial diamond films: Stress imaging of cracks,” en, *Journal of Applied Physics*, vol. 97, no. 4, p. 043530, Feb. 15, 2005, ISSN: 0021-8979, 1089-7550. DOI: 10.1063/1.1849828.
- [198] V. Mortet *et al.*, “New perspectives for heavily boron-doped diamond raman spectrum analysis,” en, *Carbon*, vol. 168, pp. 319–327, Oct. 2020, ISSN: 00086223. DOI: 10.1016/j.carbon.2020.06.075.
- [199] M. Davydova *et al.*, “Characteristics of zirconium and niobium contacts on boron-doped diamond,” en, *Diamond and Related Materials*, vol. 83, pp. 184–189, Mar. 2018, ISSN: 09259635. DOI: 10.1016/j.diamond.2018.02.009.
- [200] J. Nakanishi, A. Otsuki, T. Oku, O. Ishiwata, and M. Murakami, “Formation of ohmic contacts to *p*-type diamond using carbide forming metals,” en, *Journal of Applied Physics*, vol. 76, no. 4, pp. 2293–2298, Aug. 15, 1994, ISSN: 0021-8979, 1089-7550. DOI: 10.1063/1.357649.
- [201] K. Ushizawa *et al.*, “Boron concentration dependence of raman spectra on {100} and {111} facets of b-doped cvd diamond,” en, *Diamond and Related Materials*, vol. 7, no. 11-12, pp. 1719–1722, Dec. 1998, ISSN: 09259635. DOI: 10.1016/S0925-9635(98)00296-9.
- [202] T. Sato *et al.*, “Transport of heavily boron-doped synthetic semiconductor diamond in the hopping regime,” en, *Physical Review B*, vol. 61, no. 19,

- pp. 12 970–12 976, May 15, 2000, ISSN: 0163-1829, 1095-3795. DOI: 10.1103/PhysRevB.61.12970.
- [203] S. Kagamihara *et al.*, “Parameters required to simulate electric characteristics of sic devices for n-type 4h-sic,” en, *Journal of Applied Physics*, vol. 96, no. 10, pp. 5601–5606, Nov. 15, 2004, ISSN: 0021-8979, 1089-7550. DOI: 10.1063/1.1798399.
- [204] M. Grünewald, H. Müller, P. Thomas, and D. Würtz, “Temperature dependence of the hopping hall mobility in spatially and energetically disordered systems,” *Le Journal de Physique Colloques*, vol. 42, no. C4, pp. C4-99-C4-102, Oct. 1981, ISSN: 0449-1947. DOI: 10.1051/jphyscol:1981417.
- [205] D. M. Malta, J. A. von Windheim, H. A. Wynands, and B. A. Fox, “Comparison of the electrical properties of simultaneously deposited homoepitaxial and polycrystalline diamond films,” en, *Journal of Applied Physics*, vol. 77, no. 4, pp. 1536–1545, Feb. 15, 1995, ISSN: 0021-8979, 1089-7550. DOI: 10.1063/1.358905.
- [206] N. Lambert *et al.*, “Modeling current transport in boron-doped diamond at high electric fields including self-heating effect,” en, *Diamond and Related Materials*, vol. 109, p. 108 003, Nov. 2020, ISSN: 09259635. DOI: 10.1016/j.diamond.2020.108003.
- [207] N. Sclar and E. Burstein, “Impact ionization of impurities in germanium,” en, *Journal of Physics and Chemistry of Solids*, vol. 2, no. 1, pp. 1–23, Mar. 1957, ISSN: 00223697. DOI: 10.1016/0022-3697(57)90002-1.
- [208] V. I. Sankin, A. M. Monakhov, P. P. Shkrebiy, P. L. Abramov, N. I. Sablina, and N. S. Averkiev, “Peculiarities of impact ionization of impurity al in sic

- polytypes,” en, *Applied Physics Letters*, vol. 97, no. 26, p. 262 118, Dec. 27, 2010, ISSN: 0003-6951, 1077-3118. DOI: 10.1063/1.3527964.
- [209] V. Mortet *et al.*, “Peculiarities of high electric field conduction in p-type diamond,” en, *Applied Physics Letters*, vol. 108, no. 15, p. 152 106, Apr. 11, 2016, ISSN: 0003-6951, 1077-3118. DOI: 10.1063/1.4946853.
- [210] Y. Song *et al.*, “Investigating non-equilibrium carrier lifetimes in nitrogen-doped and boron-doped single crystal hpht diamonds with an optical method,” en, *Applied Physics Letters*, vol. 112, no. 2, p. 022 103, Jan. 8, 2018, ISSN: 0003-6951, 1077-3118. DOI: 10.1063/1.5019587.
- [211] M. E. Levinshtein, T. T. Mnatsakanov, P. A. Ivanov, J. W. Palmour, M. K. Das, and B. A. Hull, “Self-heating of 4h-sic pin diodes at high current densities,” *Materials Science Forum*, vol. 600-603, pp. 1007–1010, Sep. 2008, ISSN: 1662-9752. DOI: 10.4028/www.scientific.net/MSF.600-603.1007.
- [212] H. Ghasemi and M. H. Mozaffari, “A simple proposal to reduce self-heating effect in soi mosfets,” en, *Silicon*, vol. 13, no. 11, pp. 4189–4198, Nov. 2021, ISSN: 1876-990X, 1876-9918. DOI: 10.1007/s12633-020-00773-y.
- [213] V. A. Vashchenko and V. F. Sinkevitch, *Physical limitations of semiconductor devices*. New York: Springer, 2008, OCLC: ocn172979451, ISBN: 978-0-387-74513-8.
- [214] J. R. Olson, R. O. Pohl, J. W. Vandersande, A. Zoltan, T. R. Anthony, and W. F. Banholzer, “Thermal conductivity of diamond between 170 and 1200 k and the isotope effect,” en, *Physical Review B*, vol. 47, no. 22, pp. 14 850–14 856, Jun. 1, 1993, ISSN: 0163-1829, 1095-3795. DOI: 10.1103/PhysRevB.47.14850.

- [215] *Atlas User's Manual*, en. Oct. 4, 2018.
- [216] M. Girolami, A. Bellucci, P. Calvani, R. Flammini, and D. M. Trucchi, “Radiation-assisted frenkel-poole transport in single-crystal diamond,” en, *Applied Physics Letters*, vol. 103, no. 8, p. 083 502, Aug. 19, 2013, ISSN: 0003-6951, 1077-3118. DOI: 10.1063/1.4818904.
- [217] G. Vincent, A. Chantre, and D. Bois, “Electric field effect on the thermal emission of traps in semiconductor junctions,” en, *Journal of Applied Physics*, vol. 50, no. 8, p. 5484, 1979, ISSN: 00218979. DOI: 10.1063/1.326601.
- [218] V. Mortet and A. Soltani, “Impurity impact ionization avalanche in p-type diamond,” en, *Applied Physics Letters*, vol. 99, no. 20, p. 202 105, Nov. 14, 2011, ISSN: 0003-6951, 1077-3118. DOI: 10.1063/1.3662403.
- [219] A. W. Livingstone and J. W. Allen, “Impact ionization of deep impurities in zinc selenide,” *Journal of Physics C: Solid State Physics*, vol. 6, no. 23, pp. 3491–3500, Nov. 27, 1973, ISSN: 0022-3719. DOI: 10.1088/0022-3719/6/23/023.
- [220] D. Caughey and R. Thomas, “Carrier mobilities in silicon empirically related to doping and field,” *Proceedings of the IEEE*, vol. 55, no. 12, pp. 2192–2193, 1967, ISSN: 0018-9219. DOI: 10.1109/PROC.1967.6123.
- [221] L. Reggiani, S. Bosi, C. Canali, F. Nava, and S. F. Kozlov, “Hole-drift velocity in natural diamond,” en, *Physical Review B*, vol. 23, no. 6, pp. 3050–3057, Mar. 15, 1981, ISSN: 0163-1829. DOI: 10.1103/PhysRevB.23.3050.

- [222] G. L. Pearson and J. Bardeen, “Electrical properties of pure silicon and silicon alloys containing boron and phosphorus,” en, *Physical Review*, vol. 75, no. 5, pp. 865–883, Mar. 1, 1949, ISSN: 0031-899X. DOI: 10.1103/PhysRev.75.865.
- [223] V. Mortet, N. Lambert, P. Hubík, and A. Soltani, “Model of carrier multiplication due to impurity impact ionization in boron-doped diamond,” en, NANOCON 2018 10th Int. Conf., Brno, Czech Republic: TANGER Ltd., 2018, pp. 41–45.
- [224] J. A. Von Windheim, V. Venkatesan, D. M. Malta, and K. Das, “Electrical characterization of semiconducting diamond thin films and single crystals,” en, *Journal of Electronic Materials*, vol. 22, no. 4, pp. 391–398, Apr. 1993, ISSN: 0361-5235, 1543-186X. DOI: 10.1007/BF02661667.
- [225] V. Mortet *et al.*, “Characterization of boron doped diamond epilayers grown in a nirim type reactor,” en, *Diamond and Related Materials*, vol. 17, no. 7-10, pp. 1330–1334, Jul. 2008, ISSN: 09259635. DOI: 10.1016/j.diamond.2008.01.087.
- [226] E. P. Visser, G. J. Bauhuis, G. Janssen, W. Vollenberg, v. J. P. Enckevort, and L. J. Giling, “Electrical conduction in homoepitaxial, boron-doped diamond films,” *Journal of Physics: Condensed Matter*, vol. 4, no. 36, pp. 7365–7376, Sep. 7, 1992, ISSN: 0953-8984, 1361-648X. DOI: 10.1088/0953-8984/4/36/011.
- [227] R. Locher, J. Wagner, F. Fuchs, M. Maier, P. Gonon, and P. Koidl, “Optical and electrical characterization of boron-doped diamond films,” en, *Diamond and Related Materials*, vol. 4, no. 5-6, pp. 678–683, May 1995, ISSN: 09259635. DOI: 10.1016/0925-9635(94)05297-2.

- [228] A. Masood, M. Aslam, M. A. Tamor, and T. J. Potter, “Synthesis and electrical characterization of boron-doped thin diamond films,” en, *Applied Physics Letters*, vol. 61, no. 15, pp. 1832–1834, Oct. 12, 1992, ISSN: 0003-6951, 1077-3118. DOI: 10.1063/1.108389.
- [229] G. Hurkx, D. Klaassen, M. Knuvers, and F. O’Hara, “A new recombination model describing heavy-doping effects and low-temperature behaviour,” [Online; accessed 2020-05-29], International Technical Digest on Electron Devices Meeting, Washington, DC, USA: IEEE, 1989, pp. 307–310. DOI: 10.1109/IEDM.1989.74285. [Online]. Available: <http://ieeexplore.ieee.org/document/74285/>.
- [230] A. K. Jonscher, “Free-carrier poole-frenkel effect in crystalline solids,” *Journal of Physics C: Solid State Physics*, vol. 3, no. 8, pp. L159–L162, Aug. 1, 1970, ISSN: 0022-3719. DOI: 10.1088/0022-3719/3/8/029.
- [231] K. D. Morhard, R. P. Huebener, W. Clauss, and J. Peinke, “Low-temperature avalanche breakdown in p-ge: Influence of the acceptor concentration,” en, *Journal of Applied Physics*, vol. 71, no. 7, pp. 3336–3338, Apr. 1992, ISSN: 0021-8979, 1089-7550. DOI: 10.1063/1.350955.
- [232] A. Hiraiwa and H. Kawarada, “Figure of merit of diamond power devices based on accurately estimated impact ionization processes,” en, *Journal of Applied Physics*, vol. 114, no. 3, p. 034506, Jul. 21, 2013, ISSN: 0021-8979, 1089-7550. DOI: 10.1063/1.4816312.
- [233] A. G. Chynoweth, “Ionization rates for electrons and holes in silicon,” en, *Physical Review*, vol. 109, no. 5, pp. 1537–1540, Mar. 1, 1958, ISSN: 0031-899X. DOI: 10.1103/PhysRev.109.1537.

- [234] C. R. Crowell and S. M. Sze, “Temperature dependence of avalanche multiplication in semiconductors,” en, *Applied Physics Letters*, vol. 9, no. 6, pp. 242–244, Sep. 15, 1966, ISSN: 0003-6951, 1077-3118. DOI: 10.1063/1.1754731.
- [235] L. Tirino, M. Weber, K. F. Brennan, E. Bellotti, and M. Goano, “Temperature dependence of the impact ionization coefficients in gaas, cubic sic, and zinc-blende gan,” en, *Journal of Applied Physics*, vol. 94, no. 1, pp. 423–430, Jul. 2003, ISSN: 0021-8979, 1089-7550. DOI: 10.1063/1.1579129.
- [236] S. A. Solin and A. K. Ramdas, “Raman spectrum of diamond,” en, *Physical Review B*, vol. 1, no. 4, pp. 1687–1698, Feb. 15, 1970, ISSN: 0556-2805. DOI: 10.1103/PhysRevB.1.1687.
- [237] A. C. Victor, “Heat capacity of diamond at high temperatures,” en, *The Journal of Chemical Physics*, vol. 36, no. 7, pp. 1903–1911, Apr. 1962, ISSN: 0021-9606, 1089-7690. DOI: 10.1063/1.1701288.
- [238] V. Y. Yurov, E. V. Bushuev, A. F. Popovich, A. P. Bolshakov, E. E. Ashkinazi, and V. G. Ralchenko, “Near-infrared refractive index of synthetic single crystal and polycrystalline diamonds at high temperatures,” en, *Journal of Applied Physics*, vol. 122, no. 24, p. 243 106, Dec. 28, 2017, ISSN: 0021-8979, 1089-7550. DOI: 10.1063/1.5008387.
- [239] J. B. Khurgin, “Mitigating hot phonons in high power optoelectronic devices based on wide gap semiconductors,” K.-T. Tsen, J.-J. Song, M. J. Cohen, and J. W. Glesener, Eds., [Online; accessed 2020-07-03], *Integrated Optoelectronic Devices 2007*, San Jose, CA, Feb. 8, 2007, 64710Y. DOI: 10.1117/12.705110. [Online]. Available: <http://proceedings.spiedigitallibrary.org/proceeding.aspx?doi=10.1117/12.705110>.

- [240] J. Liberis, I. Matulioniene, A. Matulionis, M. C. Lemme, H. Kurz, and M. Först, “Hot-phonon temperature and lifetime in biased boron-implanted  $\text{SiO}_2/\text{Si}/\text{SiO}_2$  channels,” *Semiconductor Science and Technology*, vol. 21, no. 6, pp. 803–807, Jun. 1, 2006, ISSN: 0268-1242, 1361-6641. DOI: 10.1088/0268-1242/21/6/017.
- [241] S. Barman and G. P. Srivastava, “Quantitative estimate of phonon scattering rates in different forms of diamond,” en, *Physical Review B*, vol. 73, no. 7, p. 073 301, Feb. 2, 2006, ISSN: 1098-0121, 1550-235X. DOI: 10.1103/PhysRevB.73.073301.
- [242] M. Kozák, F. Trojánek, and P. Malý, “Hot-carrier transport in diamond controlled by femtosecond laser pulses,” *New Journal of Physics*, vol. 17, no. 5, p. 053 027, May 18, 2015, ISSN: 1367-2630. DOI: 10.1088/1367-2630/17/5/053027.
- [243] N. Lambert *et al.*, “Highly phosphorus-doped polycrystalline diamond growth and properties,” en, *Diamond and Related Materials*, vol. 125, p. 108 964, May 2022, ISSN: 09259635. DOI: 10.1016/j.diamond.2022.108964.
- [244] M. A. Lobaev, D. B. Radishev, A. M. Gorbachev, A. L. Vikharev, and M. N. Drozdov, “Investigation of microwave plasma during diamond doping by phosphorus using optical emission spectroscopy,” en, *physica status solidi (a)*, vol. 216, no. 21, p. 1 900 234, Nov. 2019, ISSN: 1862-6300, 1862-6319. DOI: 10.1002/pssa.201900234.
- [245] D. Glindemann, M. Edwards, and O. Schrems, “Phosphine and methylphosphine production by simulated lightning—a study for the volatile phosphorus

- cycle and cloud formation in the earth atmosphere,” en, *Atmospheric Environment*, vol. 38, no. 39, pp. 6867–6874, Dec. 2004, ISSN: 13522310. DOI: 10.1016/j.atmosenv.2004.09.002.
- [246] A. R. Bossard, R. Kamga, and F. Raulin, “Gas phase synthesis of organophosphorus compounds and the atmosphere of the giant planets,” en, *Icarus*, vol. 67, no. 2, pp. 305–324, Aug. 1986, ISSN: 00191035. DOI: 10.1016/0019-1035(86)90111-9.
- [247] J. C. Richley, O. J. L. Fox, M. N. R. Ashfold, and Y. A. Mankelevich, “Combined experimental and modeling studies of microwave activated  $\text{CH}_4/\text{H}_2/\text{Ar}$  plasmas for microcrystalline, nanocrystalline, and ultrananocrystalline diamond deposition,” en, *Journal of Applied Physics*, vol. 109, no. 6, p. 063307, Mar. 15, 2011, ISSN: 0021-8979, 1089-7550. DOI: 10.1063/1.3562185.
- [248] J. Ma, J. C. Richley, M. N. R. Ashfold, and Y. A. Mankelevich, “Probing the plasma chemistry in a microwave reactor used for diamond chemical vapor deposition by cavity ring down spectroscopy,” en, *Journal of Applied Physics*, vol. 104, no. 10, p. 103305, Nov. 15, 2008, ISSN: 0021-8979, 1089-7550. DOI: 10.1063/1.3021095.
- [249] V. Mortet *et al.*, “Effect of pulsed methane gas flow on the incorporation of phosphorous in diamond,” en, *Diamond and Related Materials*, vol. 124, p. 108928, Apr. 2022, ISSN: 09259635. DOI: 10.1016/j.diamond.2022.108928.
- [250] G. Frangieh, M.-A. Pinault, J. Barjon, F. Jomard, and J. Chevallier, “Incorporation of arsenic in diamond grown by chemical vapor deposition,”

- en, *physica status solidi (a)*, vol. 205, no. 9, pp. 2207–2210, Sep. 2008, ISSN: 18626300, 18626319. DOI: 10.1002/pssa.200879726.
- [251] O. A. Williams, O. Douhéret, M. Daenen, K. Haenen, E. Ōsawa, and M. Takahashi, “Enhanced diamond nucleation on monodispersed nanocrystalline diamond,” en, *Chemical Physics Letters*, vol. 445, no. 4-6, pp. 255–258, Sep. 2007, ISSN: 00092614. DOI: 10.1016/j.cplett.2007.07.091.
- [252] J. J. Gracio, Q. H. Fan, and J. C. Madaleno, “Diamond growth by chemical vapour deposition,” *Journal of Physics D: Applied Physics*, vol. 43, no. 37, p. 374017, Sep. 22, 2010, ISSN: 0022-3727, 1361-6463. DOI: 10.1088/0022-3727/43/37/374017.
- [253] M. Noda, A. Marui, T. Suzuki, and M. Umeno, “Deposition of diamond film on silicon and quartz substrates located near dc plasma,” en, *Diamond and Related Materials*, vol. 14, no. 11-12, pp. 1757–1760, Nov. 2005, ISSN: 09259635. DOI: 10.1016/j.diamond.2005.08.050.
- [254] J. Liu *et al.*, “High-rate homoepitaxial growth of cvd single crystal diamond by dc arc plasma jet at blow-down (open cycle) mode,” en, *Diamond and Related Materials*, vol. 46, pp. 42–51, Jun. 2014, ISSN: 09259635. DOI: 10.1016/j.diamond.2014.04.008.
- [255] O. Babchenko, Š. Potocký, T. Ižák, K. Hruška, Z. Bryknar, and A. Kromka, “Influence of surface wave plasma deposition conditions on diamond growth regime,” en, *Surface and Coatings Technology*, vol. 271, pp. 74–79, Jun. 2015, ISSN: 02578972. DOI: 10.1016/j.surfcoat.2015.01.012.
- [256] N. S. Lambert, K.-d. Sung, and V. Mortet, “Optical emission spectroscopy analysis of microwave plasma enhanced chemical vapor deposition systems

- dynamic gas response,” en, *physica status solidi (a)*, pssa.202200322, Aug. 19, 2022, ISSN: 1862-6300, 1862-6319. DOI: 10.1002/pssa.202200322.
- [257] H. Pendar and J. J. Socha, “Estimation of instantaneous gas exchange in flow-through respirometry systems: A modern revision of bartholomew’s z-transform method,” en, *PLOS ONE*, vol. 10, no. 10, J. L. Rummer, Ed., e0139508, Oct. 14, 2015, ISSN: 1932-6203. DOI: 10.1371/journal.pone.0139508.
- [258] G. A. Bartholomew, D. B. van Vleck, and C. Masters Vleck, “Instantaneous measurements of oxygen consumption during pre-flight warm-up and post-flight cooling in sphingid and saturniid moths,” *The Journal of Experimental Biology*, vol. 90, pp. 17–32, 1981.
- [259] B. Porat, *A course in digital signal processing*. New York: John Wiley, 1997, ISBN: 978-0-471-14961-3.
- [260] J. D. Hamilton, *Time series analysis*. Princeton, N.J: Princeton University Press, 1994, ISBN: 978-0-691-04289-3.
- [261] Y. G. Gogotsi, P. Kofstad, M. Yoshimura, and K. G. Nickel, “Formation of sp<sup>3</sup>-bonded carbon upon hydrothermal treatment of sic,” en, *Diamond and Related Materials*, vol. 5, no. 2, pp. 151–162, Mar. 1996, ISSN: 09259635. DOI: 10.1016/0925-9635(95)00341-X.
- [262] H. Kato *et al.*, “Heavily phosphorus-doped nano-crystalline diamond electrode for thermionic emission application,” en, *Diamond and Related Materials*, vol. 63, pp. 165–168, Mar. 2016, ISSN: 09259635. DOI: 10.1016/j.diamond.2015.08.002.

- [263] S. Curat, H. Ye, O. Gaudin, R. B. Jackman, and S. Koizumi, “An impedance spectroscopic study of n-type phosphorus-doped diamond,” en, *Journal of Applied Physics*, vol. 98, no. 7, p. 073701, Oct. 2005, ISSN: 0021-8979, 1089-7550. DOI: 10.1063/1.2058183.
- [264] S. Koizumi, “Growth and characterization of phosphorus doped n-type diamond thin films,” en, *physica status solidi (a)*, vol. 172, no. 1, pp. 71–78, Mar. 1999, ISSN: 00318965, 1521396X. DOI: 10.1002/(SICI)1521-396X(199903)172:1<71::AID-PSSA71>3.0.CO;2-N.
- [265] H. Spicka *et al.*, “Investigations of the incorporation of b, p and n into cvd-diamond films by secondary ion mass spectrometry,” en, *Diamond and Related Materials*, vol. 5, no. 3-5, pp. 383–387, Apr. 1996, ISSN: 09259635. DOI: 10.1016/0925-9635(95)00381-9.
- [266] W. Janssen *et al.*, “Substitutional phosphorus incorporation in nanocrystalline cvd diamond thin films: Substitutional phosphorus incorporation in nanocrystalline cvd diamond thin films,” en, *physica status solidi (RRL) - Rapid Research Letters*, vol. 8, no. 8, pp. 705–709, Aug. 2014, ISSN: 18626254. DOI: 10.1002/pssr.201409235.
- [267] N. Temahuki *et al.*, “New process for electrical contacts on (100) n-type diamond,” en, *physica status solidi (a)*, vol. 214, no. 11, p. 1700466, Nov. 2017, ISSN: 18626300. DOI: 10.1002/pssa.201700466.
- [268] P. Hazdra *et al.*, “Low-resistance ohmic contacts on boron-doped {113} oriented homoepitaxial diamond layers,” en, *Diamond and Related Materials*,

- vol. 121, p. 108 797, Jan. 2022, ISSN: 09259635. DOI: 10.1016/j.diamond.2021.108797.
- [269] A. Traoré, P. Muret, A. Fiori, D. Eon, E. Gheeraert, and J. Pernot, “Zr/oxidized diamond interface for high power schottky diodes,” en, *Applied Physics Letters*, vol. 104, no. 5, p. 052 105, Feb. 3, 2014, ISSN: 0003-6951, 1077-3118. DOI: 10.1063/1.4864060.
- [270] T. Hanada, S. Ohmagari, J. H. Kaneko, and H. Umezawa, “High yield uniformity in pseudo-vertical diamond schottky barrier diodes fabricated on half-inch single-crystal wafers,” en, *Applied Physics Letters*, vol. 117, no. 26, p. 262 107, Dec. 28, 2020, ISSN: 0003-6951, 1077-3118. DOI: 10.1063/5.0027729.
- [271] S. Ohmagari *et al.*, “Toward high-performance diamond electronics: Control and annihilation of dislocation propagation by metal-assisted termination,” en, *physica status solidi (a)*, vol. 216, no. 21, p. 1 900 498, Nov. 2019, ISSN: 1862-6300, 1862-6319. DOI: 10.1002/pssa.201900498.

# Appendix

## Publications

### Publications Related to the Thesis

#### Articles in Impacted Journals

- *"Optical Emission Spectroscopy Analysis of Microwave Plasma Enhanced Chemical Vapor Deposition Systems Dynamic Gas Response"*  
**N. Lambert**, K.-D. Sung, V. Mortet, *Physica Status Solidi (a)* (2022)  
(manuscript accepted for publication)
- *"Highly phosphorus-doped polycrystalline diamond growth and properties"*  
**N. Lambert**, Z. Weiss, L. Klimša, J. Kopeček, Z. Gedeonová, P. Hubík, V. Mortet, *Diamond and Related Materials* **125** (2022), 108964
- *"Effect of pulsed methane gas flow on the incorporation of phosphorous in diamond"*  
V. Mortet, A. Taylor, M. Davydova, M. Lamač, **N. Lambert**, I. Elantsev, J. Lorinčík, D. Troadec, M. Vronka, S. Potocký, *Diamond and Related Materials* **124** (2022), 108928

**Contribution:** Acid cleaning of substrates, sample weighting.

- *"Modeling current transport in boron-doped diamond at high electric fields including self-heating effect"*

**N. Lambert**, A. Taylor, P. Hubík, J. Bulíř, J. More-Chevalier, H. Karaca, C. Fleury, J. Voves, Z. Šobáň, D. Pogany, V. Mortet, *Diamond and Related Materials* **109** (2020), 108003

- *"Conductivity of boron-doped diamond at high electrical field"*

V. Mortet, L. Drbohlavová, **N. Lambert**, A. Taylor, P. Ashcheulov, M. Davydova, J. Lorinčík, M. Aleshin, P. Hubík, *Diamond and Related Materials* **98** (2019), 107476

**Contribution:** Quasi-static I-V characteristics measurement on boron-doped diamond using the TLP setup.

## Conferences

- *"Effect of pulsed precursor injection in the synthesis of doped diamond"*

K.-D. Sung, **N. Lambert**, Š. Havlová, M. Novotný, L. Klimša, Z. Weiss, V. Mortet, Poster presentation for the 18<sup>th</sup> International Conference on Plasma Surface Engineering (PSE), 12<sup>th</sup> September – 15<sup>th</sup> September 2022, Erfurt, Germany

**Contribution:** OES plasma characterization.

- *"Properties of heavily phosphorus-doped diamond"*

V. Mortet, **N. Lambert**, K.-D. Sung, P. Hubík, Z. Gedeonová, A. Laposa, V. Povolný, P. Hazdra, Poster presentation for the 32<sup>nd</sup> International Conference on Diamond and Carbon Materials (ICDCM), 4<sup>th</sup> September – 8<sup>th</sup> September

2022, Lisbon, Portugal

**Contribution:** OES plasma characterization.

- *"Study of dynamic gas response of microwave plasma enhanced chemical vapor deposition systems by optical emission spectroscopy"*

**N. Lambert**, V. Mortet, Poster presentation and proceeding for the 13<sup>th</sup> International Conference on Nanomaterials - Research & Applications (NANOCON), 20<sup>th</sup> October – 22<sup>nd</sup> October 2021, Brno, Czech Republic

- *"Highly phosphorus-doped nano-crystalline diamond growth and properties"*

**N. Lambert**, Z. Weiss, L. Klimša, L. Fekete, V. Mortet, Poster presentation for the 31<sup>st</sup> International Conference on Diamond and Carbon Materials (ICDCM), 6<sup>th</sup> September – 9<sup>th</sup> September 2021, online

- *"Experimental and modeled I-V characteristics of boron-doped diamond at high electric fields including self-heating effect"*

**N. Lambert**, A. Taylor, P. Hubík, J. Bulíř, J. More-Chevalier, H. Karaca, C. Fleury, J. Voves, Z. Šobáň, D. Pogany, V. Mortet, Oral presentation for Material Research Society (MRS) Fall Meeting & Exhibit 2019, 1<sup>st</sup> December – 6<sup>th</sup> December 2019, Boston, USA

- *"Modelling I-V characteristics of boron-doped diamond at high electric field including self-heating effect"*

**N. Lambert**, A. Taylor, P. Hubík, J. Bulíř, J. More-Chevalier, H. Karaca, C. Fleury, D. Pogany, V. Mortet, Poster presentation for the 30<sup>th</sup> International Conference on Diamond and Carbon Materials (ICDCM), 8<sup>th</sup> September – 12<sup>th</sup> September 2019, Seville, Spain

- *"Model of carrier multiplication due to impurity impact ionization"*  
V. Mortet, **N. Lambert**, P. Hubík, Ali Soltani, Poster presentation and proceeding for the 10<sup>th</sup> International Conference on Nanomaterials - Research & Applications (NANOCON), 17<sup>th</sup> October – 19<sup>th</sup> October 2018, Brno, Czech Republic  
**Contribution:** Quasi-static I-V characteristics measurement on boron-doped diamond using the TLP setup.
- *"Blumlein pulse generator "TLP 2.0"?"*  
D. Trémouilles, V. Mortet, **N. Lambert**, Oral presentation for the 2018 International Electrostatic Discharge Workshop (IEW), 14<sup>th</sup> May – 18<sup>th</sup> May 2018, Corsendonk, Belgium  
**Contribution:** Development of the Blumlein TLP measurement setup.
- *"Electrical breakdown in boron-doped diamond measured by transmission line pulsed method"*  
**N. Lambert**, A. Taylor, P. Hubík, D. Trémouilles, J. Bulíř, V. Mortet, Poster presentation for the 23<sup>rd</sup> Hasselt Diamond Workshop (SBDD), 6<sup>th</sup> March – 9<sup>th</sup> March 2018, Hasselt, Belgium
- *"Development of 100 ns Blumlein TLP generator for: study of high electric field properties in boron-doped diamond"*  
**N. Lambert**, D. Trémouilles, A. Taylor, P. Hubík, J. More-Chevalier, J. Bulíř, V. Mortet, Poster presentation and proceeding for the 9<sup>th</sup> International Conference on Nanomaterials - Research & Applications (NANOCON), 18<sup>th</sup> September – 20<sup>th</sup> September 2017, Brno, Czech Republic

## Other Publications

### Articles in Impacted Journals

- *"Pseudo-vertical Mo/Au Schottky diodes on 113 oriented boron doped homoepitaxial diamond layers"*

P. Hazdra, A. Laposa, Z. Šobáň, A. Taylor, **N. Lambert**, V. Povolný, J. Kroutil, Z. Gedeonová, P. Hubík, V. Mortet, *Diamond and Related Materials* **126** (2022), 109088

**Contribution:** Acid cleaning, hydrogen plasma treatment, and ozone treatment of samples.

- *"Low-resistance ohmic contacts on boron-doped 113 oriented homoepitaxial diamond layers"*

P. Hazdra, A. Laposa, Z. Šobáň, J. Voves, **N. Lambert**, M. Davydova, V. Povolný, A. Taylor, V. Mortet, *Diamond and Related Materials* **121** (2022), 108797

**Contribution:** Acid cleaning, hydrogen plasma treatment, and ozone treatment of samples.

- *"Properties of boron-doped (113) oriented homoepitaxial diamond layers"*

V. Mortet, A. Taylor, **N. Lambert**, Z. Gedeonová, L. Fekete, J. Lorinčík, L. Klimša, J. Kopeček, P. Hubík, Z. Šobáň, A. Laposa, M. Davydova, J. Voves, A. Pošta, V. Povolný, P. Hazdra, *Diamond and Related Materials* **111** (2021), 108223

**Contribution:** Acid cleaning of substrates, sample weighting. Hall effect measurement contacts fabrication.

- *"New perspectives for heavily boron-doped diamond Raman spectrum analysis"*  
V. Mortet, I. Gregora, A. Taylor, **N. Lambert**, P. Ashcheulov, Z. Gedeonová,  
P. Hubík, Carbon **168** (2020), 319-327

**Contribution:** Development of a Python algorithm for Raman spectra analysis. Calculation of boron concentration in doped diamond layers using this algorithm.

- *"Comparison of ohmic contact formation of titanium and zirconium on boron doped diamond"*  
V. Mortet, A. Taylor, M. Davydova, L. Fekete, Z. Vlčková Živcová, L. Klimša,  
**N. Lambert**, P. Hubík, D. Trémouilles, A. Soltani, MRS Advances **3/33**  
(2018), 1931-1935

**Contribution:** Acid cleaning of substrates, sample weighting.

## Conferences

- *"Study of cracks formation in highly – low boron-doped epitaxial (113) diamond bilayers"*

V. Mortet, L. Klimša, **N. Lambert**, M. Davydova, J. Kopeček, S. Sedláková,  
Poster presentation and proceeding for the 13<sup>th</sup> International Conference on  
Nanomaterials - Research & Applications (NANOCON), 20<sup>th</sup> October – 22<sup>nd</sup>  
October 2021, Brno, Czech Republic

**Contribution:** Acid cleaning of substrates, sample weighting.

- *"Characterization of the very low contact resistance on heavily boron doped (113) CVD diamond"*

J. Voves, A. Laposa, Z. Šobáň, P. Hazdra, V. Povolný, V. Mortet, **N. Lam-**

**bert**, M. Davydova, Oral presentation and proceeding for the 13<sup>th</sup> International Conference on Nanomaterials - Research & Applications (NANOCON), 20<sup>th</sup> October – 22<sup>nd</sup> October 2021, Brno, Czech Republic

**Contribution:** Acid cleaning, hydrogen plasma treatment, and ozone treatment of samples.

- *"Low-resistance ohmic contacts to boron-doped (113) oriented homoepitaxial diamond layers"*

P. Hazdra, A. Laposa, Z. Šobáň, J. Voves, **N. Lambert**, M. Davydova, V. Povolný, A. Taylor, V. Mortet, Poster presentation for the 31<sup>st</sup> International Conference on Diamond and Carbon Materials (ICDCM), 6<sup>th</sup> September – 9<sup>th</sup> September 2021, online

**Contribution:** Acid cleaning, hydrogen plasma treatment, and ozone treatment of samples.

- *"Effect of the crystalline orientation of the substrate on boron-doped diamond growth"*

V. Mortet, A. Taylor, J. Jiránek, L. Fekete, L. Klimša, D. Šimek, **N. Lambert**, S. Sedláková, P. Hazdra, Oral presentation for the 31<sup>st</sup> International Conference on Diamond and Carbon Materials (ICDCM), 6<sup>th</sup> September – 9<sup>th</sup> September 2021, online

**Contribution:** Acid cleaning of substrates, sample weighting.

- *"Effect of the substrate crystalline orientation on the surface morphology and boron incorporation into epitaxial diamond layers"*

J. Voves, A. Pošta, M. Davydova, A. Laposa, V. Povolný, P. Hazdra, **N. Lambert**, S. Sedláková, V. Mortet, Poster presentation and proceeding for

the 12<sup>th</sup> International Conference on Nanomaterials - Research & Applications (NANOCON), 21<sup>st</sup> October – 23<sup>rd</sup> October 2020, Brno, Czech Republic

**Contribution:** Acid cleaning of substrates, sample weighting.

- *"Properties of boron-doped diamond layers grown on atomic stepped (113) surfaces"*

V. Mortet, A. Taylor, **N. Lambert**, Z. Gedeonová, P. Ascheulov, S. Sedláková, L. Fekete, J. Lorincik, J. Bulíř, L. Klimša, P. Hubík, Poster presentation for the 30<sup>th</sup> International Conference on Diamond and Carbon Materials (ICDCM), 8<sup>th</sup> September – 12<sup>th</sup> September 2019, Seville, Spain

**Contribution:** Acid cleaning of substrates, sample weighting.

## Projects

- *"Phosphorous n-type doped diamond growth using pulsed gas in chemical vapour deposition"*

**N. Lambert** (main investigator), V. Mortet (supervisor), SGS Student Grant (Grant n° SGS21/057/OHK3/1T/13), 2021

## Contributions to the work presented in this thesis

Table 7.5: Contributions to the work presented in this thesis with the respective list of contributors

<b>Contributions</b>	<b>Contributors</b>
Boron-doped diamond growth	V. Mortet, A. Taylor
AFM imaging on boron-doped diamond	L. Fekete
Design and microfabrication of electrodes on boron-doped diamond	<b><i>N. Lambert</i></b>
SIMS measurement on boron-doped diamond	Jan Lorinčík, M. Aleshin
Raman spectroscopy measurement on boron-doped diamond	<b><i>N. Lambert</i></b>
Hall effect measurement on boron-doped diamond	P. Hubík, <b><i>N. Lambert</i></b>
TLP bench design and fabrication	V. Mortet, <b><i>N. Lambert</i></b>
TLP measurements on boron-doped diamond	<b><i>N. Lambert</i></b>
TIM measurements on boron-doped diamond	D. Pogany, H. Karaca, <b><i>N. Lambert</i></b>
Modeling of boron-doped diamond under high electric fields	<b><i>N. Lambert</i></b>
Phosphorus-doped diamond growth	<b><i>N. Lambert</i></b>
SEM imaging on phosphorus-doped diamond	L. Klimša
Growth rate measurements on phosphorus-doped diamond	<b><i>N. Lambert</i></b>
PECVD reactors time response study	<b><i>N. Lambert</i></b>
Raman spectroscopy measurement on phosphorus-doped diamond	<b><i>N. Lambert</i></b>
GDOES measurement on phosphorus-doped diamond	Z. Weiss

## **Selected publications**



# Modeling current transport in boron-doped diamond at high electric fields including self-heating effect



N. Lambert<sup>a,b,\*</sup>, A. Taylor<sup>a</sup>, P. Hubík<sup>a</sup>, J. Bulíř<sup>a</sup>, J. More-Chevalier<sup>a</sup>, H. Karaca<sup>c</sup>, C. Fleury<sup>c,d</sup>, J. Voves<sup>b</sup>, Z. Šobán<sup>a</sup>, D. Pogany<sup>c</sup>, V. Mortet<sup>a,e</sup>

<sup>a</sup> FZU - Institute of Physics of the Czech Academy of Sciences, Na Slovance 1999/2, 182 21 Prague 8, Czech Republic

<sup>b</sup> Faculty of Electrical Engineering, Czech Technical University in Prague, Technická 1902/2, 166 27 Prague, Czech Republic

<sup>c</sup> Institute of Solid State Electronics, Technische Universität Wien, Gusshausstraße 25, 1040 Vienna, Austria

<sup>d</sup> Silicon Austria Labs, Europastraße 12, 9524 Villach, Austria

<sup>e</sup> Faculty of Biomedical Engineering, Czech Technical University in Prague, Sítina 3105, 272 01 Kladno, Czech Republic

## ARTICLE INFO

### Keywords:

Boron-doped diamond  
Pulsed measurement  
Impurity impact ionization  
Self-heating  
High electric field measurement  
Thermal simulation

## ABSTRACT

In this work, current multiplication at high electric field in epitaxial boron-doped diamond with high acceptor concentration is analyzed, including self-heating effect and impurity impact ionization. Quasi-static current-voltage (I-V) characteristics were measured using a transmission-line pulse setup with 100 ns pulse duration on samples with two Ohmic titanium/gold electrodes. Unambiguous exponential and super-exponential behaviors are observed in the I-V curves along with, in some cases, negative differential resistance. The self-heating effect is analyzed using transient interferometric mapping of the thermal energy distribution between electrodes with a ns time scale. Measured I-V characteristics are modeled by finite element method and by considering boron acceptor ionization due to self-heating effect and impurity impact ionization. Simulated I-V characteristics, in particular the appearance of the negative differential resistance region attributed to self-heating, are in good agreement with experimental data.

## 1. Introduction

Diamond is a semiconductor with intrinsic properties particularly promising for power electronics with high thermal conductivity, high carrier mobility and high breakdown field [1]. The development of diamond-based electronic devices is currently supported by steady progress in n-type [2] and p-type [3] doping and hetero-epitaxial [4] diamond growth. These achievements have enabled demonstration of various diodes [5–7] and transistors [8,9]. Knowledge of diamond electrical properties in high electric fields is crucial in the design and fabrication of power electronic devices. Contrary to other low band gap semiconductors, used in microelectronics, only a small part of dopants (boron or phosphorus) is ionized at room temperature in diamond [10]. Recent experimental studies at high electric fields of boron-doped diamond reported a rapid current multiplication above a threshold voltage, which is a function of the inter-electrode gap, the boron concentration and the temperature [11,12]. This phenomenon has been attributed to Impurity Impact Ionization (III), a freeze-out regime effect, which has been also reported for germanium and silicon carbide [13,14].

In this article, we analyze by finite element simulation the experimental transient voltage/current response and related quasi-static I-V characteristics of boron-doped diamond devices. We discuss different mechanisms to interpret the observed exponential I-V characteristic and Negative Differential Resistance (NDR) regime: Poole-Frenkel Effect (PFE) [15], Phonon-Assisted Tunneling Effect (PATE) [16], III, and Self-Heating Effect (SHE), and we discuss their role regarding the observed current multiplication.

## 2. Experimental setup

Epitaxial boron-doped diamond (100) layers were grown by microwave plasma enhanced chemical vapor deposition using a commercial ASTeX 5010 reactor (Seki Technotron, Japan) in a hydrogen plasma with a minute addition of methane and trimethylborane [12]. The boron concentration [B] of the layers, which ranges from  $3.2 \times 10^{18} \text{ cm}^{-3}$  to  $6.3 \times 10^{19} \text{ cm}^{-3}$  (details are given in Table 1), was calculated from the incorporation ratio determined from Secondary Ion Mass Spectroscopy (SIMS) measurements of boron-doped diamonds samples from reference [12]. The error on the calculated boron

\* Corresponding author at: FZU - Institute of Physics of the Czech Academy of Sciences, Na Slovance 1999/2, 182 21 Prague 8, Czech Republic.  
E-mail address: [lambert@fzu.cz](mailto:lambert@fzu.cz) (N. Lambert).

<https://doi.org/10.1016/j.diamond.2020.108003>

Received 23 April 2020; Received in revised form 3 July 2020; Accepted 7 July 2020

Available online 22 July 2020

0925-9635/ © 2020 Elsevier B.V. All rights reserved.

**Table 1**

Physical characteristics of diamond samples and simulation parameters used in the finite element method simulation.

		Sample A	Sample B	Sample C	Sample D
Physical characteristics					
	Geometry of electrodes	Circular	Circular	Circular	Parallel
	Inter-electrode gap ( $\mu\text{m}$ )	16.6	12.8	14.8	14.3
	Doped diamond layer thickness ( $\mu\text{m}$ )	3.36	5.50	3.27	1.36
	Boron concentration (estimated from SIMS data in reference [12]) ( $\text{cm}^{-3}$ )	$3.2 \times 10^{18}$	$3.8 \times 10^{19}$	$6.3 \times 10^{19}$	$3.6 \times 10^{19}$
	Breakdown voltage (V)	110	125	215	255
Simulation parameters					
PATE	Carrier lifetime [20] (s)		$1.2 \times 10^{-11}$		
	Carrier capture cross section [21] ( $\text{cm}^{-2}$ )		$10^{-14}$		
SHE & III	Donor concentration ( $\text{cm}^{-3}$ )	$4.8 \times 10^{16}$	$1.9 \times 10^{18}$	$4.1 \times 10^{18}$	$3.0 \times 10^{18}$
	$A_{\alpha}$ ( $\text{cm}^{-1}$ )	$1.4 \times 10^3$	$1.2 \times 10^3$	$1.0 \times 10^3$	$1.2 \times 10^3$
	$B_{\alpha}$ ( $\text{V}\cdot\text{cm}^{-1}$ )	$8.4 \times 10^4$	$4.6 \times 10^4$	$6.2 \times 10^4$	$4.6 \times 10^4$
	$A_{\text{cv}}$ ( $\text{J}\cdot\text{cm}^{-3}\cdot\text{K}^{-1}$ )			$4.0 \times 10^{-1}$	
	$B_{\text{cv}}$ ( $\text{J}\cdot\text{cm}^{-3}\cdot\text{K}^{-2}$ )			$1.1 \times 10^{-2}$	
	$C_{\text{cv}}$ ( $\text{J}\cdot\text{cm}^{-3}\cdot\text{K}^{-3}$ )			$-4.0 \times 10^{-6}$	
	$D_{\text{cv}}$ ( $\text{J}\cdot\text{K}\cdot\text{cm}^{-3}$ )			$-1.1 \times 10^5$	
	$v_{\text{sat}}$ ( $\text{cm}\cdot\text{s}^{-1}$ )			$1.1 \times 10^7$	
	$\beta_{\text{sat}}$			$9.5 \times 10^{-1}$	

concentration is about  $2 \times 10^{18} \text{ cm}^{-3}$ . Transient response and quasi-static current-voltage (I-V) characteristics were measured using a 100 ns transmission-line pulse setup [9] on concentric ring-and-disk electrodes test structures with an inner disk electrode diameter of 150  $\mu\text{m}$  and an inter-electrode gap of around 15  $\mu\text{m}$ . The ring-disk concentric electrodes have Ohmic contacts consisting of a titanium (10 nm) and gold (200 nm) bilayer deposited by e-beam evaporation in an Edwards Auto 500 vacuum coater and annealed at 450  $^{\circ}\text{C}$  for 20 min [17]. The electrodes were patterned by photolithography and wet chemical etching of the titanium and gold bilayer. The transient heat energy distribution between the electrodes was measured by Transient Interferometric Mapping (TIM) method [18]. The temperature-variation in the boron-doped diamond layer was measured via the change in the diamond refractive index, which results in a change in phase shift of a probing laser beam [19]. The probing beam goes through the sample from the backside, reflects on the top surface, and returns to the microscope objective. The optical phase shift, which is detected interferometrically, is proportional to the heat energy density in the sample [18]. The samples are stressed by 100 ns long voltage pulses at a 1 Hz repetition frequency (assuring cooling to room temperature before the next pulse) while transient phase shift is recorded. The phase distribution is determined point-by-point by moving the beam position. As the system does not allow measurements on test structures with circular geometries, TIM measurements were carried out on 75  $\mu\text{m}$  wide parallel titanium/gold electrodes with a 14.3  $\mu\text{m}$  inter-electrode gap patterned (Table 1).

### 3. Experimental results

Fig. 1 shows typical characteristic voltage and current waveforms of boron-doped diamond sample B ( $[B] = 3.8 \times 10^{19} \text{ cm}^{-3}$ ) during voltage pulses with different charging voltages  $V_{\text{ch}}$ . At applied voltages lower than 100 V, the voltage and current waveforms are nearly flat during the 100 ns pulse, which indicates that there is no significant heating and temperature variation in the device. At larger applied voltages, both the voltage and current vary in time, which is characteristic of thermal runaway due to SHE and the current intensity further increases with the increasing  $V_{\text{ch}}$  until catastrophic breakdown. This phenomenon is also visible in Fig. 1c in which I-V curves have been plotted for four different averaging periods during the voltage pulse. For a voltage lower than 100 V, the I-V curves are very similar while a divergence is observed for a voltage higher than 100 V. The later the averaging is done during the pulse, the higher the resulting current is. A NDR region in the I-V curve also emerges for longer times at currents above 1 A. The spike at the beginning of the current pulse (observed in

Fig. 1b) is an artefact due to the propagation of the signal in the cable between the probe and the sample.

Fig. 2 shows quasi-static I-V characteristics for all samples in linear (a) and semi-logarithmic (b) scale determined from waveforms with different  $V_{\text{ch}}$  (cf. also Fig. 1). The average value of voltage and current were calculated at the end of each pulse, i.e. between 85 ns and 95 ns from the beginning of each pulse. Each curve exhibits a short linear part up to approximately 50 V which transitions to an exponential behavior as the voltage increases. Finally, the current increases even further with a super-exponential evolution until the breakdown voltage ( $V_{\text{bd}}$ ) indicated by dashed lines in Fig. 2 and reported in Table 1. Sample B shows a NDR region at currents above 1.0 A, i.e. for  $V_{\text{ch}}$  superior to 150 V, cf. also Fig. 1c. The instantaneous voltage decreases rapidly while the instantaneous current increases (Fig. 1), causing the NDR.

Besides the III effect, the origin of the non-linear increase in current, especially the NDR regime, and the following breakdown observed in I-V characteristics could be attributed to SHE. Therefore, TIM measurements were carried-out on boron-doped diamond layers with parallel electrodes to investigate the possible self-heating effect. Thermal energy distribution maps were obtained through multiple pulsed measurements. Since repeated pulses in the NDR regime gradually degrade the electrodes, TIM measurements were performed below and at the onset of the NDR region.

Fig. 3a shows the phase shift distribution in the inter-electrode gap space of sample D below the NDR regime's onset, i.e. at a constant (final) current 50 mA in the exponential region. This condition is indicated by the left arrow in the I-V curve of sample D in Fig. 2. The phase shift increases non-linearly with time until the end of the pulse ( $t = 100 \text{ ns}$ ), where it is at maximum (0.05 rad) and then decreases. The uniform phase shift along the device's electrodes width (X-direction) demonstrates a uniform current distribution.

Fig. 3b shows TIM measurement made at the onset of the NDR, i.e. at a current of 250 mA (see the right arrow label in the I-V curve of sample D in Fig. 2). While the phase shift at  $t = 50 \text{ ns}$  is still homogeneous along the X-axis, it becomes non-uniform at longer times and forms two peaks at the end of the pulse with a maximum value of approximately 0.24 rad. The two peaks are attributed to the formation of two hot spots between the electrodes due to current filamentation and thermal runaway [22].

Fig. 3c represents the measured phase shift between the electrodes along the electric current path, i.e. perpendicularly to the electrodes, for the current of 0.25 A and positive polarity on the right electrode. The heat distribution peaks in the region between the electrodes. The phase shift distribution is nearly identical for the opposite polarity between the electrodes. The sharp negative peaks of the phase shift at

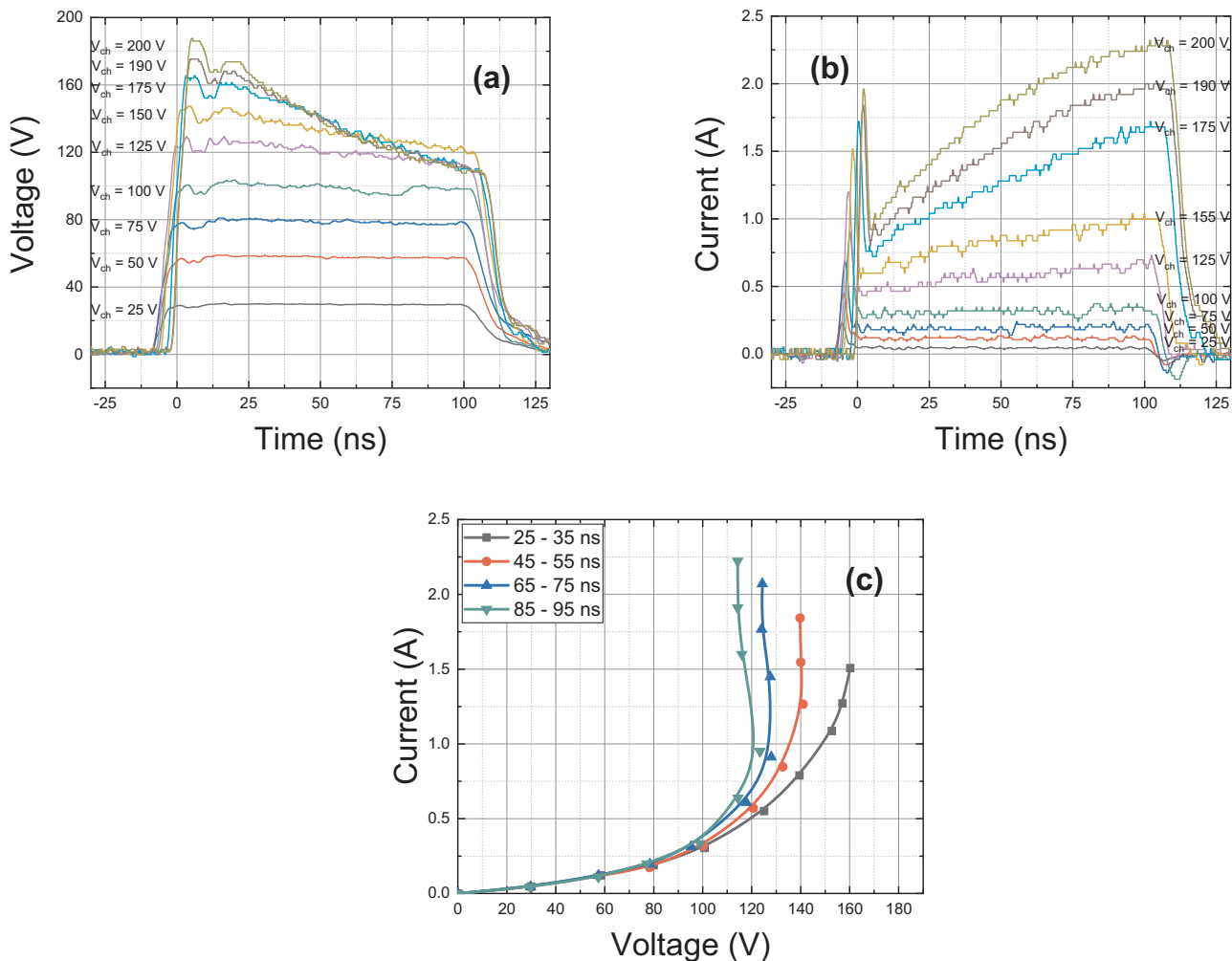


Fig. 1. Measured (a) voltage and (b) current waveform of sample B ( $[B] = 3.8 \times 10^{19} \text{ cm}^{-3}$ ) for different charging voltage  $V_{ch}$ , and I-V characteristics (c) calculated for different averaging periods in the voltage (a) and current (b) waveforms. The initial peak of current in (b) and small voltage steps in (a) are artefacts due to different spatial position of voltage and current probes and reflections. The lines in (c) are for eye-guiding.

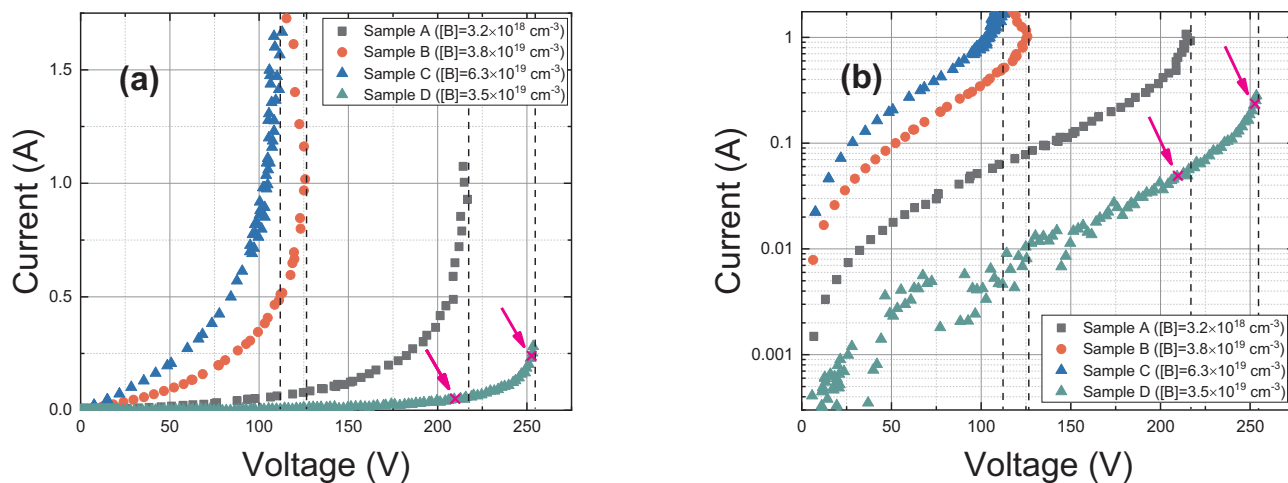
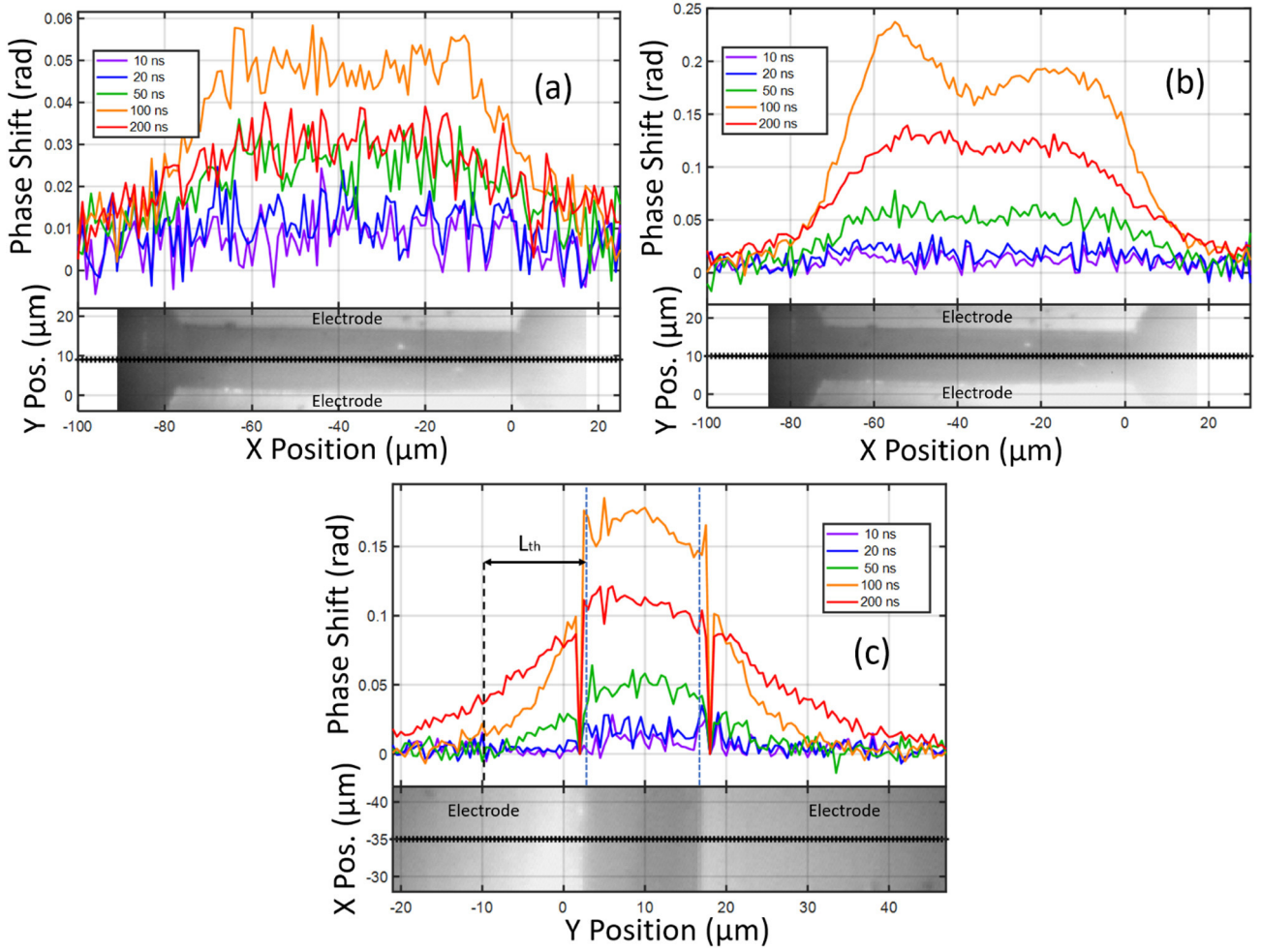


Fig. 2. Current-voltage characteristic of studied devices in linear and semi-logarithmic (b) scales. In sample D, two measurement conditions (50 mA and 250 mA) at which TIM measurements were performed are indicated by pink arrows and crosses. (For interpretation of the references to colour in this figure legend, the reader is referred to the web version of this article.)



**Fig. 3.** Phase shift measurement on sample D ( $[B] = 3.5 \times 10^{19} \text{ cm}^{-3}$ ) along a scanning line parallel to the electrodes for different times and a current of (a) 0.05 A and (b) 0.25 A. (c) is the evolution of the phase shift distribution along a scanning line perpendicular to the electrodes, in the center of the device, for currents of 0.25 A with a positive polarity on the right electrode. The photographs are backside infrared images of the device active area including the scanning direction (black bold line).

the electrodes edge (i.e. at  $Y = 3$  and  $Y = 17 \mu\text{m}$ ) are optical artefacts. Unfortunately, they are at the positions where the phase shift distribution has the largest gradient and therefore prohibit establishing its exact shape.

The spreading of phase shift with time and its apparent increase after the end of the pulse outside the spatial limits of the inter-electrode gap are due to thermal diffusion. The diffusion length in Fig. 3c is estimated as the distance from the edge of the electrode for which the temperature decreases by around 90% and it is consistent with the diamond diffusion length ( $L_{th} = 11 \mu\text{m}$  for  $t = 100 \text{ ns}$ ) as estimated from

$$L_{th} = \sqrt{\frac{k_T}{c_V} t}, \quad (1)$$

with the thermal conductivity ( $k_T = 22 \text{ W.cm}^{-1}\text{.K}^{-1}$ ) (reference [23]), the volumetric heat capacity ( $c_V = 1.83 \text{ J.cm}^{-3}\text{.K}^{-1}$ ) and the time ( $t$ ).

#### 4. Modeling

The I-V characteristics, and voltage/current transient waveforms were modeled by the finite element method (Atlas by Silvaco) using the drift diffusion and thermo-dynamic approach (i.e. drift diffusion model with thermal equation) based on the dependences of transport parameters and hole concentration on the electric field and the temperature. The concentric electrodes with their cylindrical geometry simplify the

simulations to a two-dimensional problem in space. A substrate depth of  $100 \mu\text{m}$  has been considered. A  $50 \text{ Ohm}$  resistor has been used between the simulated device and voltage source to emulate the  $50 \text{ Ohm}$  internal resistance of the transmission-line pulse generator's equivalent circuit. The simulated area is a rectangle with a height of  $150 \mu\text{m}$  and a width of  $100 \mu\text{m}$  with two Ohmic contacts on top of it. The mesh size was set to  $0.1 \mu\text{m}$  between the electrodes and in the doped diamond layer and progressively set to  $5 \mu\text{m}$  at the limit of the simulated area. The default values of tolerance from the Atlas software (Silvaco) [24] were used for the simulations (see Table A in the Appendix section).

As the super-linearity is observed at voltages for which no significant heating is expected, additional mechanisms have to be considered to explain this behavior: Phonon-Assisted Tunneling Effect (PATE), Poole-Frenkel Effect (PFE) [15,16], and Impurity Impact Ionization (III) [11,25]. The simulation parameters used for each model are reported in Table 1.

Hole mobility  $\mu_h$  and activation energy  $E_a$  dispersion with temperature and dopant concentration are crucial parameters in modeling the current and voltage in simulated devices. The temperature and impurity concentration dependence of the hole mobility was modeled using the equations derived by S. Kagamihara et al. [26] from the work of D. M. Caughey and R. E. Thomas [27] (see Eqs. (2) to (5)):

$$\mu_{h0}(T, N_{imp}) = \mu_h(T_{amb}, N_{imp}) \left( \frac{T}{300} \right)^{-\beta(N_{imp})}, \quad (2)$$

**Table 2**  
Fitting parameters for the mobility model taken from [28].

$\mu^{\min}$ (cm <sup>2</sup> .V <sup>-1</sup> .s <sup>-1</sup> )	0
$\mu^{\max}$ (cm <sup>2</sup> .V <sup>-1</sup> .s <sup>-1</sup> )	2016
$\gamma_{\mu}$	0.73
$N_{\mu}$ (cm <sup>-3</sup> )	$3.25 \times 10^{17}$
$\beta^{\min}$	0
$\beta^{\max}$	3.11
$\gamma_{\beta}$	0.617
$N_{\beta}$ (cm <sup>-3</sup> )	$4.1 \times 10^{18}$

$$\mu_{h0}(T_{amb}, N_{imp}) = \mu^{\min} + \frac{\mu^{\max} - \mu^{\min}}{1 + \left(\frac{N_{imp}}{N_{\mu}}\right)^{\gamma_{\mu}}}, \quad (3)$$

$$\beta(N_{imp}) = \beta^{\min} + \frac{\beta^{\max} - \beta^{\min}}{1 + \left(\frac{N_{imp}}{N_{\beta}}\right)^{\gamma_{\beta}}}, \quad (4)$$

$$N_{imp} = N_A + N_D, \quad (5)$$

where  $N_A$  and  $N_D$  are the acceptor and the donor concentrations, respectively and  $T_{amb} = 300$  K. The  $\beta^{\min}$ ,  $\beta^{\max}$ ,  $\gamma_{\beta}$ ,  $N_{\beta}$ ,  $\mu^{\min}$ ,  $\mu^{\max}$ ,  $\gamma_{\mu}$  and  $N_{\mu}$  parameters based on reference [28] are reported in Table 2.

The dependence of the mobility on the electric field  $E$  and the saturation velocity  $v_{sat}$  is given in (see reference [27])

$$\mu_h(E, T, N_{imp}) = \mu_{h0}(T, N_{imp}) \left( \frac{1}{1 + \left(\frac{\mu_{h0}(T, N_{imp})E}{v_{sat}}\right)^{\beta_{sat}}} \right)^{\frac{1}{\beta_{sat}}}. \quad (6)$$

The drift velocity for holes is then given by:

$$v_d(E, T, N_{imp}) = \mu_h(E, T, N_{imp})E. \quad (7)$$

$v_{sat}$  and  $\beta_{sat}$  were obtained by fitting the hole-drift velocity data from reference [29] measured on (100) diamond samples at 300 K using Eqs. (6) and (7). The resulting fitting is given in Fig. 4.

The activation energy  $E_a$  of boron acceptors decreases with increasing doping concentration due to the interaction between carriers and ionized impurities [30]. In this work, we used a modified Pearson and Bardeen [31] model, see Eq. (8), which fits the experimental data better:

$$E_a(N_A) = E_I - aN_A^b, \quad (8)$$

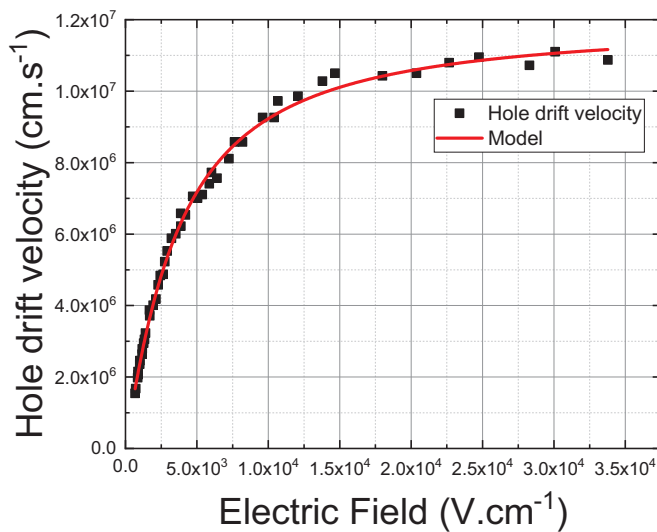


Fig. 4. Experimental [29] and calculated hole drift velocity as a function of the electric field.

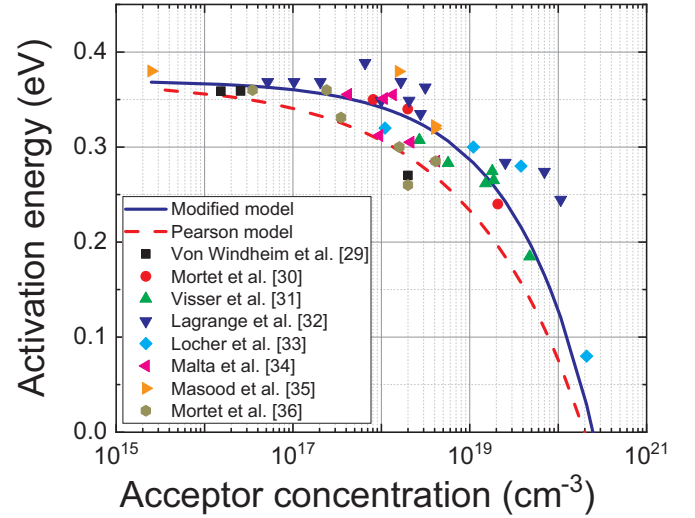


Fig. 5. Dispersion of activation energy with boron concentration.

with  $E_I = 0.37$  eV. The coefficients  $a$  ( $1.2 \times 10^{-10}$  eV.cm<sup>3/2.15</sup>) and  $b$  (1/2.15) were determined by fitting experimental values from the literature [32–39] using the least square method. In the original Pearson and Bardeen model, only  $a$  is used as a fitting parameter and  $b = 1/3$ . Fig. 5 shows that the modified model clearly offers a better fit of the experimental data compared to the original model and gives boron activation energy with a root mean square error of  $7 \times 10^{-3}$  eV.

PATE is a type of field emission due to the absorption of phonons by electrons or holes trapped at an impurity level. Thanks to the energy acquired from the phonon absorption and under the influence of an external electric field, the trapped carriers can tunnel through the energy barrier and reach the conduction or valence band. PATE is described by the equations presented in reference [40]. The comparison between experimental data and simulated I-V curves using PATE model is shown in Fig. 6 (black dashed lines). The simulated I-V characteristics do not match the experimental data. The exponential behavior is not observed and the simulated I-V curve barely deviates from a classic linear Ohmic model. PATE alone cannot explain the behavior of the I-V characteristics of the studied boron-doped diamond samples.

Besides PATE, PFE might also contribute to non-linear I-V characteristics. In PFE, the energy barrier of a charged acceptor (or donor) energy level and the valence (or conduction) band decreases because of the dissymmetry in the impurity potential well in the external electric field and facilitates carrier emission by PATE. PFE has been previously reported in undoped diamond [15]. Since the boron impurities in diamond are, for the most part, not ionized at room temperature, PFE should not have a large influence on the I-V characteristics.

The modeled I-V characteristics, including PFE and PATE, are reported in Fig. 6 (red dashed lines). PFE has been included in the simulation using the model embedded in the finite element simulator Atlas (Silvaco). These new simulated I-V characteristics are nearly identical to the one including PATE only and they show that PFE and PATE have a limited influence on the non-linear I-V characteristic of boron-doped diamond at high electric field. This result is also consistent with the study of A.K. Jonscher [41], which shows the negligible contribution of PFE effect in electrical conductivity in crystalline semiconductors.

To determine the impact of III on the electrical properties of boron-doped diamond, we followed the same approach as in reference [25] using the classical band-to-band impact ionization equations to model the current multiplication from the boron acceptor.

In this case, the current multiplication coefficient is given by

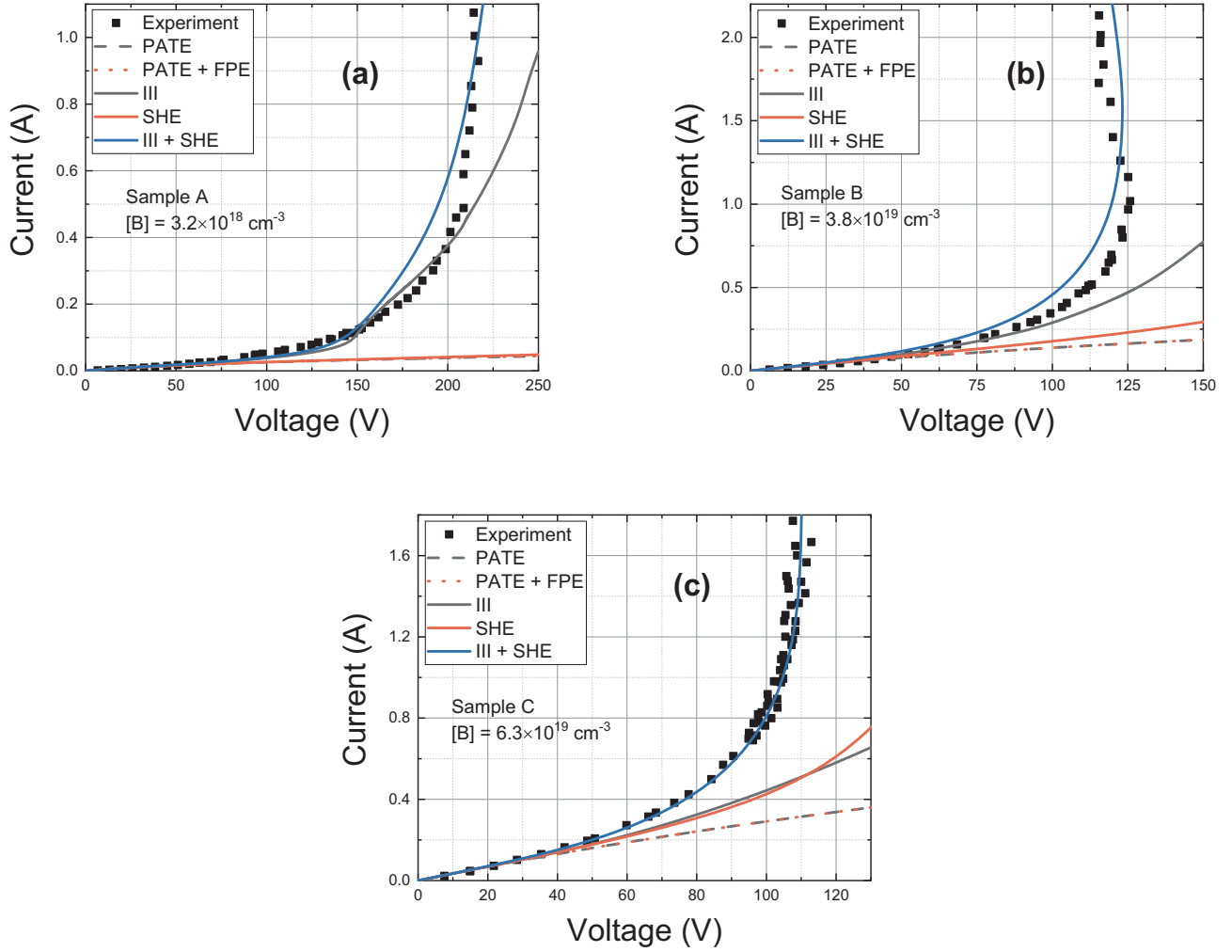


Fig. 6. Experimental (symbols) and simulated (lines and dashed lines) pulsed I-V characteristics using a combination of PATE, PFE, III, and SHE ( $t = 100$  ns) for (a) sample A, (b) B, and (c) C. (For interpretation of the references to color in this figure, the reader is referred to the web version of this article.)

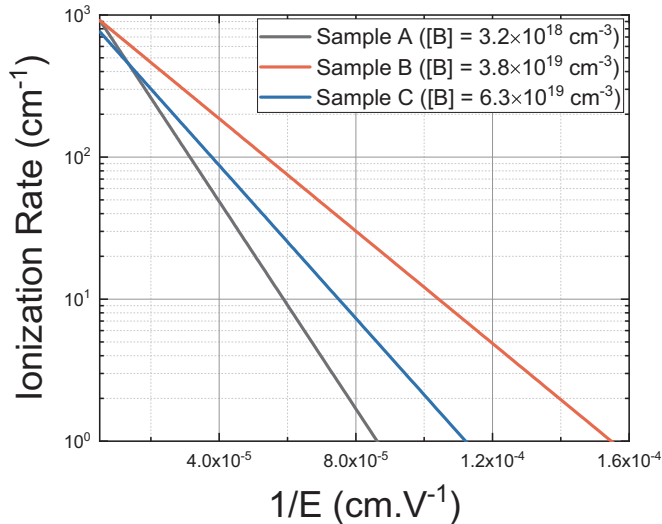


Fig. 7. Ionization rate  $\alpha$  as a function of the reciprocal electric field.

$$M = \frac{1}{1 - \int_0^L \alpha_p \exp[-\int_0^x dx'(\alpha_p - \alpha_n)] dx}, \quad (9)$$

where  $L$  is the distance between the electrodes and  $\alpha_p$  and  $\alpha_n$  are the

ionization rate for holes and electrons respectively. We assume  $\alpha_p = \alpha_n = \alpha$  [42] for simplification. The ionization rate  $\alpha$ , which reflects the number of ionization events per unit of length is given by (see reference [43])

$$\alpha(E) = A_\alpha \exp(-B_\alpha/E), \quad (10)$$

where  $E = U/L$  is the electric field,  $U$  is the voltage difference between the two electrodes, and  $A$  and  $B$  are fitting parameters. This simplification leads to a new expression of the current multiplication coefficient given in

$$M = \frac{1}{1 - L\alpha(U)}. \quad (11)$$

This model does not take into account the temperature dependence of the ionization rate observed in Si and Ge [44]. However, L. Tirino et al. [45] studied the influence of temperature for various wide band gap semiconductors and reached the conclusion that the temperature dependence of the ionization rate is mainly due to the temperature dependence of the phonon scattering rates. He also found out that the higher the optical phonon energy is, the less sensitive to temperature the impact ionization coefficients will be. For example, 3C-SiC has an optical phonon energy of 120 meV and its ionization rate was found to be almost insensible to temperature variations from 300 to 500 K. As a comparison, J. Pernot et al. [46] calculated an optical phonon energy of 165 meV for diamond from the data reported in [47]. Therefore, the ionization rate in diamond should be independent of temperature.

Ionization rates were determined by fitting the I-V curves using Eqs. (6), (10), and (11) in the region of negligible SHE, i.e. without temperature variation during the pulses (e.g. between 0 and 100 V for sample B). To simplify the calculation, the electric field is assumed to be constant between the electrodes, i.e. the edge effects due to the electrodes are neglected. Fig. 7 shows the determined ionization rate as a function of the inverse electric field for boron-doped diamond samples A, B, and C. Although there is no clear variation with boron concentration, the variation of the determined ionization rate is consistent for all boron concentrations, i.e. it increases and saturates at values of ca.  $10^3 \text{ cm}^{-1}$  for voltages (electric fields) superior to 100 V ( $70 \text{ kV.cm}^{-1}$ ).

The finite element simulated currents due to the III effect using determined ionization rates are compared to the experimental I-V curves in Fig. 6 (black lines). They reproduce correctly the exponential behavior of the current at low voltage, but are unable to reproduce its steep increase at high voltage, which is attributed to thermal runaway as indicated by TIM measurements.

To model the SHE, we used temperature dependent thermal conductivity (see reference [24]) and volumetric heat capacity given respectively by

$$k_T(T) = k_T(300 \text{ K}) \left( \frac{T}{300} \right)^{-m}, \quad (12)$$

with  $m = 1$ , and

$$c_V(T) = A_{c_V} + B_{c_V} T + C_{c_V} T^2 + \frac{D_{c_V}}{T^2}. \quad (13)$$

The parameters  $A_{c_V}$ ,  $B_{c_V}$ ,  $C_{c_V}$ , and  $D_{c_V}$  were determined by fitting the experimental values of volumetric heat capacity as a function of the temperature from reference [48]. The heat generation  $H$  term is given by

$$H = (\vec{J}_n + \vec{J}_p) \cdot \vec{E}, \quad (14)$$

where  $J_n$  and  $J_p$  are respectively the electron (negligible) and hole current density and  $E$  is the electric field. The concentration of donors is adjusted so that the simulated and experimental I-V curves have the same resistance between electrodes at low voltage. The resulting simulated I-V curves using a combination of III and SHE satisfactorily model the experimental non-linear current increase and the NDR for all samples as shown on Fig. 6 (blue lines).

In order to confirm the significant role of the III effect, I-V characteristics have been modeled using only SHE (see the red lines in Fig. 6), i.e. without the III effect. Although the simulated characteristic fits correctly the initial linear part, the current increases at a lower rate compared to the experimental I-V characteristic. This result shows that

SHE is not accountable alone for the observed I-V characteristic, even though it has a predominant effect at high electric field.

Fig. 8a shows the evolution of the simulated hole concentration at  $t = 100 \text{ ns}$  as a function of voltage for samples A, B and C. The hole concentration exhibits super linear behavior, which is consistent with the I-V characteristics shown in Fig. 6. Sample A shows a slowdown of the hole multiplication above 165 V, which can be attributed to saturation of the carrier velocity described in Eq. (6). Fig. 8b shows the corresponding evolution of the maximum temperature as a function of the dissipated power. The temperature increases proportionally with the dissipated power for sample B and C. The temperature evolution in sample A on the other hand has a sub-linear behavior. The difference might be explained by the more dominant impact of saturation velocity in sample A due to the higher mobility of holes in this sample.

As mentioned previously, the empirical model presented by S. Kagamihara et al. [26] was used to calculate the hole mobility. The main condition for this model to be applicable is that the evolution of the mobility should be dominated by phonon scattering. In order to make sure this is true in the case of this study, the temperature and hole concentration from Fig. 8a and b were used to calculate the relaxation time, i.e. the time between to scattering events, for neutral impurity scattering, ionized impurity scattering, acoustic phonon scattering, and optical phonon scattering. The calculation was done for both the minimum and maximum power (i.e. the first and last point) of each simulated curve in Fig. 8a and b. The formulas used for the calculation are presented in the work of J. Pernot et al. [46], and D. M. Caughey and R. E. Thomas [27]. The results are presented in Table 3. The phonon scattering events have a relaxation time which is about four orders of magnitude smaller than the ones of neutral and ionized impurities for minimum and maximum power. It means that the evolution of the mobility is largely dominated by phonon scattering at low applied power but also for high power despite the increase in the number of ionized impurities due to III and SHE. It also confirms the validity of the mobility model used for the simulation.

Fig. 9a and b show respectively the simulated voltage and current waveforms for sample B with  $V_{ch}$  as the varying parameter. Fig. 9c shows the corresponding evolution of the maximal temperature. For device voltages less than 110 V (i.e.  $V_{ch} < 125 \text{ V}$ ), the voltage waveform is nearly flat over time, which is consistent with the assumption used for the calculation of the ionization rate  $\alpha$ , that the temperature has little influence on the shape of the I-V characteristic at low voltage. However, for higher initial device voltage (i.e.  $V_{ch} > 125 \text{ V}$ ), the voltage is decreasing with time, due to thermal ionization of boron acceptor impurities, which decreases the resistivity of the sample during the pulse. For pulses with a starting voltage value over 200 V, the voltage value at the end of the pulse decreases when the starting

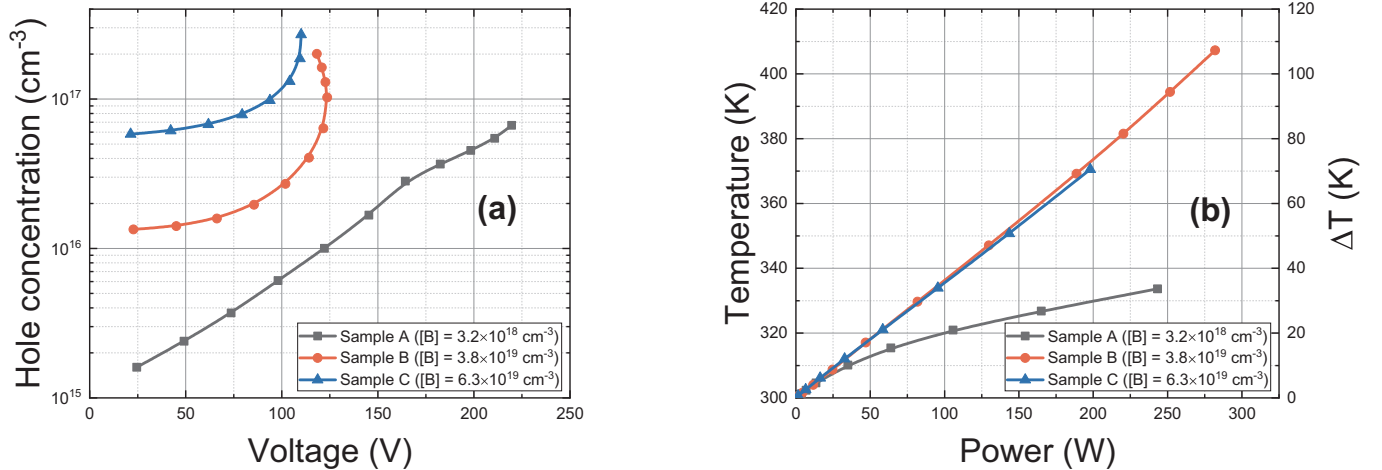


Fig. 8. Simulated hole concentration as a function of voltage (a) and maximum temperature as a function of power (b) in samples A, B and C.

**Table 3**

Relaxation times calculated for neutral impurity scattering ( $\tau_{NI}$ ), ionized impurity scattering ( $\tau_{II}$ ), acoustic phonon scattering ( $\tau_{AC}$ ), and optical phonon scattering ( $\tau_{OP}$ ) for samples A, B, and C for minimum and maximum applied power.

	Sample A	Sample B	Sample C
Relaxation times (minimum power)			
Neutral impurity $\tau_{NI}$ (s)	$4.4 \times 10^{-7}$	$3.9 \times 10^{-8}$	$2.4 \times 10^{-8}$
Ionized impurity $\tau_{II}$ (s)	$8.4 \times 10^{-8}$	$2.3 \times 10^{-9}$	$1.1 \times 10^{-9}$
Acoustic phonon $\tau_{AC}$ (s)	$5.2 \times 10^{-12}$	$5.2 \times 10^{-12}$	$5.2 \times 10^{-12}$
Optical phonon $\tau_{OP}$ (s)	$1.5 \times 10^{-12}$	$1.5 \times 10^{-12}$	$1.5 \times 10^{-12}$
Relaxation times (maximum power)			
Neutral impurity $\tau_{NI}$ (s)	$4.6 \times 10^{-7}$	$4.1 \times 10^{-8}$	$2.4 \times 10^{-8}$
Ionized impurity $\tau_{II}$ (s)	$6.0 \times 10^{-8}$	$3.4 \times 10^{-9}$	$1.4 \times 10^{-9}$
Acoustic phonon $\tau_{AC}$ (s)	$4.5 \times 10^{-13}$	$3.3 \times 10^{-13}$	$3.8 \times 10^{-13}$
Optical phonon $\tau_{OP}$ (s)	$7.5 \times 10^{-13}$	$2.5 \times 10^{-13}$	$4.1 \times 10^{-13}$

voltage increases. On the other hand, in Fig. 9b, the value of the current at the end of the pulse increases steadily when the loading DC voltage increases. The combination of the decrease of the instantaneous voltage and increase of the instantaneous current is responsible for the appearance of the NDR regime in sample B for high loading DC voltage visible in Fig. 6b. A similar behavior is observable in experimental waveforms measured on sample B in Fig. 1 and it is attributed to SHE, which causes an increase in temperature with time and with  $V_{ch}$ ,

evidenced by TIM measurements in Fig. 3 and confirmed by simulation in Fig. 9c for sample B. The simulation shows that temperature reaches a maximum value of 407 K for  $V_{ch} = 237.5$  V.

Fig. 10a shows the simulated temperature distribution for sample D under conditions similar to the ones used for TIM measurements in Fig. 3c (i.e. for a current of 0.25 A) at  $t = 100$  ns for two different depths: black squares represent the surface temperature distribution and the red dots the temperature for a distance of 10  $\mu\text{m}$  from the surface. The vertical dashed lines represent the limits of the electrodes. Due to the stripe layout of samples used for TIM, in this case, the simulation was performed in 2D rectangular geometry which is still a good approach for the use of short pulses. One can observe that the surface temperature peaks at the right electrode edge (the ground electrode) with maximum value of about 440 K. The temperature distribution in the depth is smeared. The phase shift distribution from the 2D temperature profile was also calculated using equations in reference [18] and taking into account diamond thermo-optical coefficient from the work of V. Y. Yurov et al. [49]. In brief, the phase shift is the integral of temperature along the laser beam path weighted by the thermo-optical coefficient [18,19]. The phase shift distribution at  $t = 100$  ns is plotted in Fig. 10b. The peak phase shift value near 0.14 rad is within the experimental error to the experiment in Fig. 3c. The calculated phase shift maximum in Fig. 10b is also shifted toward the right electrode but is smeared due to significant temperature contribution from the bulk. This shift in the phase shift distribution is however not distinguishable in experiment in Fig. 3c which can be

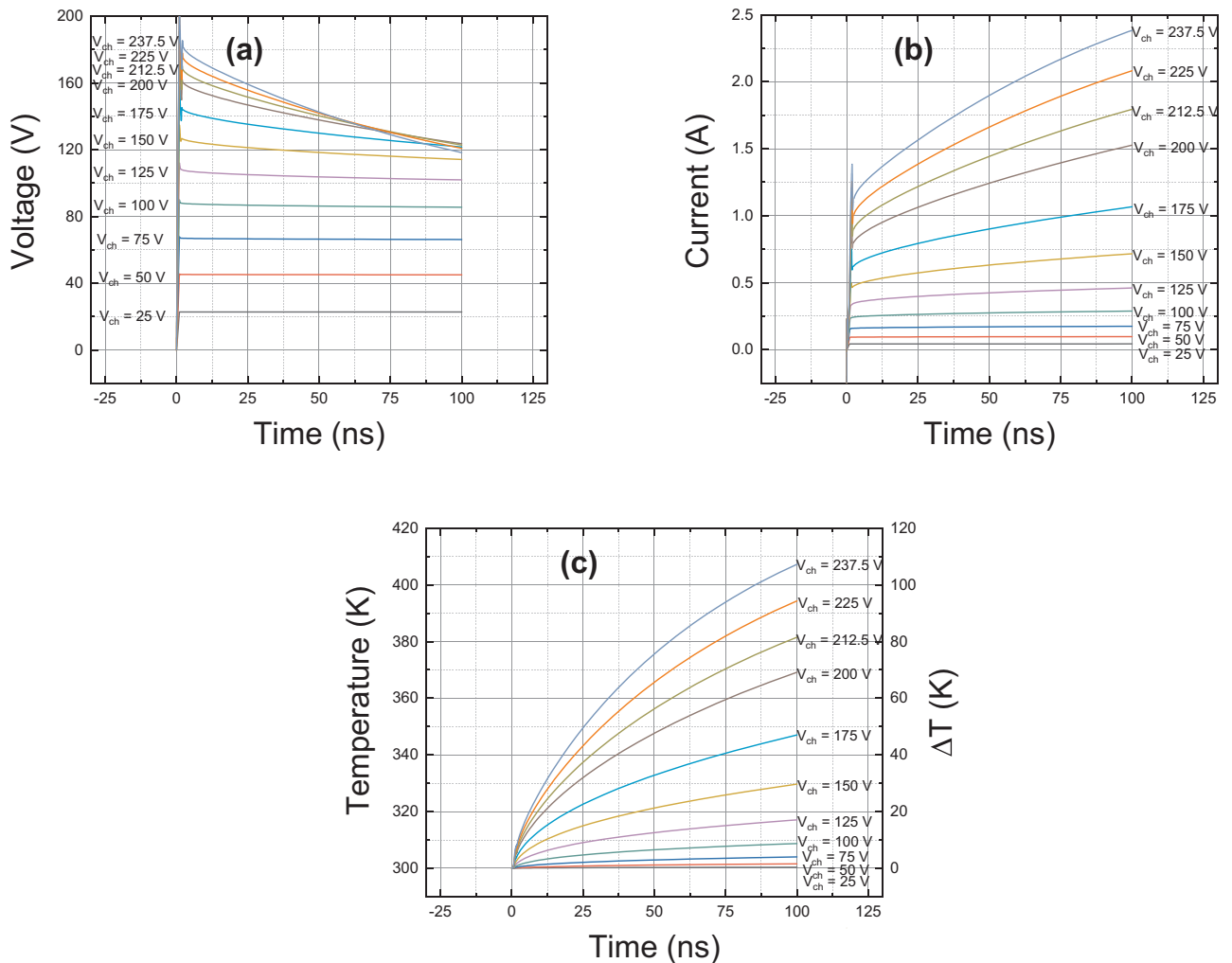


**Fig. 9.** Simulated voltage (a), current (b) waveforms, and maximum temperature (c) in sample B for an increasing amplitude of  $V_{ch}$ .

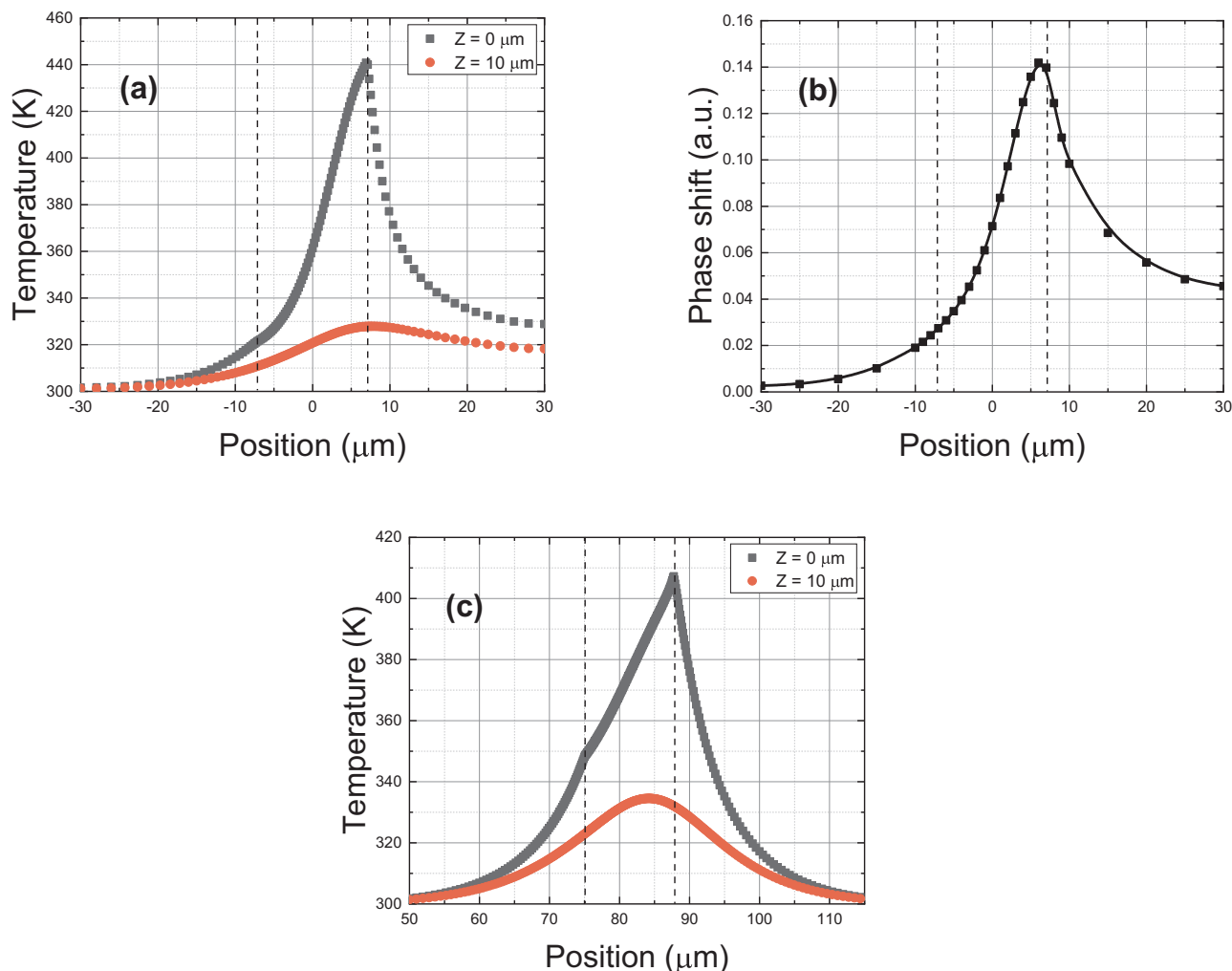


**Fig. 10.** Simulated temperature (a) and phase shift (b) distribution along a scanning line perpendicular to the electrodes for sample D at a current of 0.25 A and temperature distribution for sample B at a current of 2.4 A ( $V_{ch} = 237.5$  V) (c). The temperature is given at the surface of the sample ( $Z = 0 \mu\text{m}$ ) and for a depth of 10  $\mu\text{m}$  in the diamond ( $Z = 10 \mu\text{m}$ ). The time instant is  $t = 100$  ns.

attributed to experimental uncertainty [18] and/or model imperfection. Fig. 10c shows the simulated temperature distribution for sample B (electrodes with cylindrical geometry) for a current of 2.4 A (i.e.  $V_{ch} = 237.5$  V) and give similar results to what was observed with sample D. The surface temperature peaks at the positive electrode with a maximum value of 407 K. This maximum is consistent with the temperature value for the same condition at the pulse end (see top curve in Fig. 9c). The temperature distribution in the depth is smeared and the peak is shifted toward the middle of the inter-electrode gap.

The relatively good quantitative agreement between our experiments and simulations indicates that our model describes the transport quite satisfactorily. It means that hot carrier effects [50–53], like possible difference between the hot hole and lattice temperature does not need to be included explicitly. In particular, the carrier thermalization (energy relaxation) time constant in diamond is in the order of tens of ps [53], which is much shorter than the time scale of 10–100 ns considered in this study. The hot carrier effects are, however, included implicitly in our model since impurity impact ionization and velocity saturation are in fact due to hot carriers.

## 5. Conclusions

The experimental exponential behavior at low current/field and steep super-exponential (with NDR) behavior at high current/field of I-V characteristics measured on boron doped diamond devices were

satisfactorily modeled by finite element simulation. The exponential I-V behavior is attributed to III as previously suggested in reference [11], whereas the high currents at high electric fields can only be explained by including SHE. The short linear part of the curve for very low voltages can be attributed to simple Ohmic behavior as the electric field is not high enough to produce III. The role of SHE is supported by TIM measurements, which show a thermal runaway effect at the onset of NDR, which is consistent with simulations. In summary, the high electric field I-V characteristics of boron-doped diamond are the result of the III effect and its combination with SHE.

## Author statement

N. Lambert: Writing - Original Draft, Methodology, Investigation, Data Curation, Visualization.

A. Taylor: Resources, Visualization.

P. Hubík: Resources.

J. Bulíř: Resources.

J. More-Chevalier: Resources.

H. Karaca: Investigation, Formal analysis.

C. Fleury: Investigation, Formal analysis.

J. Voves: Resources.

Z. Šobáň: Resources.

D. Pogany: Writing - Review & Editing, Resources, Methodology.

V. Mortet: Writing - Review & Editing, Conceptualization,

## Supervision.

## Declaration of competing interest

The authors declare that they have no known competing financial interests or personal relationships that could have appeared to influence the work reported in this paper.

## Appendix A

Table A

Default values of tolerances used in the Silvaco Atlas finite element simulation [24].

PX.TOL	Relative tolerance for the potential equation	$10^{-5}$
PR.TOL	Absolute tolerance for the Poisson equation	$10^{-26}$
CX.TOL	Relative tolerance for the continuity equation	$10^{-5}$
CR.TOL	Absolute tolerance for the continuity equation	$5 \times 10^{-18}$
TCX.TOL	Relative tolerance for convergence of the carrier temperature equations	$10^{-5}$
TLX.TOL	Relative tolerance for convergence of the lattice temperature equation	$10^{-5}$
TCR.TOL	Absolute tolerance for convergence of the carrier temperature equations	100
TLR.TOL	Absolute tolerance for convergence of the lattice temperature equation	100
IX.TOL	Relative current convergence criteria	$5 \times 10^{-4}$
IR.TOL	Absolute current convergence criteria	$5 \times 10^{-11}$

## References

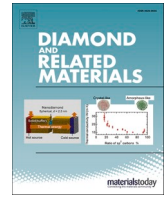
- [1] Semiconductor diamond, Ultra-wide Bandgap Semicond, Elsevier, Mater, 2019, pp. 111–261, <https://doi.org/10.1016/B978-0-12-815468-7.00002-0>.
- [2] M.-A. Pinault-Thaury, S. Temgoua, R. Gillet, H. Bensalah, I. Stenger, F. Jomard, R. Issaoui, J. Barjon, Phosphorus-doped (113) CVD diamond: a breakthrough towards bipolar diamond devices, Appl. Phys. Lett. 114 (2019) 112106, <https://doi.org/10.1063/1.5079924>.
- [3] A. Lazea, Y. Garino, T. Teraji, S. Koizumi, High quality p-type chemical vapor deposited (111)-oriented diamonds: growth and fabrication of related electrical devices, Phys. Status Solidi A 209 (2012) 1978–1981, <https://doi.org/10.1002/pssa.201228162>.
- [4] A.F. Sartori, M. Fischer, S. Gsell, M. Schreck, *In situ* boron doping during hetero-epitaxial growth of diamond on Ir/YSZ/Si, Phys. Status Solidi A 209 (2012) 1643–1650, <https://doi.org/10.1002/pssa.201200221>.
- [5] H. Umezawa, S. Shikata, T. Funaki, Diamond Schottky barrier diode for high-temperature, high-power, and fast switching applications, Jpn. J. Appl. Phys. 53 (2014), <https://doi.org/10.7567/JJAP.53.05FP06> 05FP06.
- [6] P.-N. Volpe, P. Muret, J. Pernot, F. Omnès, T. Teraji, F. Jomard, D. Planson, P. Brosselard, N. Dheilil, B. Vergne, S. Scharnholtz, High breakdown voltage Schottky diodes synthesized on p-type CVD diamond layer, Phys. Status Solidi A 207 (2010) 2088–2092, <https://doi.org/10.1002/pssa.201000055>.
- [7] J. Wang, D. Zhao, W. Wang, X. Zhang, Y. Wang, X. Chang, Z. Liu, J. Fu, K. Wang, H.-X. Wang, Diamond Schottky barrier diodes with floating metal rings for high breakdown voltage, Mater. Sci. Semicond. Process. 97 (2019) 101–105, <https://doi.org/10.1016/j.mssp.2019.03.004>.
- [8] T. Matsumoto, H. Kato, K. Oyama, T. Makino, M. Ogura, D. Takeuchi, T. Inokuma, N. Tokuda, S. Yamasaki, Inversion channel diamond metal-oxide-semiconductor field-effect transistor with normally off characteristics, Sci. Rep. 6 (2016), <https://doi.org/10.1038/srep31585>.
- [9] Z. Ren, W. Chen, J. Zhang, J. Zhang, C. Zhang, G. Yuan, K. Su, Z. Lin, Y. Hao, High performance single crystalline diamond normally-off field effect transistors, IEEE J. Electron Devices Soc. 7 (2019) 82–87, <https://doi.org/10.1109/JEDS.2018.2880005>.
- [10] V. Mortet, D. Trémouilles, J. Bulíř, P. Hubík, L. Heller, E. Bedel-Pereira, A. Soltani, Peculiarities of high electric field conduction in p-type diamond, Appl. Phys. Lett. 108 (2016) 152106, <https://doi.org/10.1063/1.4946853>.
- [11] V. Mortet, A. Soltani, Impurity impact ionization avalanche in p-type diamond, Appl. Phys. Lett. 99 (2011) 202105, <https://doi.org/10.1063/1.3662403>.
- [12] V. Mortet, L. Drbohlavova, N. Lambert, A. Taylor, P. Ashcheulov, M. Davydova, J. Lorincik, M. Aleshin, P. Hubík, Conductivity of boron-doped diamond at high electrical field, Diam. Relat. Mater. 98 (2019) 107476, <https://doi.org/10.1016/j.diamond.2019.107476>.
- [13] K.D. Morhard, R.P. Huebener, W. Claus, J. Peinke, Low-temperature avalanche breakdown in p-Ge: influence of the acceptor concentration, J. Appl. Phys. 71 (1992) 3336–3338, <https://doi.org/10.1063/1.350955>.
- [14] V.I. Sankin, A.M. Monakhov, P.P. Shkrebiz, P.L. Abramov, N.I. Sablina, N.S. Averkhev, Peculiarities of impact ionization of Impurity Al in SiC polytypes, Appl. Phys. Lett. 97 (2010) 262118, <https://doi.org/10.1063/1.3527964>.
- [15] M. Girolami, A. Bellucci, P. Calvani, R. Flammini, D.M. Trucchi, Radiation-assisted Frenkel-Poole transport in single-crystal diamond, Appl. Phys. Lett. 103 (2013) 083502, <https://doi.org/10.1063/1.4818904>.
- [16] G. Vincent, A. Chantre, D. Bois, Electric field effect on the thermal emission of traps in semiconductor junctions, J. Appl. Phys. 50 (1979) 5484, <https://doi.org/10.1063/1.326601>.
- [17] M. Davydova, A. Taylor, P. Hubík, L. Fekete, L. Klimša, D. Trémouilles, A. Soltani, V. Mortet, Characteristics of zirconium and niobium contacts on boron-doped diamond, Diam. Relat. Mater. 83 (2018) 184–189, <https://doi.org/10.1016/j.diamond.2018.02.009>.
- [18] D. Pogany, S. Bychikhin, C. Furbock, M. Litzberger, E. Gornik, G. Groos, K. Esmark, M. Stecher, Quantitative internal thermal energy mapping of semiconductor devices under short current stress using backside laser interferometry, IEEE Trans. Electron Devices 49 (2002) 2070–2079, <https://doi.org/10.1109/TED.2002.804724>.
- [19] M. Litzberger, C. Furbock, S. Bychikhin, D. Pogany, E. Gornik, Scanning heterodyne interferometer setup for the time-resolved thermal and free-carrier mapping in semiconductor devices, IEEE Trans. Instrum. Meas. 54 (2005) 2438–2445, <https://doi.org/10.1109/TIM.2005.858121>.
- [20] Y. Song, B.D. Peng, G.Z. Song, Z.Q. Yue, B.K. Li, J.M. Ma, L. Sheng, B.J. Duan, H.X. Wang, Investigating non-equilibrium carrier lifetimes in nitrogen-doped and boron-doped single crystal HPHT diamonds with an optical method, Appl. Phys. Lett. 112 (2018) 022103, <https://doi.org/10.1063/1.5019587>.
- [21] T. Shimomura, Y. Kubo, J. Barjon, N. Tokuda, I. Akimoto, N. Naka, Quantitative relevance of substitutional impurities to carrier dynamics in diamond, Phys. Rev. Mater. 2 (2018) 094601, <https://doi.org/10.1103/PhysRevMaterials.2.094601>.
- [22] V.A. Vashchenko, V.F. Sinkevitch, Physical Limitations of Semiconductor Devices, Springer, New York, 2008.
- [23] J.R. Olson, R.O. Pohl, J.W. Vandersande, A. Zoltan, T.R. Anthony, W.F. Banholzer, Thermal conductivity of diamond between 170 and 1200 K and the isotope effect, Phys. Rev. B 47 (1993) 14850–14856, <https://doi.org/10.1103/PhysRevB.47.14850>.
- [24] Atlas User's Manual, (2018).
- [25] A.W. Livingstone, J.W. Allen, Impact ionization of deep impurities in zinc selenide, J. Phys. C Solid State Phys. 6 (1973) 3491–3500, <https://doi.org/10.1088/0022-3719/6/23/023>.
- [26] S. Kagamiyama, H. Matsuura, T. Hatakeyama, T. Watanabe, M. Kushibe, T. Shinohe, K. Arai, Parameters required to simulate electric characteristics of SiC devices for n-type 4H-SiC, J. Appl. Phys. 96 (2004) 5601–5606, <https://doi.org/10.1063/1.1798399>.
- [27] D.M. Caughey, R.E. Thomas, Carrier mobilities in silicon empirically related to doping and field, Proc. IEEE 55 (1967) 2192–2193, <https://doi.org/10.1109/PROC.1967.6123>.
- [28] P.-N. Volpe, J. Pernot, P. Muret, F. Omnès, High hole mobility in boron doped diamond for power device applications, Appl. Phys. Lett. 94 (2009) 092102, <https://doi.org/10.1063/1.3086397>.
- [29] L. Reggiani, S. Bosi, C. Canali, F. Nava, S.F. Kozlov, Hole-drift velocity in natural diamond, Phys. Rev. B 23 (1981) 3050–3057, <https://doi.org/10.1103/PhysRevB.23.3050>.
- [30] G.L. Pearson, J. Bardeen, Electrical properties of pure silicon and silicon alloys containing boron and phosphorus, Phys. Rev. 75 (1949) 865–883, <https://doi.org/10.1103/PhysRev.75.865>.
- [31] V. Mortet, N. Lambert, P. Hubík, A. Soltani, Model of carrier multiplication due to impurity impact ionization in boron-doped diamond, TANGER Ltd., Brno, Czech Republic, 2018, pp. 41–45.
- [32] J.A. Von Windheim, V. Venkatesan, D.M. Malta, K. Das, Electrical characterization of semiconducting diamond thin films and single crystals, J. Electron. Mater. 22 (1993) 391–398, <https://doi.org/10.1007/BF02661667>.
- [33] V. Mortet, M. Daenen, T. Teraji, A. Lazea, V. Vorlicek, J. D'Haen, K. Haenen, M. D'Oliessaer, Characterization of boron doped diamond epilayers grown in a

- NIRIM type reactor, *Diam. Relat. Mater.* 17 (2008) 1330–1334, <https://doi.org/10.1016/j.diamond.2008.01.087>.
- [34] E.P. Visser, G.J. Bauhuis, G. Janssen, W. Vollenberg, J.P. van Enkevort, L.J. Giling, Electrical conduction in homoepitaxial, boron-doped diamond films, *J. Phys. Condens. Matter* 4 (1992) 7365–7376, <https://doi.org/10.1088/0953-8984/4/36/011>.
- [35] J.-P. Lagrange, A. Deneuville, E. Gheeraert, A large range of boron doping with low compensation ratio for homoepitaxial diamond films, *Carbon* 37 (1999) 807–810, [https://doi.org/10.1016/S0008-6223\(98\)00275-9](https://doi.org/10.1016/S0008-6223(98)00275-9).
- [36] R. Locher, J. Wagner, F. Fuchs, M. Maier, P. Gonon, P. Koidl, Optical and electrical characterization of boron-doped diamond films, *Diam. Relat. Mater.* 4 (1995) 678–683, [https://doi.org/10.1016/0925-9635\(94\)05297-2](https://doi.org/10.1016/0925-9635(94)05297-2).
- [37] D.M. Malta, J.A. von Windheim, H.A. Wynands, B.A. Fox, Comparison of the electrical properties of simultaneously deposited homoepitaxial and polycrystalline diamond films, *J. Appl. Phys.* 77 (1995) 1536–1545, <https://doi.org/10.1063/1.358905>.
- [38] A. Masood, M. Aslam, M.A. Tamor, T.J. Potter, Synthesis and electrical characterization of boron-doped thin diamond films, *Appl. Phys. Lett.* 61 (1992) 1832–1834, <https://doi.org/10.1063/1.108389>.
- [39] V. Mortet, J. Pernot, F. Jomard, A. Soltani, Z. Remes, J. Barjon, J. D'Haen, K. Haenen, Properties of boron-doped epitaxial diamond layers grown on (110) oriented single crystal substrates, *Diam. Relat. Mater.* 53 (2015) 29–34, <https://doi.org/10.1016/j.diamond.2015.01.006>.
- [40] G.A.M. Hurkx, D.B.M. Klaassen, M.P.G. Knuvers, F.G. O'Hara, A new recombination model describing heavy-doping effects and low-temperature behaviour, *Int. Tech. Dig. Electron Devices Meet., IEEE*, Washington, DC, USA, 1989, pp. 307–310, <https://doi.org/10.1109/IEDM.1989.74285>.
- [41] A.K. Jonscher, Free-carrier Poole-Frenkel effect in crystalline solids, *J. Phys. C Solid State Phys.* 3 (1970) L159–L162, <https://doi.org/10.1088/0022-3719/3/8/029>.
- [42] A. Hiraiwa, H. Kawarada, Figure of merit of diamond power devices based on accurately estimated impact ionization processes, *J. Appl. Phys.* 114 (2013) 034506, <https://doi.org/10.1063/1.4816312>.
- [43] A.G. Chynoweth, Ionization rates for electrons and holes in silicon, *Phys. Rev.* 109 (1958) 1537–1540, <https://doi.org/10.1103/PhysRev.109.1537>.
- [44] C.R. Crowell, S.M. Sze, Temperature dependence of avalanche multiplication in semiconductors, *Appl. Phys. Lett.* 9 (1966) 242–244, <https://doi.org/10.1063/1.1754731>.
- [45] L. Tirino, M. Weber, K.F. Brennan, E. Bellotti, M. Goano, Temperature dependence of the impact ionization coefficients in GaAs, cubic SiC, and zinc-blende GaN, *J. Appl. Phys.* 94 (2003) 423–430, <https://doi.org/10.1063/1.1579129>.
- [46] J. Pernot, P.N. Volpe, F. Omnès, P. Muret, V. Mortet, K. Haenen, T. Teraji, Hall hole mobility in boron-doped homoepitaxial diamond, *Phys. Rev. B* 81 (2010), <https://doi.org/10.1103/PhysRevB.81.205203>.
- [47] S.A. Solin, A.K. Ramdas, Raman spectrum of diamond, *Phys. Rev. B* 1 (1970) 1687–1698, <https://doi.org/10.1103/PhysRevB.1.1687>.
- [48] A.C. Victor, Heat capacity of diamond at high temperatures, *J. Chem. Phys.* 36 (1962) 1903–1911, <https://doi.org/10.1063/1.1701288>.
- [49] V.Yu. Yurov, E.V. Bushuev, A.F. Popovich, A.P. Bolshakov, E.E. Ashkinazi, V.G. Ralchenko, Near-infrared refractive index of synthetic single crystal and polycrystalline diamonds at high temperatures, *J. Appl. Phys.* 122 (2017) 243106, <https://doi.org/10.1063/1.5008387>.
- [50] J.B. Khurgin, K.-T. Tsen, J.-J. Song, M.J. Cohen, J.W. Glesener (Eds.), Mitigating hot phonons in high power optoelectronic devices based on wide gap semiconductors, 2007, <https://doi.org/10.1117/12.705110> San Jose, CA. p. 64710Y.
- [51] J. Liberis, I. Matulioniene, A. Matulionis, M.C. Lemme, H. Kurz, M. Först, Hot-phonon temperature and lifetime in biased boron-implanted SiO<sub>2</sub>/Si/SiO<sub>2</sub> channels, *Semicond. Sci. Technol.* 21 (2006) 803–807, <https://doi.org/10.1088/0268-1242/21/6/017>.
- [52] S. Barman, G.P. Srivastava, Quantitative estimate of phonon scattering rates in different forms of diamond, *Phys. Rev. B* 73 (2006) 073301, <https://doi.org/10.1103/PhysRevB.73.073301>.
- [53] M. Kozák, F. Trojánek, P. Malý, Hot-carrier transport in diamond controlled by femtosecond laser pulses, *New J. Phys.* 17 (2015) 053027, <https://doi.org/10.1088/1367-2630/17/5/053027>.



Contents lists available at ScienceDirect

## Diamond &amp; Related Materials

journal homepage: [www.elsevier.com/locate/diamond](http://www.elsevier.com/locate/diamond)

## Highly phosphorus-doped polycrystalline diamond growth and properties

Nicolas Lambert<sup>a,b</sup>, Zdeněk Weiss<sup>a</sup>, Ladislav Klimša<sup>a</sup>, Jaromír Kopeček<sup>a</sup>, Zuzana Gedeonová<sup>c</sup>, Pavel Hubík<sup>c</sup>, Vincent Mortet<sup>a,d,\*</sup><sup>a</sup> FZU – Institute of Physics of the Czech Academy of Sciences, Na Slovance 1999/2, 182 21 Prague 8, Czech Republic<sup>b</sup> Faculty of Electrical Engineering, Czech Technical University in Prague, Technická 1902/2, 166 27 Prague 6, Czech Republic<sup>c</sup> FZU – Institute of Physics of the Czech Academy of Sciences, Cukrovarnická 10/112, 162 00 Prague 6, Czech Republic<sup>d</sup> Faculty of Biomedical Engineering, Czech Technical University in Prague, nám. Sítná 3105, 272 01 Kladno, Czech Republic

## ARTICLE INFO

## Keywords:

Diamond growth  
 Polycrystalline diamond  
 Phosphorus doping  
 Pulsed gas  
 Microwave plasma enhanced chemical vapor deposition

## ABSTRACT

In this work, phosphorus-doped polycrystalline diamond layers were grown using a new gas control process to increase the incorporation of phosphorus in diamond. Topographical characteristics and crystalline quality of the phosphorus-doped polycrystalline diamond layers grown on Si substrates were analyzed using Scanning Electron Microscopy (SEM) and Raman spectroscopy. The phosphorus concentration was determined using Glow-Discharge Optical Emission Spectroscopy (GDOES). Polycrystalline diamond layers have a good crystalline quality with a  $sp^3/sp^2$  carbon ration over 75%. The growth rate reaches up to  $440 \text{ nm}\cdot\text{h}^{-1}$ , and the phosphorus concentration is well above  $10^{20} \text{ cm}^{-3}$ .

**Novelty statement:** This work reports on a new method for the production of phosphorus-doped polycrystalline diamond layers based on the pulsed injection of methane during the growth by microwave plasma enhanced chemical vapor deposition.

## 1. Introduction

Diamond is a material with exceptionally high thermal conductivity, carrier mobility, and breakdown electric field which potentially designates it as the best semiconductor for high power, high temperature applications. The production of high-quality phosphorus-doped diamond layers is crucial for the development of diamond-based electronic devices such as PIN diodes [1,2] and field-effect transistors [3,4]. While the boron-doped diamond MicroWave Plasma Enhanced Chemical Vapor Deposition (MWPECVD) growth is already well understood, ranging from low boron concentrations and high carrier mobility [5] to high boron concentration with metallic conductivity and superconductivity at cryogenic temperatures [6], the MWPECVD synthesis of phosphorus-doped diamond is still complex. Despite recent progress made to improve phosphorus incorporation in diamond using crystalline misorientation [7] and pulsed microwave plasma [8], the production of high quality and highly phosphorus-doped diamond layers is difficult due to crystalline imperfections, the low incorporation efficiency of phosphorus, and the passivation of phosphorus atoms by hydrogen [9,10]. In this work, we aim at improving the incorporation of phosphorus in polycrystalline diamond layers using pulsed  $\text{CH}_4$  injection

during the MWPECVD diamond growth.

Optical Emission Spectroscopy (OES) measurements of hydrogen-phosphine plasma show the disappearance of simple phosphorous radicals (PH and P) when  $\text{CH}_4$  is added to the gas mix [11]. This phenomenon is attributed to the formation of methylphosphine [12] and methinophosphide [13] in the plasma which most likely do not participate in the synthesis of phosphorus-doped diamond. In order to reduce the unwanted cross reaction between carbon and phosphorous species and therefore enhance the phosphorus incorporation ratio in the diamond layer during the MWPECVD growth,  $\text{CH}_4$  pulses were injected in the reactor instead of a continuous flow of gas. This method was already investigated by G. Frangieh et al. [14] for the fabrication of diamond layers doped with arsenic with an incorporation ratio more than twice higher compared to conventional continuous growth procedure.

## 2. Experimental setup

Polycrystalline undoped and phosphorus-doped diamond layers were grown on (100) p-type boron-doped polished Si substrates with a resistivity between  $2.5 \times 10^{-3}$  and  $4.0 \times 10^{-3} \Omega\cdot\text{m}$ . Those substrates were first cleaned in a piranha solution to remove organic residues from

\* Corresponding author at: FZU – Institute of Physics of the Czech Academy of Sciences, Na Slovance 1999/2, 182 21 Prague 8, Czech Republic.  
 E-mail address: [mortetv@fzu.cz](mailto:mortetv@fzu.cz) (V. Mortet).

<https://doi.org/10.1016/j.diamond.2022.108964>

Received 16 November 2021; Received in revised form 10 February 2022; Accepted 10 March 2022

Available online 15 March 2022

0925-9635/© 2022 Elsevier B.V. All rights reserved.

their surfaces. They were then rinsed in deionized water and cleaned in acetone and isopropyl alcohol in an ultrasonic bath. An aqueous seeding solution containing nano-diamonds [15] was spread on the surface of the substrates using a spin coater to ensure nucleation. Polycrystalline diamond layers were grown in a lab-made NIRIM type reactor [16] using microwave plasma. The reactor chamber was evacuated to a base pressure below  $10^{-6}$  mbar using a Pfeiffer DCU 501 turbo-molecular pumping system. The microwave power is provided by a WR340 downstream plasma source from SAIREM working at frequency of 2.45 GHz.  $\text{CH}_4$  (N5.5) was used as a source of carbon and  $\text{PH}_3$  (N5.0, diluted at 6000 ppm in N5.6  $\text{H}_2$ ) as a source of phosphorus dopant in a  $\text{H}_2$  microwave plasma (N5.6). Gas flows were regulated using MKS mass flow controllers. Four series of five polycrystalline diamond layers were grown on Si substrates using pulsed or continuous  $\text{CH}_4$  and with or without  $\text{PH}_3$  (see Table 1). During growths in pulsed  $\text{CH}_4$  flow mode, the  $\text{CH}_4$  gas line was open for 1 min and then closed for 4 min in 5 min cycles. The  $\text{H}_2$  and  $\text{PH}_3$  gas lines were left open during the growth. The duration of a cycle was adjusted to match the residency time of CH radicals in the reactor measured by Optical Emission Spectroscopy (OES) [33]. The different microwave power and pressure conditions used in this work were chosen to keep the size of the plasma ball constant. The distance between the substrate and the center of the plasma ball was adjusted for each combination of pressure and microwave power to set the substrate's temperature at 1000 °C during the diamond growth [17]. The combinations of pressure, microwave power and distance between the substrate and the plasma used for diamond growth are detailed in Table 2. The thickness of the polycrystalline diamond layer was measured by profilometry in a groove formed in an unseeded line on the substrate. Raman spectra were measured using a Renishaw InVia Raman Microscope with a laser excitation wavelength of 488 nm. A Scanning Electron Microscopy (SEM) TESCAN FERA3 GM microscope was used to assess the phosphorus-doped polycrystalline diamond layers' morphology. Finally, phosphorus content was determined by Glow Discharge Optical Emission Spectroscopy (GDOES) using a GDA750HR spectrometer from Spectruma GmbH.

### 3. Results and discussion

#### 3.1. Growth rate measurements

The measured growth rate (see Fig. 1) decreases with the applied microwave power, and consequently with the distance between the substrate and the center of the plasma ball, for all the polycrystalline diamond layers. This phenomenon was already observed for both polycrystalline [18] and single crystal [19] diamond growth and is attributed to the decrease in the concentration of atomic hydrogen close to the substrate's surface. Both undoped and phosphorus-doped diamond layers grown using a pulsed  $\text{CH}_4$  flow exhibit a larger variation of growth rate between low and high power compared to diamond layers grown using a continuous  $\text{CH}_4$  flow. The growth rate at low power and using a pulsed  $\text{CH}_4$  flow is higher than the one of layers grown in continuous flow of  $\text{CH}_4$  despite an average lower  $\text{CH}_4$  concentration in the reactor. This difference might be attributed to an inhomogeneous distribution of carbon species in the reactor induced by the intermittent  $\text{CH}_4$  flow, with more carbon species being present in the vicinity of the plasma. The maximum growth rate recorded is  $440 \text{ nm}\cdot\text{h}^{-1}$  for a

**Table 2**

Combinations of microwave power, pressure, and distance between substrate and plasma used for the growth of polycrystalline diamond layers.

Microwave power (W)	Pressure (mbar)	Distance substrate/plasma (mm)
280	30	3
370	50	14
500	70	20
640	90	23
780	110	26

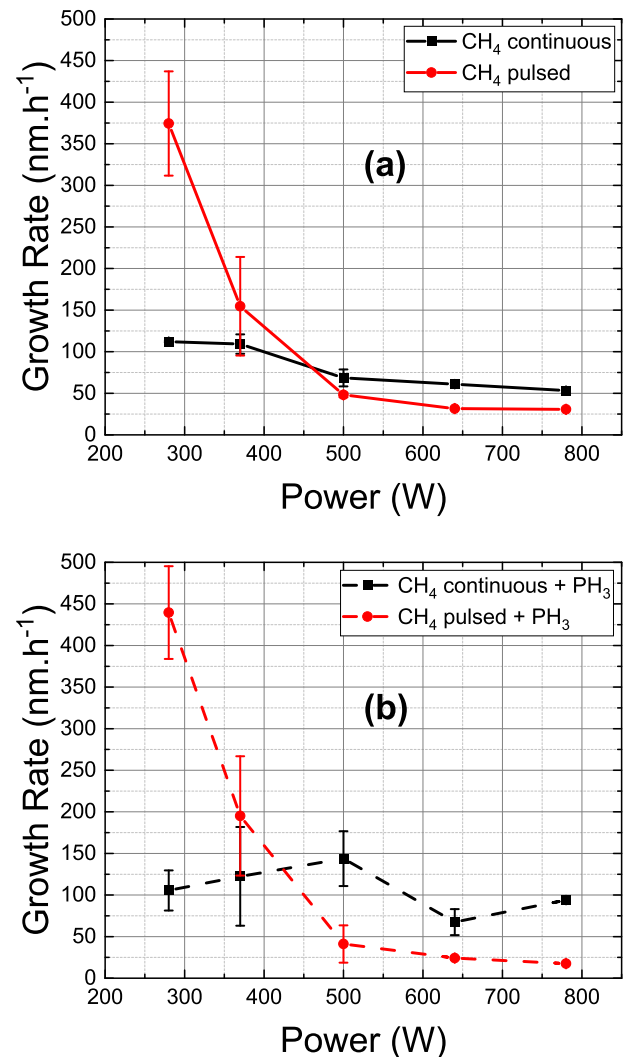


**Fig. 1.** Growth rate for the different layers as a function of the microwave power for (a) intrinsic polycrystalline diamond layers and (b) phosphorus-doped polycrystalline diamond layers.

**Table 1**

Growth conditions for undoped and phosphorus-doped polycrystalline diamond layers grown using a continuous and pulsed  $\text{CH}_4$  gas flow.

$\text{CH}_4$ gas flow	Deposition time (h)	$[\text{CH}_4]/[\text{H}_2]$ (%)	Microwave Power (W)	Pressure (mbar)	Distance substrate/plasma (mm)	Total gas flow (sccm)	Substrate temperature (°C)	$[\text{P}]/[\text{C}]_{\text{gas}}$ ratio (ppm)
Continuous	6	0.10	280 → 780	30 → 110	3 → 26	1000	1000	0
Pulsed	6	0.25	280 → 780	30 → 110	3 → 26	1000	1000	0
Continuous	6	0.10	280 → 780	30 → 110	3 → 26	1000	1000	200,000
Pulsed	6	0.25	280 → 780	30 → 110	3 → 26	1000	1000	200,000

phosphorus-doped polycrystalline diamond layer grown at 280 W and 30 mbar using a pulsed flow of CH<sub>4</sub>.

### 3.2. Raman spectroscopy

Fig. 2 shows the Raman spectra of undoped and phosphorus-doped polycrystalline diamond layers grown at 370 W and 50 mbar. All the spectra exhibit a sharp peak around 1330 cm<sup>-1</sup> which is attributed to the diamond Zone Center Phonon (ZCP) line which is characteristic of sp<sup>3</sup> carbon. For both polycrystalline undoped diamond layers, the ZCP line is centered at 1333 cm<sup>-1</sup> while a shift to lower wavenumber values is observed for phosphorus-doped layers grown using a continuous and a pulsed flow of CH<sub>4</sub>, centered at 1331.6 cm<sup>-1</sup> and 1330.1 cm<sup>-1</sup> respectively. This observation is consistent with the results obtained by M. Mermoux et al. [20] on (111) epitaxial phosphorus-doped diamond layers. Both phosphorus doping and the use of pulsed CH<sub>4</sub> injection during the growth result in an increase of intensity of the “non-diamond” band centered around 1520 cm<sup>-1</sup> [21] which is attributed to a higher sp<sup>2</sup> content. In particular, the spectrum of the undoped layer grown using a pulsed CH<sub>4</sub> flow shows the appearance of a prominent band centered around 1480 cm<sup>-1</sup> which is attributed to C–H bending and transpolyacetylene [22], while the G-band, attributed to graphite, is also visible around 1600 cm<sup>-1</sup> [21,23]. The sp<sup>3</sup>/sp<sup>2</sup> ratio calculated from Raman spectra [21] (see Fig. 3) also shows that the addition of PH<sub>3</sub> is detrimental to the crystalline quality of the polycrystalline diamond layers grown in both continuous and pulsed CH<sub>4</sub> flows. To a lesser extent, the crystalline quality of undoped and phosphorus-doped diamond layers grown using pulsed CH<sub>4</sub> flow appears to be lower compared to layers grown with a continuous flow of CH<sub>4</sub>. Overall, all layers have a quality factor above 75%.

### 3.3. SEM imaging

Well faceted diamond crystals are visible on the surface of the phosphorus-doped diamond samples grown using pulsed and continuous CH<sub>4</sub> flow. The size of the diamond crystals increases (see Table 3) when the applied power and pressure decrease with the exception of the phosphorus-doped layer grown in pulsed gas conditions under 280 W and 30 mbar which has smaller crystals and gaps between the grains. The bigger diamond crystals observed at lower applied power and lower pressure are consistent with the higher growth rate but could also be attributed to a switch from diamond re-nucleation to lateral diamond growth at lower operating pressure [24]. The samples grown using continuous CH<sub>4</sub> flow have slightly larger crystals which are more

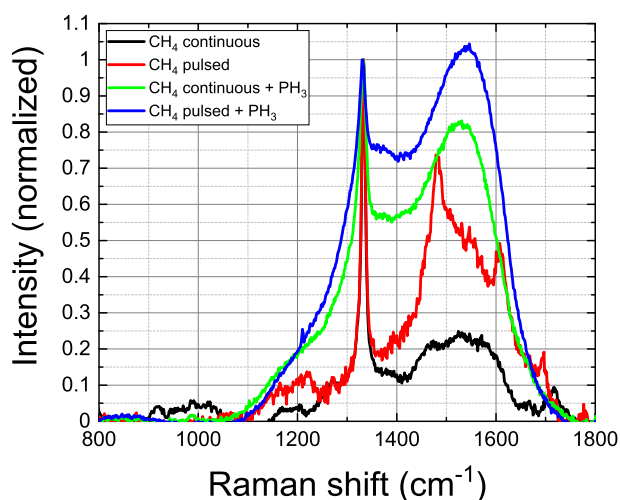


Fig. 2. Raman spectra of layers grown under 370 W and 50 mbar using the diamond ZCP peak as a reference value for normalization.

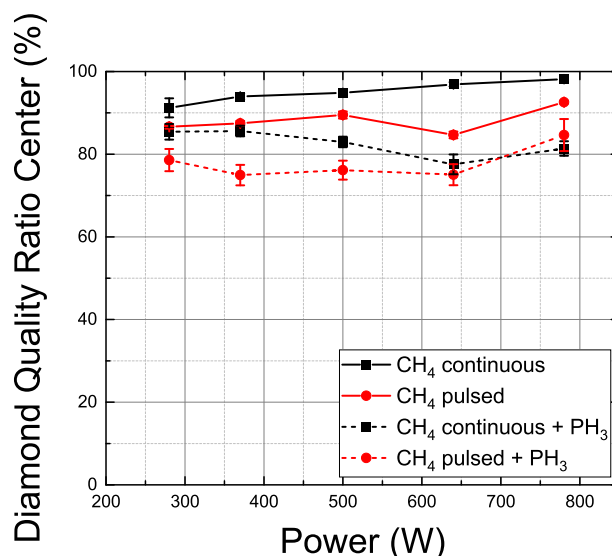


Fig. 3. sp<sup>3</sup>/sp<sup>2</sup> ratio calculated from Raman spectra measured on the different series of samples.

uniform in size compared to samples grown in pulsed gas conditions. The growth conditions of 370 W and 50 mbar offers the best crystalline quality for the phosphorus-doped layers grown using the pulsed gas method with large diamond crystals which are homogeneous in size.

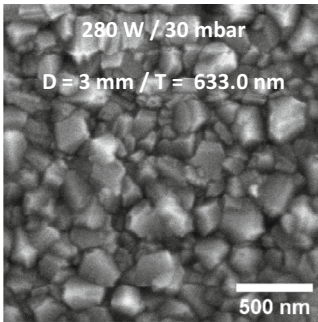
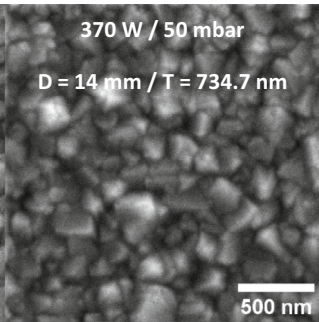
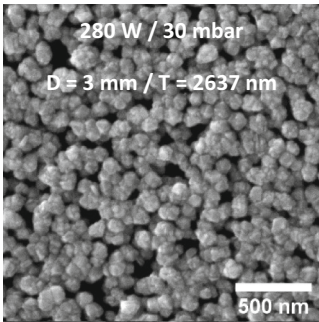
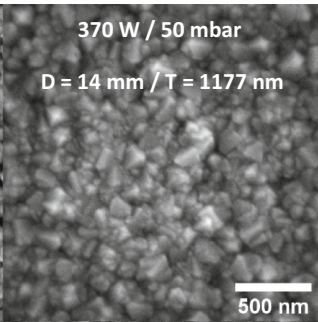
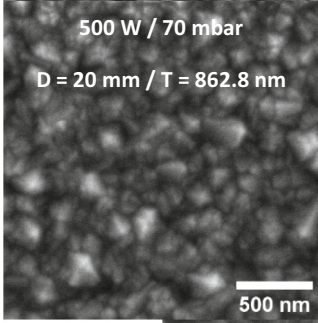
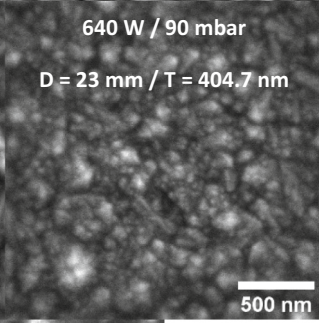
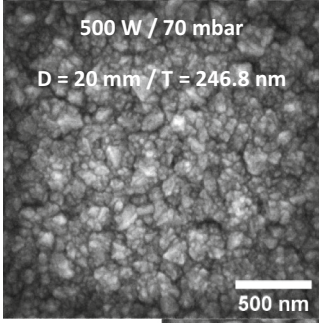
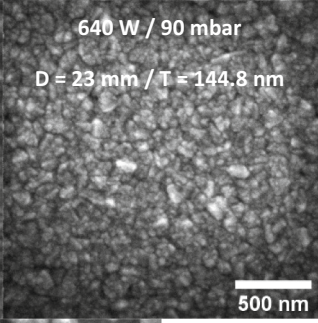
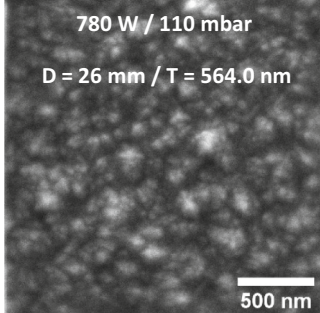
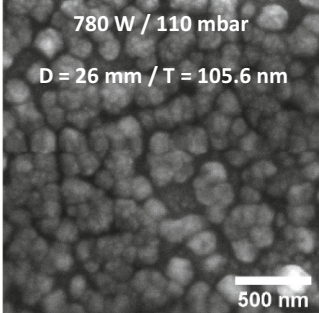
### 3.4. GDOES measurements

The phosphorus concentrations in the doped diamond layers grown using continuous and pulsed CH<sub>4</sub> flow were determined using GDOES (see Fig. 4). The P I emission line at 178.284 nm was used for phosphorus analysis. Its background was measured by analyzing boron-doped diamond layers (free of phosphorus) and its emission yield was established by sputter-rate corrected calibration [25], based on certified reference materials of steel and cast iron with phosphorus concentrations up to 0.16%. In conformity with the work from C. Schubert et al. [26], sputtering rates of the analyzed layers were found to be 40 to 50 times lower than that of steel, hence, the phosphorus signal matched well the calibration range. Estimated combined standard uncertainty of the phosphorus analysis was about 10 to 20% (relative), whilst its major component was the uncertainty of the calibration model [25]. Estimated random uncertainty of the phosphorus content is by an order of magnitude lower. Hence, prospective error of the results shown in Fig. 4 would be largely a systematic one, i.e. the same bias for all the results presented, on relative basis.

The doped polycrystalline diamond layers grown using pulsed CH<sub>4</sub> have a phosphorus content at least twice as high as the ones grown using continuous gas flow with a maximum concentration recorded of  $7.1 \times 10^{20}$  cm<sup>-3</sup> which is remarkably higher than the maximum phosphorus incorporation of  $2.2 \times 10^{20}$  cm<sup>-3</sup> reported on (111) oriented diamond crystals [27] and also higher than the highest phosphorus incorporation of  $5.0 \times 10^{20}$  cm<sup>-3</sup> currently reported in nano-crystalline diamond layers [28]. The higher phosphorus concentration in layers grown in pulsed CH<sub>4</sub> flow is coincident with the lower quality factor. Phosphorus atoms cause damages to the diamond lattice when they are incorporated due to their larger size compared to carbon [29,30]. Therefore, the deterioration in crystalline quality observed for doped polycrystalline diamond layers grown in pulsed CH<sub>4</sub> flow is consistent with their higher incorporation of phosphorus compared to samples grown in a continuous flow of CH<sub>4</sub>. Fig. 5 shows the atomic fractions for P, C, Si, and B as a function of time recorded by GDOES on two phosphorus-doped polycrystalline diamond layers grown at 370 W and 50 mbar using a continuous and a pulsed flow of CH<sub>4</sub>. The time coordinate on the x-axis

**Table 3**

SEM images of diamond layers grown using continuous and pulsed flow of CH<sub>4</sub>, with a [P]/[C] ratio of 200,000 ppm in the gas phase, for different values of pressure, microwave power, and distance D between the substrate's surface and the center of the plasma ball. T is the thickness of the deposited polycrystalline diamond layer.

Continuous		Pulsed	
<p>280 W / 30 mbar D = 3 mm / T = 633.0 nm</p> 	<p>370 W / 50 mbar D = 14 mm / T = 734.7 nm</p> 	<p>280 W / 30 mbar D = 3 mm / T = 2637 nm</p> 	<p>370 W / 50 mbar D = 14 mm / T = 1177 nm</p> 
<p>500 W / 70 mbar D = 20 mm / T = 862.8 nm</p> 	<p>640 W / 90 mbar D = 23 mm / T = 404.7 nm</p> 	<p>500 W / 70 mbar D = 20 mm / T = 246.8 nm</p> 	<p>640 W / 90 mbar D = 23 mm / T = 144.8 nm</p> 
<p>780 W / 110 mbar D = 26 mm / T = 564.0 nm</p> 		<p>780 W / 110 mbar D = 26 mm / T = 105.6 nm</p> 	

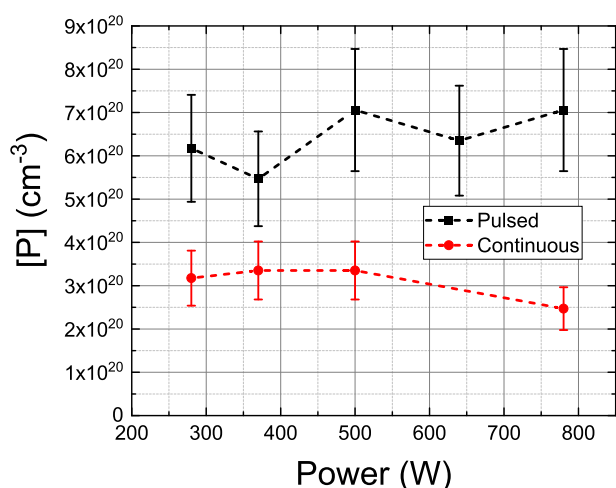


**Fig. 4.** Phosphorus content calculated from GDOES measurements for phosphorus-doped diamond layers grown using continuous and pulsed flow of CH<sub>4</sub>.

is not proportional to the depth in the sample as the sputtering rate  $q$  is about ten times higher for Si compared to diamond. Scaling factors, specified in the legend, were applied to the atomic fractions to match the ordinate scaling. As expected, the concentration of P goes down to zero in the Si substrate. The atomic fraction of P is also inhomogeneous in the depth of the layer when pulsed CH<sub>4</sub> conditions are used for the growth and it reaches its maximum at the interface between the polycrystalline diamond layer and the Si substrate. The incorporation of P atoms in substitutional sites in polycrystalline diamond has been demonstrated by phosphorus bound exciton emission of cathodoluminescence study [31]. However, it cannot be excluded that P atoms are incorporated in grains boundaries due to impurity segregation as it is the case for B atoms [32].

**4. Conclusion**

We have successfully grown highly phosphorus-doped polycrystalline diamond layers on (100) oriented Si substrates using pulsed injection of CH<sub>4</sub> during the growth by MWPECVD. A higher growth rate at low power was observed for layers grown using a pulsed flow of CH<sub>4</sub> instead of a continuous one with a maximum of 440 nm·h<sup>-1</sup>. Raman spectroscopy shows that even though the addition of PH<sub>3</sub> and the use of pulsed CH<sub>4</sub> injection is detrimental to the crystalline quality of phosphorus-doped polycrystalline diamond layers, the crystalline quality remains good with a sp<sup>3</sup>/sp<sup>2</sup> carbon ration over 75%. Most

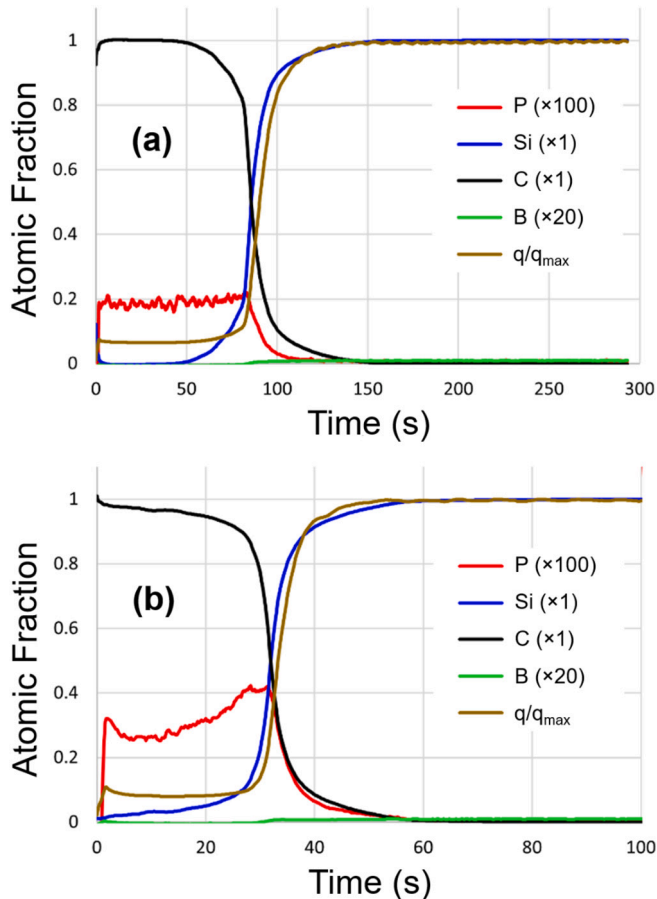


**Fig. 5.** Atomic fraction recorded as a function of time using GDOES for two phosphorus-doped diamond layers grown under 370 W and 50 mbar of pressure in (a) continuous and (b) pulsed  $\text{CH}_4$  injection. The numbers between parentheses are scaling factors and  $q$  is the sputtering rate as resulting from the quantification algorithm described in Ref [25].

importantly, with this method we managed to reach a phosphorus concentration of  $7.1 \times 10^{20} \text{ cm}^{-3}$  which is significantly higher than the maximum value previously reported on (111) oriented diamond crystals. Those results open new perspectives for the production and applications of high phosphorus concentration n-type diamond layers.

#### CRediT authorship contribution statement

As first author, Nicolas Lambert, confirms on behalf of all authors the following:

- o That all authors have participated in (a) conception and design, or analysis and interpretation of data; (b) drafted the article or revised it critically for important intellectual content; and (c) approved of the final version.
- o That this manuscript has not been submitted to, nor is under review at, another journal or other publishing venue.

#### Declaration of competing interest

The authors declare that they have no known competing financial interests or personal relationships that could have appeared to influence the work reported in this paper.

#### Acknowledgements

The financial support from the following sources is gratefully

acknowledged: The Czech Science Foundation grant ID: GACR 21-03538S, the SGS Student Grant ID: SGS21/057/OHK3/1T/13, and the CzechNanoLab Research Infrastructure supported by MEYS CR (LM2018110).

#### References

- [1] M. Saremi, R. Hathwar, M. Dutta, F.A.M. Koeck, R.J. Nemanich, S. Chowdhury, S. M. Goodnick, Analysis of the reverse I-V characteristics of diamond-based PIN diodes, *Appl. Phys. Lett.* 111 (2017), 043507, <https://doi.org/10.1063/1.4986756>.
- [2] T. Shimaoka, D. Kuwabara, A. Hara, T. Makino, M. Tanaka, S. Koizumi, Charge transport properties of intrinsic layer in diamond vertical pin diode, *Appl. Phys. Lett.* 110 (2017), 212104, <https://doi.org/10.1063/1.4984280>.
- [3] T. Matsumoto, H. Kato, K. Oyama, T. Makino, M. Ogura, D. Takeuchi, T. Inokuma, N. Tokuda, S. Yamasaki, Inversion channel diamond metal-oxide-semiconductor field-effect transistor with normally off characteristics, *Sci. Rep.* 6 (2016), <https://doi.org/10.1038/srep31585>.
- [4] T. Iwasaki, H. Kato, J. Yaita, T. Makino, M. Ogura, D. Takeuchi, H. Okushi, S. Yamasaki, M. Hatano, Current enhancement by conductivity modulation in diamond JFETs for next generation low-loss power devices, in: 2015 IEEE 27th International Symposium on Power Semiconductor Devices & IC's (ISPSD), IEEE, Hong Kong, China, 2015, pp. 77–80, <https://doi.org/10.1109/ISPSD.2015.7123393>.
- [5] J. Pernot, P.N. Volpe, F. Omnès, P. Muret, V. Mortet, K. Haenen, T. Teraji, Hall hole mobility in boron-doped homoepitaxial diamond, *Phys. Rev. B* 81 (2010), <https://doi.org/10.1103/PhysRevB.81.205203>.
- [6] T. Kageura, M. Hideko, I. Tsuyuzaki, S. Amano, A. Morishita, T. Yamaguchi, Y. Takano, H. Kawarada, Superconductivity in nano- and micro-patterned high quality single crystalline boron-doped diamond films, *Diam. Relat. Mater.* 90 (2018) 181–187, <https://doi.org/10.1016/j.diamond.2018.10.013>.
- [7] M.-A. Pinault-Thaury, T. Tillocher, D. Kobor, N. Habka, F. Jomard, J. Chevallier, J. Barjon, Phosphorus donor incorporation in (1 0 0) homoepitaxial diamond: Role of the lateral growth, *J. Cryst. Growth* 335 (2011) 31–36, <https://doi.org/10.1016/j.jcrysgro.2011.06.007>.
- [8] F.A.M. Koeck, S. Chowdhury, R.J. Nemanich, Phosphorus incorporation for n-type doping of diamond with (100) and related surface orientation, US10121657B2, n. d.
- [9] S. Koizumi, M. Kamo, Y. Sato, H. Ozaki, T. Inuzuka, Growth and characterization of phosphorus doped 111 homoepitaxial diamond thin films, *Appl. Phys. Lett.* 71 (1997) 1065–1067, <https://doi.org/10.1063/1.119729>.
- [10] T. Ando, H. Haneda, M. Akaishi, Y. Sato, M. Kamo, Oxygen impurities at the homoepitaxially grown diamond-substrate interface analyzed by secondary ion mass spectrometry, *Diam. Relat. Mater.* 5 (1996) 34–37, [https://doi.org/10.1016/0925-9635\(95\)00337-1](https://doi.org/10.1016/0925-9635(95)00337-1).
- [11] M.A. Lobaev, D.B. Radishev, A.M. Gorbachev, A.L. Vikharev, M.N. Drozdov, Investigation of microwave plasma during diamond doping by phosphorus using optical emission spectroscopy, *Phys. Status Solidi A* 216 (2019) 1900234, <https://doi.org/10.1002/psaa.201900234>.
- [12] D. Glindemann, M. Edwards, O. Schrems, Phosphine and methylphosphine production by simulated lightning—a study for the volatile phosphorus cycle and cloud formation in the earth atmosphere, *Atmos. Environ.* 38 (2004) 6867–6874, <https://doi.org/10.1016/j.atmosenv.2004.09.002>.
- [13] A.R. Bossard, R. Kamga, F. Raulin, Gas phase synthesis of organophosphorus compounds and the atmosphere of the giant planets, *Icarus* 67 (1986) 305–324, [https://doi.org/10.1016/0019-1035\(86\)90111-9](https://doi.org/10.1016/0019-1035(86)90111-9).
- [14] G. Frangieh, M.-A. Pinault, J. Barjon, F. Jomard, J. Chevallier, Incorporation of arsenic in diamond grown by chemical vapor deposition, *Phys. Stat. Solidi A* 205 (2008) 2207–2210, <https://doi.org/10.1002/psaa.200879726>.
- [15] O.A. Williams, O. Douh ret, M. Daenen, K. Haenen, E.  sawa, M. Takahashi, Enhanced diamond nucleation on monodispersed nanocrystalline diamond, *Chem. Phys. Lett.* 445 (2007) 255–258, <https://doi.org/10.1016/j.cplett.2007.07.091>.
- [16] M. Kamo, Y. Sato, S. Matsumoto, N. Setaka, Diamond synthesis from gas phase in microwave plasma, *J. Cryst. Growth* 62 (1983) 642–644, [https://doi.org/10.1016/0022-0248\(83\)90411-6](https://doi.org/10.1016/0022-0248(83)90411-6).
- [17] J.J. Gracio, Q.H. Fan, J.C. Madaleno, Diamond growth by chemical vapour deposition, *J. Phys. D: Appl. Phys.* 43 (2010), 374017, <https://doi.org/10.1088/0022-3727/43/37/374017>.
- [18] M. Noda, A. Marui, T. Suzuki, M. Umeno, Deposition of diamond film on silicon and quartz substrates located near DC plasma, *Diam. Relat. Mater.* 14 (2005) 1757–1760, <https://doi.org/10.1016/j.diamond.2005.08.050>.
- [19] J. Liu, L.F. Hei, J.H. Song, C.M. Li, W.Z. Tang, G.C. Chen, F.X. Lu, High-rate homoepitaxial growth of CVD single crystal diamond by dc arc plasma jet at blow-down (open cycle) mode, *Diam. Relat. Mater.* 46 (2014) 42–51, <https://doi.org/10.1016/j.diamond.2014.04.008>.
- [20] M. Mermoux, B. Marcus, A. Crisci, A. Tajani, E. Gheeraert, E. Bustarret, Micro-Raman scattering from undoped and phosphorus-doped (111) homoepitaxial diamond films: stress imaging of cracks, *J. Appl. Phys.* 97 (2005), 043530, <https://doi.org/10.1063/1.1849828>.
- [21] W. Fortunato, A.J. Chiquito, J.C. Galzerani, J.R. Moro, Crystalline quality and phase purity of CVD diamond films studied by Raman spectroscopy, *J. Mater. Sci.* 42 (2007) 7331–7336, <https://doi.org/10.1007/s10853-007-1575-0>.
- [22] L. Golunski, M. Sobaszek, M. Gardas, M. Gnyba, R. Bogdanowicz, M. Ficek, P. Plotka, Optimization of polycrystalline CVD diamond seeding with the use of sp

- 3/sp 2 Raman band ratio, *Acta Phys. Pol. A* 128 (2015) 136–140, <https://doi.org/10.12693/APhysPolA.128.136>.
- [23] Y.G. Gogotsi, P. Kofstad, M. Yoshimura, K.G. Nickel, Formation of sp<sup>3</sup>-bonded carbon upon hydrothermal treatment of SiC, *Diam. Relat. Mater.* 5 (1996) 151–162, [https://doi.org/10.1016/0925-9635\(95\)00341-X](https://doi.org/10.1016/0925-9635(95)00341-X).
- [24] O. Babchenko, Š. Potocký, T. Izák, K. Hruška, Z. Bryknař, A. Kromka, Influence of surface wave plasma deposition conditions on diamond growth regime, *Surf. Coat. Technol.* 271 (2015) 74–79, <https://doi.org/10.1016/j.surfcoat.2015.01.012>.
- [25] Z. Weiss, Calibration methods in glow discharge optical emission spectroscopy: a tutorial review, *J. Anal. At. Spectrom.* 30 (2015) 1038–1049, <https://doi.org/10.1039/C4JA00482E>.
- [26] C. Schubert, V. Hoffmann, A. Kümmel, J. Sinn, M. Härtel, A. Reuther, M. Thomalla, T. Gemming, J. Eckert, C. Leyens, Compositional depth profiling of diamond-like carbon layers by glow discharge optical emission spectroscopy, *J. Anal. At. Spectrom.* 31 (2016) 2207–2212, <https://doi.org/10.1039/C6JA00251J>.
- [27] N. Temahuki, R. Gillet, V. Sallet, F. Jomard, E. Chikoidze, Y. Dumont, M.-A. Pinault-Thaury, J. Barjon, New process for electrical contacts on (100) N-type diamond, *Phys. Status Solidi A* 214 (2017) 1700466, <https://doi.org/10.1002/pssa.201700466>.
- [28] H. Kato, D. Takeuchi, M. Ogura, T. Yamada, M. Kataoka, Y. Kimura, S. Sobue, C. E. Nebel, S. Yamasaki, Heavily phosphorus-doped nano-crystalline diamond electrode for thermionic emission application, *Diam. Relat. Mater.* 63 (2016) 165–168, <https://doi.org/10.1016/j.diamond.2015.08.002>.
- [29] S. Curat, H. Ye, O. Gaudin, R.B. Jackman, S. Koizumi, An impedance spectroscopic study of n-type phosphorus-doped diamond, *J. Appl. Phys.* 98 (2005), 073701, <https://doi.org/10.1063/1.2058183>.
- [30] S. Koizumi, Growth and characterization of phosphorus doped n-type diamond thin films, *Phys. Stat. Sol. A* 172 (1999) 71–78, [https://doi.org/10.1002/\(SICI\)1521-396X\(199903\)172:1<71::AID-PSSA71>3.0.CO;2-N](https://doi.org/10.1002/(SICI)1521-396X(199903)172:1<71::AID-PSSA71>3.0.CO;2-N).
- [31] W. Janssen, S. Turner, G. Sakr, F. Jomard, J. Barjon, G. Degutis, Y.-G. Lu, J. D'Haen, A. Hardy, M.V. Bael, J. Verbeeck, G.V. Tendeloo, K. Haenen, Substitutional phosphorus incorporation in nanocrystalline CVD diamond thin films: Substitutional phosphorus incorporation in nanocrystalline CVD diamond thin films, *Phys. Status Solidi RRL* 8 (2014) 705–709, <https://doi.org/10.1002/pssr.201409235>.
- [32] D.M. Malta, J.A. von Windheim, H.A. Wynands, B.A. Fox, Comparison of the electrical properties of simultaneously deposited homoepitaxial and polycrystalline diamond films, *J. Appl. Phys.* 77 (1995) 1536–1545, <https://doi.org/10.1063/1.358905>.
- [33] V. Mortet, A. Taylor, M. Davydova, M. Lamač, N. Lambert, I. Elantyevev, J. Lorincik, D. Troadec, M. Vronka, Š. Potocký, Effect of pulsed methane gas flow on the incorporation of phosphorus in diamond, *Diamond Relat. Mater.* 124 (2022), 108928, <https://doi.org/10.1016/j.diamond.2022.108928>.

# Optical Emission Spectroscopy Analysis of Microwave Plasma-Enhanced Chemical Vapor Deposition Systems Dynamic Gas Response

Nicolas Lambert, Kil-Dong Sung, and Vincent Mortet\*

Microwave plasma-enhanced chemical vapor deposition (MWPECVD) is widely used for the growth of synthetic doped diamond for electronic and electrochemical applications. Recent results have shown the possible enhancement of phosphorus incorporation using the pulsed gas injection growth method. It is therefore important to understand the dynamics of precursor gases to optimize the dopants incorporation in diamond. In this work, the dynamic response of different gases ( $N_2$ ,  $CH_4$ , and  $O_2$ ) impulses in hydrogen plasma is studied in two different MWPECVD reactors: a lab made NIRIM type reactor, and a commercial reactor made by Seki Diamond Systems. These reactors of different volumes are operated at different pressure and total gas flow. The time responses to the precursor gas injection are recorded by optical emission spectroscopy. Experimental time responses are fitted using an impulse response equation. Fitting parameters are extracted and compared for the different reactors, gases, total gas flow, and pressure conditions. The time responses of the different reactors are discussed as a function of their volume and the operating conditions.

MWPECVD is now widely used for the growth of synthetic doped diamond with applications in electronics, such as PIN diodes<sup>[6,7]</sup> and field-effect transistors,<sup>[8,9]</sup> and electrochemistry for wastewater treatment.<sup>[10,11]</sup> Even though continuous gas flows are mostly used for the growth of diamond by MWPECVD, intermittent gas flow is used for specific application such as delta doping.<sup>[12,13]</sup> Moreover, recent results show the possible enhancement of phosphorus incorporation in diamond using pulsed gas injection during MWPECVD growth.<sup>[14–16]</sup> Therefore, understanding the gas dynamic in the MWPECVD reactors is crucial for the optimization of the gas flows and doping.

In this work, we studied the dynamic of pulsed injection of different gases ( $N_2$ ,  $CH_4$ , and  $O_2$ ) in hydrogen plasma in two different MWPECVD reactors: a lab

## 1. Introduction

The growth of synthetic diamond by Chemical Vapor Deposition (CVD) was first reported by W. G. Eversole<sup>[1]</sup> and then J. C. Angus et al.<sup>[2]</sup> The growing interest for the diamond material, due to its outstanding properties including chemical inertness, good optical transparency, and high thermal conductivity,<sup>[3]</sup> led to the development of other CVD deposition methods such as hot filament CVD<sup>[4]</sup> and microwave plasma-enhanced CVD (MWPECVD).<sup>[5]</sup>

made NIRIM type reactor and a commercial AX5010 reactor from Seki Diamond Systems. These two reactors of different volumes were operated at different total pressure and total gas flow. The time dependent variation of the intensity of characteristic luminescent species (e.g., NH,  $C_2$  or OH) upon the instantaneous injection of a small quantity of precursor gas were recorded by Optical Emission Spectroscopy (OES) and analyzed using a method inspired by the work of H. Pendar et al.<sup>[17]</sup>

## 2. Experimental Section

Two different reactors were considered in this study: a lab made NIRIM reactor using a total gas flow between 200 and 1000 sccm and a commercial AX5010 reactor from Seki Diamonds Systems using a total gas between 200 and 600 sccm. Both reactors were operated at a pressure between 30 and 110 mbar. The limits of the pressure range and total gas flow investigated in this work were chosen in accordance with the usual operation conditions of each reactor. The main difference between the two reactors is their volume which is 1.4 L for the NIRIM system and 3.2 L for the Seki AX5010 system. The NIRIM and Seki AX5010 reactors are evacuated at a base pressure below  $10^{-6}$  mbar before the experiment. The base pressure was achieved using turbo molecular pumps in the NIRIM (Agilent Turbo-V 301 Navigator) and the Seki system (Pfeiffer Vacuum TMH-071). The NIRIM system operate using a 1.5 kW microwave power source in combination

N. Lambert, K.-D. Sung, V. Mortet  
Department of Functional Materials  
Institute of Physics of the Czech Academy of Sciences  
182 21 Prague, Czech Republic  
E-mail: mortetv@fzu.cz

N. Lambert  
Faculty of Electrical Engineering  
Czech Technical University in Prague  
166 27 Prague, Czech Republic

V. Mortet  
Faculty of Biomedical Engineering  
Czech Technical University in Prague  
272 01 Kladno, Czech Republic

 The ORCID identification number(s) for the author(s) of this article can be found under <https://doi.org/10.1002/pssa.202200322>.

DOI: 10.1002/pssa.202200322

with a WR340 downstream plasma source from SAIREM company. The Seki AX5010 system is operated using an AsTex S-1500 plasma source with a maximum power output of 1.5 kW.

The gases used in this study are H<sub>2</sub> (N5.6), N<sub>2</sub> (N5.0), CH<sub>4</sub> (N5.5), and O<sub>2</sub> (N4.5). The flow of gases was controlled using MKS mass flow controllers. The precursor gas pulses were generated using the gas trapped in a small volume at a constant pressure (2 bar) between two ball valves and released instantaneously in the reactor. The volume of trapped gas is ≈1 mL. The dynamic gas pulse responses were recorded using a Stellarnet BLACK-Comet-SR compact spectrometer. The full measurement setup is described in detail in a previous publication.<sup>[18]</sup> In this work, NH (336.9 nm),<sup>[19]</sup> C<sub>2</sub> (517.0 nm),<sup>[20]</sup> and OH (311.4 nm)<sup>[21]</sup> lines are analyzed to study the effect of a pulse of N<sub>2</sub>, CH<sub>4</sub>, and O<sub>2</sub> in the plasma. The detection limits of the OES system for the different gases in the NIRIM and Seki reactors are given in **Table 1**. The experimental time responses were fitted using the impulse response equation proposed by H. Pendar et al.<sup>[17]</sup>

$$f(t) = \alpha t^m e^{-t/\tau} \quad (1)$$

where  $t$  is the time and  $\alpha$ ,  $m$ , and  $\tau$  are fitting parameters.  $\tau$  is the characteristic time of the exponential decay of the signal which

**Table 1.** Detection limits of the OES system for N<sub>2</sub>, CH<sub>4</sub>, and O<sub>2</sub> in the Seki and NIRIM reactors as a function of the pressure given as a fraction of the total gas flow.

Pressure [mbar]	Detection limit Seki [%]			Detection limit NIRIM [%]		
	N <sub>2</sub>	CH <sub>4</sub>	O <sub>2</sub>	N <sub>2</sub>	CH <sub>4</sub>	O <sub>2</sub>
30	0.5	15	0.7	0.3	/	<0.2
50	0.5	3.8	0.7	0.3	/	<0.2
70	0.5	1.0	0.7	0.3	2.5	<0.2
90	0.7	0.7	0.7	0.4	0.8	<0.2
110	0.8	0.5	0.7	0.5	0.3	<0.2

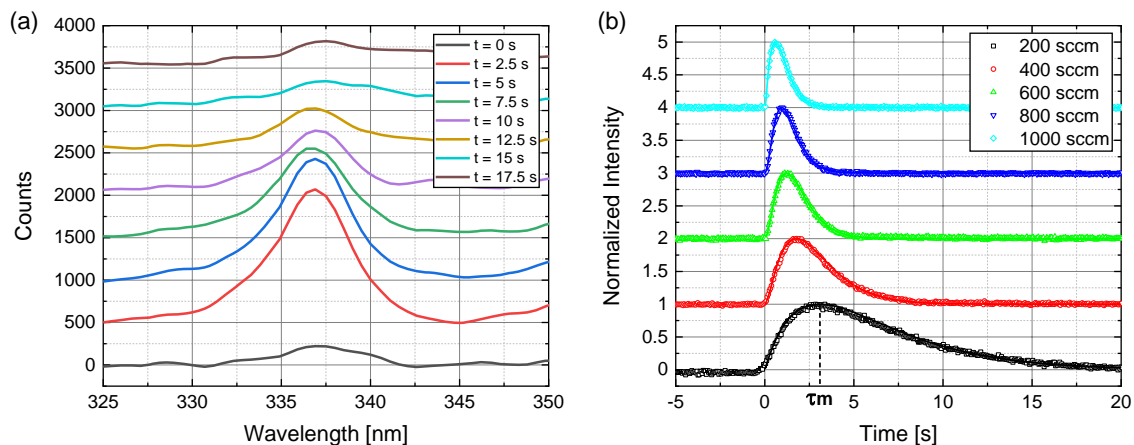


**Figure 1.** Evolution of a) the emission spectra as a function of time upon the injection of a N<sub>2</sub> gas pulse for a pressure of 110 mbar and a total gas flow of 200 sccm and b) experimental normalized intensity of the NH emission line (336.9 nm) as a function of time upon the injection of a N<sub>2</sub> gas pulse (dots) and fitting curves (solid lines) measured on the NIRIM reactor for a pressure of 110 mbar and different total gas flows. For better readability, each curve is separated by an offset of 500 count in (a) and 1 arb. unit in (b).

dominates for large value of  $t$  while  $m$  characterizes the rising portion of the signal for small value of  $t$ . The curve reaches its maximum at  $t = \tau$ .

### 3. Results and Discussion

**Figure 1a** shows the evolution of the emission spectra as a function of time upon the injection of a N<sub>2</sub> gas pulse for a total gas flow of 200 sccm and a pressure of 110 mbar in the NIRIM reactor. At  $t = 0$  s, N<sub>2</sub> is released into the reactor chamber and the intensity of the emission line of NH located at 336.9 nm increases and then gradually decreases as the gas species are removed from the reactor by the pumping system. **Figure 1b** shows the dynamic pulse responses to a N<sub>2</sub> gas pulse in a pure hydrogen plasma recorded on the NIRIM reactor for different total gas flows and a pressure of 110 mbar. The time position of maximum intensity and the time at which the signal has decreased by 99%,  $\tau m$  and  $2.7\tau$  respectively, are indicated on the figure for the signal recorded with a total gas flow of 200 sccm. The normalized intensity of the emission line of NH, was recorded as a function of time with the spectrometer and fitted using Equation (1) which offers a good fit to the experimental curves. The rising and decay times become shorter when the total gas flow increases which is consistent with a faster circulation of gases in the reactor.

**Figure 2a** shows the evolution of the parameter  $\tau$  in the Seki reactor as a function of total gas flow and pressure for a pulse of N<sub>2</sub>. Data points of the same color were recorded at the same pressure. The parameter  $\tau$  reflects the residency time of the precursor species inside the reactor and it decreases with the total gas flow. This behavior is consistent with what was observed in **Figure 1**, a higher flow rate increases the circulation speed of gas in the reactor and decreases the residency time of precursor species. The parameter  $\tau$  also increases with the pressure. Indeed, an increase in pressure translates to an increase in the quantity of gas molecules present in the reactor, therefore, for a same total gas flow, it will take longer to remove the precursor specie from the chamber. The following equation was used to fit the evolution

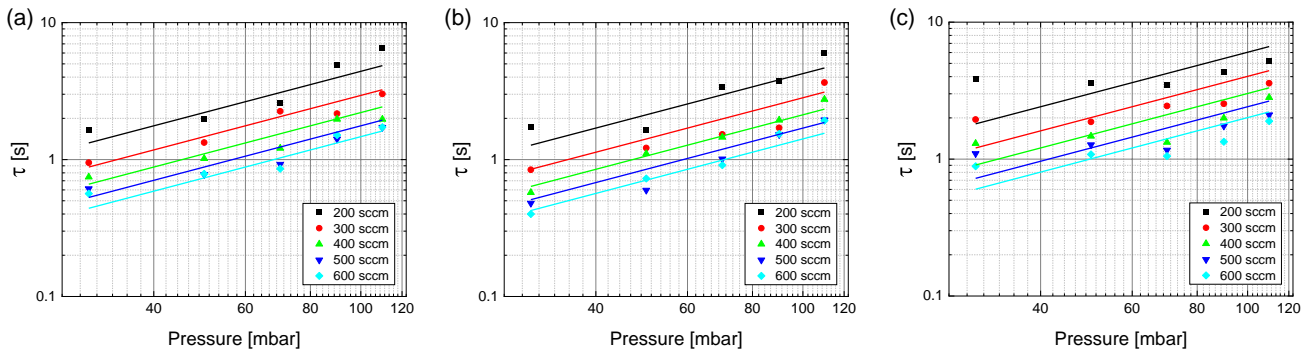


**Figure 2.** Parameter  $\tau$  as a function of the total gas flow and the pressure in the Seki reactor for a pulse of a)  $N_2$ , b)  $CH_4$ , and c)  $O_2$ . The solid lines represent fitting curves given by Equation (2).

of the parameter  $\tau$  as a function of the total gas flow and the pressure

$$\tau = \frac{kP}{F} \quad (2)$$

Where  $P$  is the pressure in mbar,  $F$  is the total gas flow under standard conditions of pressure and temperature ( $P_0 = 1.01$  bar and  $T_0 = 288$  K), and  $k$  is a constant. The parameter  $k$  was obtained by averaging the value of  $\frac{\tau F}{P}$  over each condition of pressure and total gas flow used in the OES measurement. The calculated values of  $k$  are summarized in Table 2. In Figure 2a, the fitting curves represented by the solid lines are given by Equation (2) with  $k = 1.47 \times 10^{-4}$  L mbar $^{-1}$  which matches well the evolution of  $\tau$ . This result is consistent with the simple

impulse response model presented by G. A. Bartholomew et al.,<sup>[22]</sup> where the value of  $\tau$  is given by

$$\tau = \frac{V}{\dot{V}} = \frac{VP}{P_0 F} \quad (3)$$

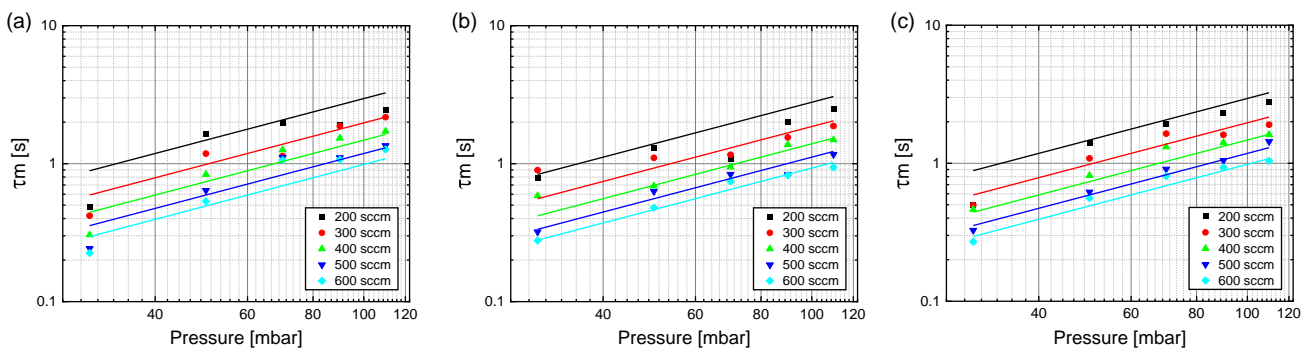
Where  $V$  is the volume of the chamber,  $\dot{V}$  is the gas flow rate, and  $P_0$  is the standard pressure. Figure 2b,c present the results of similar experiments done on the Seki system for a pulse of  $CH_4$  and  $O_2$  respectively. The evolution of the parameter  $\tau$  is close to what was observed for  $N_2$  with  $k = 1.41 \times 10^{-4}$  L mbar $^{-1}$  for  $CH_4$  and  $k = 2.01 \times 10^{-4}$  L mbar $^{-1}$  for  $O_2$ .

Figure 3 shows the evolution of  $\tau m$ , the time to reach the maximum intensity of the dynamic pulse response, as a function of the total gas flow in the Seki reactor. The position of the maximum intensity is inversely proportional to the total gas flow which can be attributed to the higher circulation speed of gas species in the reactor at higher flow rate. The time to reach the maximum intensity increases with the pressure which can be explained by the additional collisions between gas molecules which slow down the diffusion of the gas in the reactor when the pressure increases. A similar equation to Equation (2) was used to fit the experimental values of  $\tau m$

$$\tau m = \frac{k'P}{F} \quad (4)$$

**Table 2.** Fitting parameters  $k$  and  $k'$  and the calculated error on their value.

Reactor type	Gas	$k$ [L mbar $^{-1}$ ]	$k$ error [%]	$k'$ [L mbar $^{-1}$ ]	$k'$ error [%]
Seki	$N_2$	$1.47 \times 10^{-4}$	17.2	$9.88 \times 10^{-5}$	23.8
	$CH_4$	$1.41 \times 10^{-4}$	17.8	$9.29 \times 10^{-5}$	20.0
	$O_2$	$2.01 \times 10^{-4}$	36.4	$9.82 \times 10^{-5}$	14.6
NIRIM	$N_2$	$6.82 \times 10^{-5}$	25.4	$1.36 \times 10^{-4}$	30.5
	$CH_4$	$6.04 \times 10^{-5}$	25.5	$1.13 \times 10^{-4}$	19.8
	$O_2$	$1.01 \times 10^{-4}$	67.0	$2.33 \times 10^{-4}$	66.4

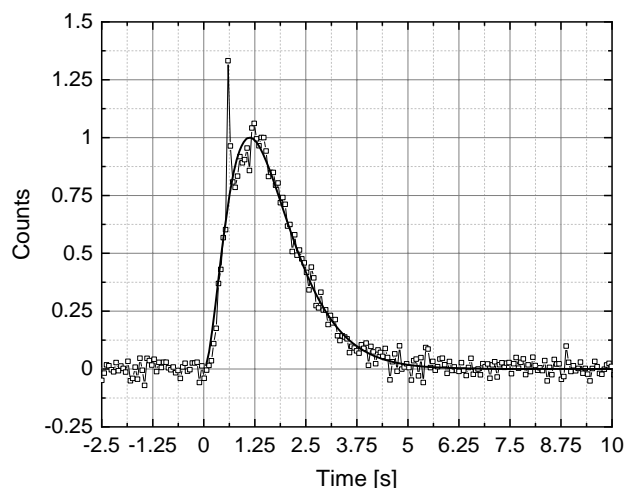


**Figure 3.** Time position of the maximum intensity  $\tau m$  as a function of the total gas flow and the pressure in the Seki reactor for a pulse of a)  $N_2$ , b)  $CH_4$ , and c)  $O_2$ . The solid lines represent fitting curves given by Equation (4).

Where  $P$  is the pressure in mbar,  $F$  is the total gas flow under standard conditions of pressure and temperature, and  $k'$  is a constant. The parameter  $k'$  was obtained using the same method used to obtain  $k$  in Equation (2). The calculated values of  $k'$  are summarized in Table 2. This equation offers a good fit of the value of  $\tau m$  for the measurements done with  $N_2$ ,  $CH_4$ , and  $O_2$  with a  $k'$  of  $9.88 \times 10^{-5}$ ,  $9.29 \times 10^{-5}$  and  $9.82 \times 10^{-5} \text{ L mbar}^{-1}$  respectively. In general, the values of  $k$  and  $k'$  are similar for all three gases.

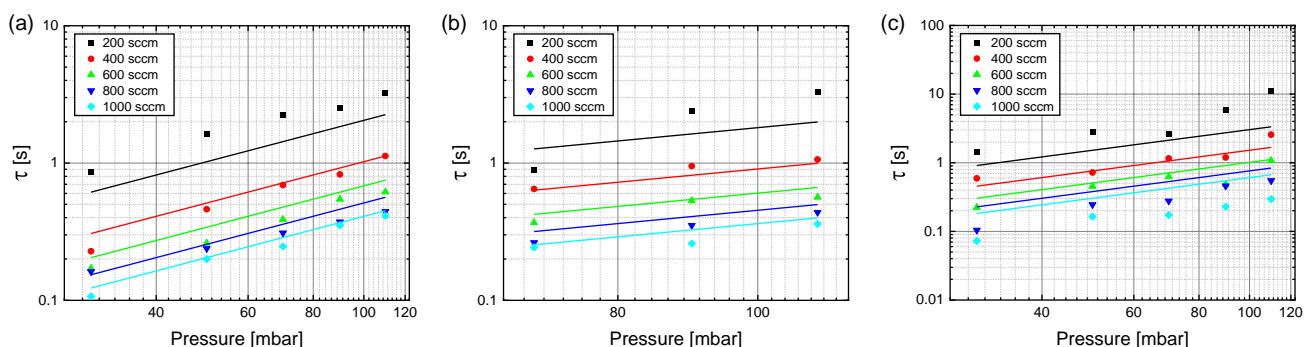
Similar measurements were done in the NIRIM reactor. Equation (2) and (4) fit well the evolution of the parameter  $\tau$  and the position of the time to reach the maximum intensity  $\tau m$  respectively for pulses of  $N_2$  and  $CH_4$  as shown in Figure 4 and 5. The intensity of the  $C_2$  line could not be measured for a pressure below 70 mbar because the signal was too weak. In the case of  $O_2$ , equation (2) doesn't match well the evolution of the  $\tau$  and  $\tau m$ . Figure 6 shows the dynamic response of the NIRIM system to a pulse of  $O_2$  for a pressure of 110 mbar and a gas flow of 800 sccm. This different behavior is not fully understood but could be attributed to the reaction between  $O_2$  and phosphorus impurities deposited on the walls of the NIRIM reactor chamber during previous phosphorus diamond growth.

Figure 7 shows the evolution of the fitting parameter  $k$  as a function of the volume of the reactors for an injection of  $N_2$ ,  $CH_4$ , and  $O_2$ . The parameter  $\tau$  increases with the volume of



**Figure 6.** Experimental dynamic response to a  $O_2$  gas pulse (connected dots) and fitting curves (solid lines) measured on the NIRIM reactor for a pressure of 110 mbar and a total gas flow of 800 sccm.

the reactor which can also be attributed to the larger quantity of gas molecules present in the reactor at larger volume. In the Equation (3) proposed by Bartholomew et al.,<sup>[22]</sup> the parameter  $\tau$  is proportional to the volume of the chamber in which the gas is injected. Even though it is not possible to



**Figure 4.** Parameter  $\tau$  as a function of the total gas flow and the pressure in the NIRIM reactor for a pulse of a)  $N_2$ , b)  $CH_4$ , and c)  $O_2$ . The solid lines represent fitting curves given by Equation (2).

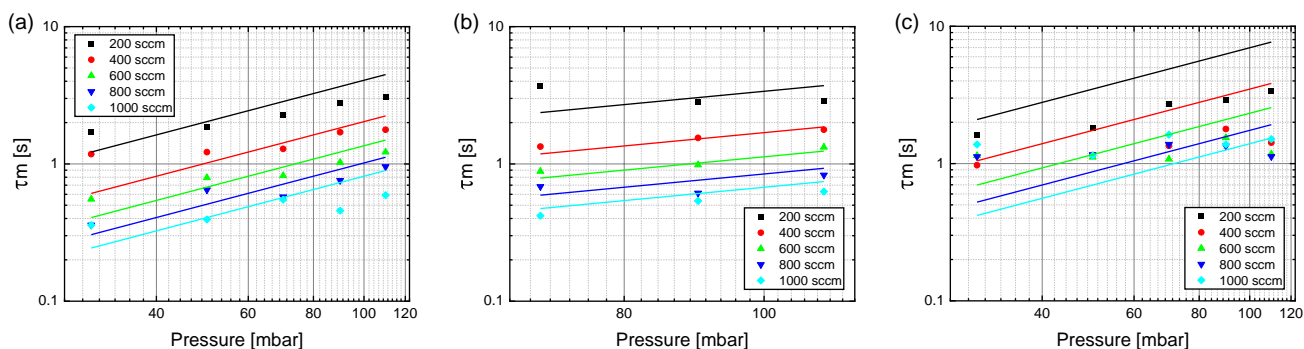


**Figure 5.** Time position of the maximum intensity  $\tau m$  as a function of the total gas flow and the pressure in the NIRIM reactor for a pulse of a)  $N_2$ , b)  $CH_4$ , and c)  $O_2$ . The solid lines represent fitting curves given by Equation (4).

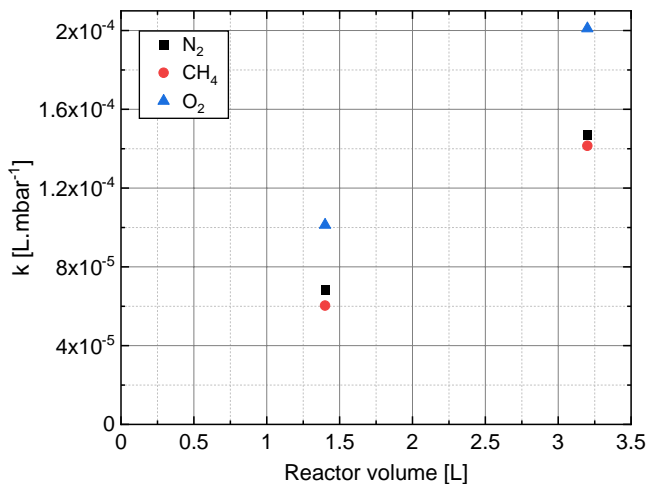


**Figure 7.** Fitting parameter  $k$  in Equation (2) as a function of the volume of the reactors for an injection of N<sub>2</sub>, CH<sub>4</sub>, and O<sub>2</sub>.

confirm this result with measurements from only two different reactors, the results presented in Figure 7 are in agreement with Equation (3).

#### 4. Conclusion

In the study of the dynamic gas pulse responses in the NIRIM and Seki systems, we show that the behavior of N<sub>2</sub>, CH<sub>4</sub>, and O<sub>2</sub> gas pulses strongly depends on the total gas flow, pressure, and volume of the reactors. The residence period of reactive species inside the reactor is proportional to the ratio of the total gas flow over the pressure and it also increases with the volume of the reactor. We also show that the residence period of reactive species inside the reactor can significantly extend after the injection of precursor gas has been shut down. This parameter is particularly important for the growth of doped diamond using pulsed gas conditions. Understanding the precursor gas dynamic in MWPECVD reactor is important for the optimization of doped diamond growth and the fabrication of electronic diamond structures. We expect this will contribute to the development of doped diamond growth and devices.

#### Acknowledgements

The financial support from the following sources—the Czech Science Foundation grant ID: GACR 21-03538S, the SGS Student Grant “Electric Discharges III: experimental research, modeling, and applications” (Reg. Number: OHK3-004/22), and the Operational Program Research, Development, and Education financed by European Structural and Investment Funds and the Czech Ministry of Education, Youth and Sports (projects SOLID21—CZ.02.1.01/0.0/0.0/16\_019/0000760)—is gratefully acknowledged.

#### Conflict of Interest

The authors declare no conflict of interest.

#### Data Availability Statement

The data that support the findings of this study are available from the corresponding author upon reasonable request.

#### Keywords

diamond growth, dynamic gas response, microwave plasma-enhanced chemical vapor deposition (MWPECVD), optical emission spectroscopy (OES)

Received: May 16, 2022

Revised: July 14, 2022

Published online:

- [1] W. G. Eversole, US3030188A, **1962**.
- [2] J. C. Angus, H. A. Will, W. S. Stanko, *J. Appl. Phys.* **1968**, *39*, 2915.
- [3] M. H. V. de C. Nazaré, A. J. M. Neves, *Properties, Growth and Applications of Diamond*, INSPEC, London **2001**.
- [4] S. Matsumoto, Y. Sato, M. Tsutsumi, N. Setaka, *J. Mater. Sci.* **1982**, *17*, 3106.
- [5] M. Kamo, Y. Sato, S. Matsumoto, N. Setaka, *J. Crystal Growth* **1983**, *62*, 642.
- [6] V. Jha, H. Surdi, M. Faizan Ahmad, F. Koeck, R. J. Nemanich, S. Goodnick, T. J. Thornton, *Solid-State Electronics* **2021**, *186*, 108154.
- [7] H. Surdi, M. F. Ahmad, F. Koeck, R. J. Nemanich, S. Goodnick, T. J. Thornton, *IEEE Microwave Wireless Compon. Lett.* **2020**, *30*, 1141.
- [8] K. Su, Z. Ren, Y. Peng, J. Zhang, J. Zhang, Y. Zhang, Q. He, C. Zhang, Y. Hao, *IEEE Access* **2020**, *8*, 20043.
- [9] M. Zhang, W. Wang, S. Fan, G. Chen, H. N. Abbasi, F. Lin, F. Wen, J. Zhang, R. Bu, H.-X. Wang, *Carbon* **2021**, *176*, 307.
- [10] L. Shi, F. Xu, J. Gao, M. Yuen, S. Sun, J. Xu, K. Jia, D. Zuo, *Diamond Relat. Mater.* **2020**, *109*, 108098.
- [11] A. V. Karim, P. V. Nidheesh, M. A. Oturan, *Curr. Opin. Electrochem.* **2021**, *30*, 100855.
- [12] J. E. Butler, A. Vikharev, A. Gorbachev, M. Lobaev, A. Muchnikov, D. Radishev, V. Isaev, V. Chernov, S. Bogdanov, M. Drozdov, E. Demidov, E. Surovegina, V. Shashkin, A. Davydov, H. Tan, L. Meshi, A. C. Pakpour-Tabrizi, M.-L. Hicks, R. B. Jackman, *Phys. Status Solidi RRL* **2017**, *11*, 1600329.
- [13] A. L. Vikharev, A. M. Gorbachev, M. A. Lobaev, A. B. Muchnikov, D. B. Radishev, V. A. Isaev, V. V. Chernov, S. A. Bogdanov, M. N. Drozdov, J. E. Butler, *Phys. Status Solidi RRL* **2016**, *10*, 324.
- [14] N. Lambert, Z. Weiss, L. Klimša, J. Kopeček, Z. Gedeonová, P. Hubík, V. Mortet, *Diamond Relat. Mater.* **2022**, *125*, 108964.
- [15] V. Mortet, A. Taylor, M. Davydova, M. Lamač, N. Lambert, I. Elantyeve, J. Lorinčík, D. Troadec, M. Vronka, S. Potocký, *Diamond Relat. Mater.* **2022**, *124*, 108928.
- [16] G. Frangieh, M.-A. Pinault, J. Barjon, F. Jomard, J. Chevallier, *Phys. Status Solidi A* **2008**, *205*, 2207.
- [17] H. Pendar, J. J. Socha, *PLoS ONE* **2015**, *10*, 0139508.
- [18] N. Lambert, V. Mortet, in *13th International Conference on Nanomaterials - Research & Application* (Ed: J. Šhrbená Váňová), Publisher, Brno, Czech Republic **2021**, pp. 411–416.
- [19] C. Huang, C.-Y. Tsai, R.-S. Juang, *J. Appl. Polym. Sci.* **2012**, *124*, E108.
- [20] M. Nur, N. Bonifaci, A. Denat, V. M. Atrazhev, *IOP Conf. Ser.: Mater. Sci. Eng* **2019**, *509*, 012084.
- [21] M. Hiramatsu, K. Kato, C. H. Lau, J. S. Foord, M. Hori, *Diamond Relat. Mater.* **2003**, *12*, 365.
- [22] G. A. Bartholomew, D. B. van Vleck, C. Masters Vleck, *J. Exp. Biol.* **1981**, *90*, 17.